Three-dimensional finite element formulation for concrete failure at high-energy impact loadings

Travaš, Vanja

Doctoral thesis / Disertacija

2009

Degree Grantor / Ustanova koja je dodijelila akademski / stručni stupanj: **University of Rijeka, Faculty of Civil Engineering / Sveučilište u Rijeci, Građevinski fakultet**

Permanent link / Trajna poveznica: https://urn.nsk.hr/urn:nbn:hr:188:118687

Download date / Datum preuzimanja: **2025-03-31**

Three-Dimensional Finite Element Formulation for Concrete Failure at High-Energy Impact Loadings

Ph.D Thesis by

Vanja Travaš

Faculty of Civil Engineering at the University of Rijeka, Croatia

Doctoral Degree Programme

Mechanics of Structures

Rijeka, 2009

Three-Dimensional Finite Element Formulation for Concrete Failure at High-Energy Impact Loadings

Ph.D Thesis by

Vanja Travaš

Faculty of Civil Engineering at the University of Rijeka, Croatia

Doctoral Degree Programme

Mechanics of Structures

Supervisor

Prof. dr. sc. Joško Ožbolt

Rijeka, 2009

Mojim roditeljima u znaku vječne zahvalnosti

Acknowledgements

I would like to express my deep gratitude and special thanks to my supervisor, prof. dr. Joško Ožbolt for his irreplaceable guidance and tremendous support during the past few years of our collaborations that resulted in the accomplishment of the present doctoral thesis. It is also thanks to professor Ožbolt that I was given the opportunity to place my doctoral thesis in the scientific filed of impact loadings which I find very exciting and fascinating.

The guidance of prof. dr. Ivica Kožar has been extremely precious beyond doubt, as well. Thanks to professor Kožar I had the opportunity to present my Ph.D thesis at the 8th World Congress on Computational Mechanics (WCCM8) and the 5th European Congress on Computational Methods in Applied Sciences and Engineering (ECCOMAS 2008) held on the Lido Island in Venice from 30 June to 4 July 2008.

Comprehensive conversations with prof. dr. Gordan Jelenić who helped me understand the rigorous theoretical backgrounds of non-linear continuum mechanics, as well as the related finite element procedures necessary for the thesis, also contributed to the completion of this work. I would like to express my gratitude to professor Jelenić who had always found the time to answer every question of mine related to the domain of finite element method.

On the other hand, prof. dr. Gojko Balabanić and our pleasant conversations on various topics, but especially on physics and scientific objectivity, have enabled me to perceive the complex physical background of high-energy impact loadings and taught me to appreciate the approximate nature of the finite element analysis.

I would like to take this opportunity to express my sincere gratitude to prof. dr. Nevenka Ožanić for her guidance and remarkable support during both my graduate and postgraduate studies.

Special thanks to prof. dr. Rolf Eligehausen who, together with my supervisor prof. dr. Joško Ožbolt, made my sixth month residence at the Institute of Construction Materials in Stuttgart (2008) possible. At that time I work on the numerical implementation of the microplane material model.

Finally, I want to thank all of my friends and colleges at the Faculty of Civil Engineering in Rijeka, as well as my friends and colleges in Stuttgart who offered me their support in difficult times and tolerated my absence during the time of my research. I wish to especially thank some of my best friends for their important intellectual contributions to my research during our frequent coffee breaks.

Above all, I would like to thank my parents and my brother for their support.

Abstract

In the present thesis a three-dimensional finite element formulation for concrete failure under high-energy impact loadings is presented. The formulation is based on the theoretical framework of continuum mechanics and irreversible thermodynamics. In order to obtain a non-unilateral contact/impact description, the spatial regions occupied by the bodies under collision are discretized with linear tetrahedral elements. The temporal discretization is traditionally conducted by finite difference method. During the time of contact, the contact constrains are satisfied with the Lagrange multiplier method adapted for the explicit time integration. The frictional behaviour on the contact interface is assumed to be of kinematic type described with the Coulomb friction model. At the numerical implementation level, the dissipative nature of friction forces is introduced via the relaxation of tangential displacement on the contact interface. The quantitative description of expected finite strains is conducted according to the Update Lagrange formulation of motion. Following the standard notations used in contact mechanics, the concrete body is denoted as target body and the body that transmits its kinetic energy, as the contractor body. The hyperelastic material model is used to define the constitutive behaviour of the contractor body. On the other hand, in order to simulate the mechanical behavior of the concrete body, the stress-strain relationship is carried out via the rate sensitive microplane material model with relaxed kinematic constraint (co-rotational formulation). It is important to note that the concrete strain rate effect can be particularly evidenced in impact loadings. Thus, to numerically replicate the concrete response in a realistically way, the strain rate effect is introduced by means of the energy activation theory of bond ruptures. For this purpose, the macroscopic strain measure is performed with the Green-Lagrange strain tensor. Damage and cracking phenomena are modeled within the concept of smeared cracking. Furthermore, the crack band method is used with the aim of assuring the objectivity of the analysis with respect to the size of the finite elements. Finally, in order to validate the developed formulation, the free fall drop weight experiment is numerically replicated. The retrieved numerical results are evaluated, discussed and compared with the experimental results. A parametric study aimed at numerical investigation of the influence of loading rate on the failure mode of beams under impact loadings, is carried out. It is shown that the plain beam resistance and failure modes strongly depend on the loading rate. Indeed, the numerical formulation predicts correctly the beam failure patterns investigated with the experimental methodology. Namely, for relative low impact velocities the numerical results coincide with the experimental results providing the expected bending mode of failure (mode-I). On the other hand, by increasing the loading rate, there is a transition of the failure mechanism from bending to shear mode (mixed mode). Based on the retrieved numerical predictions, one may conclude that the developed numerical formulation is adequate for investigating the response of concrete under high-energy impact loadings. Indeed, due to the fact that the failure process in concrete occurs in a very short period of time, the numerical study is useful and necessary for better understanding of damage phenomena occurring under impact loadings.

Contents

List of figures

Nomenclature

CHAPTER 3: SPATIAL DISCRETIZATION

CHAPTER 4: TEMPORAL DISCRETIZATION

CHAPTER 5: MICROPLANE MATERIAL MODEL

CHAPTER 6: CONTACT MECHANICS

List of figures

Nomenclature

Respecting the traditional signatures used in the theory of continuum mechanics, in the present Thesis the scalar quantities are denoted by a Latin or Greek italic letter while vectors, tensors and/or matrices are represented by the boldface characters. The subscripts *i, j, k, l, r* and *s* denote specific component of a vector or tensor quantity in question. When possible, the Einstein summation convection will be used.

$$\underbrace{\mathrm{b} \cdot \mathrm{A} \cdot \mathrm{b}}_{\substack{\text{tensor}\\\text{notation}}} = \underbrace{\mathbf{b}^{\mathrm{T}} \mathbf{A} \mathbf{b}}_{\substack{\text{matrix}\\\text{notation}}} = \underbrace{b_i A_{ij} b_j}_{\substack{\text{indicial}\\\text{notation}}}$$

Only the most frequent symbols are listed below.

Chapter 2

P	1$^{\text{st}}$ Piola-Kirchhoff stress tensor
S	2$^{\text{nd}}$ Piola-Kirchhoff stress tensor
s	back-rotated Cauchy stress tensor
ε	Cauchy strain tensor
σ	Cauchy stress tensor
X	coordinates vector for a particle in the material (referent) configuration
x	coordinates vector for a particle in the spatial (current) configuration
F	deformation gradient tensor
φ	deformation mapping function
ρ	density
F	force
E	Green-Lagrangian strain tensor
ψ	Helmholtz free energy function
I	identity matrix
J	Jacobian of deformation
K	kinetic energy

$\boldsymbol{\tau}$	Kirchhoff stress sensor
δ_{ij}	Kronecker delta
λ, μ	Lamé constants
$\mathbf{b}$	left Cauchy-Green deformation tensor
$\mathbf{v}$	left stretch tensor
m	mass
$\mathbf{R}$	material rotation tensor
$\mathcal{C}$	Material stiffness tensor
$^{0}\mathrm{C}, {}^{1}\mathrm{C}$	notations for the continuum referent and current configuration, respectively
$\hat{\mathbf{E}}, \hat{\mathbf{e}}$	orthonormal basis in the referent and current configuration, respectively
υ	Poisson ration
d	rate-of-deformation tensor
$\mathbf{C}$	right Cauchy-Green deformation tensor
$\mathbf{U}$	right stretch tensor
w	spin tensor
W	strain energy function
$\mathbf{t}$	surface traction
l	velocity gradient tensor
$\underline{\boldsymbol{\sigma}}$	Voight notation for the Cauchy stress tensor
$\mathbf{b}$	volume forces
E	Young's modules

Chapter 3

$^{n}\mathbf{X}$	coordinates vector of a FE node n
$\tilde{\mathbf{u}}(\mathbf{x})$	displacement vector for an arbitrary point inside the element domain Ω_e
Γ_c	domain boundary where the contact constraint are activated
Γ_u	domain boundary where the displacement boundary conditions are prescribed
Γ_t	domain boundary where the traction boundary conditions are prescribed

Ω_e	domain occupied by a finite element
A	FE assembling operation (relate local dof to global dof)
$\mathbf{F}^{ex}$	FE external force vector
$\mathbf{F}^{in}(\boldsymbol{\sigma})$	FE internal force vector
N	FE interpolation function matrix
r	FE out-of-balance force vector
K	FE stiffness matrix
B	FE strain-displacement matrix
V_e	FE volume in the material (referent) configuration
v_e	FE volume in the spatial (current) configuration
u	general notation for a displacement vector
Ω	general notation for a domain of a occupied special region
$\mathbf{K}_g$	geometrical stiffness matrix
$N_n(\mathbf{x})$	interpolation function defined in a element node n
J	Jacobian transformation matrix
$\overset{\triangledown}{\boldsymbol{\sigma}}$	Jaumann rate of the Cauchy stress tensor
$\mathbf{K}_m$	material stiffness matrix
$\boldsymbol{G}$	matrix that collects the direction cosines of the normal vector **n** on the boundary Γ_t
n_c	number of contact constraint violation
n_e	number of element in the spatial discretization
n_m	number of microplanes used to perform the unit sphere approximation
n_n	number of nodes over the element
D	stiffness matrix
$\mathbf{K}_T$	tangent stiffness matrix
δu	test function (virtual displacement)
δv	test function (virtual velocities)
$\boldsymbol{S}$	three-dimensional strain operator
n	unit normal vector

${}^{n}\mathbf{u}$	vector of a node n displacement components
$\boldsymbol{\xi}$	vector of tetrahedral element barcentric coordinates
$\underline{\boldsymbol{\varepsilon}}$	Voight notation for the Cauchy strain tensor

Chapter 4

Δt_{ct}	critical time increment
L	Lagrangian of the system
Π	the total potential energy for a hyperelastic continuum
t	time
Δt	time increment
$\mathbf{C}$	viscous damping matrix

Chapter 5

$\boldsymbol{\tau}_r$	back-rotated Kirchhoff stress tensor
$\mathbf{n}^{\ell}, \mathbf{m}^{\ell}, \mathbf{k}^{\ell}$	base vectors on the ℓ microplane
w_{cr}	critical concrete crack aperture
s_D^{ℓ}	deviatoric stress components on the ℓ microplane
Ψ^{ℓ}	discontinuity function dedicated to the ℓ microplane
$C_{,eff}$	effective microplane secant module
$e_{,eff}$	effective microplane strain component
H	Henky strain tensor
$E_{D,0}$	initial (undamaged) microplane deviatoric module
$E_{M,0}, E_{K,0}$	initial (undamaged) microplane shear modules
$E_{V,0}$	initial (undamaged) microplane volumetric module
ω_D	material integrity parameter related to the microplane deviatoric strain
ω_M, ω_K	material integrity parameter related to the microplane shear strain
ω_V	material integrity parameter related to the microplane volumetric strain
C_D	microplane secant deviatoric module

C_M, C_K	microplane secant shear module
C_V	microplane secant volumetric module
$\mathbf{e}_N^\ell, \mathbf{e}_T^\ell$	normal and tangential strain component on the ℓ microplane, respectively
X_1, X_2, X_3	rectangular Cartesian coordinates (material coordinates)
x_1, x_2, x_3	rectangular Cartesian coordinates (spatial coordinates)
ε_r	referent deformation value (FE cracking visualization)
$\dot{\gamma}$	scalar quantity associated to the rate of the Green-Lagrangian strain tensor
$\mathbf{e}_M^\ell, \mathbf{e}_K^\ell$	shear microplane strain components on the ℓ microplane
s_M^ℓ, s_K^ℓ	shear stress components on the ℓ microplane
$\mathbf{e}^\ell$	strain vector on the ℓ microplane
C_{ijkl}^{m}	tangent stiffness microplane tensor
e_V^ℓ, e_D^ℓ	volumetric and deviator strain component on the ℓ microplane, respectively
s_V	volumetric stress components on the ℓ microplane

Chapter 6

$\mathbf{G}$	contact displacement constrain matrix
Π_c	contact energy functional
$\mathbf{K}_T^c$	contact tangent stiffness matrix
(ξ^1, ξ^2)	contractor node and target surface intersection coordinates
$m^{\alpha\beta}$	contravariant metric tensor components
$\mathbf{x}_p$	coordinates vector of nodes over the target surface
$m_{\alpha\beta}$	covariant metric tensor components
μ	friction coefficient
$\mathbf{g}$	gap vector
$\Delta\mathbf{u}^C$	incremental displacement vector due to contact loadings
$\Delta\mathbf{u}^D$	incremental displacement vector due to dynamic loadings
$\Delta\lambda$	incremental Lagrangian multiples vector
$[[\mathbf{nu}]]$	jump in the displacement field on Γ_c

$[[\mathbf{n}\,\boldsymbol{\sigma}]]$	jump in the stress field on Γ_c
$\boldsymbol{\lambda}$	Lagrange multiplier vector
β, γ	Newmark integration parameters
$\mathbf{t}_N, \mathbf{t}_T$	normal and tangential component of a traction vector $\mathbf{t}$ on Γ_c, respectively
$\mathbf{v}_N, \mathbf{v}_T$	normal and tangential component of a velocity vector $\mathbf{v}$ on Γ_c, respectively
$\mathbf{n}^m$	normal vector in the intersection point between the contract node and target surface
N^p	shape functions of nodes over the target surface
$\overline{\mathbf{a}}_\alpha, \overline{\mathbf{a}}_\beta$	target surface tangent vectors
$\mathbf{a}_\alpha, \mathbf{a}_\beta$	target surface unit tangent vectors
κ	upper index used for the association of data for bodies under collision

Chapter 1

Introduction

1.1 Motivation

The subject of the thesis is primary concentrated on the mechanical behaviour of structures made of quasi-brittle material under severe impact loading. Particularly, the main attention is here dedicated on concrete structures subject to high-energy impact loading. Note that these kinds of events are characterized by highly concentrated strains generated in a relatively very short period of time. Under these circumstances, the considered transient event can be widely found in industrial practice as well as during the exploitation of civil structures. Thus, it is easy to agree that, due to the complex mechanism of failure, the experimental and numerical investigations are needed to accurately predict the consequence and eventual risks caused by impact accidents. The fact that impact loading can occasionally lead to structure collapse, *obliges us to study impact loadings*.

Behind the author general interest for mechanical interactions, the thesis mainly emerges from the author's wishes and intentions to modestly contribute to this wide and complex issue.

§ *Problem definition*

The structure response to impact is influenced by the structure mass and stiffness. Due to the complexity of such system, the author assumes that a productive numerical investigation can be obtained by reducing the scale of observation. According to that, the focus of the thesis is retained on concrete elements (such as beams, columns or plates) and not on the whole concrete structure. Furthermore, in order to focus the study only on the concrete behavior, the aspects related to reinforcements are here omitted.

The aforementioned assumption may be supported by the fact that the structure global stiffness degradation is always related to local damage (structure elements) which can be generally interpreted as a consequence of concrete local failure. On the other hand, with a realistic numerical prediction of the response of structural elements, the analysis of the whole structure can be obtained by extending the same concept to the entire structure. However, since at this scale of observation the presence of reinforcements cannot be neglected, passing from local to global analysis is obviously not a trivial task. In order to preserve simplicity of the analysis, the abovementioned is used as an additional argument in favor of focusing the study solely on structural elements (particularly beam elements).

By defining the subject of interest, the problem definition arises almost naturally. Namely, as the title of the thesis indicates, the intention is to numerically simulate the mechanical behavior of concrete elements under impact. The task will require a numerical formulation sensitive to a complex mechanism of the growth of concrete microstructural cracks. Thus, in order to reproduce the acute nature of failure under severe impact loading, the numerical formulation should be able to predict macrostructural (inertial forces) but also microstructural mechanical effects (strain rate effect).

It is clear that the intention required accurate model calibration. For this purpose, the proposed numerical formulation will be validated by performing a comparative study of available experimental results with related numerical predictions. In order to validate the range of applicability, the experimental reference will be chosen in a way to activate different types of failure (Bentur, Mindess & Banthia, 1986; Sukontasukku & Mindess, 2003; Sukontasukkul, Nimityongskul & Mindess, 2004).

It is important to point out the problem shows highly non-linear properties. The non-linear nature of the problem directly implies that the numerical description should provide computational stability and robustness. Namely, it is evident that:

(i)   a non-linear mechanical behavior of concrete (material non-linearity),

(ii) possibly large displacements in front of the contact/impact zone (geometrical non-linearity)

(iii) and a non-linear nature of contact description between bodies (contact non-linearity)

will require the use of an incremental-iterative solution strategy.

§ *Note on experimental observations*

The behavior of concrete under severe impact loading is currently under intensive experimental and numerical investigation (Reinhardt, 1982; Bentur, Mindess & Banthia, 1986; Comite Euro-International Du Beton (CEB), 1988; Weerheijm, 1992; Buchar, Voldřich, Rolc & Lazar, 2002; Ballew, 2004; May, Chen, Owen, Feng & Bere, 2005; Remennikov & Kaewunruen, 2007; Zinn, Stangenberg, Borgerhoff, Chauvel & Touret, 2007). Particularly, due to the presently available computational possibilities, the numerical investigations are especially attractive. However, to reproduce the real response of concrete under impact, there is an evident need for experimental observations. Namely, the validation of numerical analysis requires extensive experimental documentations, which are also related to a lot of difficulties due to the complexity of impact phenomena.

The most popular and efficient experimental method of studying concrete under impact loading is the *free fall drop weight test*. The experiment mainly consists of dropping the impact hammer (with pre-defined mass) on concrete element placed at the end of the dropping trajectory. Two typical experimental devices are shown in Fig. 1.1.

Figure 1.1 Free fall drop weight test. Pictures taken from: **a)** May et al. (2005) and **b)** Sukontasukkul et al. (2004)

Evidently, the system input energy is defined by the hammer mass and the dropping altitude. Note that the same system input energy can be obtained at a relatively low but also at a relatively high impact velocity. Accordingly, one could ask why the affiliation of impact character is here expressed in terms of energy instead of velocity. Well, from the hierarchic point of view, it can be said the description in terms of energy is more accurate then the description in terms of velocity. Namely, both the velocity and mass information are

contained in the kinetic energy of the hammer. For this reason, the energy-related description seemed the most adequate choice. However, it should be pointed out that even in case of elevated energy of impact loading, characterized by a relatively slow impact velocity, the response of concrete will be significantly different than in case of impact with the same impact energy but with a relatively high collision velocity. Therefore, the energy-related description should not be viewed as a general classification of consequences on bodies under impact.

With a pre-defined test program, the measurement of forces in the free fall drop weight experiment is performed by accelerometers. It is also important to point out that in order to transform the whole system input energy into the kinetic and strain energy of the concrete element under consideration, the dropping hammer should be made of steel with high stiffness. Only in this manner the presents of its strain energy can be minimized (Fig. 1.2).
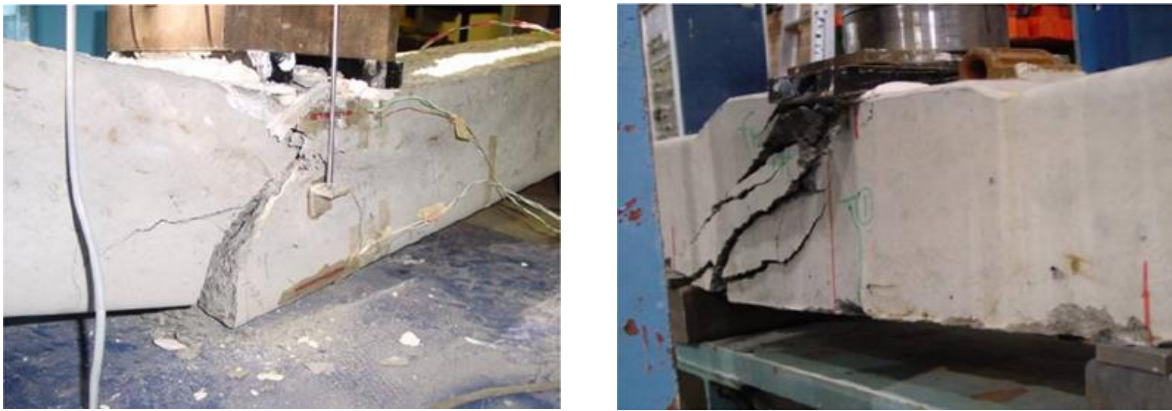
Figure 1.2 Railway concrete sleepers under impact loadings (pictures taken from Remennikov & Kaewunruen, 2007)

The results of the briefly described experimentation methodology (Fig. 1.1) show that loading rate significantly influences the response of structures made of quasi-brittle materials. In fact, by comparing the concrete response under static loading conditions with its response at high loading rate (impact loading), it can be deduced that the nominal strength increases with the increase of loading rate. Moreover, it is well known that the failure also depends on loading rate. The response depends on loading rate through three different effects. (i) Through the creep of the bulk material between the cracks. (ii) Through the dependency rate of the growing micro-cracks. (iii) Through the effect of structural inertia forces, which can significantly influence the state of stresses and strains at the material level. Principally, each one of the abovementioned influences is always present. However, depending on the type of material and loading rate, the first, the second or the third effect may become predominant. As far as cracking and damage phenomena are concerned, the first effect is important only in case of relatively low loading rates (creep-fracture interaction). The second effect predominates in case of moderate loading rates while the last one, in case of relatively high loading rates (impact loading).

Apart the influence of loading rate, an additional problem related to high-energy impact loading is rather complex mechanism of energy transfer that takes place via contact surfaces between colliding bodies (Comite Euro-International Du Beton, 1988). Furthermore, according to the work of Sukontasukkul and Mindess (2003), the experimental analysis show that impact loading cannot be viewed as a problem of strain rate or extreme case of stress rate. Also, as Bentur, Mindess and Banthia (1986) reported, the experimental tests prove that it is difficult to obtain the energy balance by measuring the mechanical energies in the experiment. A few statements taken from the relevant article (Bentur, Mindess & Banthia, 1986) may summarize some interesting experiment findings:

"Even for the relatively low impact velocities used in these tests (~3 m/s), the peak load in the specimens occurred within about 1 ms after contact."

"The use of accelerometers mounted on the beams can be used to estimate the inertia load, as well as specimen velocities and accelerations. This permits load-deflection curves for impact loading to be generated."

"At the peak load measured by the instrumented tup, the inertia load may account for more than 2/3 of the total load."

"Failure to account for the inertia load may result in misleading conclusions."

"Estimations of energy from the instrumented tup loadings do not agree with the sum of the calculated kinetic energy and the energy expended in deflecting and fracturing the beam."

In order to justify the need of the proposed numerical formulation, resume that the mechanism of energy transformation cannot be identified through an experiment (Bentur, Mindess & Banthia, 1986). However, the kinetic energy transformation can be revealed numerically with an appropriated numerical formulation. Also, it should be point out that the experimental technique is somehow limited due to the fact that, even in case of low impact loading, the peak load is registered within 1 ms after the contact take place. Consequently, the relevant part of the deformation history is trapped in a very small time period and can be hardly reached by experimental methodology.

A similar problem can be observed in the case of penetration or concrete perforation problems (Fig. 1.3 – photo taken from the web site of National University of Singapore - Impact Mechanics Laboratory). Namely, from the numerical aspect, the problems are almost identical except for that the related numerical description should

_____

be able to handle highly concentrated strain in front of the impact zone (requirement for remeshing). Another very important difference from the free fall drop weight experiment is the relevant presence of heat energy arising from friction between bodies. For both experimental and numerical researcher, the presence of temperature gradients represents a challenging problem. Numerical formulations need realistic constitutive equations, which are often poorly calibrated being directly related to difficulties with experimental measurements. Thus, the currently conducted experimental researches are based on the principle of causality. This means that for the given system input data (impact velocity) the output system data is registered (deep of penetration). In this sense, the deformation history can be hardly obtained, since the penetration trajectory cannot be followed by instrumental devices. The difficulties in measurement are not only related to spatial restrictions but, due to the fact that penetration occurs in small time interval (~1 ms), also to temporal restrictions. However, there are promising experimental methodologies (like x-ray laminography) which are already in use for investigation of damage phenomena caused by impact loadings on concrete panels (Vossoughi, Ostertag, Monteiro & Albert, 2006).

Figure 1.3 Impact of steel nail into concrete a block

§ *Note on numerical expectations*

There are various numerical studies which are conducted in order to investigate the effect of loading rate on the response of concrete structure elements (Dilger, Koch & Kowalczyk, 1978; Reinhardt, 1982; Curbach, 1987; CEB, 1988; Bažant & Gettu, 1992; Weerheijm, 1992; Ožbolt & Reinhardt, 2001, 2005; Saatci & Vecchio, 2009). Most of the studies employ different constitutive relations similar to the spring-dashpot models of visco-

elasticity. Some models cover only a limited range of loading rates whereas other models are more general and applicable to large range of loading rates. However, from the perspective of strain rate sensitivity effect, there are only a limited number of numerical studies in which the concrete failure mode is investigated as a function of loading rate (Sukontasukku & Mindess, 2003; Ožbolt & Reinhardt, 2005; Saatci & Vecchio, 2009). In the proposed numerical formulation a rate dependent model, based on the rate process theory (Krausz & Krausz, 1988) of bond ruptures, is used. The model was originally proposed by Bažant et al. (2000) and later coupled with the microplane model for concrete. The choice can be justified by simply taking into account the results of other studies where the mentioned combination of models showed impressive correspondence with experimentally evidenced phenomena (Ožbolt & Reinhardt, 2001; Ožbolt, Rah & Meštrović, 2006).

With regard to the free fall drop weight experiment (Fig. 1.1 & Fig. 2.1), the subject of thesis will be based on the failure of a plain concrete beams under impact loadings. However, the present numerical description will be principally valid for impact loadings of any type.

In order to validate the proposed formulation, the numerical experiment is conducted by reproducing the free fall droop weight experiment (Fig. 1.1) in which the altitude of the dropped hammer is set as a variable. Since the contact force between the dropped hammer and the tested concrete beam is unknown, the mechanical interaction have to be numerically simulated (contact problem). The range of investigated impact velocities will imply very high strain rates but still smaller than the strain rates at which the dropping hammer would cause extreme local damage (concrete local crashing).

According to the abovementioned, a development of the present numerical formulation represents a logical extension of the current state of knowledge in the field of concrete behavior under severe impact loadings. Namely, due to the fact that the failure process of concrete occurs in a very short period of time, the numerical study is useful and necessary for a better understanding of concrete damage phenomena under impact. Unlike the experimental investigations, by assuming isothermal conditions, the numerical simulation should reveal the kinetic energy transformation into other mechanical energies generated during the deformation history. Furthermore, it is also expected that the proposed numerical formulation will be able to reveal the contribution of inertial, viscous damping and internal forces into reaching equilibrium state with contact forces on the contact/impact surface. The formulation will consequently help defining further research directions of this still insufficiently explored scientific and engineering field.

Resuming, the primary aim of the study can be viewed as the test of whether the proposed numerical formulation is able to realistically predict the rate-dependent failure mechanism and, if it can, as investigation of the influence of impact velocity on the concrete response.

1.2   Hypothesis

The hypothesis was (2006):

> *"For concrete structures under high-energy impact loadings, the structural response is controlled by inertial forces and the influence of strain rate sensitivity is less important and can be consequently neglected in related numerical simulations."*

and in the present thesis I will verify if the proposed three-dimensional numerical formulation, for materials and loadings type under consideration, predicts my suspicions.

1.3   Purpose of the thesis

Following the conclusions drawn from experimental observation; in order to numerically replicate the concrete failure at impact load, the numerical formulation should be characterized by highly predicting abilities. This fact can be interpreted as a primary purpose of the thesis, since it is a prerequisite for the accomplishment of the following intentions.

- Based on the adopted theoretical assumptions and numerical approximations, the main purpose (that will lead to others) is to check whether the developed numerical formulation is able to realistically predict the concrete failure at different loading rates. If it can, the following purposes shall be taken into account.

- Reveal the transformation of impact kinetic energy into other mechanical energies.

- Find out the contribution of inertial, viscous damping and internal forces to reaching the equilibrium state with contact forces arises as a consequence of bodies collision.

- Based on the objective overview of the proposed numerical formulation, define further research directions for the development of numerical models for simulation of concrete penetration and perforation problems.

1.4   Outline of the thesis

Before summarizing the chapters, note that the thesis can be viewed as a unification of selected current knowledge and certain new findings in the field of computational mechanics, needed for the numerical investigation of quasi-brittle materials under severe impact loading. The thesis contains ten individual chapters which are summarized as follows.

Chapter 2 – Continuum preliminaries

It is well known that the structural response to any type of external loading is always governed by the structure micro-mechanical properties. The physical properties of practical importance emerge as a consequence of material particles interaction. Thus, it is evident that the body collision event implies a very complex mechanical system which can hardly be approached at this micro-scale of observation. Therefore, the problem is here defined in the framework of continuum mechanics. Accordantly, the presence of material particles is here ignored and the natural discontinuity is replaced by a presupposed continuous distribution of matter. For this purpose, the second chapter is dedicated to a brief overview of the continuum mechanics theory.

Chapter 3 – Spatial discretization

As the title of the thesis suggests, the finite element method (FEM) is used to perform the discretization of governing equations in the spatial regions occupied by bodies under collision. Since the temporal discretization and the discussion related to contact mechanics are addressed in two separated chapters, the time dimension and restriction on displacements (caused by contact) will be temporary ignored. Accordingly, the third chapter will address the derivation of the weak form of the previously given strong form of the problem. Later on, the neglected influences will be applied to derive the discrete form of equilibrium equation. Furthermore, as the choice of finite element (FE) directly influences the numerical description of contact/impact events, some useful properties of the here used linear tetrahedral element will be presented. At the end of the chapter, a brief overview of the Update Lagrange formulation, used to solve the non-linear deformation problem, will be given.

Chapter 4 – Temporal discretization

It is clear that impact loadings are time depended phenomenon characterized by the evident presents of inertial forces. With the aim of introducing the contribution of inertial forces in the equilibrium equation, the principle of least action (Hamilton principle) will be here presented. After that, the temporal discretization of the unconstrained equation of motion (no contact) will be carried out by application of the Newmark's Beta integration method. For this purpose, basic assumptions and related possibilities will be presented (such as switching between the implicit and explicit integration technique). The Newmark's Beta method will be also used to evidence that the original form of equations implies necessary modifications to introduce the contact displacement restrictions. This will be separately explained in a chapter dedicated to contact mechanics. Furthermore, since the deformation history is "trapped" in a relatively small time period, a discussion on an

appropriate time integration technique will be given. The attention is paid mainly to numerical stability and numerical properties required to preserve energy in numerical simulations. At the end, the traditional phenomenological manner of introducing viscous damping effect will be addressed and discussed from the perspective of the thesis subject.

Chapter 5 – Microplane material model

An almost crucial part of the proposed numerical formulation is addressed in the this chapter. Namely, in order to numerically simulate the real concrete response for severe impact loading, an appropriate constitutive material description is provided in accordance with restrictions laid down by the First and Second Law of Thermodynamics. Since the mechanical behavior of concrete implies a very complex microstructural stress transfer mechanism, the microplane material model is found to be the most appropriate choice for the constitutive definition. A discussion aimed to prove the benefit of the microplane model and the basics theoretical assumptions are provided therein. Afterwards, an extensive discussion on the choice of appropriate microplane stress and strain tensors is elaborated. The concepts of effective microplane components and the microplane discontinuity function are included. Finally, as the rate dependency effect plays an especially important role in impact loading, the respective influence is also introduced by means of the energy activation theory.

Chapter 6 – Contact mechanics

The issue of mechanical interactions is introduced at the beginning of the sixth chapter. The chapter begins by exposing the respective strong formulation of any contact problem (Signorini problem). Thereafter, the discretization of the given governing equations is conducted. The method of Lagrange multipliers is elaborated with the purpose of introducing the restriction in the solution space of kinematically admissible displacements. Some difficulties related to time integration are also addressed. Furthermore, since the presents of friction plays a special importance, its presence is taken into account by application of the phenomenological Coulomb friction model. The chapter ends with an iterative solution strategy used for solving the resulting system of equations.

Chapter 7 – Contact detection

An especially important part of the proposed numerical formulation lies in an almost "chirurgical" requirement for detection of contact between bodies under collision. Therefore, it seemed reasonable to situate the contact detection strategy in a separated chapter. Indeed, in order to accurately capture the frictional behavior on contact interfaces, the contact detection phase should give a valid geometrical approximation of the contact position (especially important in concrete perforation and penetration problems). It is necessary to point out that the accurate computation of contact position is very important since a rough contact detection algorithm can make the whole formulation extremely fragile. As a matter of fact, only one wrong contact detection can

destroy the physical meaning of the numerical analysis. For this purpose, a detailed discussion of the adopted global and local detection strategy is presented in this chapter.

Chapter 8 – Adaptive finite elements

Since impact loading may lead to a perforation of a body, the periodical finite element mesh adaptations are needed. Due to a lot of complexities related to progressive three-dimensional mesh adaptations, this chapter should be only viewed as an introduction to future related investigation. Namely, the FE adaptive strategy is here discussed in order to replace the poor conditioned mesh with a new one with better properties. However, some preliminary computations showed that penetration and perforation problems imply a special requirement of robustness of the adopted mesh generation algorithm. Also, since the transfer data operator is expecialy influenced by the discretization, an accurate adaptation in the cracking zone ought to be carried out. Namely, the quasi-brittle failure represents a challenging task for the transfer operator that should preserve the discrete nature of cracking during the mapping procedure of damage parameters from the old Gauss points to the new appropriated one. In order to meet such requirement, the new mesh should somehow be in accordance with the old mesh. This requirement directly increases the expectation of the mesh generation algorithm. All the mentioned are appropriately elaborated in this chapter.

Chapter 9 – Computational aspects

The ninth chapter arises from the need to validate the proposed formulation. Namely, the chapter retains the algorithmic structure of the program code developed according to the previously presented chapters. The chapter also contains some opinions and discussions related to possible code parallelization. Namely, note that the pretension of high mesh density around zones of special interest will lead to a rapid increase of computational time. In particular, since the non-coupled systems of equations are spread over the entire program code (vectorial operations); the author opinion is that implementing the OpenMP parallelization technique is especially attractive. Such opinion can be appropriately justified by taking into account the previously introduced computational phases and taking into account the perspective of their parallelization.

Chapter 10 – Numerical examples

The penultimate chapter embodies the whole thesis by demonstrating few numerical examples. In order to validate the formulation, the numerical results are compared with the experimental data available in the literature. Since there are well documented experimental observations of plain concrete beams under impact loading, the numerical experiment is performed by simulating three-point bending failure. In particular, the transitions between failure modes, attained at different velocity of impact, are observed and discussed. An interesting overview of the numerical possibility to investigate the dynamics of fracture is also evidenced. Furthermore, it is shown that the propagation of compressive stress wave can be used as an additional argument for the validation of the presented but also similar numerical formulation. In all cases, the energy balance diagram shows that the sum of mechanical energies is equal to the total energy (isothermal conditions), which

confirms that the dynamic equilibrium has been reached. To illustrate the delivered adaptive finite element strategy, the chapter ends with a numerical example of penetration of steal anchor into a concrete block. Due to the large concentrated displacements in front of the contact/impact zone, the FE mesh is progressively adapted to the occurred deformations. However, since the computations related to remeshing and refinement is computationally expensive; the given example should be viewed only as a preliminary example which will serve to define future research directions.

Chapter 11 – Summary and conclusions

The last chapter is dedicated to objective and subjective conclusions. The objective part refers to the validation of the proposed numerical formulation and the subjective part refers to some conclusions on future expansions of the formulation. The weak points of the proposed formulation are also discussed and, according to such weak points, some preliminary directions for further activities are given.

Chapter 2

Continuum preliminaries

2.1 Introduction

The subject of the thesis might be defined as fracturing of monolith concrete mass into discrete fragments as a consequence of high-energy impact loading. However, in order to avoid the complex description of fragmentation (Pandolfi & Ortiz, 2002), the development of the proposed numerical formulation starts with the application of *continuum mechanics* (Bowen, 2007). By introducing the continuum concept, it is possible to define tensor fields as continuous functions of spatial coordinates. In order to make this assumption acceptable, the scale of observation must abide by the principle of *representative elementary volume* (REV) that also sets up the limit of continuum mechanics applicability. The principle requires that in all REV cells the property on a material macroscopic level should be defined as an average data of the property at the microscopic level. The macroscopic material level is defined by a finite number of REV cells, further denoted as continuum point. By contrast, material points refer to an infinite number of particles contained in the material structure and denote microscopic material level. According to the REV principle, the impact event is monitored on the macroscopic scale where all mechanical data are interpreted as average data of material points proximity. Since the subject

of the thesis is placed in the framework of continuum mechanics, before proceeding with the development of the related numerical description, it seems appropriated to give a basic overview of the continuum theory.

2.2   Finite strain

It is reasonable to expect that under high-energy impact the concrete body will suffer finite deformation, translation and rotation. In order to numerically simulate the history of deformation, an appropriated and accurate description of motion is inevitable. For this purpose, the basic concepts and mathematical relations of finite strain kinematic are hereafter summarized. It must be stressed out that the presented relations, valid in continuum mechanics theory, are also valid inside FE, as well.

2.2.1 Kinematics of finite strain

Consider an undeformed continuum body at time $t \subset \Re^+$ occupying a geometric region $\boldsymbol{B} \subset \Re^3$ denoted as ^{0}C configuration. In order to track the spatial and temporal evolution of mater, a fixed rectangular Cartesian coordinate system, with origin O and orthonormal basis $\hat{\mathbf{E}}_J$ (2.1), is attributed to position ^{0}C (Fig. 2.1). The ^{0}C configuration is known as *reference configuration* (*reference frame*).

$$\hat{\mathbf{E}}_J = \left\{ \hat{E}_1 \quad \hat{E}_2 \quad \hat{E}_3 \right\}^{\mathrm{T}} \quad \text{where} \quad J = 1,2,3 \tag{2.1}$$

In addition, suppose a force field that causes the continuum to move and deform. The change in configurations is the result of the existing displacement field which is defined by a displacement vector **u** attributed to each point in the continuum. Principally, each displacement vector $\mathbf{u}=\{u_1,u_2,u_3\}^{\mathrm{T}}$ contains two displacement components characterized as *rigid-body motion* (translation and rotation) and *deformation*. During the time of evolution, ^{0}C configuration suffers respective matter transformations governed by the fundamental laws of physics. At an arbitrary time $t \in [t_0,t_1]$, the space occupied by the continuum body is denoted by ^{1}C configuration (Fig. 2.1), usually referred to as the *current configuration* (*current frame*). This frame is related to a coordinate system with origin o and orthonormal basis $\hat{\mathbf{e}}_i$ (2.2).

$$\hat{\mathbf{e}}_i = \left\{ \hat{e}_1 \quad \hat{e}_2 \quad \hat{e}_3 \right\}^{\mathrm{T}} \quad \text{where} \quad i = 1,2,3 \tag{2.2}$$

Before proceeding, it is opportune to discuss some geometrical aspects of the basis vectors in the reference (2.1) and current configuration (2.2). First of all, note that due to the orthogonal property of covariant basis $\hat{\mathbf{E}}_J$ and $\hat{\mathbf{e}}_i$, their dot product with contravariant vectors $\hat{\mathbf{E}}^J$ and $\hat{\mathbf{e}}^i$ is defined as (Bonet & Wood, 1997):

$$\hat{\mathbf{E}}_I \, \hat{\mathbf{E}}^J = \delta_I^J \qquad \text{and} \qquad \hat{\mathbf{e}}_i \, \hat{\mathbf{e}}^j = \delta_i^j \, , \tag{2.3}$$

where $\delta_I{}^J$ and $\delta_i{}^j$ are components of *Kronecker δ* (2.4).

$$\delta_{ij} = \begin{cases} 1 & \text{if} \quad i = j \\ 0 & \text{if} \quad i \neq j \end{cases} \tag{2.4}$$

The metric of the Euclidian space in ^{0}C configuration is characterized by the metric tensor $\widehat{\mathbf{E}}$ (2.5).

$$\widehat{\mathbf{E}} = (\hat{\mathbf{E}}_I \, \hat{\mathbf{E}}_J)\hat{\mathbf{E}}^I \otimes \hat{\mathbf{E}}^J = \hat{E}_{IJ}\hat{\mathbf{E}}^I \otimes \hat{\mathbf{E}}^J = (\hat{\mathbf{E}}^I \, \hat{\mathbf{E}}^J)\hat{\mathbf{E}}_I \otimes \hat{\mathbf{E}}_J = \hat{E}_{IJ}\,\hat{\mathbf{E}}_I \otimes \hat{\mathbf{E}}_J \tag{2.5}$$

Similarly, the tensor $\hat{\mathbf{e}}$ defines the metric in ^{1}C configuration (2.6).

$$\hat{\mathbf{e}} = (\hat{\mathbf{e}}_i \, \hat{\mathbf{e}}_j)\hat{\mathbf{e}}^i \otimes \hat{\mathbf{e}}^j = \hat{e}_{ij}\hat{\mathbf{e}}^i \otimes \hat{\mathbf{e}}^j = (\hat{\mathbf{e}}^i \, \hat{\mathbf{e}}^j)\hat{\mathbf{e}}_i \otimes \hat{\mathbf{e}}_j = \hat{e}_{ij}\,\hat{\mathbf{e}}_i \otimes \hat{\mathbf{e}}_j \tag{2.6}$$

From ^{0}C to ^{1}C, the coordinate axes rotations are given by the dot product of basis $\hat{\mathbf{E}}_J$ and $\hat{\mathbf{e}}_i$ as

$$\hat{\mathbf{E}}_J \, \hat{\mathbf{e}}_i = \alpha_{Ji} = \alpha_{iJ} \, , \tag{2.7}$$

where α_{ji} denote the cosines directions between the reference and current coordinate axes. The coordinate system translation, between ^{0}C to ^{1}C configurations (Fig. 2.1), is given by vector $\mathbf{j} = \{j_1, j_2, j_3\}^T$.
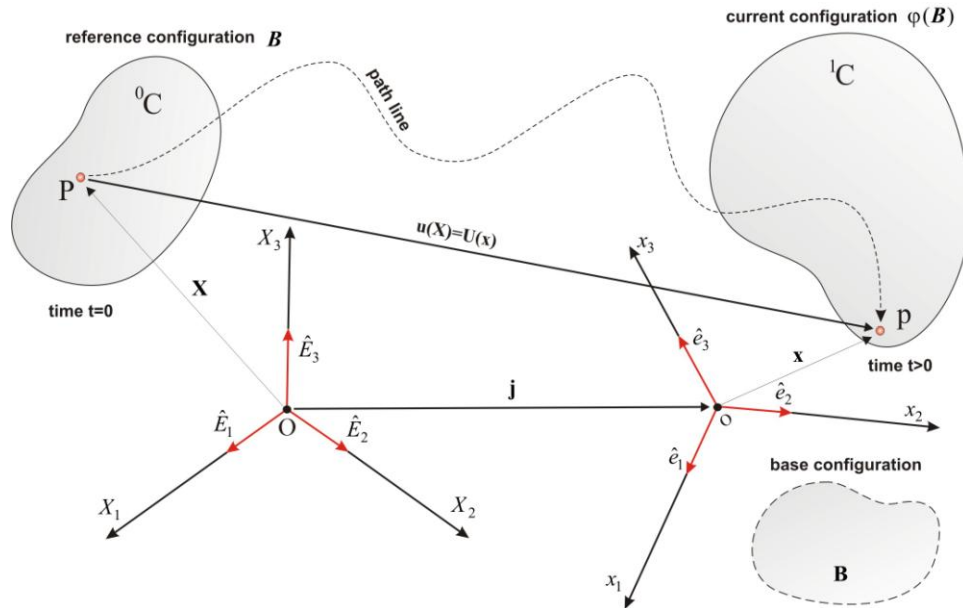
Figure 2.1 Lagrangian kinematics (description of motion from the reference to the current configuration)

In order to illustrate the kinematical aspect of motion (Fig. 2.1), consider a particle $P \subset B$ in the reference configuration with position vector $\mathbf{X} = X_J\hat{\mathbf{E}}_J = \{X_1, X_2, X_3\}^T$. At the end of the deformation process, the related particle $p \subset \varphi(B)$ in ^{1}C configuration will be given by position vector $\mathbf{x} = x_i\hat{\mathbf{e}}_i = \{x_1, x_2, x_3\}^T$. Now, the particle motion can be completely defined by function φ as

$$\mathbf{x} = \varphi(\mathbf{X}, t) \quad \forall \ \mathbf{x}, \mathbf{X} \in \mathfrak{R}^3 , \tag{2.8}$$

where the mapping restriction is:

$$\varphi(\mathbf{X}, t) : \boldsymbol{B} \to \mathfrak{R}^3 \quad \forall \ \mathbf{X} \in \boldsymbol{B}. \tag{2.9}$$

Within the deformation history, for each time *t* the parametric function φ contains the information of successive particle $P \subset \boldsymbol{B}$ position. In such way, φ describes the *path trajectory* of particle P (Fig. 2.1). From the fact that two material points cannot occupy the same space at the same time, it can be deduced that two distinct particles can have the same position in any configuration and that in the given configuration two distinct points cannot be located in the same particle. Consequently, the parametric function φ is unique and its inverse function exist as

$$\mathbf{X} = \varphi^{-1}(\mathbf{x}, t) \quad \forall \ \mathbf{x}, \mathbf{X} \in \mathfrak{R}^3. \tag{2.10}$$

In other words, the deformation process can not involve tearing and interpenetrations of matter. Therefore, in both cases the deformation mapping is defined by an *injective* function such as the one in Eq. (2.8) and in Eq. (2.10). Consequently, the inverse deformation mapping can be defined as (Bowen, 2007):

$$\varphi^{-1} : \varphi(\mathbf{X}, t) \to \boldsymbol{B} \quad \forall \ \mathbf{X} \in \boldsymbol{B}. \tag{2.11}$$

Note that the functions (2.8) and (2.10) describe the same motion but under different circumstances. The first one (2.8), describes the motion with respect to the so-called *material coordinates* and characterize material particles in movement. Accordingly, the independent variables ($\mathbf{X}$,*t*) are referred to as *material variables*. The second one (2.10), defines the motion with respect to the *spatial coordinates*, focusing on a point in space. In this case, the independent variables ($\mathbf{x}$,*t*) are referred to as *spatial variables*. Following the standard notation in continuum mechanics, the material description of motion is denoted as the *Lagrangian description*, and the spatial description, as the *Eulerian description*. Traditionally, the uppercase letter is used to indicate material coordinates and the lowercase latter to indicate the spatial coordinates (Crisfield, 1991; Bonet & Wood, 1997; Crisfield, 2000).

Due to the fact that the event under consideration is non-linear, which implies an incremental-iterative solution strategy with a considerable number of successive spatial configurations; it should be pointed out that the total deformation should not be understood as a superposition of successive deformations between configurations. This fact can be supported by imagining the existence of two neighboring mapping function $\varphi_1 : \boldsymbol{B} \to \mathfrak{R}^3$ and $\varphi_2 : \boldsymbol{B} \to \mathfrak{R}^3$. In this case, the total continuum deformation can be obtained as

$$\varphi(\mathbf{X}, t) = \varphi_2(\varphi_1(\mathbf{X}, t), t) = \varphi_2 \circ \varphi_1(\mathbf{X}, t). \tag{2.12}$$

It is clear that with a finite number of mapping functions, the total deformation is defined by composition of all mapping functions in accordance with the given example (2.12). Obviously, the current deformation state is clearly influenced by all previously deformation states. This is especially valid in case of materials like concrete that "store" the information of their initial virgin state (*path-dependency*).

In order to proceed with the kinematical aspects of finite strains, the components of the position vector **X**, in respect to basis $\hat{\mathbf{E}}_J$ in the reference configuration, are introduced as

$$\mathbf{X} = X_J \, \hat{\mathbf{E}}_J \, . \tag{2.13}$$

Analogically, the position **x** related to basis $\hat{\mathbf{e}}_i$ in the current configuration is given as

$$\mathbf{x} = x_i \, \hat{\mathbf{e}}_i \, . \tag{2.14}$$

Note that a special attention should be paid to the selection of coordinate system that will be used for measuring the motion of bodies. Namely due to the fact that the constitutive laws are often given in terms of material coordinates (Bowen, 2007), the numerical formulation in question should be placed in the framework of the *Lagrangian description of motion*.

When describing the motion in displacement terms, the vector **u**(**X**,*t*) that joins the position of particle P ⊂ *B* in the reference configuration with its position p ⊂ φ(*B*) in the current configuration, can be expressed in terms of material coordinates as

$$\mathbf{u}(\mathbf{X},t) = u_i \, \hat{\mathbf{e}}_i \, , \tag{2.15}$$

or in terms of spatial coordinates as

$$\mathbf{U}(\mathbf{x},t) = U_J \, \hat{\mathbf{E}}_J \, . \tag{2.16}$$

Usually, the displacement field **u**(**X**,*t*) is defined by

$$\mathbf{u}(\mathbf{X},t) = \mathbf{b}(\mathbf{X},t) + \mathbf{x}(\mathbf{X},t) - \mathbf{X} \qquad \text{or} \qquad u_i = \alpha_{iJ} b_J + x_i - \alpha_{iJ} X_J \, , \tag{2.17}$$

and the displacement field **U**(**x**,*t*) expressed in terms of spatial coordinates by

$$\mathbf{U}(\mathbf{x},t) = \mathbf{b}(\mathbf{x},t) + \mathbf{x} - \mathbf{X}(\mathbf{x},t) \qquad \text{or} \qquad U_J = b_j + \alpha_{Ji} x_i - X_J \, . \tag{2.18}$$

When using Eq. (2.7), **u**(**X**,*t*) can be related to a spatial coordinate by

$$u_i = \alpha_{iJ} U_J \, , \tag{2.19}$$

while $\mathbf{U}(\mathbf{x},t)$ can be related to material coordinates through

$$U_J = \alpha_{Ji}u_i. \tag{2.20}$$

Knowing that

$$\hat{\mathbf{e}}_i = \alpha_{iJ}\hat{\mathbf{E}}_J, \tag{2.21}$$

it can be demonstrate that the field $\mathbf{u}(\mathbf{X},t)$ is associated to $\mathbf{U}(\mathbf{x},t)$ via

$$\mathbf{u}(\mathbf{X}, t) = u_i\hat{\mathbf{e}}_i = u_i(\alpha_{iJ}\hat{\mathbf{E}}_j) = U_J\hat{\mathbf{E}}_J = \mathbf{U}(\mathbf{x}, t). \tag{2.22}$$

In order to simplify the description of finite strain, it is a usually practice to assume that the coordinate basis $\hat{\mathbf{E}}_J$ (2.1) and $\hat{\mathbf{e}}_i$ (2.2) coincide. In such case, the continuum motion is monitored from a single coordinate system (Fig. 2.2) and, as a consequence, the coordinate system translation disappears ($\mathbf{j=0}$).
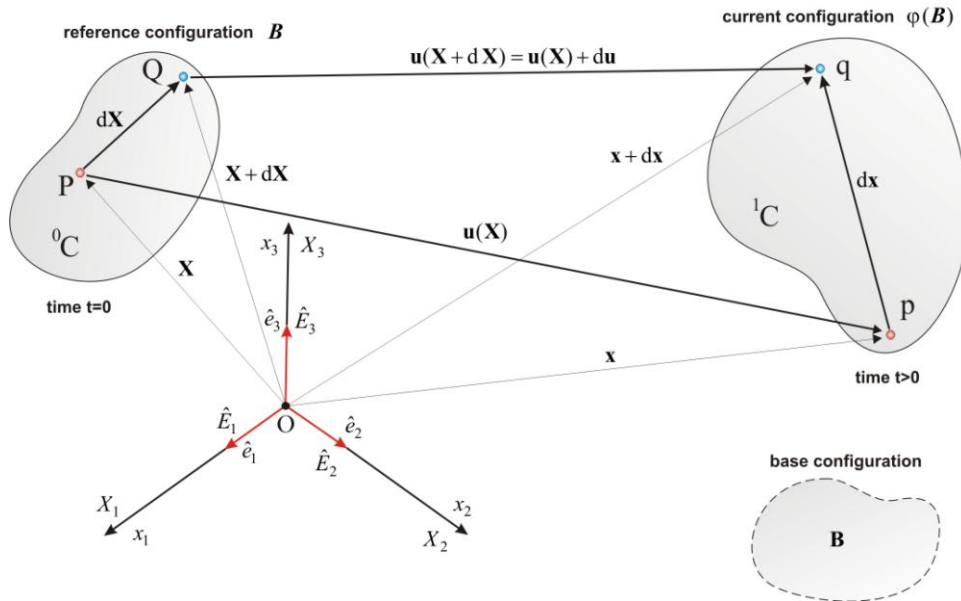
Figure 2.2 Lagrangian kinematics (deformation of a material line segment)

With coinciding basis, the dot product in Eq. (2.7) becomes Kronecker δ (2.23).

$$\hat{\mathbf{E}}_J\,\hat{\mathbf{e}}_i = \delta_{iJ} = \delta_{Ji} \tag{2.23}$$

Therefore, the filed $\mathbf{U}(\mathbf{x},t)$ can be rewritten as

$$\mathbf{U}(\mathbf{X},t) = \mathbf{x}(\mathbf{X},t) - \mathbf{X} \qquad \text{or} \qquad u_i = x_i - \delta_{iJ}X_J. \tag{2.24}$$

Similarly, $\mathbf{u}(\mathbf{x},t)$ in Eq. (2.17) can be calculated by means of

$$\mathbf{u}(\mathbf{x},t) = \mathbf{x} - \mathbf{X}(\mathbf{x},t) \qquad \text{or} \qquad U_J = \delta_{Ji}x_i - X_J. \tag{2.25}$$

Since the collision event is obviously time-depended, the rate of change of mechanical quantity should be taken into account. For this purpose, assume a tensor or scalar quantity $q(\mathbf{X},t)$ defined in material coordinates $\mathbf{X}$ at time t. The rate of change is well defined by

$$\dot{q}(\mathbf{X},t) = \frac{Dq}{Dt},\tag{2.26}$$

where the notation $D\cdot/Dt$ denotes the so-called *material time-derivative*, and it is commonly introduced to distinguish it from the *spatial time derivative*, traditionally indicated by $\partial\cdot/\partial t$ (Belytschko, Liu & Moran, 2001). According to Eq. (2.8), the material time-derivative of $q(\mathbf{x},t)$ is given by definition as (Bonnet & Wood, 1997)

$$\dot{q}(\mathbf{x},t) = \frac{Dq}{Dt} = \lim_{\Delta t \to 0} \frac{q(\varphi(\mathbf{X},t+\Delta t),t+\Delta t) - q(\varphi(\mathbf{X},t),t)}{\Delta t},\tag{2.27}$$

with the derivative structure:

$$\dot{q}(\mathbf{x},t) = \frac{Dq}{Dt} = \frac{\partial q(\mathbf{x},t)}{\partial t} + \underbrace{\frac{\partial \varphi(\mathbf{X},t)}{\partial t}}_{\boldsymbol{v}} \frac{\partial q(\mathbf{x},t)}{\partial \mathbf{x}} = \frac{\partial q(\mathbf{x},t)}{\partial t} + \boldsymbol{v}\, grad\, q.\tag{2.28}$$

The first term on the RHS denotes the spatial time-derivative and the second one denotes the so-called convective influence that describes the change of spatial position of a particle with velocity $\boldsymbol{v}(\mathbf{X},t)$ and material coordinates $\mathbf{X}$ (2.13).

2.2.2 Deformation gradient

Suppose that the movement from ^{0}C to ^{1}C configuration (Fig. 2.2) causes the continuum to suffer deformation that results in change of its shape and/or size. In order to quantify the deformation at an arbitrary particle P $\subset$ $\boldsymbol{B}$, the changes of its neighboring particle Q $\subset$ $\boldsymbol{B}$ should be considered (Fig. 2.3).

Assume that the line segment d$\mathbf{X}$ (connecting the particles P $\subset$ $\boldsymbol{B}$ and Q $\subset$ $\boldsymbol{B}$ in reference configuration) and the line segment d$\mathbf{x}$ (connecting the related particles p $\subset$ $\varphi(\boldsymbol{B})$ and q $\subset$ $\varphi(\boldsymbol{B})$ in current configuration) are relatively small, making the differential calculus possible. The absolute position of a particle Q in the reference configuration is defined by $\mathbf{X}$+d$\mathbf{X}$, and in the current configuration by $\mathbf{x}$+d$\mathbf{x}$. The change in distance (stretching) may be measured by expressing the current position $\mathbf{x}$+d$\mathbf{x}$ in terms of its reference position $\mathbf{X}$+d$\mathbf{X}$ and adding the contribution of the respective displacement $\mathbf{u}$ (2.29).

$$\mathbf{x} + d\mathbf{x} = \mathbf{X} + d\mathbf{X} + \mathbf{u}(\mathbf{X} + d\mathbf{X})\tag{2.29}$$

The line segment d$\mathbf{x}$ can be further expressed as

$$d\mathbf{x} = \mathbf{X} - \mathbf{x} + d\mathbf{X} + \mathbf{u}(\mathbf{X} + d\mathbf{X}) = d\mathbf{X} + \underbrace{\mathbf{u}(\mathbf{X} + d\mathbf{X}) - \mathbf{u}(\mathbf{X})}_{d\mathbf{u}}, \tag{2.30}$$

and upon introduction of the differential notation d$\mathbf{u}$, by

$$d\mathbf{x} = d\mathbf{X} + d\mathbf{u}. \tag{2.31}$$

In this Eq. d$\mathbf{u}$ denotes the *relative displacement vector* of particle Q in respect to particle P. According to the continuum principles (Bowen, 2007), the continuity of the displacement field allows to apply the *Taylor series expansion* around particle P in order determine the value of d$\mathbf{u}$ in the immediate vicinity of Q. By ignoring higher-order terms, $\mathbf{u}(\mathbf{X}+d\mathbf{X})$ in Eq. (2.30) is approximated as

$$\mathbf{u}(\mathbf{X} + d\mathbf{X}) = \mathbf{u}(\mathbf{X}) + d\mathbf{u} \approx \mathbf{u}(\mathbf{X}) + \mathbf{u}\nabla_{\mathbf{x}}\, d\mathbf{X}. \tag{2.32}$$

Eq. (2.31), that links the line segment d$\mathbf{x}$ to the line segment d$\mathbf{X}$, can be rewritten as

$$d\mathbf{x} = d\mathbf{X} + d\mathbf{u} = d\mathbf{X} + \mathbf{u}\nabla_{\mathbf{x}}\, d\mathbf{X} = \underbrace{\left[\, \mathbf{I} + \mathbf{u}\nabla_{\mathbf{x}} \right]}_{\mathbf{F}} d\mathbf{X}. \tag{2.33}$$

The term in brackets can be represented in a compact form by introducing the symbol $\mathbf{F}$, such that

$$d\mathbf{x} = \mathbf{F}\, d\mathbf{X}. \tag{2.34}$$

$\mathbf{F}$ denotes a second-order tensor quantity which is traditionally called *deformation gradient matrix*. It follows that $\mathbf{F}$ represents the gradient of the mapping function (2.9) that describes the continuum motion from ^{0}C to ^{1}C configuration (2.8). It can be also said that $\mathbf{F}$ "lives" in both reference ^{0}C and current ^{1}C configuration, therefore, it is usually referred to as *two-point tensor* (Zienkiewicz & Taylor, 2002).

As a fundamental quantity in finite deformation analysis, $\mathbf{F}$ defines the local deformation around the particle P $\subset \boldsymbol{B}$ by transforming the neighboring infinitesimal line segment d$\mathbf{X}$ into the respective line segment d$\mathbf{x}$ in current configuration (2.35).

$$d\mathbf{x} = \begin{Bmatrix} dx_1 \\ dx_2 \\ dx_3 \end{Bmatrix} = \mathbf{F} \begin{Bmatrix} dX_1 \\ dX_2 \\ dX_3 \end{Bmatrix} = \mathbf{F}\, d\mathbf{X} \tag{2.35}$$

By using indicial notation, $\mathbf{F}$ can be written as

$$F_{iJ} = \frac{\partial x_i}{\partial X_J} = \delta_{iJ} + \frac{\partial u_i}{\partial X_J}, \tag{2.36}$$

from which it can be deduced that the tensor structure contains derivatives d$\mathbf{x}=\{x_1,x_2,x_3\}^{\mathrm{T}}$ with respect to the components of d$\mathbf{X}=\{X_1,X_2,X_3\}^{\mathrm{T}}$, all of which are arranged in *Jacobian format* (2.37).

$$\mathbf{F} = \frac{\partial \mathbf{x}}{\partial \mathbf{X}} = \begin{bmatrix} \partial x_1/\partial X_1 & \partial x_1/\partial X_2 & \partial x_1/\partial X_3 \\ \partial x_2/\partial X_1 & \partial x_2/\partial X_2 & \partial x_2/\partial X_3 \\ \partial x_3/\partial X_1 & \partial x_3/\partial X_2 & \partial x_3/\partial X_3 \end{bmatrix} = \begin{bmatrix} 1 & 0 & 0 \\ 0 & 1 & 0 \\ 0 & 0 & 1 \end{bmatrix} + \begin{bmatrix} \partial u_1/\partial X_1 & \partial u_1/\partial X_2 & \partial u_1/\partial X_3 \\ \partial u_2/\partial X_1 & \partial u_2/\partial X_2 & \partial u_2/\partial X_3 \\ \partial u_3/\partial X_1 & \partial u_3/\partial X_2 & \partial u_3/\partial X_3 \end{bmatrix} \quad (2.37)$$

Since the mapping (2.11) is unique, the deformation gradient inversion is valid (2.38).

$$d\mathbf{X} = \mathbf{F}^{-1} d\mathbf{x} \tag{2.38}$$

$\mathbf{F}^{-1}$ is given as

$$F_{Ij} = \frac{\partial X_I}{\partial x_j} = \delta_{Ij} + \frac{\partial u_I}{\partial x_j}, \tag{2.39}$$

or, by expanding tensors components, as

$$\mathbf{F}^{-1} = \frac{\partial \mathbf{X}}{\partial \mathbf{x}} = \begin{bmatrix} \partial X_1/\partial x_1 & \partial X_1/\partial x_2 & \partial X_1/\partial x_3 \\ \partial X_2/\partial x_1 & \partial X_2/\partial x_2 & \partial X_2/\partial x_3 \\ \partial X_3/\partial x_1 & \partial X_3/\partial x_2 & \partial X_3/\partial x_3 \end{bmatrix} = \begin{bmatrix} 1 & 0 & 0 \\ 0 & 1 & 0 \\ 0 & 0 & 1 \end{bmatrix} + \begin{bmatrix} \partial u_1/\partial x_1 & \partial u_1/\partial x_2 & \partial u_1/\partial x_3 \\ \partial u_2/\partial x_1 & \partial u_2/\partial x_2 & \partial u_2/\partial x_3 \\ \partial u_3/\partial x_1 & \partial u_3/\partial x_2 & \partial u_3/\partial x_3 \end{bmatrix}. \quad (2.40)$$

Resuming, the gradient deformation matrix **F** enables the transformation of a material line segment from one configuration into another (2.35), appropriate one, and *vice versa* (2.38). Note that the mapping is linear, so **F** can be interpreted as a linear affine operator. Following the traditional practice in continuum mechanics, Eq. (2.35) is usually denoted as *push forward operation* and Eq. (2.38) as *pull back operation*. The reciprocal operations are possible due to the nonsingular property of **F**. To illustrate the consequences of this property, consider an infinitesimal volume d*V* in reference configuration and an infinitesimal neighborhood **X**+d**X**. The volume d*V* is defined by the parallelepiped product

$$dV = (d\mathbf{X}^{(1)} \times d\mathbf{X}^{(2)}) \, d\mathbf{X}^{(3)}, \tag{2.41}$$

or by matrix determinant as:

$$dV = \det(\ d\mathbf{X}^{(1)} \mid d\mathbf{X}^{(2)} \mid d\mathbf{X}^{(3)}). \tag{2.42}$$

d**X**^{i} denotes the vectors on the d*V* edges with *i*=1..3. The related volume d*v*, situated in the corresponding spatial neighborhood, is defined with the triple product

$$dv = (d\mathbf{x}^{(1)} \times d\mathbf{x}^{(2)}) \, d\mathbf{x}^{(3)}, \tag{2.43}$$

or, analogically to Eq. (2.42), with the following matrix determinant (2.44).

$$dv = \det(\ d\mathbf{x}^{(1)} \mid d\mathbf{x}^{(2)} \mid d\mathbf{x}^{(3)}) \tag{2.44}$$

According to Eq. (2.34), the next few assortment steps establish the relation between d*v* and d*V* (2.45).

$$dv = \det(\,d\mathbf{x}^{(1)} \mid d\mathbf{x}^{(2)} \mid d\mathbf{x}^{(3)}\,) = \det(\mathbf{F}d\mathbf{X}^{(1)} \mid \mathbf{F}d\mathbf{X}^{(2)} \mid \mathbf{F}d\mathbf{X}^{(3)}\,) = \ldots$$
$$\ldots = \det(\mathbf{F}\,(d\mathbf{X}^{(1)} \mid d\mathbf{X}^{(2)} \mid d\mathbf{X}^{(3)})) = \det\mathbf{F}\,\det(\,d\mathbf{X}^{(1)} \mid d\mathbf{X}^{(2)} \mid d\mathbf{X}^{(3)}\,) = \det\mathbf{F}\,dV \tag{2.45}$$

It follows that the ration between dv and dV is defined through $\det\mathbf{F}$ via (Bonet & Wood, 1997)

$$\frac{dv}{dV} = \det\mathbf{F}(\mathbf{X},t) = J(\mathbf{X},t) = \frac{\rho_0}{\rho}. \tag{2.46}$$

In this Eq., J denotes the so-called *Jacobian of deformation* and links the continuum mass density ρ_0 to ρ in reference and current configuration, respectively. Since φ is injective (2.11), the linear mapping is locally *one-to-one* at $\mathbf{X}$ in time t, if:

$$J(\mathbf{X},t) > 0. \tag{2.47}$$

Eq. (2.47) is usually interpreted as the *local invertibility condition*, and ensures that the material volume element remains positive throughout deformation history.

2.2.3 Multiplicative polar decomposition

For a displacement field with *inhomogeneous* property (Nam, 2004), which means that $\mathbf{F}$ does not depend on its position on the continuum (i.e. material coordinates $\mathbf{X}$), the deformation from ${}^0C$ to ${}^1C$ is partly *deformation* and partly *rigid-body rotation*. This is due to the fact that:

$$\mathbf{x} = \mathbf{F}\mathbf{X} + \mathbf{j}, \tag{2.48}$$

where the translation vector $\mathbf{j}$ stands alone and so has no contribution on the deformation. The information about continuum deformations and rigid-body rotations are contained in the deformation gradient matrix $\mathbf{F}$. In order to separate the deformation from rigid-body rotation, the *polar decomposition theorem* ought to be introduced. Since $\mathbf{F}$ is non-singular and positively definite second-order tensor, the polar decomposition is a valid operation and can apply on the basis of the next theorem.

For any non-singular second-order tensor $\mathbf{F}$ there exist unique positive definite, symmetric second-order tensor $\mathbf{U}$ and $\mathbf{v}$, and orthogonal second-order tensor $\mathbf{R}$ such that $\mathbf{F}=\mathbf{R}\mathbf{U}=\mathbf{v}\mathbf{R}$.

Like every orthogonal tensor, $\mathbf{R}$ has the property

$$\mathbf{R}\mathbf{R}^{\mathrm{T}} = \mathbf{I}, \tag{2.49}$$

while the symmetric tensors $\mathbf{U}$ and $\mathbf{v}$ have the well-known characteristics:

$$\mathbf{U} = \mathbf{U}^{\mathrm{T}} \qquad \text{and} \qquad \mathbf{v} = \mathbf{v}^{\mathrm{T}}. \tag{2.50}$$

According to standard notations, **v** denotes the *left stretch tensor*, **U** the *right stretch tensor* while **R** denotes the *material rotation tensor*. The tensors are linked by means of multiplicative polar decomposition theorem, given as (Bonet & Wood, 1997)

$$\mathbf{F} = \mathbf{RU} = \mathbf{vR}. \tag{2.51}$$

The problem of decomposition can be now formulated as follows: If for a given **F** the deformation contained in **U** and the rotation in **R** must be determined, it is necessary to separate **U** or **v** (or even **R**) from the known **F**. The problem can be solved by introducing the next lemma.

To any symmetric, positive definite second-order tensor **T** *there correspond a unique symmetric, positive definite second-order tensor* **U** *such that* $\mathbf{U}^2 = \mathbf{T}$.

According to lemma, $\mathbf{U}^2$ can be related to $\mathbf{F}^T\mathbf{F}$ due to the fact that such product generates a positive definite second-order tensor. The tensor product will be attributed to a new tensor **C** (2.52), which will be appropriately discussed later on.

$$\mathbf{U}^2 = \mathbf{UU} = \mathbf{U}^T\mathbf{U} = \mathbf{U}^T\mathbf{R}^T\mathbf{RU} = \mathbf{F}^T\mathbf{F} = \mathbf{C} \tag{2.52}$$

The problem is now reduced to determining the square root of $\mathbf{U}^2$ since it is related to **R** through **F** (2.53).

$$\mathbf{F} = \mathbf{RU} \qquad \text{where} \quad \mathbf{U} = \sqrt{\mathbf{C}} = \sqrt{\mathbf{F}^T\mathbf{F}} \tag{2.53}$$

According to the *spectral decomposition theorem*, the square root of **C** can be calculated by the *eigenprojection procedure* (Hirota, 2002). For the sake of introducing the mentioned procedure, suppose that λ^2_1, λ^2_2 and λ^2_3 indicate the eigenvalues of **C**, and [$\mathbf{N}_1$ $\mathbf{N}_2$ $\mathbf{N}_3$] the related eigenvectors. In such case, the following equality is valid (2.54).

$$\mathbf{C}\begin{bmatrix} \mathbf{N}_1 & \mathbf{N}_2 & \mathbf{N}_3 \end{bmatrix} = \begin{bmatrix} \mathbf{N}_1 & \mathbf{N}_2 & \mathbf{N}_3 \end{bmatrix} \begin{bmatrix} \lambda_1^2 & 0 & 0 \\ 0 & \lambda_2^2 & 0 \\ 0 & 0 & \lambda_3^2 \end{bmatrix} \tag{2.54}$$

Being **C** and $\mathbf{U}^2$ symmetric and positively defined tensors, and being λ_i positive real numbers, the tensors can be rewritten by adopting the spectral decomposition theorem as (Marsden & Hughes, 1983):

$$\mathbf{C} = \sum_{i=1}^{3} \lambda_i^2 \mathbf{N}_i \otimes \mathbf{N}_i \qquad \text{and} \qquad \mathbf{U}^2 = \sum_{i=1}^{3} \lambda_i^2 \mathbf{N}_i \otimes \mathbf{N}_i. \tag{2.55}$$

Furthermore, the next few assortment steps (2.56) demonstrate that the tensors **C** and $\mathbf{U}^2$ have the same stretching directions $\mathbf{N}_i$ (Hirota, 2002).

$$\mathbf{U}^2 = \sum_{i,j=1}^{3} (\lambda_i \mathbf{N}_i \otimes \mathbf{N}_i)(\lambda_j \mathbf{N}_j \otimes \mathbf{N}_j) = \sum_{i,j=1}^{3} \lambda_i \lambda_j (\mathbf{N}_i \otimes \mathbf{N}_i)(\mathbf{N}_j \otimes \mathbf{N}_j) = \dots$$

$$\dots = \sum_{i,j=1}^{3} \lambda_i \lambda_j ((\mathbf{N}_i \otimes \mathbf{N}_i)\mathbf{N}_j \otimes \mathbf{N}_j) = \sum_{i,j=1}^{3} \lambda_i \lambda_j ((\mathbf{N}_j \otimes \mathbf{N}_i)\mathbf{N}_i \otimes \mathbf{N}_j) = \dots \qquad (2.56)$$

$$\dots = \sum_{i,j=1}^{3} \lambda_i \lambda_j (\delta_{ij} \mathbf{N}_i \otimes \mathbf{N}_j) = \sum_{i=1}^{3} \lambda_i^2 (\mathbf{N}_i \otimes \mathbf{N}_i)$$

Since the tensors basis do not change, it is clear that λ_i can be interpreted as principal stretches and $\mathbf{N}_i$ as principal stretches direction of the unknown tensor $\mathbf{U}$ (2.52). It follows that $\mathbf{U}$ can be calculated by performing the spectral decomposition of $\mathbf{C}$ (2.57).

$$\mathbf{U} = \sum_{i=1}^{3} \lambda_i^* \mathbf{N}_i \otimes \mathbf{N}_i \quad \text{where} \quad \lambda_i^* = \sqrt{\lambda_i^{**}} \quad \text{and} \quad \mathbf{C} = \sum_{i=1}^{3} \lambda_i^{**} \mathbf{N}_i \otimes \mathbf{N}_i \qquad (2.57)$$

Resuming, the multiplicative polar decomposition of $\mathbf{F}$ is obtained by performing the spectral decomposition of $\mathbf{C}$, where the calculated eigenvalues of $\mathbf{C}$ represent squared eigenvalues of $\mathbf{U}$. As it was illustrated (2.56), the principal stretches $\mathbf{N}_i$ of $\mathbf{U}$ and $\mathbf{C}$ are the same. The same conclusion can be reached by nothing that (Brodersen, 2004)

$$\mathbf{v}^2 = \mathbf{F}\mathbf{F}^\mathrm{T}, \qquad (2.58)$$

which is an alternative to (2.52). From the geometrical aspect, the polar decomposition can be interpreted as follows. According to Eq. (2.45), the material line segment d$\mathbf{X}$ in the reference configuration is transformed into a line segment d$\mathbf{x}$ in the current configuration by linear affine mapping (2.59).

$$\mathrm{d}\mathbf{x} = \mathbf{F}\mathrm{d}\mathbf{X} = \mathbf{R}(\mathbf{U}\mathrm{d}\mathbf{X}) \qquad (2.59)$$

The multiplication $\mathbf{U}\mathrm{d}\mathbf{X}$ stretches d$\mathbf{X}$ by the factor λ_i in the direction of the principal axis $\mathbf{N}_i$, and then the second multiplication rotates the material line segment d$\mathbf{X}$ to its current configuration. However, note that (2.60) is also valid.

$$\mathrm{d}\mathbf{x} = \mathbf{F}\mathrm{d}\mathbf{X} = \mathbf{v}(\mathbf{R}\mathrm{d}\mathbf{X}) \qquad (2.60)$$

In this case, the material line segment d$\mathbf{X}$ is first rotated by $\mathbf{R}$ and then stretched by $\mathbf{v}$, reaching the same current configuration d$\mathbf{x}$, as defined by Eq. (2.59). A conclusion may be drawn: the current configuration will be always the same regardless of which one is applied first, the rigid-body rotation or deformation.

2.2.4 Strain tensors

Suppose a continuum body immersed in an inhomogeneous displacement field **u**. Under this circumstance, the continuum body suffers change in shape and/or volume. In order to quantify the deformation, the deformation tensor should provide information on length alteration of the infinitesimal material line segment with respect to the difference in its material and spatial configuration. Resume, the deformation gradient matrix (2.37) performs the mapping of the material line segment form the given configuration to the neighboring one (2.35). Obviously, the rigid-body rotation **R** present in **F** is not a measure of deformation. As a consequence, the crucial requirement for any deformation tensor is that it must be able to isolate the pure deformation and to be immune to rigid-body rotation. Such requirement implies that the tensor should be *a priori* symmetric.

2.2.4.1 Green-Lagrangian strain tensor

A measure of deformation is obviously contained in **U** or **v**. In order to isolate the deformation from rigid-body rotation, a proper operation on **F** should be carried out. Indeed, since the material rotation tensor **R** is incorporated in **F**, and its presence is undesirable, its influence should be removed. For this purpose, note that the tensor orthogonal property (2.49) indicates that the **R** followed by its transpose, or *vice versa*, defines the identity matrix **I**. It can be deduced that the rigid-body rotation can be excluded from **F** by simply multiplying **F** by its transpose **F**$^\mathrm{T}$. The operation will produce a symmetric tensor that is here required. The abovementioned tensor (2.52) is the so-called *right Cauchy-Green deformation tensor* **C** (2.61). Mention that **C** can be also obtained by squaring **U** (2.52).

$$\mathbf{C} = \mathbf{F}^\mathrm{T}\mathbf{F} = \mathbf{U}^\mathrm{T}\mathbf{U} = \mathbf{U}^2 \qquad \text{or} \qquad C_{IJ} = F_{kI}F_{kJ} = \frac{\partial x_k}{\partial X_I}\frac{\partial x_k}{\partial X_J} \tag{2.61}$$

Note that six independent deformation components are referred to as reference configuration (material coordinates) and can be determined from the non-interdependent nine components of **F**. Note also that the backward operation (from the given tensor **C** to **F**) is not possible. A similar deformation tensor can be obtained by performing the inverse multiplication of the abovementioned (2.61). In this case, the generated tensor will be the *left Cauchy-Green deformation tensor* **b** (2.62), also referred to as *left stretch tensor* **v**.

$$\mathbf{b} = \mathbf{F}\mathbf{F}^\mathrm{T} = \mathbf{v}^\mathrm{T}\mathbf{v} = \mathbf{v}^2 \qquad \text{or} \qquad b_{ij} = F_{iK}F_{jK} = \frac{\partial x_i}{\partial X_K}\frac{\partial x_j}{\partial X_K} \tag{2.62}$$

The tensor components are obtained in respect to the current configuration (spatial coordinates) and it is why the backward operation from the given tensor **b** to tensor **F** is not possible. In both cases, Eq. (2.61) and Eq. (2.62), the deformation tensors represent a link between the squared line segment d*l* in the current configuration

and the square of its related line segment dL in the reference configuration. In order to measure the deformation, the square of the line segment in the current configuration is introduced as (Lehmann, 2008)

$$(\mathrm{d}l)^2 = \mathrm{d}x_k \mathrm{d}x_k = \frac{\partial x_k}{\partial X_I}\frac{\partial x_k}{\partial X_J}\mathrm{d}X_I\mathrm{d}X_J \qquad \text{or} \qquad (\mathrm{d}l)^2 = C_{IJ}\mathrm{d}X_I\mathrm{d}X_J . \tag{2.63}$$

On the other hand, the square of the line segment dL in the reference configuration is given by

$$(\mathrm{d}L)^2 = \mathrm{d}X_K \mathrm{d}X_K = \frac{\partial X_K}{\partial x_i}\frac{\partial X_K}{\partial x_j}\mathrm{d}x_i\mathrm{d}x_j \qquad \text{or} \qquad (\mathrm{d}L)^2 = b^{-1}{}_{ij}\mathrm{d}x_i\mathrm{d}x_j . \tag{2.64}$$

Before proceeding, let's recapitulate. The deformation tensors (2.61) and (2.62) represent in what way the square of the line segment is linked between its current and reference configuration. In order to define the strain measure, the change in length of the square line segment should be examined. So, in the reference configuration the length of the vector d$\mathbf{X}$ may be defined as the dot product with itself (2.65).

$$(\mathrm{d}L)^2 = \mathrm{d}\mathbf{X}\mathrm{d}\mathbf{X} \tag{2.65}$$

Analogically, the length of the vector d$\mathbf{x}$ will be

$$(\mathrm{d}l)^2 = \mathrm{d}\mathbf{x}\mathrm{d}\mathbf{x}. \tag{2.66}$$

As the interest is here paid on the difference between them, the following Eq. ought to be introduced (2.67).

$$(\mathrm{d}L)^2 - (\mathrm{d}l)^2 = \mathrm{d}X_i\mathrm{d}X_i - \mathrm{d}x_i\mathrm{d}x_i \tag{2.67}$$

Suppose that the measures of material squeezing (2.67) is defined as (Bonet & Wood, 1997)

$$(\mathrm{d}L)^2 - (\mathrm{d}l)^2 = 2\mathrm{d}x_i E_{ij}\mathrm{d}x_j , \tag{2.68}$$

where E_{ij} denotes an unknown strain tensor. Eq. (2.67) can be rewritten from Eq. (2.68) as

$$\mathrm{d}X_i F_{ki} F_{kj}\mathrm{d}X_j - \mathrm{d}X_i\mathrm{d}X_i = 2\mathrm{d}x_i E_{ij}\mathrm{d}x_j , \tag{2.69}$$

and, since $\mathrm{d}X_i F_{ki} = \mathrm{d}x_k$ and $F_{kj}\mathrm{d}X_j = \mathrm{d}x_k$, after replacing the index k with the index i, the following equality can be obtained (2.70).

$$\mathrm{d}X_i F_{ki} F_{kj}\mathrm{d}X_j = \mathrm{d}x_i\mathrm{d}x_i = \mathrm{d}x_i \delta_{ij}\mathrm{d}x_j \tag{2.70}$$

The strain definition in Eq. (2.69) can now be rewritten as

$$\mathrm{d}x_i F_{ki} F_{kj}\mathrm{d}x_j - \mathrm{d}x_i \delta_{ij}\mathrm{d}x_j = \mathrm{d}x_i(F_{ki} F_{kj} - \delta_{ij})\,\mathrm{d}x_j = 2\mathrm{d}x_i E_{ij}\mathrm{d}x_j , \tag{2.71}$$

which directly leads to tensor $\boldsymbol{E}$ expressed in terms of deformation gradient components (2.72).

$$E_{ij} = \frac{1}{2}(F_{ki}F_{kj} - \delta_{ij}) \tag{2.72}$$

The derived second order symmetric tensor is the *Green-Lagrangian strain tensor* E which gives the information about stretching of the material line segment dL, regardless of the line segment rigid-body rotation. In accordance with Eq. (2.72), the components of E are given as

$$E_{ij} = \begin{cases} \dfrac{\partial u_i}{\partial X_i} + \dfrac{1}{2}\left[\left(\dfrac{\partial u_1}{\partial X_i}\right)^2 + \left(\dfrac{\partial u_2}{\partial X_i}\right)^2 + \left(\dfrac{\partial u_3}{\partial X_i}\right)^2\right] & \text{if } i = j \\[4mm] \dfrac{1}{2}\left(\dfrac{\partial u_i}{\partial X_j} + \dfrac{\partial u_j}{\partial X_i}\right) + \dfrac{1}{2}\left[\dfrac{\partial u_1}{\partial X_i}\dfrac{\partial u_1}{\partial X_j} + \dfrac{\partial u_2}{\partial X_i}\dfrac{\partial u_2}{\partial X_j} + \dfrac{\partial u_3}{\partial X_i}\dfrac{\partial u_3}{\partial X_j}\right] & \text{if } i \neq j. \end{cases} \tag{2.73}$$

Note that for infinitesimal small strains, for which the reference and current configuration almost coincide, the components of Green-Lagrangian strain tensor E are reduced to the "naïve" engineering strain definition ε. It should be stressed out that in the proposed numerical formulation the Green-Lagrangian strain tensor plays a crucial role due to the fact that its presence in the adopted constitutive description is inevitable. The statement will be properly supported later on (*Chapter 5 – 5.4 Microplane strain tensor*).

2.2.4.2 Material strain tensors

As the continuum under consideration is of *nonpolar type* (Boltzmann continuum), a family of strain tensors $\mathbf{E}^{(m)}$ can be retrieved from the general strain notation given as (Başar & Weichert, 2000)

$$\mathbf{E}^{(m)}(\mathbf{U}) = \begin{cases} \dfrac{1}{m}\left[\mathbf{U}^m - \mathbf{I}\right] & \text{for } m \neq 0 \\[4mm] \ln \mathbf{U} & \text{for } m = 0, \end{cases} \tag{2.74}$$

where m represents an arbitrary positive integer number. Depending on m, Eq. (2.74) generates a strain tensors universally denoted by $\mathbf{E}^{(m)}$. As the strain measures obtained in this way are related to right stretch tensor $\mathbf{U}$ (which is attributed to the reference configuration), their measure will refer to the continuum state in the material configuration. A set of corresponding strain tensors is presented in (2.75).

$$\begin{aligned} \text{Green - Lagange strain tensor} \quad &: \quad m = 2 \quad : \quad \mathbf{E}^{(2)} = E = 0.5(\mathbf{U}^2 - \mathbf{I}) \\ \text{Biot material strain tensor} \quad &: \quad m = 1 \quad : \quad \mathbf{E}^{(1)} = B = \mathbf{U} - \mathbf{I} \\ \text{Hencky material strain tensor} \quad &: \quad m = 0 \quad : \quad \mathbf{E}^{(0)} = H = \ln \mathbf{U} \end{aligned} \tag{2.75}$$

The same sets of tensors can be obtained by the generalized form of Eq. (2.74) given as

$$\mathbf{E}^{(m)}(\mathbf{U}) = \frac{1}{2m}\left[\mathbf{U}^{2m} - \mathbf{I}\right] = \sum_{i=1}^{3}\frac{1}{2m}(\lambda_i^{2m} - 1)\ \mathbf{N}_i \otimes \mathbf{N}_i \ . \tag{2.76}$$

In this case, m denotes an arbitrary positive or negative integer number, λ_i represents the eigenvalues of $\mathbf{U}$ (i.e. principal stretches) while $\mathbf{N}_i$ represents eigenvectors of $\mathbf{U}$ (i.e. principal stretching directions).

2.2.4.3 Spatial strain tensors

A family of spatial strain tensors can be also introduced by (Başar & Weichert, 2000)

$$\mathbf{e}^{(m)}(\mathbf{v}) = \begin{cases} \dfrac{1}{m}\left[\mathbf{v}^m - \mathbf{I}\right] & \text{for}\quad m \neq 0 \\[2ex] \ln\mathbf{v} & \text{for}\quad m = 0 \ , \end{cases} \tag{2.77}$$

with m as a negative integer number. A set of corresponding strain tensors is presented in (2.78).

$$\begin{aligned} \text{Almansi strain tensor} \quad &: \quad m = -2 \quad : \quad \mathbf{e}^{(2)} = \boldsymbol{a} = 0.5(\mathbf{I} - \mathbf{v}^2) \\ \text{Biot spatial strain tensor} \quad &: \quad m = -1 \quad : \quad \mathbf{e}^{(1)} = \boldsymbol{b} = \mathbf{I} - \mathbf{v} \\ \text{Hencky spatial strain tensor} \quad &: \quad m = \ 0 \quad : \quad \mathbf{e}^{(0)} = \boldsymbol{h} = \ln\mathbf{v} \end{aligned} \tag{2.78}$$

Since the given strain measures are related to the left stretch tensor $\mathbf{v}$ they represent the strains in the spatial configuration. The same sets of tensors can be obtained by the generalized form of Eq. (2.77) given as

$$\mathbf{e}^{(m)}(\mathbf{v}) = \frac{1}{2m}\left[\mathbf{v}^{2m} - \mathbf{I}\right] = \sum_{i=1}^{3}\frac{1}{2m}(\lambda_i^{2m} - 1)\,\mathbf{N}_i \otimes \mathbf{N}_i \ , \tag{2.79}$$

where λ_i represents the eigenvalues of $\mathbf{v}$ and $\mathbf{N}_i$ the related eigenvectors.

2.2.4.4 Velocity gradient tensor

By definition, the velocity gradient tensor $\boldsymbol{l}$ is the partial derivative of the velocity field $\boldsymbol{v}(\mathbf{X},t)$ with respect to the spatial coordinates (2.80). Therefore, $\boldsymbol{l}$ will describe the velocity of transition between the material and spatial continuum configurations (Bonet & Wood, 1997).

$$\boldsymbol{l} = \frac{\partial \boldsymbol{v}(\mathbf{X},t)}{\partial \mathbf{x}} = \nabla \boldsymbol{v}(\mathbf{X},t) \qquad \text{or} \qquad l_{ij} = v_{i,j} \tag{2.80}$$

It is also known that $\boldsymbol{l}$ can be retrieved by manipulation of the time-derivative of $\mathbf{F}$ (2.81).

$$\dot{\mathbf{F}} = \frac{\mathrm{d}}{\mathrm{d}t}\left(\frac{\partial \mathbf{x}}{\partial \mathbf{X}}\right) = \frac{\partial}{\partial \mathbf{X}}\left(\frac{\partial \mathbf{x}}{\partial t}\right) = \frac{\partial \boldsymbol{v}}{\partial \mathbf{X}} = \frac{\partial \boldsymbol{v}}{\partial \mathbf{x}}\frac{\partial \mathbf{x}}{\partial \mathbf{X}} = \boldsymbol{l}\,\mathbf{F} \qquad \text{where}\quad \boldsymbol{l} = \dot{\mathbf{F}}\mathbf{F}^{-1} \tag{2.81}$$

2.2.4.5 Rate-of-deformation

In most cases, but especially under severe impact loading, concrete failure takes place in extremely short period of time (Bentur, Mindess & Banthia, 1986). Consequently, the temporal change in deformation, from the initial standstill configuration throughout the deformation history to the finial standstill configuration, is considerable. This fact would not be of any interest if concrete would demonstrate no sensitivity to the rate-of-deformation. However, the reality is exactly the opposite. The experiment confirmed that at loading rate out of static or quasi-static range (impact load); the concrete mechanical behavior is especially influenced by the rate-of-deformation (Sukontasukkul & Mindess, 2003). Accordingly, the constitutive model used for numerical simulation should be sensitive on a rate-of-deformation. A proper discussion on that subject will be given later. Before that, the rate-of-deformation should be introduced.

The rate-of-deformation tensor can be retrieved by taking the time-derivative of the scalar product

$$d\mathbf{x}_1 \, d\mathbf{x}_2 = d\mathbf{X}_1 \, \mathbf{C} \, d\mathbf{X}_2 \,, \tag{2.82}$$

where the line segments $\mathbf{F}d\mathbf{X}_1$ and $\mathbf{F}d\mathbf{X}_2$, in the reference configuration are related to line segments $d\mathbf{x}_1$ and $d\mathbf{x}_2$ in the current configuration, respectively. Given that $\boldsymbol{E}=(1/2)(\mathbf{C}\text{-}\mathbf{I})$, the time-derivative of Eq. (2.82) reads:

$$\frac{d}{dt}(d\mathbf{x}_1 \, d\mathbf{x}_2) = d\mathbf{X}_1 \, \dot{\mathbf{C}} \, d\mathbf{X}_2 = 2d\mathbf{X}_1 \, \dot{\boldsymbol{E}} \, d\mathbf{X}_2 \,. \tag{2.83}$$

By introducing $d\mathbf{X}_1 = \mathbf{F}^{-1} d\mathbf{x}_1$ and $d\mathbf{X}_2 = \mathbf{F}^{-1} d\mathbf{x}_2$ into the former expression, it can be rewritten as

$$\frac{1}{2}\frac{d}{dt}(d\mathbf{x}_1 \, d\mathbf{x}_2) = d\mathbf{x}_1 \underbrace{\left[\mathbf{F}^{-T} \, \dot{\boldsymbol{E}} \, \mathbf{F}^{-1}\right]}_{\boldsymbol{d}} d\mathbf{x}_2 \,, \tag{2.84}$$

where the term in brackets represents the rate-of-deformation tensor $\boldsymbol{d}$ which is the symmetric part of the velocity gradient tensor $\boldsymbol{l}$ (2.85).

$$\boldsymbol{d} = sym(\boldsymbol{l}) = \frac{1}{2}\left[\boldsymbol{l} + \boldsymbol{l}^{\mathrm{T}}\right] \qquad \text{or} \qquad d_{ij} = \frac{1}{2}\left[v_{i,j} + v_{j,i}\right] \tag{2.85}$$

The antisymmetric (skew-symmetric) part of $\boldsymbol{l}$ is known as *spin tensor* $\boldsymbol{w}$ given as (Brodersen, 2004)

$$\boldsymbol{w} = skew(\boldsymbol{l}) = \frac{1}{2}\left[\boldsymbol{l} - \boldsymbol{l}^{\mathrm{T}}\right] \qquad \text{or} \qquad w_{ij} = \frac{1}{2}\left[v_{i,j} - v_{j,i}\right], \tag{2.86}$$

and it describes the rotation of a material particle around a certain point. Concluding, the rate-of-deformation tensor $\boldsymbol{d}$ measures the rate of change of a square material line segment $d\mathbf{x}$. It should be pointed out that the time integral of $\boldsymbol{d}$ does not vanish in the reversible cycle of deformation and, as a consequence, $\boldsymbol{d}$ is *path-depended* (Belytschko, Liu & Moran, 2001).

2.2.4.6 Tensors and objectivity

The meaning of *objective tensor* (*frame-indifference principle*) represents a fundamental concept in continuum mechanics and has a particular importance in development of material constitutive models (Bowen, 2007). Namely, it is clear that the constitutive law should not depend on the choice of the place from where the continuum movement is observed. In order to illustrate the tensor objectivity concept, consider the definition: *Any second order tensor* **T** *is objective only if its transformation from the current configuration to the configuration where it is denoted by* $\mathbf{T}^*$ *is in conformity with*

$$\mathbf{T}^* = \mathbf{R}\,\mathbf{T}\,\mathbf{R}^\mathrm{T}, \tag{2.87}$$

where **R** *represents the previously introduced material rotation tensor* (Bonet & Wood, 1997).

In order to dispose with an invariant type of the constitutive description, the objectivity requirement must be met with regard to any further adapted strain and stress tensor. According to the rule in Eq. (2.87), any second-order tensor can be tested for objectivity (Lai, Rubin & Krempl, 1993). At the moment, mention that the Green-Lagrangian strain tensor *E*, and the rate of deformation tensor *d* have this key tensor property. Nevertheless, in the proposed numerical formulation both quantities have special importance (*Chapter 5 – 5.4 Microplane strain tensor*).

2.2.5 Cauchy's stress theory

Before moving onto the next topic regarding conjugate law, it seems opportune to introduce some aspects of the *Cauchy's stress theory* (Brodersen, 2004). For this purpose, Fig. 2.3 illustrates the continuum body *B* that in time *t*=0 occupies the geometric region Ω_0 bounded with the boundary $\partial\Omega_0$. Suppose that the body *B* is influenced by volume and surface forces that cause the continuum to move and deform. Furthermore, following the academic strategy of introducing the concept of stresses, the body in movement is truncate in two sections (Fig. 2.3). It is assumed that certain internal forces, that substitute the missing part of the continuum, exist on the generated surfaces in order to keep force balance. Furthermore, imagine an elementary surface $\mathrm{d}s \subset \partial\Omega$ on the cross section in the current continuum configuration. The direction of d*s* is defined through the normal unit vector **n**. On the other hand, in the reference configuration, $\mathrm{d}S \subset \partial\Omega_0$ denotes an elementary surface with its normal unit vector **N**.

The d**f** part of the total force **f**, that acts on the continuum cross sections, can be related to the elementary surfaces d*s* and d*S*. The *Cauchy postulated* says that the relation in Eq. (2.88) is valid for each elementary surface in the continuums body (Brodersen, 2004).

$$\mathrm{d}\mathbf{f} = \mathbf{t}\mathrm{d}s = \mathbf{T}\mathrm{d}S \tag{2.88}$$

_____
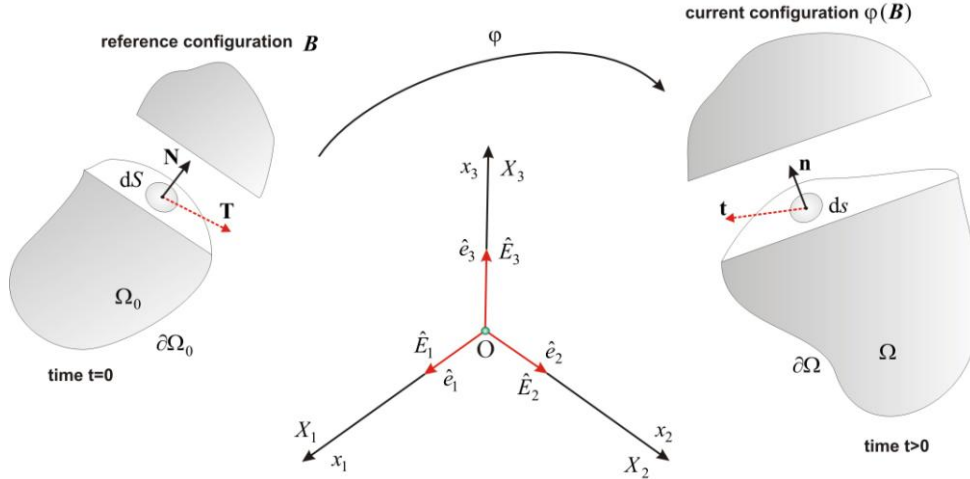
Figure 2.3 Stress vectors in the reference and current configuration

In this expression **t** denotes the *Cauchy traction vector* and **T** the 1st *Piola-Kirchoff traction vector*. In the *Cauchy's theorem of stresses*, there exists the stress tensors **σ** and **P**, linearly with **n** and **N**, and valid for (Truesdell & Noll, 1992):

$$\mathbf{t}(\mathbf{x},t,\mathbf{n}) = \boldsymbol{\sigma}(\mathbf{x},t)\mathbf{n} \quad ; \quad t_i = \sigma_{ij}n_j,$$
$$\mathbf{T}(\mathbf{X},t,\mathbf{N}) = \mathbf{P}(\mathbf{X},t)\mathbf{N} \quad ; \quad T_i = P_{iJ}N_J. \tag{2.89}$$

The stress tensor **σ** denotes a symmetric tensor, called *Cauchy stress tensor* (related to the reference configuration) and **P** represents the non-symmetric 1st *Piola-Kirchhoff stress tensor* (PK1). PK1 is a dual type tensor due to the fact that the index *i* refer to the spatial coordinates while the other index *J* refers to the material coordinates. Note that if the continuum body rotates, without generating change in stresses, PK1 and **σ** will vary with material orientation. In order to examine the relation between **σ** and **P**, the *Nanson's formula*, which links material line segments d*l* and d*L*, is introduced (2.90).

$$\mathrm{d}l = J\,\mathbf{F}^{-\mathrm{T}}\mathrm{d}L \tag{2.90}$$

Introducing the line segments d*l* and d*L* into Eq. (2.89), so that:

$$\mathbf{t}(\mathbf{x},t,\mathbf{n}) = \mathbf{T}(\mathbf{X},t,\mathbf{N}), \tag{2.91a}$$

$$\boldsymbol{\sigma}(\mathbf{x},t)\mathbf{n}\mathrm{d}l = \mathbf{P}(\mathbf{X},t)\mathbf{N}\mathrm{d}L, \tag{2.91b}$$

$$\boldsymbol{\sigma}(\mathbf{x},t)\mathrm{d}l = \mathbf{P}(\mathbf{X},t)\mathrm{d}L, \tag{2.91c}$$

and by substituting Eq. (2.91c) in Eq. (2.90), it can be obtained that

$$\boldsymbol{\sigma} = J\,\mathbf{P}^{-\mathrm{T}}\mathbf{F}^{\mathrm{T}}, \tag{2.92}$$

for the Cauchy stress tensor **σ**, and

$$\mathbf{P} = J\,\boldsymbol{\sigma}\mathbf{F}^{\mathrm{T}}, \tag{2.93}$$

for the 1$^{\text{st}}$ *Piola-Kirchhoff stress tensor* **P** (Brodersen, 2004). Note that the term $J\boldsymbol{\sigma}$ on the left side of the former expression is usually referred to as *Kirchhoff stress sensor* $\boldsymbol{\tau}$. In case of small deformations (small displacements), $\boldsymbol{\tau}$ is reduced to $\boldsymbol{\sigma}$ (2.93) since $J \approx 1$ (2.94).

$$\boldsymbol{\tau} \approx J\,\boldsymbol{\sigma} \tag{2.94}$$

Note that **P** is asymmetric and as such not suitable for any conventional constitutive model. However, a quantity called 2$^{\text{nd}}$ *Piola-Kirchoff stress tensor* (PK2) and denoted by *S* is defined in material coordinates and is suitable for the formulation of constitutive equations. Namely, PK1 is a *dual type of tensor* that owns its asymmetric property to tensor indexes relation with different configurations. On the other hand, PK2 corrects this impropriety by the *pull-back operation* (2.38) in the contravariant tensor field $\boldsymbol{\tau}$ (2.94) giving

$$S = J\,\mathbf{F}^{-1}\boldsymbol{\sigma}\mathbf{F}^{-\mathrm{T}}, \tag{2.95}$$

which also illustrates the direct relation between *S* and $\boldsymbol{\sigma}$. From the aspect of the well-known stress definition, one can say that the Cauchy stress tensor $\boldsymbol{\sigma}$ associates forces with the surface area in the current configuration. Due to its physical meaning, this property makes $\boldsymbol{\sigma}$ also known as the *true stress tensor*. On the other hand, PK1 relates the forces in the current configuration with the areas in the reference configuration. It is evident that in this case a physical meaning is missing. Similarly, PK2 relates the force in the reference configuration with a surface area in the current configuration (Ruigomez, 1985). In this case the physical meaning is also hard to interpret but, as being a symmetric tensor, its benefit is evident in the formulation of material constitutive models.

Finally, the so called *back-rotated Cauchy stress tensor s* should be also introduced since its presence in the proposed numerical formulation is inevitable. The stress measure is defined by Eq. (2.96).

$$s = \mathbf{R}^{\mathrm{T}}\boldsymbol{\sigma}\mathbf{R} \tag{2.96}$$

The back-rotated Cauchy stress tensor *s* is linked to an imaginary *intermediate configuration*, where is defined by stretching **U** before the rotation **R** is applied. In other words, *s* is expressed in terms of components in a coordinate system that follows the continuum motion (Belytschko, Liu & Moran, 2001). Its importance in the proposed numerical formulation will be discussed later (*Chapter 5 – 5.3 Microplane stress tensor*).

Before proceeding, it is opportune to introduce the traditional *Voigt notation* (Zienkiewicz & Taylor, 2002); adopted to simplify the equations delivered in the framework of FE. Namely, since the tensors under consideration are symmetric tensors, the six independed components are rewritten in compact form by regrouping them as is illustrated in (2.97).

$$\boldsymbol{\sigma} \ \xrightarrow{\ \text{Voight}\ } \ \underline{\boldsymbol{\sigma}} = \left\{ \sigma_{11} \quad \sigma_{22} \quad \sigma_{33} \quad \sigma_{12} \quad \sigma_{23} \quad \sigma_{13} \right\}^{\mathrm{T}} \tag{2.97}$$

2.2.6 Conjugate law

Generally, the internal system energy can be always expressed in terms of system internal state variables. For continuum deformation analysis, the internal energy can be defined as a product of internal force with related displacements. Therefore, force and displacement form *work-conjugate pair*. To discuss the work-conjugacy importance, resume that the displacement field is related to external loading through a system of fifteen differential equations, where six of them are attributed to the material constitutive model. Furthermore, assume that the constitutive equations are expressed in terms of stress and strain. In order to preserve the system energy, the stress tensor (force norm at the elementary surface) and the adopted strain tensor should be work-conjugate (Bonet & Wood, 1997). Only in this way an eventual energy perturbation, related to a material constitutive model, can be avoided.

To illustrate the principle, imagine an elementary volume under compression. In this case, the pressure force can be generalized by the stress tensors $\boldsymbol{\sigma}$ while the change in volume by the volume V multiplied with the strain tensor $\boldsymbol{\varepsilon}$. The related mechanical work dw, as result of a stress-induced infinitesimal strain d$\boldsymbol{\varepsilon}$, can be calculated as

$$\mathrm{d}w = -V\sigma_{ij}\mathrm{d}\varepsilon_{ij}\,, \tag{2.98}$$

where $\boldsymbol{\sigma}$ and $\boldsymbol{\varepsilon}$ represent a work-conjugate pair (2.99).

$$\boldsymbol{\sigma} \xleftrightarrow{\text{work conjugate}} \boldsymbol{\varepsilon} \tag{2.99}$$

Generalizing, for any strain measure $\mathbf{E}^{(m)}$, the related work-conjugate stress tensor $\mathbf{T}^{(m)}$ should be chosen in the way that the stress power per unit volume complies with (Lubarda, 1999)

$$\mathbf{T}^{(m)} : \dot{\mathbf{E}}^{(m)} = \boldsymbol{\tau} : \boldsymbol{d}\,, \tag{2.100}$$

in which $\boldsymbol{\tau}$ (2.94) and $\boldsymbol{d}$ (2.85) represent the earlier introduced tensors. According to the former equality, the following, here important, stress-strain conjugate pairs (2.101) are retrieved by changing the value of m in Eq. (2.74).

$$S \xleftrightarrow{\text{work conjugate}} E$$

$$\tag{2.101}$$

$$J\,s \xleftrightarrow{\text{work conjugate}} H$$

It should be mentioned that the use of a non-conjugated stress-strain pair is sometimes inevitable. In fact, to numerically simulate complex material behavior, one may need to decide whether to preserve the work-conjugacy or to retain tensors pairs that does not fit well in Eq. (2.100) but poses physical meaning which is obviously an important requirement. The mentioned reflects the here present compromise situation that will be discussed later on (*Chapter 5 – 5.4 Microplane strain tensor*).

2.2.7 Generalized Hooke's law

It is well known that the *Hooke's law of elasticity* defines the relationship between stress and strain in the displacement range where the **σ**-**ε** relationship is linear. Furthermore, as a prerequisite for linearity, the *strain energy function W* should be homogeneous and quadratic function of strain components with coefficients that increase proportionally with the increase of deformation. Particularly, $W(\boldsymbol{\varepsilon}) \geq 0$, and for no continuum deformation, $W(\mathbf{I})=0$. In such case, W can be written for Hooke material as (Lehmann, 2008)

$$W = \frac{1}{2}C_{ijkl}\varepsilon_{ij}\varepsilon_{kl} \qquad \text{where} \quad i,j,k,l = 1,2,3. \tag{2.102}$$

The first derivation respect to strains will lead to the proportionality of **σ** respect to **ε** as

$$\sigma_{ij} = \frac{\partial W}{\partial \varepsilon_{ij}}, \tag{2.103}$$

while the second derivative will give the fourth-order *stiffness tensor* C_{ijkl} with 81 components (2.104).

$$C_{ijkl} = \frac{\partial^2 W}{\partial \varepsilon_{ij}\partial \varepsilon_{kj}} \tag{2.104}$$

The linear **σ**-**ε** constitutive relationship is then given by

$$\sigma_{ij} = C_{ijkl}\,\varepsilon_{kl}. \tag{2.105}$$

Since the order of differentiation should not matter, the Eq. (2.106) holds.

$$C_{ijkl} = C_{klij} \tag{2.106}$$

According to $\sigma_{ij} = \sigma_{ji}$, Eq. (2.107) is also valid.

$$C_{jikl} = C_{ijkl} \tag{2.107}$$

Finally, $\varepsilon_{kl} = \varepsilon_{lk}$ so Eq. (2.108) is also true.

$$C_{ijkl} = C_{ijlk} \tag{2.108}$$

All these symmetries reduce the final number of independent components of C_{ij} to 21. For a general anisotropic material, **σ** and **ε** can be now related in compact form by rewriting the stress and strain tensors in a vectorial notation (*Voigt notation*). In this case, the obtained system of Eq. represents the *generalized Hooke's law of elasticity* (2.109).

$$\begin{Bmatrix} \sigma_{11} \\ \sigma_{22} \\ \sigma_{33} \\ \sigma_{12} \\ \sigma_{23} \\ \sigma_{13} \end{Bmatrix} = \begin{bmatrix} C_{1111} & C_{1122} & C_{1133} & C_{1112} & C_{1123} & C_{1113} \\ \cdot & C_{2222} & C_{2233} & C_{2212} & C_{2223} & C_{2213} \\ \cdot & \cdot & C_{3333} & C_{3312} & C_{3323} & C_{3313} \\ \cdot & \cdot & \cdot & C_{1212} & C_{1223} & C_{1213} \\ \cdot & \cdot & \cdot & \cdot & C_{2323} & C_{2313} \\ sym & \cdot & \cdot & \cdot & \cdot & C_{1313} \end{bmatrix} \begin{Bmatrix} \varepsilon_{11} \\ \varepsilon_{22} \\ \varepsilon_{33} \\ \varepsilon_{12} \\ \varepsilon_{23} \\ \varepsilon_{13} \end{Bmatrix} \tag{2.109}$$

Nevertheless, the former system of Eq. is valid only for displacement gradients such as (Lehmann, 2008):

$$u_{i,j} u_{k,l} << u_{i,j}, \tag{2.110}$$

making the approximation $u_{ij} \approx \partial u_i / \partial X_j$ valid and enabling to write

$$\varepsilon_{ij} \approx E_{ij} \approx \frac{1}{2}(u_{i,j} + u_{j,i}). \tag{2.111}$$

In this case, ^0C and ^1C configurations almost coincide. However, observe that for any magnitude of deformation, Eq. (2.111) is over-determined. In fact, 6 strain components are related to 3 displacement components. In order to obtain a unique solution, an additional condition is imposed on the strain components. The *linear strain compatibility equations* (2.112) provide the needed restriction.

$$\begin{aligned} \frac{\partial^2 \varepsilon_{11}}{\partial x_2^2} + \frac{\partial^2 \varepsilon_{22}}{\partial x_1^2} = \frac{\partial^2 \varepsilon_{12}}{\partial x_1 \partial x_2} \quad &; \quad 2\frac{\partial^2 \varepsilon_{11}}{\partial x_2 \partial x_3} = \frac{\partial}{\partial x_1}\left(\frac{\partial \varepsilon_{12}}{\partial x_3} + \frac{\partial \varepsilon_{13}}{\partial x_2} - \frac{\partial \varepsilon_{23}}{\partial x_1} \right) \\ \frac{\partial^2 \varepsilon_{22}}{\partial x_3^2} + \frac{\partial^2 \varepsilon_{33}}{\partial x_2^2} = \frac{\partial^2 \varepsilon_{23}}{\partial x_2 \partial x_3} \quad &; \quad 2\frac{\partial^2 \varepsilon_{22}}{\partial x_1 \partial x_3} = \frac{\partial}{\partial x_2}\left(\frac{\partial \varepsilon_{12}}{\partial x_3} - \frac{\partial \varepsilon_{13}}{\partial x_2} + \frac{\partial \varepsilon_{23}}{\partial x_1} \right) \\ \frac{\partial^2 \varepsilon_{33}}{\partial x_1^2} + \frac{\partial^2 \varepsilon_{11}}{\partial x_3^2} = \frac{\partial^2 \varepsilon_{31}}{\partial x_1 \partial x_3} \quad &; \quad 2\frac{\partial^2 \varepsilon_{33}}{\partial x_1 \partial x_2} = \frac{\partial}{\partial x_3}\left(\frac{\partial \varepsilon_{12}}{\partial x_3} + \frac{\partial \varepsilon_{13}}{\partial x_2} + \frac{\partial \varepsilon_{23}}{\partial x_1} \right) \end{aligned} \tag{2.112}$$

Before proceeding, mention that the principles contained in Eq. (2.103) and Eq. (2.104) hold for non-linear material, as well.

2.2.8 Hyperelasticity

As already mentioned (*Chapter 1 – 1.1 Motivation*), the main purpose of the thesis is to develop a numerical formulation for concrete failure under high-energy impact loading. With the aim of validating such formulation, the proposed numerical description is translated into a program code which offers the possibility to investigate different types of collision (at low but especially at high loading rates). As far as the area of high-energy collision is concerned, including large deformation in the description of occasionally elastic solids seems logical. For this purpose, and since the Hooke's law is valid only for the linear **σ**-**ε** relationship (2.110), it is appropriate to introduce a briefly overview of material *hyperelasticity*.

According to the general definition of hyperelasticity, the strain energy function *W* depends on **F** via

$$\mathrm{W}(\mathbf{F}) = \int_{\Gamma} \boldsymbol{P}\,\mathbf{dF},$$

(2.113)

where, for the given deformation path Γ, *W* has the property that $W(\mathbf{I})=0$, $W(\mathbf{F})\geq 0$ and (Brodersen, 2004)

$$W(\mathbf{F}) \rightarrow \infty \quad \text{if} \quad \det(\mathbf{F}) \rightarrow \infty \quad \text{and} \quad W(\mathbf{F}) \rightarrow \infty \quad \text{if} \quad \det(\mathbf{F}) \rightarrow 0.$$

(2.114)

Eq. (2.114) denotes that an infinite amount of energy is required to infinitely expand the body and to compress it to zero volume. Due to large elastic deformations, note that *W* should be also objective. This means that if the reference frame rotates, *W* must be transformed by the same rotation (2.115).

$$\mathbf{R}W(\mathbf{F})\mathbf{R}^{\mathrm{T}} = W(\mathbf{R}\,\mathbf{F})$$

(2.115)

According to Eq. (2.49), the former expression can be rewritten as

$$W(\mathbf{R}\mathbf{F}) = W(\mathbf{F}),$$

(2.116)

that confirms the objectivity of *W*. However, for isotropic material, Eq. (2.117) should be also valid.

$$W(\mathbf{F}\mathbf{R}) = W(\mathbf{F})$$

(2.117)

Furthermore, according to Eq. (2.103), *P* in Eq. (2.113) can be expressed as

$$\boldsymbol{P} = \frac{\partial W(\mathbf{F})}{\partial \mathbf{F}}.$$

(2.118)

The objectivity criterion implies that *W* depends implicitly on **F** through **C** (Brodersen, 2004). Hence

$$\boldsymbol{S} = 2\frac{\partial W(\mathbf{F})}{\partial \mathbf{C}} = \frac{\partial W(\mathbf{F})}{\partial \boldsymbol{E}},$$

(2.119)

where *W* is expressed as a function of *E* which is work-conjugated to *S* (2.101). To reproduce the linear elastic response, the character of *W* mast be appropriately defined. The so-called *Saint Venant-Kirchhoff model* has been adopted for this purpose (Bonet & Wood, 1997). The model is just an extension of the linear model to non-linear regime and it is formulated as

$$\mathrm{W}(\boldsymbol{E}) = \frac{\lambda}{2}(\mathbf{tr}\,\boldsymbol{E})^2 + \mu\,\mathbf{tr}\,\boldsymbol{E}^2,$$

(2.120)

where λ and μ are *Lamé constants* related to Young's modules *E* and Poisson ration υ by

$$\lambda = \frac{E\upsilon}{(1+\upsilon)(1-2\upsilon)} \quad \text{and} \quad \mu = \frac{E}{2(1+\upsilon)},$$

(2.121)

since it is assumed that the material is isotropic (2.117).

Note that W (2.157) describes *thermodynamic isothermal conditions* with entropy production reduced to zero. Consequently, it represents a perfect (ideal) elastic material for which the components of **C** (2.109) are given according to Eq. (2.104) as

$$C_{ijkl} = 2\frac{\partial^2 W}{\partial C_{ij}\partial C_{kl}} = \frac{\partial^2 W}{\partial E_{ij}\partial E_{kl}}. \tag{2.122}$$

To conclude the constitutive description, the ***S-E*** relationship in the *Saint Venant-Kirchhoff model* is given by (Bonet & Wood, 1997)

$$\mathbf{S} = \lambda\,\mathrm{tr}(\mathbf{E})\mathbf{I} + 2\mu\mathbf{E}. \tag{2.123}$$

According to the usual notations, tr(·) in Eq. (2.120) and Eq. (2.123) represents the trace of a tensor. It ought to be pointed out that (2.120) is *polyconvex* type of function and so does not represent a reasonable criterion for materials under compression. Indeed, if def**F** is equals to zero, which reflects total implosion of an elementary volume, the components of E will be equal to -0.5**I** (see Eq. 2.72).

2.3   Conservation laws

It is well known that every physical event is governed by the fundamental conservation laws and thermodynamic restrictions. Consequently, every numerical formulation delivered for the purpose of simulating physical events must preserve the quantity prescribed by the conservation laws. For this reason, the conservation laws are summarized as follow.

2.3.1 Conservation of mass

According to the basic principles of continuum mechanics, it is assumed that the mass m is continuous functions of spatial coordinates in the volume V. In this case, the scalar values m and V can be related through the density definition as

$$\rho = \lim_{dV \to 0}\frac{dm}{dV}, \tag{2.124}$$

where dm denotes the mass of the infinitesimal volume dV. The total mass is simply given by

$$m = \int_V \rho\,dV, \tag{2.125}$$

and in order to preserve the continuum mass, the material time-derivative of Eq. (2.125) should vanish (Dm/Dt=0). According to the previously introduced (*2.2.1 Kinematics of finite strain*), m can be expressed in terms of Lagrangian (m^*) and Eulerian (m) coordinates (2.126).

$$m^*(V_{\mathbf{X}},t) = \int\limits_{V_{\mathbf{X}}} \rho^*(\mathbf{X},t)\,\mathrm{d}\mathbf{X} \qquad \text{and} \qquad m(V_{\mathbf{x}},t) = \int\limits_{V_{\mathbf{x}}} \rho^*(\mathbf{x},t)\,\mathrm{d}\mathbf{x} \tag{2.126}$$

The material time-derivative of m^* will lead to

$$\frac{Dm^*(V_{\mathbf{X}},t)}{Dt} = \lim_{\mathrm{d}t\to 0} \frac{1}{\mathrm{d}t}\left[\int\limits_{V_{\mathbf{X}}} \left[\rho^*(\mathbf{X},t+\mathrm{d}t) - \rho^*(\mathbf{X},t)\right]\mathrm{d}\mathbf{X}\right] = \int\limits_{V_{\mathbf{X}}} \frac{\partial \rho^*(\mathbf{X},t)}{\partial t}\,\mathrm{d}\mathbf{X}\,. \tag{2.127}$$

Thus, the continuum mass will be preserved if (2.128) is true.

$$\frac{\partial \rho^*(\mathbf{X},t)}{\partial t} = 0 \tag{2.128}$$

The aforesaid is obvious since the material in the Lagrangian control volume is constant. As the density $\rho^*(\mathbf{X},t)$ depends on the Lagrangian coordinates $\mathbf{X}$, its value will not change even if the coordinate system does. Note that it is opposite to the Eulerian description of motion. From the Eulerian point of view, the material time-derivative of the second integral in Eq. (2.126) produces

$$\frac{Dm(V_{\mathbf{x}},t)}{Dt} = \lim_{\mathrm{d}t\to 0} \frac{1}{\mathrm{d}t}\left[\int\limits_{V_{\mathbf{x}}^t} \rho(\mathbf{x},t+\mathrm{d}t)\mathrm{d}\mathbf{x} - \int\limits_{V_{\mathbf{x}}} \rho(\mathbf{x},t)\mathrm{d}\mathbf{x}\right], \tag{2.129}$$

where the first integral is calculated according to the volume $V_{\mathbf{x}}$ in time t. In fact, due to the continuum deformation, the boundary S of the initial domain $V_{\mathbf{x}}$ will reshape to become a new boundary S^t. If the new volume is denoted by $V+\Delta V$, the former integral can be rewritten as

$$\frac{Dm(V_{\mathbf{x}},t)}{Dt} = \lim_{\mathrm{d}t\to 0} \frac{1}{\mathrm{d}t}\left[\int\limits_{V_{\mathbf{x}}^t} \left[\rho(\mathbf{x},t+\mathrm{d}t) - \rho(\mathbf{x},t)\right]\mathrm{d}\mathbf{x}\right] + \frac{1}{\mathrm{d}t}\int\limits_{\Delta V_{\mathbf{x}}} \rho(\mathbf{x},t)\mathrm{d}\mathbf{x}, \tag{2.130}$$

where the domain of integration ΔV in the second integral represents the volume swept out by particles on the surface S with velocity $v(\mathbf{x},t)$. For this integral the infinitesimal volume $\mathrm{d}\mathbf{x}$ is equal to $v \cdot \mathbf{n}\,\mathrm{d}S\,\mathrm{d}t$ where $\mathbf{n}$ denotes the unit normal outward vector on the elementary surface $\mathrm{d}S$. On the other hand, the second integral can be converted to a surface integral giving

$$\frac{Dm(V_{\mathbf{x}},t)}{Dt} = \int\limits_{V_{\mathbf{x}}} \frac{\partial \rho(\mathbf{x},t)}{\partial t}\,\mathrm{d}x + \frac{1}{\mathrm{d}t}\int\limits_{S_{\mathbf{x}}} \rho(\mathbf{x},t)v \cdot \mathbf{n}\,\mathrm{d}S = \int\limits_{V} \frac{\partial \rho}{\partial t}\,\mathrm{d}V + \frac{1}{\mathrm{d}t}\int\limits_{S} \rho\, v_j n_i\,\mathrm{d}S, \tag{2.131}$$

from where the relation (2.132) can be obtained by applying the divergence theorem.

$$\frac{\partial \rho}{\partial t} + \frac{\partial (\rho v_i)}{\partial x_i} = 0 \qquad \text{or} \qquad \frac{D\rho}{Dt} + \rho \frac{\partial v_i}{\partial x_i} = 0 \tag{2.132}$$

The former Eq. is usually called *equation of continuity* and it ensures the mass conservation by providing that the material time-derivative of *m* is zero (in the Eulerian frame).

2.3.2 Conservation of linear momentum

From the 2st *Newton's law*, the linear momentum changes only if a force **F** acts on a body (2.133).

$$F = ma \tag{2.133}$$

For a body immersed in a gravity field, the weight **w** is a vector function related to body density as

$$\mathbf{w} = \rho \mathbf{b}, \tag{2.134}$$

in which **b** denotes the vector of volume forces. Therefore, for a given surface traction **t** on the elementary surface d*S*, Eq. (2.133) can be rewritten as

$$F = \int_{V(t)} \rho \mathbf{b}\, dV + \int_{S(t)} \mathbf{t}\, dS. \tag{2.135}$$

By using Eq. (2.89), the former expression can be further restated as

$$F = \int_{V(t)} \rho \mathbf{b}\, dV + \int_{S(t)} \boldsymbol{\sigma}^{\mathrm{T}} \mathbf{n}\, dS. \tag{2.136}$$

If the following is introduced (Brodersen, 2004)

$$ma = \frac{D}{Dt} \int_{V(t)} \rho \mathbf{v}\, dV, \tag{2.137}$$

Eq. (2.133) can be expanded in terms of stresses on d*S*, producing:

$$\int_{V(t)} \rho \mathbf{b}\, dV + \int_{S(t)} \boldsymbol{\sigma}^{\mathrm{T}} \mathbf{n}\, dS = \frac{D}{Dt} \int_{V(t)} \rho \boldsymbol{v}\, dV. \tag{2.138}$$

In order to satisfy the equilibrium condition, Eq. (2.139) must be true.

$$\int_{V(t)} \rho \mathbf{b}\, dV + \int_{S(t)} \boldsymbol{\sigma}^{\mathrm{T}} \mathbf{n}\, dS = 0 \tag{2.139}$$

The Gauss divergence theorem applied to the 2st integral of the former Eq. will give

$$\int_{V(t)} \rho \mathbf{b}\, dV + \int_{S(t)} \boldsymbol{\sigma}\mathbf{n}\, dS = \int_{V(t)} (\rho \mathbf{b} + \nabla \boldsymbol{\sigma})\, dV = \int_{V} \rho \frac{D\boldsymbol{v}}{Dt}\, dV.$$
(2.140)

Finally, the given volume integral will be true if (Belytschko, Liu & Moran, 2001)

$$\rho \mathbf{b} + \nabla \boldsymbol{\sigma} = \rho \mathbf{a} \qquad \text{or} \qquad \rho b_i + \sigma_{ij,j} = \rho a_i,$$
(2.141)

where **a** denotes the body acceleration. If **a**=**0,** the former Eq. represent the *equilibrium equations*.

2.3.3 Conservation of angular momentum

According to classical dynamics, the rate of change of angular momentum *L* is directly related to the torque *T* via

$$T = \frac{dL}{dt}.$$
(2.142)

As is well known, *T* is zero for a body in equilibrium. On the basis of the definition of torque, the conservation of angular momentum can be expressed by expanding the concept in Eq. (2.139) over the entire body (2.143).

$$T = \int_{V(t)} \mathbf{r} \times \rho \mathbf{b}\, dV + \int_{S(t)} \mathbf{r} \times \boldsymbol{\sigma}\mathbf{n}\, dS = 0$$
(2.143)

By applying the divergence theorem to the second integral in Eq. (2.186), and by generalizing (2.143) in respect to local infinitesimal angular momentum, Eq. (2.143) can be arranged as follows (2.144):

$$T = \int_{V(t)} \varepsilon_{ijk}\, x_j\, \rho b_k\, dV + \int_{S(t)} \varepsilon_{ijk}\, x_j\, \sigma_{kl}\, n_i\, dS,$$

$$T = \int_{V(t)} \varepsilon_{ijk}\, x_j\, \rho b_k + (\varepsilon_{ijk}\, x_j\, \sigma_{kl})_{,l}\, dV,$$

$$T = \int_{V(t)} \varepsilon_{ijk}\, (x_j\, \rho b_k + (x_j\, \sigma_{kl})_{,l})\, dV,$$
(2.144)

$$T = \int_{V(t)} \varepsilon_{ijk}\, (x_j\, \rho b_k + x_{j,l}\, \sigma_{kl} + x_j\, \sigma_{kl,l})\, dV,$$

$$T = \int_{V(t)} \varepsilon_{ijk}\, \left\{ x_j\, (\rho b_k + \sigma_{kl,l}) + x_{j,l}\, \sigma_{kl} \right\} dV.$$

Since $x_{j,l} = \delta_{jl}$ and $\rho b_k + \sigma_{kl,l} = 0$, the last expression together with the equilibrium condition *T*=0 lead to

$$\int\limits_{V(t)} \varepsilon_{ijk}\sigma_{kj}\mathrm{d}V = 0 \qquad \rightarrow \qquad \varepsilon_{ijk}\sigma_{kl} = 0. \tag{2.145}$$

Then, few assortment operations like:

$$\begin{aligned} \varepsilon_{lmi}\,\varepsilon_{ijk}\,\sigma_{kj} &= 0, \\ \varepsilon_{lmi}\,\varepsilon_{jki}\,\sigma_{kj} &= 0, \\ (\delta_{lj}\,\delta_{mk} - \delta_{lk}\,\delta_{mj})\,\sigma_{kj} &= 0, \\ \sigma_{ml} - \sigma_{lm} &= 0, \end{aligned} \tag{2.146}$$

will finally leads to

$$\sigma_{ml} = \sigma_{lm} \qquad \text{or} \qquad \boldsymbol{\sigma} = \boldsymbol{\sigma}^{\mathrm{T}}, \tag{2.147}$$

which ensures the preservation of angular momentum, demanding the symmetry of stress tensor.

2.3.4 Conservation of energy

The energy conservation law will be presented by taking into account only mechanical energies in the system. Therefore, the kinetic energy K of a moving continuum can be calculated as

$$K(t) = \frac{1}{2}\int\limits_{V} \rho\,\mathbf{v}\,\mathbf{v}\,\mathrm{d}V, \tag{2.148}$$

and the work P done by volume and surfaces forces as

$$P(t) = \int\limits_{S} \mathbf{t}\cdot\mathbf{v}\,\mathrm{d}S + \int\limits_{V} \rho\mathbf{b}\,\mathbf{v}\,\mathrm{d}V. \tag{2.149}$$

The change in kinetic energy can be traced through the material time-derivative as

$$\frac{DK(t)}{Dt} = \int\limits_{V} \rho\,\mathbf{v}\cdot\frac{D\mathbf{v}}{Dt}\,\mathrm{d}V = \int\limits_{V} \rho\,v_i\,\frac{Dv_i}{Dt}\,\mathrm{d}V. \tag{2.150}$$

According to Eq. (2.141), the former Eq. can be rewritten as

$$\frac{DK(t)}{Dt} = \int\limits_{V} v_i\,(\sigma_{ij,j} + \rho b_i)\,\mathrm{d}V, \tag{2.151}$$

and since $(v_i\sigma_{ij})_{,j} = v_i\sigma_{ij,j} + v_{i,j}\sigma_i$, as

$$\frac{DK(t)}{Dt} = \int_V \left[(v_i \sigma_{ij})_{,j} + v_i \rho b_i - v_{i,j} \sigma_{ij} \right] dV.$$ (2.152)

By adopting the divergence theorem, the upper Eq. can be further restated as

$$\frac{DK(t)}{Dt} = \int_V v_i \rho b_i \, dV + \int_S t_i v_i \, dS - \int_V \sigma_{ij} D_{ij} \, dV,$$ (2.153)

where D_{ij} represents the symmetric part of $v_{i,j}$. By introducing the notations:

$$S = \int_V \sigma_{ij} D_{ij} \, dV \quad \text{where} \quad D_{ij} = sym(v_{i,j}),$$ (2.154)

it can be deduced that the mechanical power P, produced by external forces (2.149), is related to the change of kinetic energy (2.148) and internal energy S. The relations are defined by $(DK/Dt)+S=P$, and denotes the conservation of mechanical energies in the system.

2.4   Thermodynamic restrictions

In order to discuss the thermodynamic restriction imposed by the Second Law of Thermodynamics (entropy production), the multiplicative decomposition of $\mathbf{F}$ (2.37) is introduced by

$$\mathbf{F} = \mathbf{F}_e \mathbf{F}_p,$$ (2.155)

where $\mathbf{F}_e$ denotes the elastic part of deformation (*reversible part*) and $\mathbf{F}_p$ the plastic part of deformation (*irreversible part*). In this case, the continuum deformation can be interpreted as follows. According to

$$\mathbf{F} d\mathbf{X} = \mathbf{F}_e (\mathbf{F}_p d\mathbf{X}) = \mathbf{F}_e d\mathbf{x}_p,$$ (2.156)

instead of moving directly towards the current configuration, the continuum moves across an imaginary *intermediate configuration* (composed only by plastic strain) before it reach the current configuration. Congruently, the additive decomposition of strains is valid (2.157).

$$\varepsilon = \varepsilon_e + \varepsilon_p$$ (2.157)

To illustrate the consequences of thermodynamic restriction, assume that the material constitutive relations are given in terms of τ. The yield function is then expressed as a function of τ (2.94) and $\mathbf{q}$ as material hardening variable (Bonet & Wood, 1997). The variables τ and $\mathbf{q}$ represent the state variables and define the yield function E_{ye} as

$$E_{ye} \equiv \left\{ \ (\tau, \mathbf{q}) \ | \ f(\tau, \mathbf{q}) \leq 0 \ \right\}.$$ (2.158)

Note that due to material isotropy, the yield function (2.158) does not depend on the orientation of $\boldsymbol{\tau}$. In this case, the *Helmholtz free energy function* ψ (Nguyen, 2005) is given by

$$\psi = \psi(\mathbf{b}_e, \boldsymbol{\xi}), \tag{2.159}$$

and is a function of elastic part of the *left Cauchy-Green deformation tensor*

$$\mathbf{b}_e = \mathbf{F}_e \mathbf{F}_e^{\mathrm{T}}, \tag{2.160}$$

and the internal variable $\boldsymbol{\xi}$, which is work conjugated to $\mathbf{q}$ (2.161).

$$\mathbf{q} = -\frac{\partial \psi}{\partial \boldsymbol{\xi}} \tag{2.161}$$

In this case, the free energy function ψ depends only on $\mathbf{F}_e$ and $\mathbf{b}_e$. By ignoring the contributions of heat energy, the dissipation function D can be expressed as

$$D \equiv \boldsymbol{\tau} : \mathbf{d} - \frac{\mathrm{d}}{\mathrm{d}t} \psi(\mathbf{b}_e, \boldsymbol{\xi}) \geq 0, \tag{2.162}$$

and describe the principle of irrecoverable system energy due to plastic deformations. To obtain the time derivative of ψ, note that $\mathbf{b}_e$ lies in the *intermediate configuration*. For this reason, it should be transform according to Eq. (2.62) in the following manner (2.163).

$$\mathbf{b}_e = \mathbf{F}_e \mathbf{F}_e^{\mathrm{T}} = (\mathbf{F}\mathbf{F}_p^{-1})\,(\mathbf{F}_p^{-\mathrm{T}}\mathbf{F}^{\mathrm{T}}) = \mathbf{F}(\mathbf{F}_p^{-1}\mathbf{F}_p^{-\mathrm{T}})\mathbf{F}^{\mathrm{T}} = \mathbf{F}\,\mathbf{C}_p^{-1}\mathbf{F}^{\mathrm{T}} \tag{2.163}$$

The time derivative of $\mathbf{b}_e$ can be now calculated as

$$\dot{\mathbf{b}}_e = \dot{\mathbf{F}}\mathbf{C}_p^{-1}\mathbf{F}^{\mathrm{T}} + \mathbf{F}\mathbf{C}_p^{-1}\dot{\mathbf{F}}^{\mathrm{T}} + \mathbf{F}\frac{\mathrm{d}}{\mathrm{d}t}(\mathbf{C}_p^{-1})\,\mathbf{F}^{\mathrm{T}}, \tag{2.164}$$

where the last term indicates the *Lie derivative* defined as (Belytschko, Liu & Moran, 2001)

$$\mathbf{F}\frac{\mathrm{d}}{\mathrm{d}t}(\mathbf{C}_p^{-1})\,\mathbf{F}^{\mathrm{T}} = \mathit{l}_v\,\mathbf{b}_e. \tag{2.165}$$

Resume that, the *Lie derivative* denotes the return of $\mathbf{C}_p$ to the reference configuration and, after performing its time derivative, it pushes $\mathbf{C}_p$ towards to the current configuration. Furthermore, the derivative of deformation gradient in Eq. (2.164) can be related to the elastic part $\mathbf{b}_e$ by

$$\dot{\mathbf{F}} = \frac{\partial \mathbf{v}}{\partial \mathbf{X}}\mathbf{F}_p^{-1}\,\mathbf{F}_p^{-\mathrm{T}}\mathbf{F}^{\mathrm{T}} = \frac{\partial \mathbf{v}}{\partial \mathbf{x}}\mathbf{F}\,\mathbf{F}_p^{-1}\mathbf{F}_p^{-\mathrm{T}}\mathbf{F}^{\mathrm{T}} = \mathit{l}\,\mathbf{F}_e\mathbf{F}_e^{\mathrm{T}} = \mathit{l}\,\mathbf{b}_e. \tag{2.166}$$

Using Eq. (2.165) and Eq. (2.166), Eq. (2.164) can be rewritten by separating its elastic and plastic part as

$$\dot{\mathbf{b}}_e = \underbrace{\boldsymbol{l}\,\mathbf{b}_e + \mathbf{b}_e \boldsymbol{l}^{\mathrm{T}}}_{\text{elasti part}} + \underbrace{\boldsymbol{l}_v \mathbf{b}_e}_{\text{plastic part}} \quad . \tag{2.167}$$

The dissipation function D in Eq. (2.162) may be now rewritten in terms of $\mathbf{b}_e$, such that

$$D \equiv \boldsymbol{\tau} : \boldsymbol{d} - \frac{\mathrm{d}\psi}{\mathrm{d}t} : \dot{\mathbf{b}}_e - \frac{\partial \psi}{\partial \boldsymbol{\xi}} \cdot \boldsymbol{\xi}, \tag{2.168}$$

while according to Eq. (2.161) and Eq. (2.167), as

$$D \equiv \boldsymbol{\tau} : \boldsymbol{d} - \frac{\mathrm{d}\psi}{\mathrm{d}\mathbf{b}^e} : (\boldsymbol{l}\,\mathbf{b}_e + \mathbf{b}_e \boldsymbol{l}^{\mathrm{T}} + \boldsymbol{l}_v \mathbf{b}_e) + \mathbf{q} \cdot \dot{\boldsymbol{\xi}},$$

$$D \equiv \boldsymbol{\tau} : \boldsymbol{d} - 2\frac{\mathrm{d}\psi}{\mathrm{d}\mathbf{b}_e}\mathbf{b}_e : \boldsymbol{l} + \left(2\frac{\partial \psi}{\partial \mathbf{b}_e}\mathbf{b}_e\right) : \left[-\frac{1}{2}(\boldsymbol{l}_v \mathbf{b}_e)\mathbf{b}_e^{-1}\right] + \mathbf{q} \cdot \dot{\boldsymbol{\xi}}, \tag{2.169}$$

which finally leads to

$$D \equiv \left(\boldsymbol{\tau} - 2\frac{\partial \psi}{\partial \mathbf{b}_e}\mathbf{b}_e\right) : \boldsymbol{d} + \left(2\frac{\partial \psi}{\partial \mathbf{b}_e}\mathbf{b}_e\right) : \left[-\frac{1}{2}\underbrace{(\boldsymbol{l}_v \mathbf{b}_e)}_{\text{plastic part}}\mathbf{b}_e^{-1}\right] + \mathbf{q} \cdot \dot{\boldsymbol{\xi}} \geq 0. \tag{2.170}$$

Concluding, the thermodynamic restriction implies that inequality (2.170) must be satisfied in respect to all admissible stresses and internal state variables. It denotes the so-called *principle of maximal dissipation* (Nguyen, 2005). In other words, plastic deformations always occur in the direction that maximizes D.

It should be pointed out that in the case of elastic and hyperelastic materials, the thermodynamic restrictions are not present since there are no plastic strains (no entropy production). On the other hand, in the case of non-linear material (such as concrete), the maintenance of thermodynamic restriction plays a fundamental role in numerical simulation of deformations (Nguyen, 2005).

In order to numerically obtain the *principle of maximal dissipation* (2.170), a proper constitutive description of concrete must be adopted due to its property of non-elastic strain localization (Carol, Jirásek & Bažant, 2001; Kuhl, Steinmann & Carol, 2001).

Chapter 3

Spatial discretization

3.1 Introduction

It is difficult, usually impossible, to obtain a *closed-form solution* of the governing differential equations that describe the continuum deformations caused by pre-defined force fields. In order to overcome this problem, an approximate solution can be obtained by adopting one of the few numerical methods.

In the proposed numerical formulation, the *finite element method* is found to be the most appropriate for simulation of concrete failure under impact loading. As illustrated later, an extensive theory aimed at describing mechanical interactions has been developed in accordance with finite elements. Furthermore, over the past few decades, many similar numerical formulations have shown that the use of the finite element method, to approximately describe such a complex physical event, is well justified (Unosson, 2000; Buchar, Voldřich, Rolc & Lazar, 2002; Ballew, 2004; Ramm, Erhart & Wall, 2005; Zinn, Stangenberg, Borgerhoff, Chauvel & Touret, 2007).

At this point it should be mentioned that the *temporal discretization* and *contact mechanics* are discussed in two separate chapters. The current chapter is dedicated only to the derivation of FE equations for static loading condition and non-constrained equations of motion (no contact). Also, mention that the differential equations are defined within the space occupied by the material in question and, in accordance with the usual mathematical notations, they will be hereinafter referred to as domain Ω bounded by Γ.

The numerical approximation of the event covered by the thesis begins with the process of *spatial discretization*. With regard to the physical domain Ω, occupied by body $\boldsymbol{B} \subset \Re^3$, the spatial discretization involves the subdivision of Ω into a finite number n_e of sub-domains Ω_e (3.1), i.e. FE.

$$\Omega \approx \bigcup_{e=1}^{n_e} \Omega_e \tag{3.1}$$

In order to remain in the framework of continuum mechanics, possible gaps inside the discretized spatial region must be avoided. For this purpose, the generated sub-domains Ω_e are interconnected by points i.e. FE nodes. With a finite number of nodes, the real physical body (concrete treated as a continuum) is exchanged with an approximate domain, represented by a mesh of finite elements (Fig. 3.1).
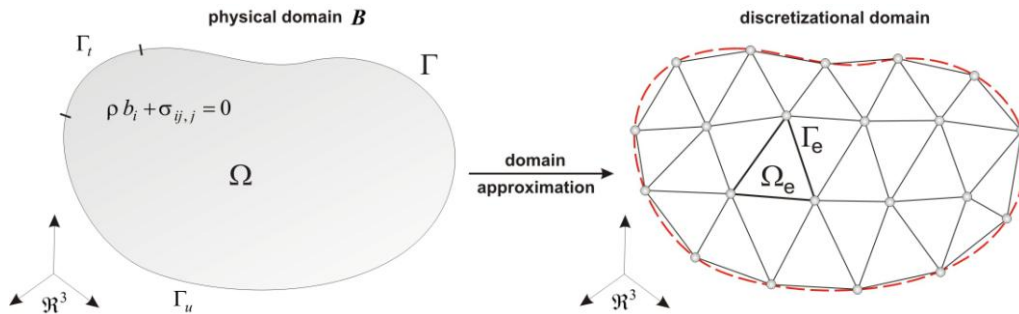
Figure 3.1 Approximation of the real physical domain by a finite number of sub-domains (finite elements)

Accordingly, spatial discretization "translates" the real physical domain Ω, containing an infinite number of degrees of freedom (DOF), to an approximate domain characterized by a finite number of DOF. Mention also that as the displacement filed *u* plays a fundamental role in deformation analysis, the nodal DOF are assumed to represent discrete displacement values of the continuous displacement function. Consequently, each finite element node (here identified by an upper index *n*) keeps the information on three orthogonal displacement components, collected in a vector $^n\mathbf{u}$ as

$$^n\mathbf{u} = \begin{Bmatrix} ^n u_1 \\ ^n u_2 \\ ^n u_3 \end{Bmatrix} \quad \text{or} \quad ^n u_i \quad \text{where} \quad i = 1,2,3. \tag{3.2}$$

3.2   Governing equations

As mentioned, the conservation laws and imposed thermodynamic restrictions must be respected in every time interval $[t_1,t_2] \subset \mathfrak{R}^+$ of the deformations history (*Chapter 2 – 2.3 Conservation laws & 2.4 Thermodynamic restrictions*). Furthermore, under static loading conditions without mechanical interactions among bodies, the essential and natural boundary conditions are needed to define a single solution of the continuum deformation problem (Zienkiewicz & Taylor, 2002). Finally, to characterize the continuum under consideration, and the range of expected deformations, the material constitutive description and the strain-displacement relationship should be also properly defined. The formed sets of differential equations govern the continuum deformation process and are consequently referred to as *governing equations*.

3.2.1 Strong form – indicial notation

Using rigorous mathematical notations, the abovementioned description is usually restated as:

$$\text{find} \quad u \in \mathfrak{R}^3 \quad \text{such that}:$$

$$\rho b_i + \sigma_{ij,j} = 0 \quad \text{in} \quad \Omega, \tag{3.3a}$$

$$\text{respect to}:$$

$$\sigma_{ij} = f(\varepsilon_{ij}, \dot{\varepsilon}_{ij}, \text{ect.}), \tag{3.3b}$$

$$\varepsilon_{ij} = f(u_i), \tag{3.3c}$$

$$\text{and subject to}:$$

$$t_i = \sigma_{ji} n_j = \bar{t}_i \quad \text{on} \quad \Gamma_t, \tag{3.3d}$$

$$u_i = \bar{u}_i \quad \text{on} \quad \Gamma_u, \tag{3.3e}$$

$$\text{where}:$$

$$\Gamma = \Gamma_t \cup \Gamma_u \qquad \text{and} \qquad \Gamma_t \cap \Gamma_u = \notin,$$

representing the so-called strong problem formulation for continuum deformation analysis. In the given notation, (3.3d) denotes the *stress boundary condition* (*Neumann boundary condition*) imposed on the continuum boundary Γ_t and on prescribed surface traction $\bar{t}_i$ (characterized by the unit normal vector n_i). The *displacement boundary condition*s (*Dirichlet boundary condition*) are given in Eq. (3.3e) and are predefined by the displacement values $\bar{u}_i$ on the boundary Γ_u. Since the problem is formulated in terms of displacement u, and the balance of linear momentum is expressed in terms of stresses σ (3.3a), the link between them is established by an appropriate constitutive description (3.3b), as well as by the defined measure of deformation (3.3c). Note that the strong formulation does not abide neither by conservation laws (expect from the conservation of linear momentum) nor by the imposed thermodynamic restrictions. Namely, in the FE environment, their presence is typically artificially incorporated by means of material constitutive definition (*Chapter 5 – Microplane material model*).

3.2.2 Strong form – matrix notation

Following the usual FE practice, the matrix notations of quantities under consideration is firstly introduced. For this purpose, assume small deformations (2.110) of a linear elastic material defined by the generalized Hooke's law (2.109). In this case, the stress tensor σ_{ij} is translated into the vector form $\underline{\sigma}$ (2.97), while the components of the strain tensor ε_{ij} are congruently contained in vector $\underline{\varepsilon}$ as

$$\underline{\varepsilon} \xrightarrow{\text{Voight}} \underline{\varepsilon} = \left\{ \varepsilon_{11} \quad \varepsilon_{22} \quad \varepsilon_{33} \quad \gamma_{12} \quad \gamma_{23} \quad \gamma_{31} \right\}^{\mathrm{T}} \quad \text{where} \quad \gamma_{ij} = 2\varepsilon_{ij} \quad \text{if} \quad i \neq j. \tag{3.4}$$

The strain-displacement relation is given by

$$\underline{\varepsilon} = \boldsymbol{S}\mathbf{u}, \tag{3.5}$$

where $\boldsymbol{S}$ denotes the three-dimensional strain operator (3.6).

$$\boldsymbol{S} = \begin{bmatrix} \partial \cdot / \partial x_1 & 0 & 0 \\ 0 & \partial \cdot / \partial x_2 & 0 \\ 0 & 0 & \partial \cdot / \partial x_3 \\ \partial \cdot / \partial x_2 & \partial \cdot / \partial x_1 & 0 \\ 0 & \partial \cdot / \partial x_3 & \partial \cdot / \partial x_2 \\ \partial \cdot / \partial x_3 & 0 & \partial \cdot / \partial x_1 \end{bmatrix} \tag{3.6}$$

According to Eq. (2.105), the constitutive description is formulated as

$$\underline{\sigma} = \mathbf{D}\underline{\varepsilon}, \tag{3.7}$$

where the matrix $\mathbf{D}$ gathers the stiffness parameters contained in C_{ijkl} (2.109) by extracting values associated to index pairs ij and kl as is illustrated by Zienkiewicz & Taylor (2002).

The displacement boundary conditions are simply redefined as

$$\mathbf{u} = \bar{\mathbf{u}} \quad \text{on} \quad \Gamma_u, \tag{3.8}$$

and the traction boundary conditions are given by

$$\mathbf{t} = \boldsymbol{G}^{\mathrm{T}}\underline{\sigma} = \bar{\mathbf{t}} \quad \text{on} \quad \Gamma_t, \tag{3.9}$$

where $\boldsymbol{G}$ (3.10) collects the direction cosines of the normal vector $\mathbf{n}$ on boundary Γ_t.

$$\boldsymbol{G}^{\mathrm{T}} = \begin{bmatrix} n_1 & 0 & 0 & n_2 & 0 & n_3 \\ 0 & n_2 & 0 & n_1 & n_3 & 0 \\ 0 & 0 & n_3 & 0 & n_2 & n_1 \end{bmatrix} \tag{3.10}$$

With the given matrix notations, the previously introduced strong form (3.3) can be rewritten as

$$\text{find} \quad u \in \Re^3 \quad \text{such that}:$$

$$\rho \mathbf{b} + \boldsymbol{S}^{\mathrm{T}} \underline{\boldsymbol{\sigma}} = 0 \quad \text{in} \quad \Omega,$$

$$\text{respect to}:$$

$$\underline{\boldsymbol{\sigma}} = \mathbf{D}\underline{\boldsymbol{\varepsilon}},$$

$$\underline{\boldsymbol{\varepsilon}} = \boldsymbol{S}\,\mathbf{u},$$

$$\text{and subject to}:$$

$$\mathbf{t} = \boldsymbol{G}^{\mathrm{T}}\underline{\boldsymbol{\sigma}} = \bar{\mathbf{t}} \quad \text{on} \quad \Gamma_t,$$

$$\mathbf{u} = \bar{\mathbf{u}} \quad \text{on} \quad \Gamma_u,$$

$$\text{where}:$$

$$\Gamma = \Gamma_t \cup \Gamma_u \qquad \text{and} \qquad \Gamma_t \cap \Gamma_u = \notin.$$

To obtain an approximate solution in form of *kinematically admissible displacement* **u**, the so-called weak formulation of the problem, which leads to the *principle of virtual work*, is introduced (Zienkiewicz & Taylor, 2002).

3.2.3 Weak form

Assume that δu represents an arbitrary test function defined on the continuum body $\boldsymbol{B} \subset \Re^3$. In order to make the test function admissible, δu should vanish on the boundary part Γ_u for which the displacement boundary conditions $\bar{u}$ are prescribed. The weak form is than obtained from the strong formulation (3.3) by multiplying Eq. (3.3a) of linear momentum and traction boundary condition (3.3d) by δu. Subsequently, the integrals over the domain Ω and boundaries Γ_t are set to vanish (3.11).

$$-\int_{\Omega} \delta u_i (\sigma_{ij,j} + b_i)\, \mathrm{d}\Omega + \int_{\Gamma_t} \delta u_i (\sigma_{ij} n_j - \bar{t}_i)\, \mathrm{d}\Gamma_t = \ldots$$

$$\ldots = -\int_{\Omega} \delta u_i\, \sigma_{ij,j}\, \mathrm{d}\Omega - \int_{\Omega} \delta u_i\, b_i\, \mathrm{d}\Omega + \int_{\Gamma_t} \delta u_i\, \sigma_{ij} n_j\, \mathrm{d}\Gamma_t - \int_{\Gamma_t} \delta u_i\, \bar{t}_i\, \mathrm{d}\Gamma_t = 0 \tag{3.11}$$

Generally, the stresses σ will depend on strains ε which are derivative of displacements u. By consequence, to obtain the integrands, the integrals in Eq. (3.11) will require displacements second derivative. However, the need to compute second derivatives may be bypassed by performing *integration by parts* which will produce:

$$-\int_{\Omega} \delta u_i\, \sigma_{ij,j}\, \mathrm{d}\Omega = -\int_{\Omega} (\delta u_i\, \sigma_{ij})_{,j}\, \mathrm{d}\Omega + \int_{\Omega} \delta u_{i,j}\, \sigma_{ij}\, \mathrm{d}\Omega. \tag{3.12}$$

The first integral on the RHS can be converted into a surface integral as

$$-\int_{\Omega}(\delta u_i\,\sigma_{ij})_{,j}\,\mathrm{d}\Omega=-\int_{\Gamma_t}\delta u_i\sigma_{ij}n_j\,\mathrm{d}\Gamma_t,\tag{3.13}$$

which, if introduced in Eq. (3.12), gives

$$-\int_{\Omega}\delta u_i\,\sigma_{ij,j}\,\mathrm{d}\Omega=-\int_{\Gamma_t}\delta u_i\sigma_{ij}n_j\,\mathrm{d}\Gamma_t+\int_{\Omega}\delta u_{i,j}\sigma_{ij}\,\mathrm{d}\Omega.\tag{3.14}$$

By substituting Eq. (3.12) in Eq. (3.14), the weak form is obtained as

$$\int_{\Omega}\delta u_{i,j}\,\sigma_{ij}\,\mathrm{d}\Omega-\int_{\Omega}\delta u_i\,b_i\,\mathrm{d}\Omega-\int_{\Gamma_u}\delta u_i\,\bar{t}_i\,\mathrm{d}\Gamma_u=0,\tag{3.15}$$

or in matrix notation as

$$\int_{\Omega}\delta(\boldsymbol{S}\mathbf{u})^{\mathrm{T}}\underline{\boldsymbol{\sigma}}\,\mathrm{d}\Omega-\int_{\Omega}\delta\mathbf{u}^{\mathrm{T}}\mathbf{b}\,\mathrm{d}\Omega-\int_{\Gamma_t}\delta\mathbf{u}^{\mathrm{T}}\bar{\mathbf{t}}\,\mathrm{d}\Gamma_t=0.\tag{3.16}$$

The obtained Eq. represents the statement of virtual work with *δu* as *virtual displacements* (Bonet & Wood, 1997). Particularly, the first integral denotes the virtual work of stresses while the other two reflect the virtual work of body and traction forces, respectively.

Note that the form does not consider any material behavior in particular. Conditionally speaking, in contrast to the variational principles (Zienkiewicz & Taylor, 2002), the benefit of using this kind of formulation is shown by the need for specifying the constitutive material description and strain definition. In other words, the procedure enables to construct a numerical formulation for non-linear materials subject to large deformations.

3.2.4 Finite element approximation

To introduce the concept of FE discretization, consider a continuum body $\boldsymbol{B}\subset\Re^3$ with smoothed boundaries fragmentized in a number *n* of disjoint parts. Obviously, the union of all disjoint parts $\boldsymbol{B}_1$, $\boldsymbol{B}_2,\ldots\boldsymbol{B}_n\subset\boldsymbol{B}$ will lead back to $\boldsymbol{B}$ (3.17).

$$\boldsymbol{B}=\bigcup_{i=1}^{n}\boldsymbol{B}_i\quad\text{and}\quad\boldsymbol{B}_i\cap\boldsymbol{B}_j=\notin\quad\text{for}\quad i\neq j\tag{3.17}$$

The equality is trivial since every irregular arbitrary shape retrieved from $\boldsymbol{B}$ has the property that $\boldsymbol{B}_i\subset\boldsymbol{B}$. Similarly, the volume integral of an arbitrary function *g* taken over the domain of body $\boldsymbol{B}$, can be split into respective disjoint parts $\boldsymbol{B}_i$ as

$$\int_{\boldsymbol{B}} g \, dV = \int_{\cup_{i=1}^{n} \boldsymbol{B}_i} g \, dV = \sum_{i=1}^{n} \int_{\boldsymbol{B}_i} g_i \, dV_i. \tag{3.18}$$

On the other hand, imagine a number n_e of disjoint parts, such that $\boldsymbol{B}_1^{h}, \boldsymbol{B}_2^{h}, \dots \boldsymbol{B}_{n_e}^{h} \subset \boldsymbol{B}^h \subset \boldsymbol{B}$, which are characterized by regular shapes like polygons or parallelograms. The union of all disjoint parts will approximately describe the geometrical region $\boldsymbol{B}$, since the assumed regular shapes cannot exactly capture the supposed smoothed continuum boundaries. In this case, the geometric region occupied by the body $\boldsymbol{B}$ can be approximated as

$$\boldsymbol{B} \approx \boldsymbol{B}^h = \bigcup_{e=1}^{n_e} \boldsymbol{B}_e^h \quad \text{and} \quad \boldsymbol{B}_i^h \cap \boldsymbol{B}_j^h = \notin \quad \text{for} \quad i \neq j, \tag{3.19}$$

and the integral of a function g as

$$\int_{\boldsymbol{B}} g \, dV \approx \int_{\boldsymbol{B}^h} g \, dV = \int_{\cup_{e=1}^{n_e} \boldsymbol{B}_e^h} g^h \, dV = \sum_{e=1}^{n_e} \int_{\boldsymbol{B}_e^h} g_e^h \, dV_e. \tag{3.20}$$

Consequently, with a finite number n_e of FE used for the discretization of body $\boldsymbol{B}$, the related weak form will represent the contribution of all domains Ω_e (3.21).

$$\sum_{e=1}^{n_e} \left[\int_{\Omega_e} \delta(\boldsymbol{S}\mathbf{u})^{\mathrm{T}} \underline{\boldsymbol{\sigma}} \, d\Omega_e - \int_{\Omega_e} \delta\mathbf{u}^{\mathrm{T}}\mathbf{b} \, d\Omega_e \right] - \sum_{e=1}^{n_e} \int_{\Gamma_{t_e}} \delta\mathbf{u}^{\mathrm{T}}\bar{\mathbf{t}} \, d\Gamma_{t_e} = 0 \tag{3.21}$$

It is opportune to mention that the additive sum is allowed if the highest derivates appearing in the functional (3.21) are piecewise continuous so that all integrals exist and no contribution on the interelement boundaries is present (Zienkiewicz & Taylor, 2002). Generally speaking, for a function containing the highest derivative of order $m + 1$, the function adopted to approximate the unknown variable must have the property according to which all derivatives up to order m must give a continuous function over Ω_e (continuity condition). Such functions are usually denoted as C^m functions.

The choice of interpolation functions C^m is additionally limited by the property prescribing that C^m must contain complete polynomials up to the order $m + 1$. The property enables derivatives up to order $m + 1$ to assume constant values. Note that the aforementioned requirements do not change regardless of the type of FE adopted for the discretization.

On the other hand, it should be specified that there are finite element formulations which violate the continuity conditions leading to a so-called *incompatible formulation* (incompatible mode). The formulations are based on the so-called principle of *variational crime* and introduce additional DOF in FE (Wilson, Taylor, Doherty & Ghaboussi, 1973; Wilson, 1995).

3.2.4.1 Bubnov-Galerkin method

The essence of the *Bubnov-Galerkin method* (BG) lies in the proper approximation of the dependent variables u and their virtual (variational) forms δu in the weak formulation (3.15). To illustrate the Bubnov-Galerkin method, consider a problem in which the approximate solution u^h is obtained from:

$$\text{find} \quad u^h \in \mathcal{V}^h \quad \text{so that}:$$
$$\mathcal{A}^h(u^h, \delta u^h) = \mathcal{F}^h(\delta u^h) \quad \forall \delta u^h \in \mathcal{W}^h. \tag{3.22}$$

$\mathcal{V}^h$ is the finite-dimensional space of functions (where u^h is the approximate solution) and $\mathcal{W}^h$ is the discrete space of test functions δu^h. $\mathcal{A}^h$ and $\mathcal{F}^h$ are approximation functions of bilinear and linear form, respectively. In the Bubnov-Galerkin method the approximation of dependent variables u and their variational forms δu are chosen such that (Belytschko, Liu & Moran, 2001):

$$u = \left\{ u \mid u_i^h \in \mathcal{V}^h(\boldsymbol{B}^h), u^h = \bar{u} \text{ on } \Gamma_u^h \right\},$$
$$\delta u = \left\{ \delta u \mid \delta u_i^h \in \mathcal{W}^h(\boldsymbol{B}^h), \delta u^h = 0 \text{ on } \Gamma_u^h \right\}, \tag{3.23}$$

and are subject to

$$\mathcal{W}^h = \mathcal{V}^h. \tag{3.24}$$

3.2.4.2 Displacement interpolation

The element degrees of freedom are assumed to be displacement components u_1, u_2 and u_3 associated to directions of orthogonal Cartesian coordinate axes x_1, x_2 and x_3, respectively. Depending on the number of nodes (n_n), the element displacement vector $\mathbf{u}$ collects displacement components ${}^n u_1, {}^n u_2$ and ${}^n u_3$, associated to node n with ${}^n \mathbf{u}$. Adopting the usual node-wise strategy, $\mathbf{u} = \{ {}^1\mathrm{u}_1 \ {}^1\mathrm{u}_2 \ {}^1\mathrm{u}_3 \ \ldots \ {}^n\mathrm{u}_1 \ {}^n\mathrm{u}_2 \ {}^n\mathrm{u}_3 \}^{\mathrm{T}}$. The related force components are analogically collected in a vector $\mathbf{F}$ as $\{ {}^1F_1 \ {}^1F_2 \ {}^1F_3 \ \ldots \ {}^n F_1 \ {}^n F_2 \ {}^n F_3 \}^{\mathrm{T}}$.

The displacement values $\tilde{\mathbf{u}}(\mathbf{x})$, where $\mathbf{x} \subset \Omega_e \subset \boldsymbol{B}^h$, are calculated by taking the sum of displacements contributions (3.25) obtained by interpolation of element nodal displacement ${}^n\mathbf{u}$ with predefined interpolation functions $N_n(\mathbf{x})$.

$$\tilde{\mathbf{u}}(\mathbf{x}) = \begin{Bmatrix} \tilde{u}_1 \\ \tilde{u}_2 \\ \tilde{u}_3 \end{Bmatrix} \approx \sum_{n=1}^{n_n} N_n(\mathbf{x}) \, {}^n\mathbf{u} = \mathbf{N}(\mathbf{x})\mathbf{u} \quad \text{where} \quad \mathbf{N}(\mathbf{x}) = \left\{ N_1 \ \ N_2 \ \ \ldots \ \ N_{n_n} \right\}^{\mathrm{T}} \tag{3.25}$$

In order to preserve the continuity statement, the previously introduced interpolations N_n (i.e. element shape function associated to element node n) are supposed to meet the abovementioned C^0 requirement. Similarly to Eq. (3.25), the approximation of virtual displacement $\delta\tilde{\mathbf{u}}(\xi)$ is given by

$$\delta\tilde{\mathbf{u}}(\xi) = \begin{Bmatrix} \delta\tilde{u}_1 \\ \delta\tilde{u}_2 \\ \delta\tilde{u}_3 \end{Bmatrix} \approx \sum_{n=1}^{n_n} N_n(\xi)\,{}^n\mathbf{u} = \mathbf{N}(\xi)\mathbf{u} \quad \text{where} \quad \mathbf{N}(\xi) = \left\{ N_1 \quad N_2 \quad \dots \quad N_{n_n} \right\}^{\mathrm{T}}, \tag{3.26}$$

where ξ denotes the vector of parametric coordinates, which will be properly discussed later on. Note that the interpolation of displacement $\tilde{\mathbf{u}}(\mathbf{x})$ and related variational values $\delta\tilde{\mathbf{u}}(\xi)$ are conducted by the same interpolation function N_n with different arguments (*3.2.4.1 Bubnov-Galerkin method*).

3.2.4.3 Partial derivatives

Since the weak form requires first derivative of displacements (3.21), the interpolation functions are derived with respect to $\mathbf{x}$ by the chain rule (Zienkiewicz & Taylor, 2002)

$$\frac{\partial N_n}{\partial \xi_i} = \frac{\partial x_j}{\partial \xi_i} \frac{\partial N_n}{\partial x_j}. \tag{3.27}$$

The former expression can be rewritten in matrix form as

$$\frac{\partial N_n}{\partial \boldsymbol{\xi}} = \mathbf{J} \frac{\partial N_n}{\partial \mathbf{x}}, \tag{3.28}$$

in which

$$\frac{\partial N_n}{\partial \boldsymbol{\xi}} = \begin{Bmatrix} \dfrac{\partial N_n}{\partial \xi_1} \\[2mm] \dfrac{\partial N_n}{\partial \xi_2} \\[2mm] \dfrac{\partial N_n}{\partial \xi_3} \end{Bmatrix} \quad , \quad \mathbf{J} = \begin{bmatrix} \dfrac{\partial x_1}{\partial \xi_1} & \dfrac{\partial x_2}{\partial \xi_1} & \dfrac{\partial x_3}{\partial \xi_1} \\[2mm] \dfrac{\partial x_1}{\partial \xi_2} & \dfrac{\partial x_2}{\partial \xi_2} & \dfrac{\partial x_3}{\partial \xi_2} \\[2mm] \dfrac{\partial x_1}{\partial \xi_3} & \dfrac{\partial x_2}{\partial \xi_3} & \dfrac{\partial x_3}{\partial \xi_3} \end{bmatrix} \quad , \quad \frac{\partial N_n}{\partial \mathbf{x}} = \begin{Bmatrix} \dfrac{\partial N_n}{\partial x_1} \\[2mm] \dfrac{\partial N_n}{\partial x_2} \\[2mm] \dfrac{\partial N_n}{\partial x_3} \end{Bmatrix}, \tag{3.29}$$

with $\mathbf{J}$ denoting the *Jacobian transformation matrix*. Subsequently, the required derivatives are given by

$$\frac{\partial N_n}{\partial \mathbf{x}} = \mathbf{J}^{-1} \frac{\partial N_n}{\partial \boldsymbol{\xi}}, \tag{3.30}$$

where the notation is often simplified as $\partial N_n / \partial x_i = N_{n,x_i}$ and $\partial N_n / \partial \xi_i = N_{n,\xi_i}$.

3.2.4.4 Strain-displacement matrix

According to Eq. (3.5), the strain vector $\underline{\boldsymbol{\varepsilon}}$ (3.4) can be expressed in terms of $\tilde{\mathbf{u}}$ via

$$\underline{\boldsymbol{\varepsilon}} = \boldsymbol{\mathcal{S}}\,\mathbf{u} \approx \sum_{n=1}^{n_n} (\boldsymbol{\mathcal{S}}\,N_n)\,^n\mathbf{u} = \sum_{n=1}^{n_n} \mathbf{B}_n\,^n\mathbf{u} = \mathbf{B}\,\mathbf{u},\tag{3.31}$$

giving rise to the structure of the matrix $\mathbf{B}_n$ as:

$$\mathbf{B}_n = \begin{bmatrix} N_{n,x_1} & 0 & 0 & N_{n,x_2} & 0 & N_{n,x_3} \\ 0 & N_{n,x_2} & 0 & N_{n,x_1} & N_{n,x_3} & 0 \\ 0 & 0 & N_{n,x_3} & 0 & N_{n,x_2} & N_{n,x_1} \end{bmatrix}^{\mathrm{T}},\tag{3.32}$$

which denotes the FE *strain-displacement matrix* associated to node n.

3.2.4.5 FE force equilibrium

By rewriting Eq. (3.15) in form of

$$\int_{\Omega_e} \delta\underline{\boldsymbol{\varepsilon}}^{\mathrm{T}}\underline{\boldsymbol{\sigma}}\,\mathrm{d}\Omega_e - \int_{\Omega_e} \delta\mathbf{u}^{\mathrm{T}}\mathbf{b}\,\mathrm{d}\Omega_e - \int_{\Gamma_{t_e}} \delta\mathbf{u}^{\mathrm{T}}\bar{\mathbf{t}}\,\mathrm{d}\Gamma_{t_e} = 0,\tag{3.33}$$

and by taking into account that $\delta\underline{\boldsymbol{\varepsilon}}^{\mathrm{T}} = \mathbf{B}^{\mathrm{T}}\delta\tilde{\mathbf{u}}$ and $\delta\mathbf{u}^{\mathrm{T}} = \mathbf{N}^{\mathrm{T}}\delta\tilde{\mathbf{u}}$, Eq. (3.54) becomes

$$\delta\tilde{\mathbf{u}}\left[\int_{\Omega_e} \mathbf{B}^{\mathrm{T}}\underline{\boldsymbol{\sigma}}\,\mathrm{d}\Omega_e - \int_{\Omega_e} \mathbf{N}^{\mathrm{T}}\mathbf{b}\,\mathrm{d}\Omega_e - \int_{\Gamma_{t_e}} \mathbf{N}^{\mathrm{T}}\bar{\mathbf{t}}\,\mathrm{d}\Gamma_{t_e}\right] = 0.\tag{3.34}$$

In case of arbitrary small displacement variations $\delta\tilde{\mathbf{u}}$, Eq. (3.38) becomes:

$$\underbrace{\int_{\Omega_e} \mathbf{B}^{\mathrm{T}}\underline{\boldsymbol{\sigma}}\,\mathrm{d}\Omega_e}_{\mathbf{F}^{in}(\boldsymbol{\sigma})} = \underbrace{\int_{\Omega_e} \mathbf{N}^{\mathrm{T}}\mathbf{b}\,\mathrm{d}\Omega_e + \int_{\Gamma_{t_e}} \mathbf{N}^{\mathrm{T}}\bar{\mathbf{t}}\,\mathrm{d}\Gamma_{t_e}}_{\mathbf{F}^{ex}},$$

and denotes the equality of element internal and external nodal forces. Furthermore, the internal force vector $\mathbf{F}^{in}$ can be rewritten by expressing $\boldsymbol{\sigma}$ in terms of element nodal displacement $\mathbf{u}$ as

$$\mathbf{F}^{in}(\boldsymbol{\sigma}) = \int_{\Omega_e} \mathbf{B}^{\mathrm{T}}\underline{\boldsymbol{\sigma}}\,\mathrm{d}\Omega_e = \underbrace{\left[\int_{\Omega_e} \mathbf{B}^{\mathrm{T}}\mathbf{D}\mathbf{B}\,\mathrm{d}\Omega_e\right]}_{\mathbf{K}}\mathbf{u} \qquad \text{since} \quad \underline{\boldsymbol{\sigma}} = \mathbf{D}\underline{\boldsymbol{\varepsilon}} = \mathbf{D}\boldsymbol{\mathcal{S}}\,\mathbf{N}\mathbf{u} = \mathbf{D}\mathbf{B}\mathbf{u},\tag{3.35}$$

denoting the *irreducible displacement method* (Zienkiewicz & Taylor, 2002). The term in the brackets represents the *finite element stiffness matrix* **K**, which directly relates element nodal displacement **u** related to external nodal forces $\mathbf{F}^{ex}$ with $\mathbf{K}\mathbf{u}$. Since the time discretization is not yet involved, Eq. (3.35) represents the *semi-discrete form* of equilibrium. Also, as the essential displacement boundary conditions are not present, the prescribed displacement values $\bar{\mathbf{u}}$ at FE nodes on Γ_u should be artificially imposed (Zienkiewicz, Taylor & Zhu, 2000).

3.2.4.6   *Numerical integration*

It is convenient to numerically integrate the FE arrays by quadrature (Zienkiewicz & Taylor, 2002). Particularly, since the interpolation functions N_n are here assumed to be polynomials, the most accurate procedure is the *Gauss-Legendre quadrature*. For illustration, assume that the range of shape function $N_n(\xi)$ is defined between -1 and 1. In this case, the Gauss-Legendre quadrature integrates a function such as

$$\int_{-1}^{1} f(\xi)\,\mathrm{d}\xi = \sum_{i=1}^{n} f(\xi_i)\,w_i + O\!\left(\frac{\mathrm{d}^{2n} f(\xi)}{\mathrm{d}\xi^{2n}}\right), \tag{3.36}$$

in which ξ_i are function f coordinates and w_i are weight coefficients defined in a variety of literature (Hutton, 2004). It is important to point out that the given *n-point formula* (3.36) integrates exactly a polynomial of order $2n-1$. For a general three-dimensional FE, defined in local coordinates ξ, η and ζ, the integration is determined by (Zienkiewicz & Taylor, 2002):

$$\int_{-1}^{1}\int_{-1}^{1}\int_{-1}^{1} f(\xi,\eta,\zeta)\,\mathrm{d}\xi\,\mathrm{d}\eta\,\mathrm{d}\zeta = \sum_{i=1}^{n}\sum_{j=1}^{n}\sum_{k=1}^{n} f(\xi_i,\eta_j,\zeta_k)\,w_i\,w_j\,w_k . \tag{3.37}$$

The integration gives an exact result if the polynomials order is less than *2n*.

3.2.4.7   *Global assembling*

In an arbitrary spatial discretization, with a number n_{el} of finite elements, the local element DOF will never coincide with the order of DOF present in the FE mesh. The discrete form of equilibrium is obtained by the standard finite element assembling operator **A** (Chawla & Laursen, 1998), which link local element DOF into global notation (3.38).

$$\left[\overset{n_{el}}{\underset{e=1}{\mathbf{A}}} \int_{\Omega_e} \mathbf{B}^{\mathrm{T}}\mathbf{D}\mathbf{B}\,\mathrm{d}\Omega_e\right]\left\{\overset{n_{el}}{\underset{e=1}{\mathbf{A}}}\mathbf{u}\right\} = \left\{\overset{n_{el}}{\underset{e=1}{\mathbf{A}}} \int_{\Omega_e} \mathbf{N}^{\mathrm{T}}\mathbf{b}\,\mathrm{d}\Omega_e + \overset{n_{el}}{\underset{e=1}{\mathbf{A}}} \int_{\Gamma_{t_e}} \mathbf{N}^{\mathrm{T}}\bar{\mathbf{t}}\,\mathrm{d}\Gamma_{t_e}\right\} \tag{3.38}$$

3.3   Linear tetrahedral element

The linear tetrahedral element falls in the group of solid elements used for three-dimensional spatial discretization. The element geometry is fully described by four nodes situated on different coordinates in the rectangular Cartesian coordinate system. Six-edge and four faces are obtained by joining nodal coordinates with lines. A typical tetrahedral element is illustrated in Fig. 3.2.
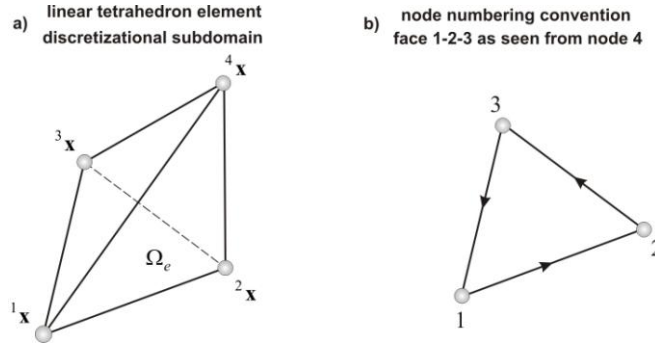
Figure 3.2 Tetrahedral element: **a)** element shape and **b)** node numbering convection

By introducing *n* for the geometrical and mechanical data association, the corresponding element nodal coordinates are traditionally stored in a vector $^n\mathbf{x}$ as

$$^n\mathbf{x} = \begin{Bmatrix} ^n x_1 \\ ^n x_2 \\ ^n x_3 \end{Bmatrix} \quad \text{where} \quad n = 1,2,3,4. \tag{3.39}$$

The volume occupied by the element domain Ω_e, in the spatial and material configuration, is defined by

$$\overset{\text{volume in the spatial configuration}}{v_e = \frac{1}{6}\det\begin{bmatrix} 1 & 1 & 1 & 1 \\ ^1x_1 & ^2x_1 & ^3x_1 & ^4x_1 \\ ^1x_2 & ^2x_2 & ^3x_2 & ^4x_2 \\ ^1x_3 & ^2x_3 & ^3x_3 & ^4x_3 \end{bmatrix}} \quad \text{and} \quad \overset{\text{volume in the material configuration}}{V_e = \frac{1}{6}\det\begin{bmatrix} 1 & 1 & 1 & 1 \\ ^1X_1 & ^2X_1 & ^3X_1 & ^4X_1 \\ ^1X_2 & ^2X_2 & ^3X_2 & ^4X_2 \\ ^1X_3 & ^2X_3 & ^3X_3 & ^4X_3 \end{bmatrix}}. \tag{3.40}$$

It is important to note that the node numbering strategy directly influences the interpretation of element geometrical properties. Namely, in order to avoid possible computations with negative element volume, the node numbering condition must be strictly respected for all elements in the discretization. Following the standard procedure, the node numbering convention can be summarized in two steps. First, an element face that will contain the first three nodes is selected. On that face any corner can be chosen to represent the first element node. The excluded element corner will be the last numbered node. Second, the nodes on the selected element face should be numbered counterclockwise respecting the viewing direction defined from the excluded element corner to the picked element face.

3.3.1 Geometrical description

In order to introduce simplicity in the geometrical description of tetrahedral elements, the local *barycentric coordinates* are introduced (also known as *natural coordinates*). For this purpose, imagine a point $P(x,y,z) \subset \Omega_e$ defined by Cartesian coordinates in a rectangular coordinate system. Since the element shape varies linearly (Fig. 3.2), the coordinates $\tilde{x}_1$, $\tilde{x}_2$ and $\tilde{x}_3$ of point P can be calculated by the element nodal coordinates $^n\mathbf{x}$ through the first order polynomial (3.41).

$$
\begin{aligned}
\tilde{x}_1 &= \xi_1 \, ^1x_1 + \xi_2 \, ^2x_1 + \xi_3 \, ^3x_1 + \xi_4 \, ^4x_1 \\
\tilde{x}_2 &= \xi_1 \, ^1x_2 + \xi_2 \, ^2x_2 + \xi_3 \, ^3x_2 + \xi_4 \, ^4x_2 \\
\tilde{x}_3 &= \xi_1 \, ^1x_3 + \xi_2 \, ^2x_3 + \xi_3 \, ^3x_3 + \xi_4 \, ^4x_3
\end{aligned}
\tag{3.41}
$$

The coefficients ξ_1, ξ_2, ξ_3 and ξ_4, also previously introduced in Eq. (3.36), are the barycentric coordinates of point P. Congruently, like the nodal position vectors $^n\mathbf{x}=\{ \; ^nx_1 \;\; ^nx_2 \;\; ^nx_3 \; \}^{\mathrm{T}}$, any position $\mathbf{x}$ inside the element domain Ω_e can be completely defined by vector $\boldsymbol{\xi}=\{ \; \xi_1 \;\; \xi_2 \;\; \xi_3 \;\; \xi_4 \; \}^{\mathrm{T}}$. The coordinates will vary linearly through the element domain Ω_e between 0 and 1. Mention that for any point inside or in element domain the sum of barycentric coordinates is always one (3.42).

$$
\xi_1 + \xi_2 + \xi_3 + \xi_4 = 1 \quad \text{and} \quad 0 \le \xi_n \le 1 \quad \text{where} \quad n = 1,2,3,4
\tag{3.42}
$$

Note that this property introduces the correlation independency between three arbitrary barycentric coordinates. The relationship between the barycentric and rectangular coordinates can be simply obtained by rewriting the geometrical interpolation from Eq. (3.41) in matrix form and by adding the coordinates sum constrain (3.42) to the formed system of Eq. (3.43).

$$
\begin{Bmatrix} 1 \\ x_1 \\ x_2 \\ x_3 \end{Bmatrix} =
\begin{bmatrix}
1 & 1 & 1 & 1 \\
^1x_1 & ^2x_1 & ^3x_1 & ^4x_1 \\
^1x_2 & ^2x_2 & ^3x_2 & ^4x_2 \\
^1x_3 & ^2x_3 & ^3x_3 & ^4x_3
\end{bmatrix}
\begin{Bmatrix} \xi_1 \\ \xi_2 \\ \xi_3 \\ \xi_4 \end{Bmatrix}
\tag{3.43}
$$

On the other hand, the barycentric coordinates $\boldsymbol{\xi}=\{ \; \xi_1 \;\; \xi_2 \;\; \xi_3 \;\; \xi_4 \; \}^{\mathrm{T}}$ can be also calculated from the given rectangular coordinates by inverting the matrix of the former expression (Zienkiewicz & Taylor, 2002), which will result in

$$
\xi_n(x_1,x_2,x_3) = \frac{1}{6v_e}(\alpha_n + x_1\,\beta_n + x_2\,\gamma_n + x_3\,\delta_n) \quad \text{where} \quad n = 1,2,3,4.
\tag{3.44}
$$

The coefficients α_n, β_n, γ_n, and δ_n are calculated in the same manner as the determinants given in Eq. (3.45) which is written for the first local coordinates ξ_1. The other three coefficients are obtained analogically by cyclic permutations of indexes n.

$$
\alpha_1 = \begin{vmatrix} {}^2x_1 & {}^2x_2 & {}^2x_3 \\ {}^3x_1 & {}^3x_2 & {}^3x_3 \\ {}^4x_1 & {}^4x_2 & {}^4x_3 \end{vmatrix} \ ; \ \beta_1 = -\begin{vmatrix} 1 & {}^2x_2 & {}^2x_3 \\ 1 & {}^3x_2 & {}^3x_3 \\ 1 & {}^4x_2 & {}^4x_3 \end{vmatrix} \ ; \ \gamma_1 = -\begin{vmatrix} {}^2x_1 & 1 & {}^2x_3 \\ {}^3x_1 & 1 & {}^3x_3 \\ {}^4x_1 & 1 & {}^4x_3 \end{vmatrix} \ ; \ \delta_1 = -\begin{vmatrix} {}^2x_1 & {}^2x_2 & 1 \\ {}^3x_1 & {}^3x_2 & 1 \\ {}^4x_1 & {}^4x_2 & 1 \end{vmatrix} \quad (3.45)
$$

The geometrical interpretations of barycentric coordinates can be illustrated by splitting the one element into four smaller tetrahedral regions. The generated regions are defined by three element nodes and point P. A typical element division is illustrated in Fig. 3.3.
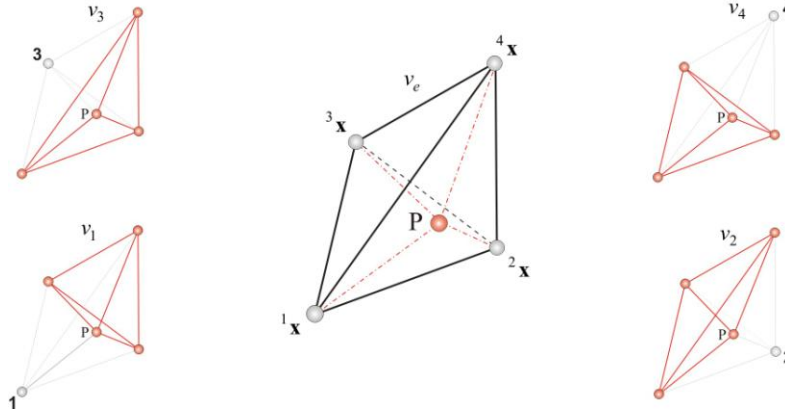
Figure 3.3 Geometrical interpretation of tetrahedral element barycentric coordinates

As can be seen, each of the formed volume v_n describes a part of the tetrahedral volume defined by point P and three nodes that lie opposite to node n. With the volume measure $(\alpha_n + x_1\beta_n + x_2\gamma_n + x_3\delta_n)/6$ for v_n (3.44), it can be concluded that the barycentric coordinates represent the two volumes ratio (3.46) which directly explains the previously introduced sum limit (3.42).

$$
\xi_n = \frac{v_n}{v_e} \quad \text{where} \quad n = 1,2,3,4 \quad (3.46)
$$

For the purpose of proving the benefits of element barycentric coordinates application, the element displacement properties are hereafter introduced.

3.3.2 Isoparametric property

The three-dimensional nodal degrees of freedom are three independent orthogonal displacement components, gathered in form of a vector ${}^n\mathbf{u}$ (for n node) as

$$
{}^n\mathbf{u} = \begin{Bmatrix} {}^nu_1 \\ {}^nu_2 \\ {}^nu_3 \end{Bmatrix} \quad \text{where} \quad n = 1,2,3,4. \quad (3.47)
$$

Having four nodes, the tetrahedral element disposes of twelve independent displacement components. By arranging all nodal displacements in vector $\mathbf{u}$, the element nodal displacements can be represented in compact form by the following vector (3.48).

$$\mathbf{u} = \left\{ {}^{1}\mathbf{u} \quad {}^{2}\mathbf{u} \quad {}^{3}\mathbf{u} \quad {}^{4}\mathbf{u} \right\}^{\mathrm{T}} \tag{3.48}$$

To obtain the element displacement vector $\mathbf{u}$, assume a tetrahedral element immersed in a continuous displacement field $\hat{\mathbf{u}}(x_1, x_2, x_3)$. The displacement $\hat{\mathbf{u}}$ is distributed over the element by three first order polynomials given as (Zienkiewicz & Taylor, 2002):

$$\begin{aligned}
\hat{u}_1 &= a_1 + a_2 x_1 + a_3 x_2 + a_4 x_3, \\
\hat{u}_2 &= a_5 + a_6 x_1 + a_7 x_2 + a_8 x_3, \\
\hat{u}_3 &= a_9 + a_{10} x_1 + a_{11} x_2 + a_{12} x_3.
\end{aligned} \tag{3.49}$$

The coefficients a_1, a_2,…, a_{12} are unknown in advance and should be determined so that displacement components $\mathbf{u}$ (3.48) satisfy the displacement field $\hat{\mathbf{u}}$. In order to separate the unknown coefficient, the former expressions (3.49) are rewritten in matrix form by collecting all coefficients a_c (where $c=1..12$) in vector $\mathbf{a}$, and coordinates x_1, x_2 and x_3 in matrix $\boldsymbol{\alpha}$ (3.50).

$$\hat{\mathbf{u}} = \begin{Bmatrix} \hat{u}_1 \\ \hat{u}_2 \\ \hat{u}_3 \end{Bmatrix} = \begin{bmatrix} 1 & x_1 & x_2 & x_3 & 0 & 0 & 0 & 0 & 0 & 0 & 0 & 0 \\ 0 & 0 & 0 & 0 & 1 & x_1 & x_2 & x_3 & 0 & 0 & 0 & 0 \\ 0 & 0 & 0 & 0 & 0 & 0 & 0 & 0 & 1 & x_1 & x_2 & x_3 \end{bmatrix} \begin{Bmatrix} a_1 \\ a_2 \\ a_3 \\ \vdots \\ a_{12} \end{Bmatrix} = \boldsymbol{\alpha}\,\mathbf{a} \tag{3.50}$$

By expanding this concept over all nodes, the unknown nodal displacement $\mathbf{u}$ can be related to element nodal coordinates ${}^{n}\mathbf{x}$ through coefficients a_c. In this case, the matrix that collects the nodal coordinates ${}^{n}\mathbf{x}$ is denoted by $\mathbf{C}$ and has the following structure (3.51).

$$\mathbf{u} = \begin{Bmatrix} {}^{1}u_1 \\ {}^{1}u_2 \\ {}^{1}u_3 \\ {}^{2}u_1 \\ {}^{2}u_2 \\ {}^{2}u_3 \\ {}^{3}u_1 \\ {}^{3}u_2 \\ {}^{3}u_3 \\ {}^{4}u_1 \\ {}^{4}u_2 \\ {}^{4}u_3 \end{Bmatrix} = \begin{bmatrix} 1 & {}^{1}x_1 & {}^{1}x_2 & {}^{1}x_3 & 0 & 0 & 0 & 0 & 0 & 0 & 0 & 0 \\ 0 & 0 & 0 & 0 & 1 & {}^{1}x_1 & {}^{1}x_2 & {}^{1}x_3 & 0 & 0 & 0 & 0 \\ 0 & 0 & 0 & 0 & 0 & 0 & 0 & 0 & 1 & {}^{1}x_1 & {}^{1}x_2 & {}^{1}x_3 \\ 1 & {}^{2}x_1 & {}^{2}x_2 & {}^{2}x_3 & 0 & 0 & 0 & 0 & 0 & 0 & 0 & 0 \\ 0 & 0 & 0 & 0 & 1 & {}^{2}x_1 & {}^{2}x_2 & {}^{2}x_3 & 0 & 0 & 0 & 0 \\ 0 & 0 & 0 & 0 & 0 & 0 & 0 & 0 & 1 & {}^{2}x_1 & {}^{2}x_2 & {}^{2}x_3 \\ 1 & {}^{3}x_1 & {}^{3}x_2 & {}^{3}x_3 & 0 & 0 & 0 & 0 & 0 & 0 & 0 & 0 \\ 0 & 0 & 0 & 0 & 1 & {}^{3}x_1 & {}^{3}x_2 & {}^{3}x_3 & 0 & 0 & 0 & 0 \\ 0 & 0 & 0 & 0 & 0 & 0 & 0 & 0 & 1 & {}^{3}x_1 & {}^{3}x_2 & {}^{3}x_3 \\ 1 & {}^{4}x_1 & {}^{4}x_2 & {}^{4}x_3 & 0 & 0 & 0 & 0 & 0 & 0 & 0 & 0 \\ 0 & 0 & 0 & 0 & 1 & {}^{4}x_1 & {}^{4}x_2 & {}^{4}x_3 & 0 & 0 & 0 & 0 \\ 0 & 0 & 0 & 0 & 0 & 0 & 0 & 0 & 1 & {}^{4}x_1 & {}^{4}x_2 & {}^{4}x_3 \end{bmatrix} \begin{Bmatrix} a_1 \\ a_2 \\ a_3 \\ a_4 \\ a_5 \\ a_6 \\ a_7 \\ a_8 \\ a_9 \\ a_{10} \\ a_{11} \\ a_{12} \end{Bmatrix} = \mathbf{C}\mathbf{a} \tag{3.51}$$

The unknown coefficients a_c are determined by solving the system of Eq. (3.51) as

$$\mathbf{a} = \mathbf{C}^{-1}\mathbf{u}, \tag{3.52}$$

in which the structure of $\mathbf{C}^{-1}$ is defined as:

$$\mathbf{C}^{-1} = \frac{1}{6v_e}
\begin{bmatrix}
\alpha_1 & 0 & 0 & \alpha_2 & 0 & 0 & \alpha_3 & 0 & 0 & \alpha_4 & 0 & 0 \\
\beta_1 & 0 & 0 & \beta_2 & 0 & 0 & \beta_3 & 0 & 0 & \beta_4 & 0 & 0 \\
\gamma_1 & 0 & 0 & \gamma_2 & 0 & 0 & \gamma_3 & 0 & 0 & \gamma_4 & 0 & 0 \\
\delta_1 & 0 & 0 & \delta_2 & 0 & 0 & \delta_3 & 0 & 0 & \delta_4 & 0 & 0 \\
0 & \alpha_1 & 0 & 0 & \alpha_2 & 0 & 0 & \alpha_3 & 0 & 0 & \alpha_4 & 0 \\
0 & \beta_1 & 0 & 0 & \beta_2 & 0 & 0 & \beta_3 & 0 & 0 & \beta_4 & 0 \\
0 & \gamma_1 & 0 & 0 & \gamma_2 & 0 & 0 & \gamma_3 & 0 & 0 & \gamma_4 & 0 \\
0 & \delta_1 & 0 & 0 & \delta_2 & 0 & 0 & \delta_3 & 0 & 0 & \delta_4 & 0 \\
0 & 0 & \alpha_1 & 0 & 0 & \alpha_2 & 0 & 0 & \alpha_3 & 0 & 0 & \alpha_4 \\
0 & 0 & \beta_1 & 0 & 0 & \beta_2 & 0 & 0 & \beta_3 & 0 & 0 & \beta_4 \\
0 & 0 & \gamma_1 & 0 & 0 & \gamma_2 & 0 & 0 & \gamma_3 & 0 & 0 & \gamma_4 \\
0 & 0 & \delta_1 & 0 & 0 & \delta_2 & 0 & 0 & \delta_3 & 0 & 0 & \delta_4
\end{bmatrix}. \tag{3.53}$$

The coefficients α_n, β_n, γ_n and δ_n are function of nodal coordinates and are calculated from Eq. (3.54), (3.55), (3.56) and (3.57), respectively.

$$\begin{aligned}
\alpha_1 &= {}^2x_1\,{}^3x_2\,{}^4x_3 + {}^4x_1\,{}^3x_2\,{}^4x_3 + {}^4x_2\,{}^3x_1\,{}^3x_3 - {}^2x_1\,{}^4x_2\,{}^3x_3 - {}^3x_1\,{}^2x_2\,{}^4x_3 - {}^3x_2\,{}^4x_1\,{}^2x_3 \\
\alpha_2 &= {}^1x_1\,{}^4x_2\,{}^1x_3 + {}^4x_1\,{}^3x_3\,{}^1x_2 + {}^1x_1\,{}^3x_2\,{}^4x_3 - {}^3x_1\,{}^4x_3\,{}^1x_2 - {}^4x_1\,{}^3x_2\,{}^1x_3 - {}^1x_1\,{}^3x_3\,{}^4x_2 \\
\alpha_3 &= {}^1x_1\,{}^1x_2\,{}^2x_3 + {}^2x_1\,{}^4x_2\,{}^1x_3 + {}^1x_1\,{}^4x_3\,{}^2x_2 - {}^4x_1\,{}^1x_3\,{}^2x_2 - {}^1x_1\,{}^4x_2\,{}^2x_3 - {}^2x_1\,{}^4x_3\,{}^1x_2 \\
\alpha_4 &= {}^1x_1\,{}^2x_2\,{}^3x_3 + {}^3x_1\,{}^1x_2\,{}^2x_3 + {}^2x_1\,{}^1x_3\,{}^3x_2 - {}^1x_1\,{}^2x_3\,{}^3x_2 - {}^3x_1\,{}^1x_3\,{}^2x_2 - {}^2x_1\,{}^1x_2\,{}^3x_3
\end{aligned} \tag{3.54}$$

$$\begin{aligned}
\beta_1 &= {}^3x_2\,{}^2x_3 + {}^2x_2\,{}^4x_3 + {}^3x_3\,{}^4x_2 - {}^3x_2\,{}^4x_3 - {}^2x_3\,{}^4x_2 - {}^2x_2\,{}^3x_3 \\
\beta_2 &= {}^4x_3\,{}^1x_2 + {}^3x_2\,{}^1x_3 + {}^3x_3\,{}^4x_2 - {}^4x_2\,{}^1x_3 - {}^3x_3\,{}^1x_2 - {}^3x_2\,{}^4x_3 \\
\beta_3 &= {}^1x_3\,{}^2x_2 + {}^4x_2\,{}^2x_3 + {}^4x_3\,{}^1x_2 - {}^1x_2\,{}^2x_3 - {}^4x_3\,{}^2x_2 - {}^4x_2\,{}^1x_3 \\
\beta_4 &= {}^2x_3\,{}^3x_2 + {}^1x_2\,{}^3x_3 + {}^1x_3\,{}^2x_2 - {}^2x_2\,{}^3x_3 - {}^1x_3\,{}^3x_2 - {}^1x_3\,{}^2x_2
\end{aligned} \tag{3.55}$$

$$\begin{aligned}
\gamma_1 &= {}^2x_1\,{}^3x_3 + {}^3x_1\,{}^4x_3 + {}^4x_1\,{}^2x_3 - {}^2x_1\,{}^4x_3 - {}^3x_1\,{}^2x_3 - {}^4x_1\,{}^3x_3 \\
\gamma_2 &= {}^3x_1\,{}^4x_3 + {}^4x_1\,{}^1x_3 + {}^1x_1\,{}^3x_3 - {}^3x_1\,{}^1x_3 - {}^4x_1\,{}^3x_3 - {}^1x_1\,{}^4x_3 \\
\gamma_3 &= {}^4x_1\,{}^1x_3 + {}^1x_1\,{}^2x_3 + {}^2x_1\,{}^4x_3 - {}^4x_1\,{}^2x_3 - {}^1x_1\,{}^4x_3 - {}^2x_1\,{}^1x_3 \\
\gamma_4 &= {}^1x_1\,{}^2x_3 + {}^2x_1\,{}^3x_3 + {}^3x_1\,{}^1x_3 - {}^1x_1\,{}^3x_3 - {}^2x_1\,{}^1x_3 - {}^3x_1\,{}^2x_3
\end{aligned} \tag{3.56}$$

$$\begin{aligned}
\delta_1 &= {}^2x_1\,{}^4x_2 + {}^3x_1\,{}^2x_2 + {}^4x_1\,{}^3x_2 - {}^2x_1\,{}^3x_2 - {}^3x_1\,{}^4x_2 - {}^4x_1\,{}^2x_2 \\
\delta_2 &= {}^3x_1\,{}^1x_2 + {}^4x_1\,{}^3x_2 + {}^1x_1\,{}^4x_2 - {}^3x_1\,{}^4x_2 - {}^4x_1\,{}^1x_2 - {}^1x_1\,{}^4x_2 \\
\delta_3 &= {}^4x_1\,{}^2x_2 + {}^1x_1\,{}^2x_2 + {}^2x_1\,{}^1x_2 - {}^4x_1\,{}^1x_2 - {}^1x_1\,{}^2x_2 - {}^2x_1\,{}^4x_2 \\
\delta_4 &= {}^1x_1\,{}^3x_2 + {}^2x_1\,{}^1x_2 + {}^3x_1\,{}^2x_2 - {}^1x_1\,{}^2x_2 - {}^2x_1\,{}^3x_2 - {}^3x_1\,{}^1x_2
\end{aligned} \tag{3.57}$$

The displacement vector $\mathbf{u}$ can be now related to the displacement field $\hat{\mathbf{u}}$ (x_1, x_2, x_3) by simply rewriting vector $\mathbf{a}$ in terms of nodal displacements (3.58).

$$\hat{\mathbf{u}} = \boldsymbol{\alpha}\,\mathbf{a} = \boldsymbol{\alpha}\,\mathbf{C}^{-1}\,\mathbf{u} \tag{3.58}$$

The matrix product $\boldsymbol{\alpha}\mathbf{C}^{-1}$ (usually denoted by $\mathbf{N}$) maps the field $\hat{\mathbf{u}}$ (x_1, x_2, x_3) onto nodal displacement components ($\hat{\mathbf{u}} = \mathbf{N}\mathbf{u}$) and represent the *interpolation function matrix* of the tetrahedral element. The matrix collects element interpolation functions N_n, uniquely associated with the corresponding node n and possesses the structure

$$\mathbf{N} = \boldsymbol{\alpha}\,\mathbf{C}^{-1} = \begin{bmatrix} N_1 & 0 & 0 & N_2 & 0 & 0 & N_3 & 0 & 0 & N_4 & 0 & 0 \\ 0 & N_1 & 0 & 0 & N_2 & 0 & 0 & N_3 & 0 & 0 & N_4 & 0 \\ 0 & 0 & N_1 & 0 & 0 & N_2 & 0 & 0 & N_3 & 0 & 0 & N_4 \end{bmatrix}, \tag{3.59}$$

in which the functions N_n are given by (Zienkiewicz & Taylor, 2002)

$$N_n(x_1, x_2, x_3) = \frac{1}{6v_e}(\alpha_n + x_1\,\beta_n + x_2\,\gamma_n + x_3\,\delta_n) \quad \text{where} \quad n = 1,2,3,4. \tag{3.60}$$

Eq. (3.6) clearly explains why the tetrahedral element is preceded by the prefix "linear". Obviously, the reason lies in the fact that the displacement field is interpolated over the element domain by linear functions. The function value in the corresponding node n is one, while in the remaining three nodes is zero.

By comparing Eq. (3.44) with Eq. (3.60) it can be deduced that the element functions ξ_n are equal to functions N_n. For sake of illustration of the property in question, assume an element immersed in Cartesian coordinates system where the displacement field $u(x_1, x_2, x_3)$ is given in terms of spatial coordinates. In each node n the function $u(x_1, x_2, x_3)$ has its specific value that can be split in three orthogonal components, collected in vector $^n\mathbf{u}$ (3.77). For a point P defined by position vector $\boldsymbol{\xi} = \{ \xi_1 \ \xi_2 \ \xi_3 \ \xi_4 \}^{\mathrm{T}}$, the components of $\tilde{\mathbf{u}} = \{ \tilde{u}_1 \ \tilde{u}_2 \ \tilde{u}_3 \}^{\mathrm{T}}$ are approximated by summing nodal contributions of displacement values $^n\mathbf{u}$, obtained by interpolation from node n to the position $\boldsymbol{\xi}$ (3.61).

$$\begin{Bmatrix} \tilde{u}_1 \\ \tilde{u}_2 \\ \tilde{u}_3 \end{Bmatrix} = \begin{bmatrix} {}^1u_1 & {}^2u_1 & {}^3u_1 & {}^4u_1 \\ {}^1u_2 & {}^2u_2 & {}^3u_2 & {}^4u_2 \\ {}^1u_3 & {}^2u_3 & {}^3u_3 & {}^4u_3 \end{bmatrix} \begin{Bmatrix} \xi_1 \\ \xi_2 \\ \xi_3 \\ \xi_4 \end{Bmatrix} \quad \rightarrow \quad \tilde{\mathbf{u}} = \sum_{n=1}^{4} \xi_n\,{}^n\mathbf{u} \quad \text{or} \quad \tilde{\mathbf{u}} = \sum_{n=1}^{4} N_n\,{}^n\mathbf{u} \tag{3.61}$$

On the other hand, by analyzing the geometrical aspect of the element functions ξ_n, for a same point P defined by $\boldsymbol{\xi}$, the related coordinates $\tilde{\mathbf{x}} = \{ \tilde{x}_1 \ \tilde{x}_2 \ \tilde{x}_3 \}^{\mathrm{T}}$ can be obtained as in Eq. (3.61) by summing the contribution of coordinate interpolation from element nodes to the position $\boldsymbol{\xi}$ (3.62).

$$
\begin{Bmatrix} \tilde{x}_1 \\ \tilde{x}_2 \\ \tilde{x}_3 \end{Bmatrix} = \begin{bmatrix} {}^1x_1 & {}^2x_1 & {}^3x_1 & {}^4x_1 \\ {}^1x_2 & {}^2x_2 & {}^3x_2 & {}^4x_2 \\ {}^1x_3 & {}^2x_3 & {}^3x_3 & {}^4x_3 \end{bmatrix} \begin{Bmatrix} \xi_1 \\ \xi_2 \\ \xi_3 \\ \xi_4 \end{Bmatrix} \quad \rightarrow \quad \tilde{\mathbf{x}} = \sum_{n=1}^{4} \xi_n \, {}^n\mathbf{x} \quad \text{or} \quad \tilde{\mathbf{x}} = \sum_{n=1}^{4} N_n \, {}^n\mathbf{x} \tag{3.62}
$$

An important property arises from the comparison of Eq. (3.61) and Eq. (3.62). As it can be perceived, both geometrical (coordinates) and mechanical data (displacements) can be interpolated through the element domain Ω_e by means of the same interpolation functions. In the finite element terminology, this concept is known as the *isoparametric element property*. By joining matrix Eq. (3.61) and Eq. (3.62), and upon adding the constraint in Eq. (3.42), the isoparametric property can be restated as

$$
\begin{Bmatrix} 1 \\ \tilde{x}_1 \\ \tilde{x}_2 \\ \tilde{x}_3 \\ \tilde{u}_1 \\ \tilde{u}_2 \\ \tilde{u}_3 \end{Bmatrix} = \begin{bmatrix} 1 & 1 & 1 & 1 \\ {}^1x_1 & {}^2x_1 & {}^3x_1 & {}^4x_1 \\ {}^1x_2 & {}^2x_2 & {}^3x_2 & {}^4x_2 \\ {}^1x_3 & {}^2x_3 & {}^3x_3 & {}^4x_3 \\ {}^1u_1 & {}^2u_1 & {}^3u_1 & {}^4u_1 \\ {}^1u_2 & {}^2u_2 & {}^3u_2 & {}^4u_2 \\ {}^1u_3 & {}^2u_3 & {}^3u_3 & {}^4u_3 \end{bmatrix} \begin{Bmatrix} \xi_1 \\ \xi_2 \\ \xi_3 \\ \xi_4 \end{Bmatrix} = \begin{bmatrix} 1 & 1 & 1 & 1 \\ {}^1x_1 & {}^2x_1 & {}^3x_1 & {}^4x_1 \\ {}^1x_2 & {}^2x_2 & {}^3x_2 & {}^4x_2 \\ {}^1x_3 & {}^2x_3 & {}^3x_3 & {}^4x_3 \\ {}^1u_1 & {}^2u_1 & {}^3u_1 & {}^4u_1 \\ {}^1u_2 & {}^2u_2 & {}^3u_2 & {}^4u_2 \\ {}^1u_3 & {}^2u_3 & {}^3u_3 & {}^4u_3 \end{bmatrix} \begin{Bmatrix} N_1 \\ N_2 \\ N_3 \\ N_4 \end{Bmatrix}. \tag{3.63}
$$

At this point, it is important to mention that the property makes the linear tetrahedral element very attractive for numerical contact/impact simulation. Namely, modeling of mechanical interaction (like those in the thesis) requires coherence between interpolations of geometrical and mechanical data.

3.3.3 Linearization

High-energy impact loadings may occasionally cause the penetration (or even perforation) of one body into another (Fig. 1.3 & Fig. 3.4). It is clear that such scenario is accompanied by large displacements, concentrated in front of the bodies contact/impact zone. In this case, the relationship between strain and displacements is non-linear and the *incremental-iterative solution strategy* is inevitable.
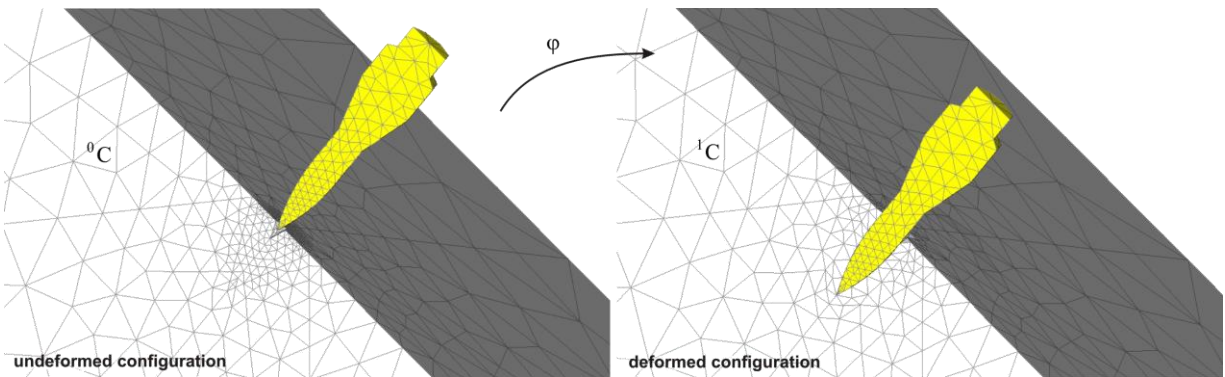
Figure 3.4 Large displacements in front of the body contact/impact zone (non-linear strain-displacement relationship)

The incremental-iterative solution strategy is based on the decomposition of deformation history in a discrete number of spatial configurations. For each spatial configuration, the balance between external and internal forces is enforced in an iterative fashion.

Note that when the equilibrium equations are defined in the deformed configuration (spatial configuration), the position of loads can change under the influence of deformation and give rise to magnification effect, which is known as *P–Δ effect* (Wilson, 1995). In order to incorporate such effect, the linearization of the discrete form of equilibrium Eq. should be introduced.

The equilibrium in the spatial configuration is reached when

$$\mathbf{r} = \mathbf{F}^{in}(\ S\left[\ E\ (\mathbf{u})\ \right]) - \mathbf{F}^{ex} = \mathbf{0}, \tag{3.64}$$

where $\mathbf{r}$ denotes the *out-of-balance force vector* (Crisfield, 1991). Since the mathematical background of linearization lies in the Taylor series expansion, the linearization of the given non-linear function produces

$$\mathbf{r}\big|_{\overline{\mathbf{u}}} + \Delta\mathbf{r} = \mathbf{0}, \tag{3.65}$$

where

$$\Delta\mathbf{r} = \Delta\mathbf{F}^{in}(S) - \underbrace{\Delta\mathbf{F}^{ex}}_{0} = \frac{\partial\mathbf{F}^{in}(S)}{\partial\mathbf{u}} \cdot \Delta\mathbf{u} = \operatorname{grad}\mathbf{F}^{in}(S)\big|_{\overline{\mathbf{u}}} \cdot \Delta\mathbf{u} \ .$$
$$\downarrow$$
$$\text{since it is assumed that}$$
$$\mathbf{F}^{ex} = constant$$
$$\tag{3.66}$$

By substituting $\Delta\mathbf{r}$ into Eq. (3.65), it can be obtain that (Laursen, Attaway & Zadoks, 1999)

$$\operatorname{grad}\mathbf{F}^{in}(S)\big|_{\overline{\mathbf{u}}} \cdot \Delta\mathbf{u} = -\mathbf{r}\big|_{\overline{\mathbf{u}}}, \tag{3.67}$$

which defines the solution procedure by the *Newton-Raphson's technique* (3.68).

$$\mathbf{K}_{\mathrm{T}}(\ ^{k}\overline{\mathbf{u}})\Delta\mathbf{u} = -\ ^{k}\mathbf{r}\big|_{\overline{\mathbf{u}}} \tag{3.68a}$$

$$^{k,k+1}\overline{\mathbf{u}} = \ ^{k}\overline{\mathbf{u}} + \Delta\mathbf{u} \tag{3.68b}$$

For the system of Eq. (3.68), the displacement vector $^{k}\overline{\mathbf{u}}$ in the *k*-th iteration step is the result if the Euclidian norm $\|\ ^{k}\mathbf{r}\|$ is smaller than a pre-defined tolerance value (Crisfield, 1991). The iterative displacement values $\Delta\mathbf{u}$ are calculated through the *tangent stiffness matrix* $\mathbf{K}_{\mathrm{T}}(\ ^{k}\overline{\mathbf{u}})$, defined as the gradient of internal forces in the *k*-th iteration step (3.68a). Being the internal nodal force necessary for obtaining the structure of the tangent stiffness matrix $\mathbf{K}_{\mathrm{T}}$, it will be dealt with in the next subtitle.

3.3.3.1 Internal force vector

Since the current configuration is unknown *a priori*, the element internal force vector is rewritten in terms of 1st *Piola-Kirchhoff stress tensor* (2.93). Resume, PK1 relates forces in the current configuration to areas in the reference configuration. In this case, the stress integration is carried out over the element volume V_e in the known reference configuration (3.69).

$$\mathbf{F}^{in} = \int_{\Omega_e} \mathbf{P} \, \nabla N_n(\mathbf{X}) \, dV_e \qquad \text{where} \quad \nabla = \begin{Bmatrix} \partial/\partial X_1 \\ \partial/\partial X_2 \\ \partial/\partial X_3 \end{Bmatrix} \tag{3.69}$$

Since $\mathbf{P}=\mathbf{F}S$ (Brodersen, 2004), the former expression can be rewritten as

$$\mathbf{F}^{in} \int_{\Omega_e} \mathbf{F} \, S \, \nabla N_n(\mathbf{X}) \, dV_e . \tag{3.70}$$

Before carrying out the Taylor series expansion (linearization), note that in Eq. (3.70) S is given in a tensor format. Therefore, it is not suitable for the FE implementation where the vectorial Voight notation is required (Belytschko, Liu & Moran, 2001). For illustrating the stress format transformation, assume the *Saint Venant-Kirchhoff material model* (2.123) given by

$$\begin{Bmatrix} S_{11} \\ S_{22} \\ S_{33} \\ S_{12} \\ S_{23} \\ S_{31} \end{Bmatrix} = \begin{bmatrix} \lambda+2\mu & \lambda & \lambda & 0 & 0 & 0 \\ \cdot & \lambda+2\mu & \lambda & 0 & 0 & 0 \\ \cdot & \cdot & \lambda+2\mu & 0 & 0 & 0 \\ \cdot & \cdot & \cdot & \mu & 0 & 0 \\ \cdot & \cdot & \cdot & \cdot & \mu & 0 \\ sym & \cdot & \cdot & \cdot & \cdot & \mu \end{bmatrix} \begin{Bmatrix} E_{11} \\ E_{22} \\ E_{33} \\ 2E_{12} \\ 2E_{23} \\ 2E_{31} \end{Bmatrix} , \tag{3.71}$$

where the components of S are grouped in vector $\underline{S}$. The adaptation from S to $\underline{S}$ is performed via

$$\mathbf{F}^{in} = \int_{\Omega_e} \mathbf{F} \begin{bmatrix} S_{11} & S_{12} & S_{13} \\ S_{21} & S_{22} & S_{23} \\ S_{31} & S_{32} & S_{33} \end{bmatrix} \begin{Bmatrix} N_{n,X_1} \\ N_{n,X_2} \\ N_{n,X_3} \end{Bmatrix} dV_e = \int_{\Omega_e} \mathbf{F} \begin{Bmatrix} S_{11} \cdot N_{n,X_1} + S_{12} \cdot N_{n,X_2} + S_{13} \cdot N_{n,X_3} \\ S_{21} \cdot N_{n,X_1} + S_{22} \cdot N_{n,X_2} + S_{23} \cdot N_{n,X_3} \\ S_{31} \cdot N_{n,X_1} + S_{32} \cdot N_{n,X_2} + S_{33} \cdot N_{n,X_3} \end{Bmatrix} dV_e , \tag{3.72}$$

from which the stresses components can be extracted in Voight notation, such that

$$\mathbf{F}^{in} = \int_{\Omega_e} \mathbf{F} \underbrace{\begin{bmatrix} N_{n,X_1} & 0 & 0 & N_{n,X_2} & 0 & N_{n,X_3} \\ 0 & N_{n,X_2} & 0 & N_{n,X_1} & N_{n,X_3} & 0 \\ 0 & 0 & N_{n,X_3} & 0 & N_{n,X_2} & N_{n,X_1} \end{bmatrix}}_{\mathbf{B}_n^{\mathrm{T}}} \underline{S} \, dV_e , \tag{3.73}$$

which gives rise to the strain-displacement matrix $\mathbf{B}_n$ (3.74).

$$\mathbf{B}_n^{\mathrm{T}} = \begin{bmatrix} \frac{\partial x_1}{\partial X_1}\frac{\partial N_n}{\partial X_1} & \frac{\partial x_1}{\partial X_2}\frac{\partial N_n}{\partial X_2} & \frac{\partial x_1}{\partial X_3}\frac{\partial N_n}{\partial X_3} & \frac{\partial x_1}{\partial X_1}\frac{\partial N_n}{\partial X_2}+\frac{\partial x_1}{\partial X_2}\frac{\partial N_n}{\partial X_1} & \frac{\partial x_1}{\partial X_2}\frac{\partial N_n}{\partial X_3}+\frac{\partial x_1}{\partial X_3}\frac{\partial N_n}{\partial X_2} & \frac{\partial x_1}{\partial X_1}\frac{\partial N_n}{\partial X_3}+\frac{\partial x_1}{\partial X_3}\frac{\partial N_n}{\partial X_1} \\ \frac{\partial x_2}{\partial X_1}\frac{\partial N_n}{\partial X_1} & \frac{\partial x_2}{\partial X_2}\frac{\partial N_n}{\partial X_2} & \frac{\partial x_2}{\partial X_3}\frac{\partial N_n}{\partial X_3} & \frac{\partial x_2}{\partial X_1}\frac{\partial N_n}{\partial X_2}+\frac{\partial x_2}{\partial X_2}\frac{\partial N_n}{\partial X_1} & \frac{\partial x_2}{\partial X_2}\frac{\partial N_n}{\partial X_3}+\frac{\partial x_2}{\partial X_3}\frac{\partial N_n}{\partial X_2} & \frac{\partial x_2}{\partial X_1}\frac{\partial N_n}{\partial X_3}+\frac{\partial x_2}{\partial X_3}\frac{\partial N_n}{\partial X_1} \\ \frac{\partial x_3}{\partial X_1}\frac{\partial N_n}{\partial X_1} & \frac{\partial x_3}{\partial X_2}\frac{\partial N_n}{\partial X_2} & \frac{\partial x_3}{\partial X_3}\frac{\partial N_n}{\partial X_3} & \frac{\partial x_3}{\partial X_1}\frac{\partial N_n}{\partial X_2}+\frac{\partial x_3}{\partial X_2}\frac{\partial N_n}{\partial X_1} & \frac{\partial x_3}{\partial X_2}\frac{\partial N_n}{\partial X_3}+\frac{\partial x_3}{\partial X_3}\frac{\partial N_n}{\partial X_2} & \frac{\partial x_3}{\partial X_1}\frac{\partial N_n}{\partial X_3}+\frac{\partial x_3}{\partial X_3}\frac{\partial N_n}{\partial X_1} \end{bmatrix} \tag{3.74}$$

The internal force vector $\mathbf{F}^{in}$ can be now given by

$$\mathbf{F}^{in} = \int_{\Omega_e} \mathbf{B}_n^{\mathrm{T}}\,\underline{S}\,\mathrm{d}V_e, \tag{3.75}$$

which is in conformity with (3.35). Furthermore, the given strain-displacement matrix $\mathbf{B}_n$ can be split into its linear and non-linear part. For this purpose, $\mathbf{F}^{in}$ is rewritten as (Crisfield, 1991)

$$\mathbf{F}^{in} = \int_{\Omega_e} \underbrace{\mathbf{G}_n^{\mathrm{T}}(\mathbf{X})}_{\substack{\text{linear} \\ \text{contribution}}} \cdot \underbrace{\left[\mathbf{A}^{\mathrm{T}}\big[\mathbf{u}(\mathbf{X})\big]+\mathbf{H}^{\mathrm{T}} \right]}_{\substack{\text{nonlinear} \\ \text{contribution}}} \cdot \underbrace{\underline{S}\big\{\underline{E}\big[\mathbf{u}(\mathbf{X})\big]\big\}}_{\substack{\text{stress} \\ \text{vector}}}\,\mathrm{d}V_e, \tag{3.76}$$

where the linear part of $\mathbf{B}_n$ is contained in matrix

$$\mathbf{G}_n^{\mathrm{T}}(\mathbf{X}) = \begin{bmatrix} \frac{\partial N_n}{\partial X_1} & \frac{\partial N_n}{\partial X_2} & \frac{\partial N_n}{\partial X_3} & 0 & 0 & 0 & 0 & 0 & 0 \\ 0 & 0 & 0 & \frac{\partial N_n}{\partial X_1} & \frac{\partial N_n}{\partial X_2} & \frac{\partial N_n}{\partial X_3} & 0 & 0 & 0 \\ 0 & 0 & 0 & 0 & 0 & 0 & \frac{\partial N_n}{\partial X_1} & \frac{\partial N_n}{\partial X_2} & \frac{\partial N_n}{\partial X_3} \end{bmatrix}, \tag{3.77}$$

and the non-linear part is given by

$$\mathbf{A}\big[\mathbf{u}(\mathbf{X})\big] = \begin{bmatrix} \frac{\partial u_1}{\partial X_1} & 0 & 0 & \frac{\partial u_2}{\partial X_1} & 0 & 0 & \frac{\partial u_3}{\partial X_1} & 0 & 0 \\ 0 & \frac{\partial u_1}{\partial X_2} & 0 & 0 & \frac{\partial u_2}{\partial X_2} & 0 & 0 & \frac{\partial u_3}{\partial X_2} & 0 \\ 0 & 0 & \frac{\partial u_1}{\partial X_3} & 0 & 0 & \frac{\partial u_2}{\partial X_3} & 0 & 0 & \frac{\partial u_3}{\partial X_3} \\ \frac{\partial u_1}{\partial X_2} & \frac{\partial u_1}{\partial X_1} & 0 & \frac{\partial u_2}{\partial X_2} & \frac{\partial u_2}{\partial X_1} & 0 & \frac{\partial u_3}{\partial X_2} & \frac{\partial u_3}{\partial X_1} & 0 \\ 0 & \frac{\partial u_1}{\partial X_3} & \frac{\partial u_1}{\partial X_2} & 0 & \frac{\partial u_2}{\partial X_3} & \frac{\partial u_2}{\partial X_2} & 0 & \frac{\partial u_3}{\partial X_3} & \frac{\partial u_3}{\partial X_2} \\ \frac{\partial u_1}{\partial X_3} & 0 & \frac{\partial u_1}{\partial X_1} & \frac{\partial u_2}{\partial X_3} & 0 & \frac{\partial u_2}{\partial X_1} & \frac{\partial u_3}{\partial X_3} & 0 & \frac{\partial u_3}{\partial X_1} \end{bmatrix}. \tag{3.78}$$

Additionally, the matrix $\mathbf{H}$ collects constants as

$$\mathbf{H} = \begin{bmatrix} 1 & 0 & 0 & 0 & 0 & 0 & 0 & 0 & 0 \\ 0 & 0 & 0 & 0 & 1 & 0 & 0 & 0 & 0 \\ 0 & 0 & 0 & 0 & 0 & 0 & 0 & 0 & 1 \\ 0 & 1 & 0 & 1 & 0 & 0 & 0 & 0 & 0 \\ 0 & 0 & 0 & 0 & 0 & 1 & 0 & 1 & 0 \\ 0 & 0 & 1 & 0 & 0 & 0 & 1 & 0 & 0 \end{bmatrix}. \tag{3.79}$$

Note that for relatively small displacements (2.110), $\mathbf{A}[\mathbf{u}(\mathbf{X})]$ collect only zeros (3.78). As a consequence, the element strain-displacement matrix $\mathbf{B}$ (defined as $\mathbf{AG}$) is reduced to (3.32). In this case, the shape function derivatives are defined by the chain rule

$$\frac{\partial N}{\partial X_1} = \frac{\partial N}{\partial \xi_i}\frac{\partial \xi_i}{\partial X_1} = \frac{1}{6V_e}\left(\frac{\partial N}{\partial \xi_1}\beta_1 + \frac{\partial N}{\partial \xi_2}\beta_2 + \frac{\partial N}{\partial \xi_3}\beta_3 + \frac{\partial N}{\partial \xi_4}\beta_4\right) = \frac{1}{6V_e}\frac{\partial N}{\partial \xi_i}\beta_i,$$

$$\frac{\partial N}{\partial X_2} = \frac{\partial N}{\partial \xi_i}\frac{\partial \xi_i}{\partial X_2} = \frac{1}{6V_e}\left(\frac{\partial N}{\partial \xi_1}\gamma_1 + \frac{\partial N}{\partial \xi_2}\gamma_2 + \frac{\partial N}{\partial \xi_3}\gamma_3 + \frac{\partial N}{\partial \xi_4}\gamma_4\right) = \frac{1}{6V_e}\frac{\partial N}{\partial \xi_i}\gamma_i, \tag{3.80}$$

$$\frac{\partial N}{\partial X_3} = \frac{\partial N}{\partial \xi_i}\frac{\partial \xi_i}{\partial X_3} = \frac{1}{6V_e}\left(\frac{\partial N}{\partial \xi_1}\delta_1 + \frac{\partial N}{\partial \xi_2}\delta_2 + \frac{\partial N}{\partial \xi_3}\delta_3 + \frac{\partial N}{\partial \xi_4}\delta_4\right) = \frac{1}{6V_e}\frac{\partial N}{\partial \xi_i}\delta_i,$$

giving the matrix structure for small displacements as

$$\mathbf{B} = \frac{1}{6V_e}\begin{bmatrix} \beta_1 & 0 & 0 & \beta_2 & 0 & 0 & \beta_3 & 0 & 0 & \beta_4 & 0 & 0 \\ 0 & \gamma_1 & 0 & 0 & \gamma_2 & 0 & 0 & \gamma_3 & 0 & 0 & \gamma_4 & 0 \\ 0 & 0 & \delta_1 & 0 & 0 & \delta_2 & 0 & 0 & \delta_3 & 0 & 0 & \delta_4 \\ \gamma_1 & \beta_1 & 0 & \gamma_2 & \beta_2 & 0 & \gamma_3 & \beta_3 & 0 & \gamma_4 & \beta_4 & 0 \\ 0 & \delta_1 & \gamma_1 & 0 & \delta_2 & \gamma_2 & 0 & \delta_3 & \gamma_3 & 0 & \delta_4 & \gamma_4 \\ \delta_1 & 0 & \beta_1 & \delta_2 & 0 & \beta_2 & \delta_3 & 0 & \beta_3 & \delta_4 & 0 & \beta_4 \end{bmatrix}. \tag{3.81}$$

The matrix components are coefficients identified in Eq. (3.54), Eq. (3.55), Eq. (3.56) and Eq. (3.57), multiplied by a constant given in terms of element volume V_e (Taylor, 2002). Since the element volume can be explicitly calculated (3.40), it follows that there is no need to compute the integral over the element domain by quadrature rule (3.37). As one can see, the strain-displacement matrix $\mathbf{B}$ produces a constant field of deformation over the element domain Ω_e. Consequently, the element stress field is also constant which enables the *monotonic convergence criteria*, since the rigid body displacements and the ability to reproduce constant field of deformations are possible.

Finally, note that the attractive element simplicity makes it inadequate for the simulation of complex stress and stain fields. However, complex mechanical fields can be numerical accurately reproduced by increasing the number of elements in a particular region of interest (*h refinement procedure*). The procedure will be appropriately discussed later on (*Chapter 8 – Adaptive finite elements*).

3.3.3.2 Tangent stiffness matrix

The element tangent stiffness matrix $\mathbf{K}_T$ derives from the same concept of linearization given in Eq. (3.65). By introducing the definition (Bonet & Wood, 1997)

$$\Delta \mathbf{F}^{in} = \operatorname{grad} \mathbf{F}^{in}\Big|_{\overline{\mathbf{u}}} \cdot \Delta \mathbf{u} = \frac{\mathrm{d}}{\mathrm{d}\epsilon}\Big|_{\epsilon=0} \int_{\Omega_e} \mathbf{B}_n^{\mathrm{T}}(\mathbf{u}+\epsilon\,\Delta\mathbf{u})\,\underline{S}\,(\mathbf{u}+\epsilon\,\Delta\mathbf{u})\Bigg|_{\overline{\mathbf{u}}} \mathrm{d}V_e = \mathbf{K}_T \Delta\mathbf{u}, \tag{3.82}$$

and carry out displacement variations as

$$\Delta\mathbf{F}^{in} = \int_{\Omega_e}\mathbf{G}_n^{\mathrm{T}}\frac{\mathrm{d}}{\mathrm{d}\epsilon}\Big|_{\epsilon=0}\Big[\mathbf{A}^{\mathrm{T}}(\mathbf{u}+\epsilon\,\Delta\mathbf{u})+\mathbf{H}^{\mathrm{T}}\Big]\underline{S}\,\Bigg|_{\overline{\mathbf{u}}}\mathrm{d}V_e + \int_{\Omega_e}\mathbf{B}_n^{\mathrm{T}}\frac{\mathrm{d}}{\mathrm{d}\epsilon}\Big|_{\epsilon=0}\underline{E}\,(\mathbf{u}+\epsilon\,\Delta\mathbf{u})\Bigg|_{\overline{\mathbf{u}}}\mathrm{d}V_e, \tag{3.83}$$

the *geometrical stiffness matrix* $\mathbf{K}_g$ is given from the variations of $\mathbf{B}_n$ as (Crisfield, 1991)

$$\mathbf{K}_g = \int_{\Omega_e}\mathbf{G}_n^{\mathrm{T}}\,\hat{S}\,\mathbf{G}_n\Bigg|_{\overline{\mathbf{u}}}\mathrm{d}V_e, \tag{3.84}$$

where

$$\hat{S} = \begin{bmatrix} S & \mathbf{0} & \mathbf{0} \\ \mathbf{0} & S & \mathbf{0} \\ \mathbf{0} & \mathbf{0} & S \end{bmatrix} \quad \text{and} \quad \mathbf{0} = \begin{bmatrix} 0 & 0 & 0 \\ 0 & 0 & 0 \\ 0 & 0 & 0 \end{bmatrix}. \tag{3.85}$$

The *material stiffness matrix* $\mathbf{K}_m$ follows from the variations of S (3.86).

$$\mathbf{K}_m = \int_{\Omega_e}\mathbf{B}_n^{\mathrm{T}}\,\mathbf{D}\,\mathbf{B}_n\Bigg|_{\overline{\mathbf{u}}}\mathrm{d}V_e \tag{3.86}$$

In order to obtain the displacement solution, the iterative strategy (3.87) should be followed.

$$(\mathbf{K}_m + \mathbf{K}_g(^k\overline{\mathbf{u}}))\Delta\mathbf{u} = -\,^k\mathbf{r}\Big|_{\overline{\mathbf{u}}}$$
$$^{k,k+1}\overline{\mathbf{u}} = \,^k\overline{\mathbf{u}} + \Delta\mathbf{u} \tag{3.87}$$

To follow the incremental-iterative solution strategy, the next subtitle contains a briefly overview of the adopted formulation for the incremental decomposition of motion.

3.4   UL formulation

The proposed numerical formulation is based on the *Updated Lagrange* (UL) *formulation* (Belytschko, Liu & Moran, 2001). In contrast to the Total Lagrange (TL) formulation (where the equations of motion are formulated with respect to material coordinates), the governing equations are here formulated with respect to the spatial coordinates (Refaat & Meguid, 1997)**.**
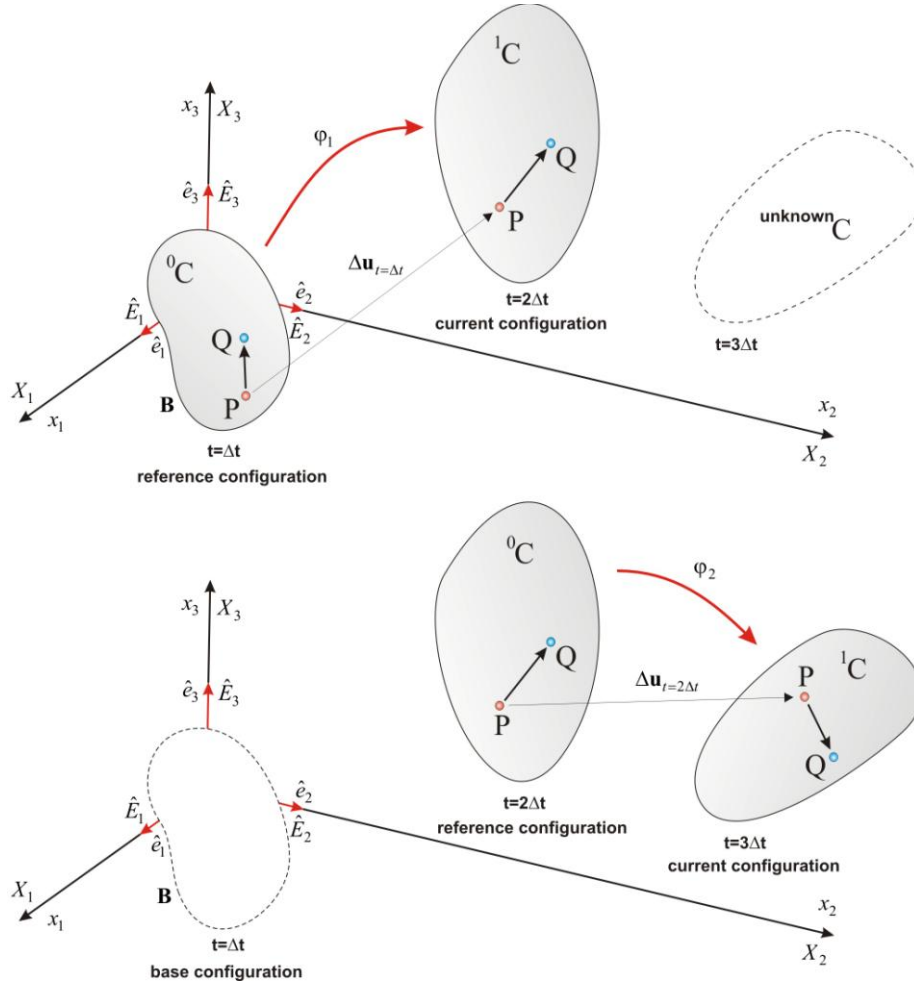
Figure 3.5 Updated Lagrangian formulation (successive update of continuum reference configuration)

The derivatives are taken with respect to the spatial (Eulerian) coordinates while the integrals are computed over the elements domain in the spatial configuration. However, the integral computed in the spatial coordinates can be related to the material coordinates by *J* (3.88).

$$\int\limits_{\Omega_e} f(\mathbf{x},t)\,dv_e = \int\limits_{\Omega_e} f(\varphi(\mathbf{X},t),t)\,J\,dV_e \tag{3.88}$$

At the numerical implementation level, the continuum motion is split into a finite number of intermediate configurations that are progressively used as reference frame (Fig. 3.5). The procedure is in accordance with

the concept of incremental analysis of non-linear problems. Indeed, the last known equilibrium state is set as the reference configuration (temporally frozen), and is then used for stress and strain measurement in the current configuration. On the other hand, note that the last equilibrium state can be either related to the base continuum configuration (Fig. 3.6) by the composition of incremental mapping functions φ (2.12).
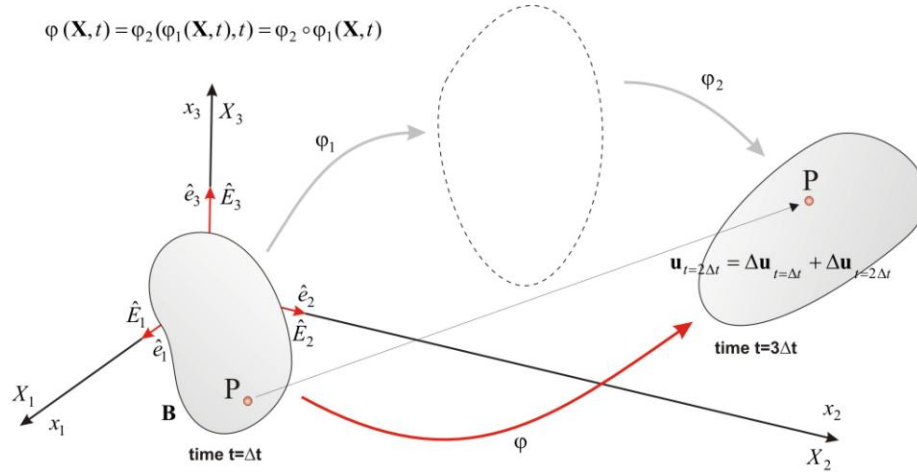
Figure 3.6 Composition of deformation (from Updated Lagrange to Total Lagrange formulation)

The essence of the UL formulation lies in the successive updating of reference frame. Therefore, by knowing the incremental displacement $\Delta \mathbf{u}$ between neighboring configurations, the updating process begins with setting the current configuration (defined by the coordinate vector $\mathbf{X}$) as the *new* reference configuration (defined by the coordinate vector $\mathbf{x}$) for the next incremental of the analysis (3.89).

$$\mathbf{x} = \mathbf{X} + \Delta \mathbf{u} \tag{3.89}$$

Not only coordinates but also the stress field must be updated. With the convergence state obtained by a set of 2nd Piola-Kirchoff stress tensors, the components of the true Cauchy stress tensor (related to the new configuration) are calculated according to Eq. (2.95) as

$$\boldsymbol{\sigma} = J^{-1} \mathbf{F}(\Delta \mathbf{u}) \, S \, \mathbf{F}^{\text{T}}(\Delta \mathbf{u}). \tag{3.90}$$

The stress tensors are then superposed to the previously defined stress state $\boldsymbol{\sigma}_0$ as $\boldsymbol{\sigma}_0 + \boldsymbol{\sigma}$. After performing these updates, the next increment of the analysis is taken within a new reference frame. At the beginning of the increment, the stress state is given by

$$S = \boldsymbol{\sigma}_0 + \Delta S \left(\Delta E \left(\Delta \mathbf{u} \right) \right), \tag{3.91}$$

where the stress components $\boldsymbol{\sigma}_0$ (defined at the end of the previous increment) are added to the current PK2 stress values ΔS. The incremental PK2 values are progressively calculated in an iterative fashion until $\|\mathbf{r}\| <$ predefined tolerance value (3.87). Note that at the beginning of the iteration loop $\boldsymbol{\sigma}_0$ coincides with PK2 since the incremental displacements $\Delta \mathbf{u}$ are set to zero at the entry of each increment.

3.4.1 Principle of virtual power

In the UL formulation the Cauchy stress tensor $\boldsymbol{\sigma}(\mathbf{X},t)$ and the spatial velocity $\boldsymbol{v}(\mathbf{X},t)$ are independent variables. Both are function of material coordinates $\mathbf{X}$ and time t. In accordance with the aforementioned, the weak form of governing equations in the spatial configuration is obtained by adopting the concept of *virtual power*. In this case the test functions are virtual velocities δv, and the weak form becomes

$$\int_{\Omega_e} \delta v_i \frac{\partial \sigma_{ij}}{\partial x_j}\, dv_e + \int_{\Omega_e} \delta v_i \rho b_i\, dv_e = 0. \tag{3.92}$$

The first integral can be further expanded by the product rule

$$\int_{\Omega_e} \delta v_i \frac{\partial \sigma_{ij}}{\partial x_j}\, dv_e = \int_{\Omega_e} \frac{\partial}{\partial x_j}(\delta v_i \sigma_{ij})\, dv_e - \int_{\Omega_e} \frac{\partial(\delta v_i)}{\partial x_j}\sigma_{ij}\, dv_e. \tag{3.93}$$

Then, the first integral on the RHS can be transformed by the Gauss's theorem as

$$\int_{\Omega_e} \frac{\partial}{\partial x_j}(\delta v_j \sigma_{ij})\, dv_e = \int_{\Gamma_t} \delta v_i\, n_j \sigma_{ij} d\Gamma_t = \sum_i \int_{\Gamma_t} \delta v_i\, \bar{t}_i\, d\Gamma_t \quad \textbf{where} \quad \delta v_i = 0 \textbf{ on } \Gamma_t. \tag{3.94}$$

By substituting Eq. (3.94) into Eq. (3.93) it can be obtained that

$$\int_{\Omega_e} \delta v_i \frac{\partial \sigma_{ij}}{\partial x_j}\, dv_e = \sum_i \int_{\Gamma_t} \delta v_i \bar{t}_i\, d\Gamma - \int_{\Omega_e} \frac{\partial(\delta v_i)}{\partial x_j}\sigma_{ij}\, dv_e, \tag{3.95}$$

while by introducing Eq. (3.95) into Eq. (3.92), the weak statement arises as

$$\int_{\Omega_e} \frac{\partial(\delta v_i)}{\partial x_j}\sigma_{ij} dv_e - \int_{\Omega_e} \delta v_i \rho b_i\, dv_e - \sum_i \int_{\Gamma_t} \delta v_i \bar{t}_i\, d\Gamma_t = 0, \tag{3.96}$$

denoting the *principal of virtual power* (Malvern, 1969).

3.4.2 Finite element approximation

According to the BG method, the space $\mathcal{U}_o$ of trial v_i and test functions δv_i are defined as:

$$v_i(\mathbf{X},t) \in \mathcal{U}_0, \qquad \mathcal{U}_0 = \left\{ v_i \mid v_i \in C^0(\mathbf{X}),\ v_i = \bar{v}_i \text{ on } \Gamma_{v_i} \right\}, \tag{3.97}$$

$$\delta v_i(\mathbf{X}) \in \mathcal{U}_0, \qquad \mathcal{U}_0 = \left\{ \delta v_i \mid \delta v_i \in C^0(\mathbf{X}),\ \delta v_i = 0 \text{ on } \Gamma_{v_i} \right\}, \tag{3.98}$$

from where the function should be chosen. The functions are subject to continuity condition (which should be fulfilled for compatibility reasons) and to the boundary conditions of velocity (Belytschko, Liu & Moran, 2001). Note that the δv_i vanishes wherever the trial velocity is prescribed.

Congruently with Eq. (3.97) and Eq. (3.98), the approximation of velocities v_i is given by

$$\mathbf{v}(\mathbf{X},t) = N_n(\mathbf{X})\,{}^n\mathbf{v}, \tag{3.99}$$

and the approximation of test function δv_i as

$$\delta\mathbf{v}(\mathbf{X}) = N_n(\mathbf{X})\delta^n\mathbf{v}. \tag{3.100}$$

${}^n\mathbf{v}$ and $\delta^n\mathbf{v}$ denote the velocity and the quantity of its variation at node n. By introducing the approximation of test function into the principle of virtual power (3.96), the following result is obtained:

$$\delta^n v_i \int\limits_{\Omega_e} \frac{\partial N_n}{\partial x_j} \sigma_{ij}\, \mathrm{d}v_e - \delta^n v_i \int\limits_{\Omega_e} N_n\, \rho\, b_i\, \mathrm{d}v_e - \sum_i \delta^n v_i \int\limits_{\Gamma_t} N_n\, \bar{t}_i\, \mathrm{d}\Gamma_t = 0. \tag{3.101}$$

Since the virtual velocities vanish where the velocities are prescribed, only the virtual nodal velocities which are not on Γ_v are arbitrary. In this case, the weak form becomes (Belytschko, Liu & Moran, 2001)

$$\int\limits_{\Omega_e} \frac{\partial N_n}{\partial x_j}\sigma_{ij}\mathrm{d}v_e - \int\limits_{\Omega_e} N_n\, \rho\, b_i\, \mathrm{d}v_e - \sum_i \int\limits_{\Gamma_t} N_n\, \bar{t}_i\, \mathrm{d}\Gamma = 0 \quad \forall\,(n,i) \notin \Gamma_v, \tag{3.102}$$

from where the prescribed DOF are excluded.

3.4.3 Jaumann rate & stress update

Since the equilibrium equations are written in successive updated configurations, expressing them in form of tensor rate seems logical. This is particularly suitable for numerical analysis of materials like concrete that possess memory of its initial virgin state (Ruigomez, 1985). A common practice in this case is to use the rate-of-deformation tensor $\mathbf{d}$ (2.106) as the strain measure.

For this purpose, assume a constitutive description in which the rate of the true Cauchy stress tensor is given as a function of $\mathbf{d}$ and $\boldsymbol{\sigma}$ through the tensor of material constants $\mathbf{C}^{\sigma d}$ (Belytschko, Liu & Moran, 2001) as:

$$\overset{\triangledown}{\boldsymbol{\sigma}} = \mathbf{C}^{\sigma d}(\mathbf{d},\boldsymbol{\sigma},\text{ect.}). \tag{3.103}$$

In this Eq. $\overset{\triangledown}{\boldsymbol{\sigma}}$ denotes the *Jaumann rate* of the Cauchy stress tensor and it is defined by

$$\overset{\triangledown}{\boldsymbol{\sigma}} = \frac{D\boldsymbol{\sigma}}{Dt} - \boldsymbol{w}\cdot\boldsymbol{\sigma} - \boldsymbol{\sigma}\cdot\boldsymbol{w}^{\mathrm{T}}. \tag{3.104}$$

The need to introduce the Jaumann rate lies in the requirement for tensor objectivity (Belytschko, Liu & Moran, 2001). Namely, the given expression indicates that the material time-derivative $D\boldsymbol{\sigma}/Dt$ (2.28) consists of two parts (3.105).

$$\frac{\mathbf{D\sigma}}{\mathrm{Dt}} = \overset{\nabla}{\mathbf{\sigma}} + \mathbf{w} \cdot \mathbf{\sigma} + \mathbf{\sigma} \cdot \mathbf{w}^{\mathbf{T}} = \underbrace{\mathbf{C}^{\sigma d} : \mathbf{d}}_{\mathbf{material\,response}} + \underbrace{\mathbf{w} \cdot \mathbf{\sigma} + \mathbf{\sigma} \cdot \mathbf{w}^{\mathbf{T}}}_{\mathbf{material\,rotation}} \tag{3.105}$$

The first part denotes the change in rate due to material response and the second one (made of two parts influenced by the spin tensors $\mathbf{w}$ (2.86)), denotes the rate of change due to material rotations (Stoker, 1999).

With the constitutive description defined through tensors rate (3.103), the stress update will be different to the previously discussed (3.91). Namely, in this case the stress update is carried out by integration of the material time-derivative $D\mathbf{\sigma}/Dt$ of the Cauchy true stress.

By assuming constant velocities $\dot{\mathbf{u}} = \Delta\mathbf{u}/\Delta t$ of continuum transition between two neighboring configurations, the stress state at time $t+\Delta t$ is defined as the stress state superposition at time t (rotated in the current configuration) and incrementally computed stresses.

Considering that $\mathbf{R}_t$ represents the rotation of the continuum reference frame at time t towards the continuum current frame at $t+\Delta t$, the former description can be restated as

$$\mathbf{\sigma}_{t+\Delta t} = \mathbf{R}_t \cdot \left[\mathbf{R}_t \cdot \mathbf{\sigma}_t \cdot \mathbf{R}_t^{\mathbf{T}} + \int_t^{t+\Delta t} \frac{D\mathbf{\sigma}}{Dt} \mathrm{d}t \right] \cdot \mathbf{R}_t^{\mathbf{T}}. \tag{3.106}$$

Eq. (3.106) defines the stress update procedure between the assumed reference and current configuration but also for all other neighboring intermediated configurations.

Chapter 4

Temporal discretization

4.1   Introduction

Since impact loadings are time-depended phenomenon, the temporal monitoring of system state variables is necessary. In order to follow the system time evolution, the time period $t \in [t_0, t_1] \subset \Re^+$, in which contact/impact occurs, is discretized with a finite number n of time increments Δt (n – time step counter). As a consequence, the continuous time line is replaced (discretized) by a set of points (usually equidistant) in which the governing equations are satisfied (Fig. 4.1). The changes of internal variables (state variable), between neighborhood time points, are then obtained by some pre-defined interpolations. In this case, by knowing the initial conditions at time $t_n = n\Delta t$ (usually given in terms of velocities and accelerations), the unknown continuum configuration at time $t_{n+1} = n\Delta t + \Delta t$ can be calculated from the fully discretized Eq. of motion. However, the procedure is legitimate if static loading conditions are assumed in each time interval $\Delta t \in [t_n, t_{n+1}]$. When calculating successive temporal states, the continuum motion can be tracked by augmenting neighboring temporal states. The procedure is known as *time stepping*.

4.2   Dynamic equilibrium equation

In order to retrieve the fully discrete equation of motion (valid for a dynamic system), from the previously introduced semi-discrete equation of motion (valid for a static system), the *Hamilton variational* is hereafter briefly introduced (*principle* i.e. principle of least action).

4.2.1 Hamilton variational principle

Upon introducing the notation *K* for the kinetic energy of continuum body in motion, and relating the internal potential energy and energy of external forces (volume and surface forces) to Π, the Hamilton variational principle can be written as

$$\int_{t_n}^{t_{n+1}} \delta \underbrace{(K - \Pi)}_{L} \, \mathrm{d}t = 0. \tag{4.1}$$

The term in the brackets denotes the *Lagrangian* of the system *L* (Lui & Quek, 2003). In words, the Hamilton principle states that the displacement solution of all admissible time histories makes the Lagrangian functional *L* minimum. Note that the admissible displacements field is the one that fulfills: the compatibility Eq. (2.112), the Neumann (3.3d) and Dirichlet boundary conditions (3.3e), and; the conditions at times t_n and t_{n+1}. To obtain the related FE approximation, focus on a discrete mechanical system which is in conformity with FE. In this case, Eq. (4.1) can be rewritten in matrix form as

$$\int_{t_n}^{t_{n+1}} \left(\delta \mathbf{u}^{\mathrm{T}} \frac{\partial L}{\partial \mathbf{u}} + \delta \dot{\mathbf{u}}^{\mathrm{T}} \frac{\partial L}{\partial \dot{\mathbf{u}}} \right) \mathrm{d}t = 0, \tag{4.2}$$

and, by integrating the second term by parts, as

$$\delta \mathbf{u}^{\mathrm{T}} \frac{\partial L}{\partial \dot{u}} \bigg|_{t_n}^{t_{n+1}} + \int_{t_n}^{t_{n+1}} \delta \mathbf{u}^{\mathrm{T}} \left(\frac{\partial L}{\partial \mathbf{u}} - \frac{\mathrm{d}}{\mathrm{d}t} \frac{\partial L}{\partial \dot{\mathbf{u}}} \right) \mathrm{d}t = 0. \tag{4.3}$$

Due to the restriction $\delta \mathbf{u}(t_n) = \delta \mathbf{u}(t_{n+1}) = \mathbf{0}$, the former Eq. is reduced to

$$\int_{t_n}^{t_{n+1}} \delta \mathbf{u}^{\mathrm{T}} \left(\frac{\partial L}{\partial \mathbf{u}} - \frac{\mathrm{d}}{\mathrm{d}t} \frac{\partial L}{\partial \dot{\mathbf{u}}} \right) \mathrm{d}t = 0, \tag{4.4}$$

and, since the displacement variations are arbitrary, to

$$\frac{\partial L}{\partial \mathbf{u}} - \frac{\mathrm{d}}{\mathrm{d}t} \frac{\partial L}{\partial \dot{\mathbf{u}}} = 0, \tag{4.5}$$

which represent the *Lagrange's equation* of motion.

4.2.2 Finite element approximation

In order to derive the FE approximation from the Lagrange's equation of motion (4.5), consider a deformable continuum in a displacement field $\hat{\mathbf{u}}\,(x_1, x_2, x_3)$. In this case, the kinetic energy K, associated to a domain Ω with boundary Γ and density ρ, can be expressed as

$$K = \frac{1}{2}\rho\int_{\Omega}\dot{\hat{\mathbf{u}}}^{\mathrm{T}}\,\dot{\hat{\mathbf{u}}}\,\mathrm{d}\Omega. \tag{4.6}$$

By presupposing hyperelastic continuum, the total potential energy can be represented as

$$\Pi = \frac{1}{2}\int_{\Omega}\boldsymbol{\varepsilon}^{\mathrm{T}}\mathbf{D}\boldsymbol{\varepsilon}\,\mathrm{d}\Omega - \int_{\Omega}\hat{\mathbf{u}}^{\mathrm{T}}\mathbf{b}\,\mathrm{d}\Omega - \int_{\Gamma}\hat{\mathbf{u}}^{\mathrm{T}}\bar{\mathbf{t}}\,\mathrm{d}\Gamma. \tag{4.7}$$

As already introduced, for a discretized continuum (Fig. 2.1), the displacement $\mathbf{u}$, velocity $\dot{\mathbf{u}}$ and $\boldsymbol{\varepsilon}$ in the FE domain $\Omega_e \subset \Omega$ are defined through the related nodal values $\hat{\mathbf{u}} = \mathbf{N}\mathbf{u}$, $\dot{\hat{\mathbf{u}}} = \mathbf{N}\dot{\mathbf{u}}$ and $\boldsymbol{\varepsilon} = \mathbf{B}\mathbf{u}$, respectively. Accordingly, the element kinetic energy is obtained as

$$K = \frac{1}{2}\dot{\mathbf{u}}^{\mathrm{T}}\left(\int_{\Omega_e}\mathbf{N}^{\mathrm{T}}\rho\mathbf{N}\,\mathrm{d}\Omega_e\right)\dot{\mathbf{u}}, \tag{4.8}$$

and the total potential energy as

$$\Pi = \frac{1}{2}\mathbf{u}^{\mathrm{T}}\left(\int_{\Omega_e}\mathbf{B}^{\mathrm{T}}\mathbf{D}\mathbf{B}\,\mathrm{d}\Omega_e\right)\mathbf{u} - \mathbf{u}^{\mathrm{T}}\left(\int_{\Omega_e}\mathbf{N}^{\mathrm{T}}\mathbf{b}\,\mathrm{d}\Omega_e\right) - \mathbf{u}^{\mathrm{T}}\left(\int_{\Gamma_e}\mathbf{N}^{\mathrm{T}}\bar{\mathbf{t}}\,\mathrm{d}\Gamma_e\right). \tag{4.9}$$

Finally, the discrete FE form of dynamic equilibrium arises by inserting Eq. (4.8) and Eq. (4.9) into the *Lagrange's equation* of motion (4.5), producing:

$$\underbrace{\left(\int_{\Omega_e}\mathbf{N}^{\mathrm{T}}\rho\mathbf{N}\,\mathrm{d}\Omega_e\right)}_{\mathbf{M}}\ddot{\mathbf{u}} + \underbrace{\left(\int_{\Omega_e}\mathbf{B}^{\mathrm{T}}\mathbf{D}\mathbf{B}\,\mathrm{d}\Omega_e\right)}_{\mathbf{K}}\mathbf{u} = \underbrace{\left(\int_{\Omega_e}\mathbf{N}^{\mathrm{T}}\mathbf{b}\,\mathrm{d}\Omega_e\right) + \left(\int_{\Gamma_e}\mathbf{N}^{\mathrm{T}}\bar{\mathbf{t}}\,\mathrm{d}\Gamma_e\right)}_{\mathbf{F}^{ex}}. \tag{4.10}$$

Usually, the former Eq. is rewritten in compact form as

$$\mathbf{M}\ddot{\mathbf{u}} + \mathbf{K}\mathbf{u} = \mathbf{F}^{ex}(t), \tag{4.11}$$

where $\mathbf{M}$ denotes the so-called *consistent element mass matrix* and the related term represents the contribution of inertial forces in reaching equilibrium state with external forces $\mathbf{F}^{ex}$. Note that the external force vector $\mathbf{F}^{ex}$ is now a function of time.

Since the displacement and displacement time derivatives are discrete space functions but continuous time function, the equilibrium Eq. (4.11) is given in a semi discrete form. The fully discrete Eq. of motion can be obtained by performing the temporal discretization of displacement and related characteristic time derivatives. The procedure is performed by attributing discrete value in a continuous time line. Accordingly, the equilibrium state at the end of the current time increment Δt (defined as $t_{n+1}=n\Delta t+\Delta t$) is reached when

$$\mathbf{M}\ddot{\mathbf{u}}_{n+1} + \mathbf{K}\mathbf{u}_{n+1} = \mathbf{F}^{ex}(t)_{n+1}. \tag{4.12}$$

Note that the equilibrium Eq. (4.12) is satisfied only at discrete time intervals. Within each time interval, a variation of displacement, velocity and nodal acceleration is presupposed with the adopted time integration technique. In the proposed numerical formulation, the equations are solved in their original form (4.12) denoting *direct time integration*. It is important to point out that the accuracy of results is limited by a variety of theoretical assumptions and restrictions deriving from computational implementation. However, that issue will be properly discussed soon.

4.2.3 Phenomenological damping

As well known, the response of real structures to external forces is always accompanied by a certain amount of energy dissipation manifested through the damping behavior of structure oscillations. Since the origin of dissipation lies in the material microstructural level, the damping description is usually simplified by assuming that the value of energy dissipation is proportional to the structure displacements and that is represented by a non-linear function of displacements magnitude. The dissipation effect is here introduced by including the viscous damping force that tends to damp the structure oscillation. Thus, the dynamic equilibrium Eq. (4.12) is rewritten as

$$\mathbf{M}\ddot{\mathbf{u}}_{n+1} + \mathbf{C}\dot{\mathbf{u}}_{n+1} + \mathbf{K}\mathbf{u}_{n+1} = \mathbf{F}^{ex}(t)_{n+1}, \tag{4.13}$$

where the damping behavior is represented by the viscous damping matrix $\mathbf{C}$ defined as (Wilson, 1995)

$$\mathbf{C} = \alpha\mathbf{M} + \beta\mathbf{K}. \tag{4.14}$$

The coefficients α and β are empirical parameters which should be appropriately chosen for the considered dynamic analysis (*Rayleigh damping*). The model reflects the damping ration by linear combination of the mass and stiffness matrixes. Particularly, the damping related to $\beta\mathbf{K}$ increases as the frequency increases while the damping related $\alpha\mathbf{M}$ increases as the frequency of oscillation decreases. However, it will be illustrated that for high-energy impact loadings the presence of viscous damping forces can be ignored, which is expected considering the usual low amplitude of oscillation (*Chapter 10 – 10.3.2.2 Contact force, force equilibrium and reactions*).

4.3 Time integration

The time integration of Eq. (4.13) is performed with the *finite difference method* (Hutton, 2004). According to the standard notation for temporal association of system state variables, the lower index n denotes the time position of quantities on a discrete time line (i.e. at the beginning of the time increment nΔt). Two related neighboring quantities, those at the beginning of a particular time increment and at the end of the time increment, are then defined by indexes n−1 and n+1, respectively.

4.3.1 Assumption, approximations and errors

In order to solve Eq. (4.13) for unknown nodal displacements $\mathbf{u}_{n+1}$, the FE nodal accelerations $\ddot{\mathbf{u}}_n$ and nodal velocities $\dot{\mathbf{u}}_n$ are approximated through displacements. However, to make the finite difference method suitable for approximation, the highest displacement derivatives (i.e. nodal accelerations) should be smooth functions of time.

For the purpose of illustrating the approximation of first (velocity) and the second displacement derivative (acceleration), let consider a smooth displacement function $u(t)$. For the displacement $u(t+\Delta t)$ the Taylor series expansion produce:

$$u_{n+1} = u_n + \dot{u}_n\Delta t + \frac{\Delta t^2}{2}\ddot{u}_n + \frac{\Delta t^3}{6}\dddot{u}_n + \ldots, \tag{4.15}$$

while for the displacement $u(t-\Delta t)$:

$$u_{n-1} = u_n - \dot{u}_n\Delta t + \frac{\Delta t^2}{2}\ddot{u}_n - \frac{\Delta t^3}{6}\dddot{u}_n + \ldots. \tag{4.16}$$

By truncating the series after the second derivative and by subtracting (4.16) from (4.15), the *central difference formula* will be obtained. For relatively small time increments Δt, the central difference formula enable the approximation of first displacement derivations as

$$\dot{u}_n \approx \frac{1}{2\Delta t}(u_{n+1} - u_{n-1}). \tag{4.17}$$

By adding Eq. (4.15) to Eq. (4.16), the second displacement derivatives is approximated as

$$\ddot{u}_n \approx \frac{1}{\Delta t^2}(u_{n-1} - 2u_n + u_{n+1}). \tag{4.18}$$

Mention that the presented time integration algorithm is affected by two types of errors. The first one, the so-called *truncation error*, is associated with the accuracy of finite difference method. Namely, as the example

above shows (4.15), the error arises from the truncation of the Taylor series expansion by introducing the approximation of the right solution. The second type of error, referred to as *round-off error*, is associated with the finite number of digits used in computer arithmetic. However, both errors are influenced by the choice of Δt. Particularly, by reducing Δt both errors will decrease. In case of large Δt, the truncation error dominates the solution but it decreases together with Δt. On the other hand, the round-off error decreases more slowly and dominates the solution process for small Δt. Note that the numerical description of impact loading will be especially influenced by the round-off error. Namely, in order to accurately simulate the concrete deformation history, which is "trapped" in small time periods (~1 ms), the numerical description requires a relatively large number of small time increments Δt. Therefore, to minimize the presence of the round-off error, the use of computer 64-bit precision is inevitable. Abiding by the standard nomenclature used in computer program languages, this condition corresponds to the *double precision* declaration of program code variables. The declaration helps to keep the round-off errors as less as possible. Mention that other similar problems arise in contact detection procedure. The relevant problematic will be discussed in a separate chapter (*Chapter 7 – Contact detection*).

It is important to point out that the previously introduced assumption (smooth feature of accelerations) is rarely preserved in impact analysis. Indeed, the functions of accelerations for bodies under collision are characterized by discontinuities (shock phenomena). However, with a careful choice of Δt, the discontinuities can be simulated by a finite number of discrete sloping segments (regularization).

4.3.2 Newmark β integration method

The essence of the Newmark method lies in the introduction of parameters β and γ into the truncated Taylor series expansion for displacements and velocities, respectively (Newmark, 1959). In this manner, the displacement value at time n+1 is approximated as

$$u_{n+1} = u_n + \Delta t\, \dot{u}_n + \Delta t^2 \left[\left(\frac{1}{2} - \beta \right) \ddot{u}_n + \beta\, \ddot{u}_{n+1} \right],$$

(4.19)

and velocities as

$$\dot{u}_{n+1} = \dot{u}_n + \Delta t \left[(1-\gamma)\ddot{u}_n + \gamma\, \ddot{u}_{n+1} \right].$$

(4.20)

The parameters introduced in the numerical simulation are constants defined in intervals: $0 \leq \beta \leq 0.5$ and $0 \leq \gamma \leq 1$. Depending on the chosen parameters β and γ, Newmark approximations determine the order and accuracy of the integration method (Ngo & Mendis, 2008). Consequently, the Newmark family of single-step integration methods can be applied to both extreme loading type, i.e. loading characterized by short-time periods (e.g. blast loadings) and loading characterized by long-time periods (e.g. seismic loadings).

4.3.2.1 Implicit time integration

The implicit time integration is obtained by setting the integration parameters in Eq. (4.19) and in Eq. (4.20) as $\beta>0$ and $\gamma\neq0$ (Wilson, 1995). For this purpose, it is convenient to formulate the Newmark integration method by setting the displacements value u_{n+1} as primary variables. Consequently, the acceleration $\ddot{u}_{n+1}$ at time n+1 is determined form the displacements u_n and u_{n+1} as

$$\ddot{u}_{n+1} = \alpha_1(u_{n+1} - u_n) - \alpha_2\dot{u}_n - \alpha_3\ddot{u}_n, \tag{4.21}$$

and the velocities $\dot{u}_{n+1}$ as

$$\dot{u}_{n+1} = \alpha_4(u_{n+1} - u_n) + \alpha_5\dot{u}_n + \alpha_6\ddot{u}_n. \tag{4.22}$$

The coefficients α_1, α_2, α_3, α_4, α_5 and α_6 are given as follows (4.23).

$$
\begin{aligned}
\alpha_1 &= \frac{1}{\beta\,\Delta t^2} \\[2mm]
\alpha_2 &= \frac{1}{\beta\,\Delta t} \\[2mm]
\alpha_3 &= \frac{1-2\beta}{2\beta} \\[2mm]
\alpha_4 &= \frac{\gamma}{\beta\,\Delta t} \\[2mm]
\alpha_5 &= 1-\frac{\gamma}{\beta} \\[2mm]
\alpha_6 &= \Delta t - \frac{\gamma\,\Delta t}{2\beta}
\end{aligned}
\tag{4.23}
$$

By introducing Eq. (4.21) and Eq. (4.22) into Eq. (4.13), the dynamic equilibrium Eq. becomes:

$$\mathbf{M}\big[\alpha_1(\mathbf{u}_{n+1}-\mathbf{u}_n) - \alpha_2\dot{\mathbf{u}}_n - \alpha_3\ddot{\mathbf{u}}_n\big] + \mathbf{C}\big[\alpha_4(\mathbf{u}_{n+1}-\mathbf{u}_n) + \alpha_5\dot{\mathbf{u}}_n + \alpha_6\ddot{\mathbf{u}}_n\big] + \mathbf{F}^{in}(\mathbf{u}_{n+1}) = \mathbf{F}^{ex}(\mathbf{u}_{n+1}). \tag{4.24}$$

By applying the previously introduced Newton-Raphson's solution strategy (3.87), the unknown displacement vector $\mathbf{u}_{n+1}$ will be determined through the tangent stiffness matrix $\mathbf{K}_T$, by performing the iteration loop over the index k at each time step t_{n+1} (4.25).

$$
\begin{aligned}
\big[\alpha_1\mathbf{M} + \alpha_4\mathbf{C} + \mathbf{K}_T(\mathbf{u}_{n+1}^k)\big]\Delta\mathbf{u}_{n+1}^{k+1} &= -\mathbf{r}(\mathbf{u}_{n+1}^k) \\
\mathbf{u}_{n+1}^{k+1} &= \mathbf{u}_{n+1}^k + \Delta\mathbf{u}_{n+1}^{k+1}
\end{aligned}
\tag{4.25}
$$

The iterative loop is conducted until the Euclidian norm $\|\mathbf{r}(\mathbf{u}_{n+1}^k)\|$ becomes smaller than the predefined tolerance value. The benefit of the implicit time integration is that the procedure is unconditionally stable.

However, the strategy requires an evident computational time effort since the tangent stiffness matrix should be calculated at the beginning of each iteration. An alternative to that could be the *modified Newton-Raphson's solution strategy* where the tangent stiffness matrix is computed only once, i.e. at the beginning of each increment of the analysis. Also, even though the implicit time integration is an adequate choice for simulation of low frequency modes, it is not suitable for time integration of equations of motion where body's collision is expected. Indeed, high-energy impact loading are often accompanied by high frequency of oscillation. Therefore, and for other reasons (Wriggers, 2002); the explicit integration method turns out to be more appropriate choice.

4.3.2.2 Explicit time integration

By setting the parameters of integration in Eq. (4.19) and Eq. (4.20) as *β*=0 and *γ*=0.5, the Newmark method will produce the previously introduced central difference scheme. In this case, the velocity $\dot{u}_\text{n}$ in time n is approximated as

$$\dot{u}_\text{n} = \frac{u_{\text{n}+1} - u_{\text{n}-1}}{2\Delta t}, \tag{4.26}$$

and acceleration $\ddot{u}_\text{n}$ as

$$\ddot{u}_\text{n} = \frac{u_{\text{n}+1} - 2u_\text{n} + u_{\text{n}-1}}{\Delta t^2}. \tag{4.27}$$

The discrete dynamic equilibrium Eq. can be rewritten as

$$\mathbf{M}\,\ddot{\mathbf{u}}_\text{n} + \mathbf{C}\,\dot{\mathbf{u}}_\text{n} + \mathbf{F}_\text{n}^{in} = \mathbf{F}^{ex}(t)_\text{n}, \tag{4.28}$$

giving the unknown displacement vector $\mathbf{u}_{\text{n}+1}$ as

$$\left[\mathbf{M} + \frac{\Delta t}{2}\mathbf{C}\right]\mathbf{u}_{\text{n}+1} = \Delta t^2\left\{\mathbf{F}_\text{n}^{ex} - \mathbf{F}_\text{n}^{in}\right\} + \frac{\Delta t}{2}\mathbf{C}\left\{\mathbf{u}_{\text{n}-1}\right\} + \mathbf{M}\left\{2\mathbf{u}_\text{n} - \mathbf{u}_{\text{n}-1}\right\}. \tag{4.29}$$

Since the matrix **M** and **C** do not change during the solution process (for no remeshing), the triangularization of coefficient matrix on the LHS has to be calculated only once. Also, note that all nonlinearities are introduced via the internal force vector $\mathbf{F}_\text{n}^{in}$ and, as the displacement solution in the explicit time integration is based on displacements at time n, there is no need to perform an iterative convergence loop. An especially attractive property of the strategy emerges when the matrix **M** and **C** are taken as diagonal matrixes. Indeed, if the consistent mass matrix (4.10) is transformed into a lumped mass matrix (by distributing FE mass uniformly to all element nodes), the triangularization of the LHS is trivial.

It should be noted that the damping matrix **C** is defined only by the mass matrix (not as in Eq. 4.14), since the diagonalization of stiffness matrix is not possible. On the other hand, such restriction does not inflict any harm to a formulation, since the presence of viscous damping forces in high-energy impact loading can be ignored. Having said that, the former Eq. can be rewritten as

$$\mathbf{u}_{n+1} = \underbrace{\left[\mathbf{M} + \frac{\Delta t}{2}\mathbf{C}\right]^{-1}}_{\text{diagona matrix}} \Delta t^2 \left\{\mathbf{F}_n^{ex} - \mathbf{F}_n^{in}\right\} + \frac{\Delta t}{2}\mathbf{C}\left\{\mathbf{u}_{n-1}\right\} + \mathbf{M}\left\{2\mathbf{u}_n - \mathbf{u}_{n-1}\right\} \quad \text{where} \quad \mathbf{C} = \alpha\mathbf{M}. \tag{4.30}$$

Note that no global matrix needs to be computed. In fact, the explicit time integration enables the computing of unknown displacements by using only local element matrixes. Furthermore, from the computational point of view, obtaining the solution by the explicit time integration is much cheaper than by the implicit time integration (4.25). As a matter of fact, the explicit integration produces a system of uncoupled algebraic equations in which the displacement value at arbitrary DOF is not a function of other DOF (4.30).

However, the definition of initial values requires special treatment since at time t=0 the displacement values $\mathbf{u}_{0-1}$ are needed. These displacement values are determined from the given initial conditions of displacement $\mathbf{u}_0$ and velocities $\dot{\mathbf{u}}_0$, defined at the beginning of the simulation. Indeed, the displacement vector $\mathbf{u}_{0-1}$ is determined from the Taylor series expansion at time t_{0-1} via (Bathe, 1996)

$$\mathbf{u}_{0-1} = \mathbf{u}_0 - \Delta t\,\dot{\mathbf{u}}_0 + \frac{\Delta t^2}{2}\ddot{\mathbf{u}}_0. \tag{4.31}$$

The acceleration at time t=0 arise from Eq. (4.28) as

$$\mathbf{a}_0 = \mathbf{M}^{-1}\left\{-\mathbf{C}\,\dot{\mathbf{u}}_0 - \mathbf{K}\,\mathbf{u}_0 + \mathbf{F}^{ex}(0)\right\}. \tag{4.32}$$

With the explicit time integration the solution process is conditionally stable and is influenced by the adopted time increment Δt. Particularly, if the chosen time increment Δt is greater that the critical one Δt_{cr}, the displacement solution divergence (numerical instability). In order to avoid this numerical instability, the acquired time increment Δt must be smaller than the critical one Δt_{cr} (*Courant criterion*), that is calculated for each finite element e according to Eq. (4.33).

$$\Delta t_{cr}^e = \frac{L_{min}^e}{\sqrt{\dfrac{E_e}{\rho_e}}} \quad \text{where} \quad e = 1..n_e \tag{4.33}$$

In this Eq. L_{min}^e denotes the minimum length of a finite element while E_e and ρ_e are Young's modulus and density related to the respective finite element e. By knowing the critical time increment Δt_{cr}, the time increment in the analysis should be chosen according to Eq. (4.43).

$$\Delta t \le \Delta t_{cr} = \min\left\{\Delta t_{cr}^e\right\} \tag{4.34}$$

In case of non-linear problems (such as those under consideration), the critical time step should be additionally reduced by a *safety factor* below one (Wriggers, 2002). From the physical point of view, the critical time increment ensures that the propagation of stresses in Δt is slower than the speed of sound for the considered continuum. In this sense, the time increment requirement preserve the physical significance of the obtained results. However, with explicit time integration, the discussion of mesh stability is also valid. Indeed, depending on the shape of tetrahedral elements, the uncoupled system of equations (4.30) can give rise to displacements values that may violate the element local invertibility condition (2.47). As disused by Cheng, Quan and Sou-Yizheng (1993), the mesh stability can be preserved by ensuring that the *Hilbert norm* of element displacement vector **u** is smaller than the product of the element characteristic length L and control parameter η (4.35).

$$\left\| \mathbf{u} \right\| < L \cdot \eta \tag{4.35}$$

The control parameter η is chosen respect to the finite element under consideration (Cheng, Quan & Sou-Yizheng; 1993). When the conditions in Eq. (4.34) and Eq. (4.35) are fulfilled, the physical significance is preserved and the dangerous mesh instability, which can transiently grow through the solution process, is avoided. Note that, since the presence of non-linearity requires an incremental analysis, the solution process is decomposed into a finite number of discrete time increments Δt. The update procedure between successive time increments is illustrated in Fig. 4.1.
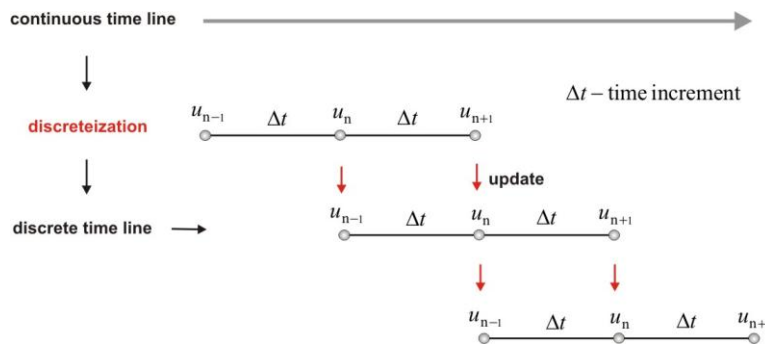
Figure 4.1 Time stepping procedure

It is important to mention that eventually changes of Δt during the solution process may harm the requirement for energy preservation. Namely, in case of penetration problems (Fig. 1.3), where the remeshing procedure is inevitable, the critical time increment Δt_{cr} will rapidly vary due to the change of L_{min}^e (4.33). In this case, the adopted time increment should not be adapted during the solution process. To avoid numerical instabilities, a significantly smaller time increment Δt, compared to Δt_{cr} (4.33), should be calculated for the initial discretization and used until the end of the simulation (Fig. 8.7).

Chapter 5

Microplane material model

5.1 Introduction

From examining the uniaxial σ-ε relationship of concrete, it can be deduced that this composite falls into the group of quasi-brittle materials. At this phenomenological macro-scale of observation, the concrete response to external loading is governed by the micro-structural mechanical property of the material particle interactions. As a composite made of aggregate interconnected by cement matrix, the concrete mechanical behaviour is influenced by the micro-structural phenomena such as cohesion, friction and aggregate interlocking. In order to numerically simulate these effects, the material model should be formulated by respecting the composite nature of concrete. Therefore, from the various types of constitutive models used to simulate concrete, in the proposed numerical formulation the *microplane material model* is adopted. The choice can be justified by the concept of model itself that consists in representing the macroscopic material behavior by uniaxial σ-ε relationship on planes located at the concrete microscopic level. These planes with arbitrary spatial orientations (microplanes) are interpreted as damage planes or weak planes of contact layers between the concrete aggregate and cement matrix (Fig. 5.1).

_____

From the historical point of view, the origin of such pioneering idea can be traced back to 1938 when G.I. Taylor proposed the basic concepts of the microplane theory. The original model, known as the "*slip theory of plasticity*", was developed for the purpose of description of plastic slip in *crystalline materials*. At first, the model passed unnoticed in the scientific concrete community that, at that time, widely accepted the softening plasticity and continuum damage mechanics for the constitutive description of concrete. However, the physical background of plastic models imposed conceptual problems due to the fact that, being a composite material, the concrete behavior did not fit well in the plastic description. On the other hand, the concept of scalar damage gave rise to the theory of damage description in the concrete heterogeneous microstructure (Chaboche, 1988; Lemaitre, 1992). However, in order to reproduce the three-dimensional anisotropic damage state, the theory leads to damage tensors of second, fourth and even eighth order. It was based on the promising stiffness degradation principle but the tensor components could not be easily identified. Therefore, the model was inapplicable to practical problems and consequently abandoned.
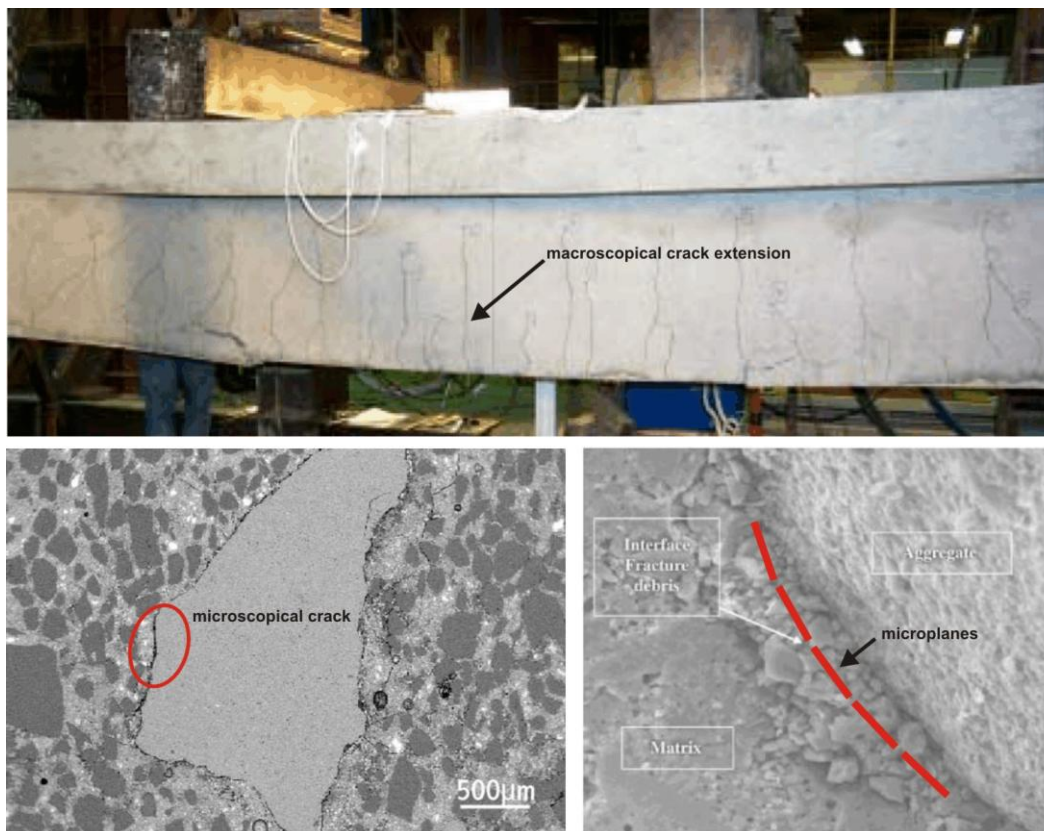
Figure 5.1 Idealistic representation of the microplane model (microplanes on microstructural interaction)

Later on, Bažant and Gambarova (1984) found the microplane idea very interesting. They realized that a proper model extension would generate adequate properties for the numerical simulation of concrete. The proposed model was based on a compromise between the scalar damage theory and the microplane theory, introducing the concrete damage description by differently oriented planes on which the uniaxial stress-strain laws are enforced through the uniaxial scalar damage model.

Before proceeding to the description of the model, mention that the adopted FE discretization does not provide any information on possible local material imperfections or macroscopic non-homogeneities in the domain Ω occupied by concrete body. However, following the REV assumption (*Chapter 2 – 2.1 Introduction*), the non-homogenous concrete microstructural properties are replaced by a uniform, homogenous mass distribution over the entire domain Ω. Indeed, the complex concrete microstructure stress transfer mechanism is artificially introduced by the microplane model. Such models indicate the microscopic mechanical behavior at the macroscopic level by taking into account an average response of the concrete microstructural mechanical properties. Consequently, the model falls into the group of macroscopic types of constitutive models.

Mention that the microplane model can be easily incorporated in any continuum deformation analysis performed by FEM. For the sake of illustration, assume that the macro-micro transitions of mechanical quantity are performed in a FE mesh. The microplane model requires transitions by projecting macroscopic values, which are carried out at every continuum point, onto tangent planes of the unit microsphere that surrounds the micro-heterogeneous material. Indeed, at the numerical implementation level, the microplane model fits almost naturally in the FE environment, since continuum points are here represented by Gauss points, i.e. position inside Ω_e where the FE macroscopic data are integrated. However, as it has been discussed (*Chapter 3 – 3.3 Linear tetrahedral element*), if the domain is discretized by linear tetrahedral elements (Fig. 3.2), there is no need to perform the numerical integration at the Gauss point level. The microplane model can be still incorporated in the numerical formulation by assuming an imaginary integration point located at the tetrahedral barycenter coordinates. The passage from the known macroscopic (Gauss point) to the unknown microscopic values (microplane) is conducted through pre-defined projection tensors that relate macroscopic data to tangential planes defined at each point of the unit sphere (Fig. 5.2).

Since the number of points on the unit sphere is infinite, it is obvious that the described idealistic strategy cannot be approached computationally. For this purpose, the unit sphere is usually replaced by a geometrical approximation composed of finite number of planes (usually triangular planes). However, as far as the unit sphere discretization delicacy is concerned, if a coarse geometrical approximation is applied, the model will be computationally acceptable but physically poorly conditioned. On the other hand, by increasing the number of planes for the geometrical approximation of the unit microsphere, the computational efficiency will rapidly decrease. To preserve the model efficiency and, in the same time, to overcome computational time effort, Bažant and Oh (1986) propose the unit sphere approximation by triangular planes generated between 42 points (vertex), as a good compromise between efficiency and computational effort. Following this conclusion, in the proposed numerical formulation the unit sphere is replaced by a discrete geometrical approximation shown in Fig. 5.2 (for alternative see: Němeček, Patzák, Rypl & Bittnar, 2002).

In order to avoid any doubts, note that the generated triangular planes should not be interpreted as microplanes themselves. Indeed, once the macroscopic values at FE Gauss points are known, their projections are performed

on planes that lie on edges of the generated three-dimensional object. Particularly, the spatial orientations of planes are defined by an average approximation of planes that surrounds each vertices and edges (Fig 5.2). Note that, due to the fact that the discrete approximation is symmetric, it is sufficient to project the macroscopic data only on half the total number of microplanes.
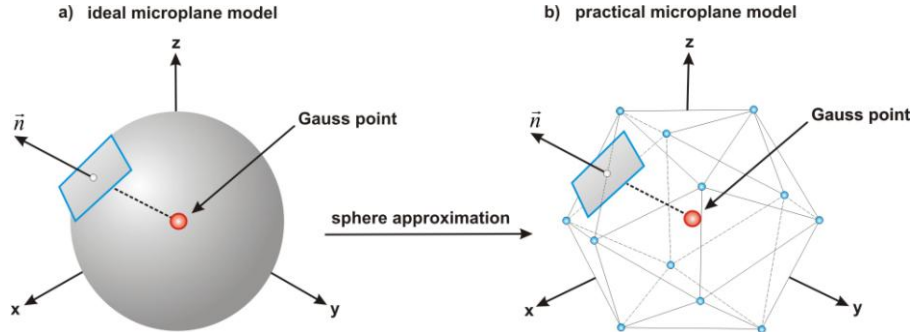
Figure 5.2 Microplane: **a)** Ideal microsphere and **b)** discrete microsphere approximated by 42 points

By taking into account tensorial invariants restrictions, the microplane concept does not require the invariant restrictions to be directly enforced. Indeed, the conditions are automatically fulfilled since considering microplanes with different spatial orientations have been taken into account. This fact introduces advantages in respect to other tensorial constitutive models which are based on tensorial invariants. Namely, a weak point of other invariant types of models is the prediction of correct concrete expansion caused by the triaxial compressive loading. Furthermore, from the theoretical point of view, such models are based on the theory of continuum mechanics and are not acceptable for the description of complex **σ-ε** relationship that implies discontinuity like cracking in the assumed material continuum. On the other hand, for materials that are subject to damage phenomena and non-elastic strain localization (cracking), the microplane model realistically reproduces the material response. The statement is supported by a variety of numerical experiments which are in accordance with experimental observations (Ožbolt, Li & Kožar, 2001).

In order to validate the proposed numerical formulation, a need for cracking description in the environment of FE should be satisfied. The so-called *smeared cracking concept*, taken from the few developed strategies, is used for this purpose (Willam, Pramono & Sture, 1987). In this case, the cracking trajectories are manifested in contour of principal tensile deformation (Weihe, Kröplin & de Borst, 1998). Following the principal tensile deformation, the concrete cracks can be tracked by scaling deformations values to the reference deformation value ε_r that causes the cracks to open. According to the engineering strain definition, ε_r can be simply determined as

$$\varepsilon_r = \frac{w_{cr}}{L^e_{\min}}, \tag{5.1}$$

where w_{cr} denotes the critical crack aperture (depended on the concrete under consideration) and L^e_{min} the minimum element edge length of all elements in the discretization. An example of the smeared cracking concept is illustrated in Fig. 5.3. Differently from smeared cracking concept, that lies within the framework of continuous mechanics, note that it would be appropriate to describe the formed crack as an aperture in the FE mesh. This kind of scenario can be numerically reproduced by means of the so-called *discrete cracking concept*. However, the mentioned concept considerably increases the computational effort (especially in the three-dimensional environment), since it introduces a significant amount of geometrical and topological FE mesh adaptations also known as mesh fragmentation (Shen, 2000; Pandolfi & Ortiz, 2002). To preserve simplicity as much as possible, the description of continuum fragmentation process, i.e. the discrete cracking description, is here abandoned.

The smeared cracking concept introduces austerity in the aforementioned challenging cracking description by simply excluding the contribution of internal forces (to the total internal force field) of those FE that lie on the crack trajectory. In such way the mesh continuity is preserved, satisfying the continuous mechanics assumptions. At the same time, the crack extension is simply tracked by monitoring the principal traction strain contour, as previously introduced in Eq. (5.1).
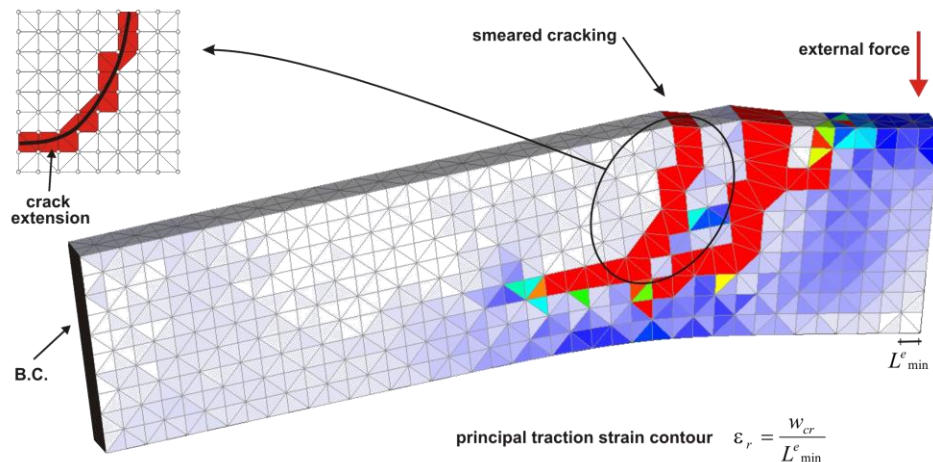
Figure 5.3 Smeared cracking concept (red elements represent the cracks extension)

Concluding, there are three relevant features that support the benefit of using the microplane model for the concrete constitutive definition. (i) By adopting the microplane material model, the material behaviour at the microscopic scale of observation is artificially incorporated at the macroscopic level. (ii) A simple constitutive uniaxial σ-ε relationship, defined at the microplane level, ensures very accurate macroscopic prediction of material behavior (Bažant & Oh, 1983). (iii) With regard to the general three-dimensional case, the microplane material model enables to include the initial and induced material anisotropy in a simple way (Ožbolt, Li & Kožar, 2001).

5.2   Microplane theory preliminaries

During the early phase of the theory development (Batdorf & Budianski, 1949), it was assumed that the stress vector, which acts on microplanes with a different spatial orientation, is the projection of the macroscopic stress tensor **σ** integrated at FE Gauss points. Due to the fact that the stress tensor holds the information on internal forces, the procedure was named *static constrain condition*. Later on, Bažant realized that in order to obtain the unique solution for softening, the static constraint should be replaced by the so-called *kinematic constraint condition* in which the microplane strain components are calculated by projection of the macroscopic strain tensor **ε** (Bažant & Caner, 2005). Moreover, the here proposed numerical formulation is based on the *relaxed kinematic constraint principle* (Ožbolt, Li & Kožar, 2001), which is an extension of the model proposed by Bažant et al. (2005) and will be appropriately discussed after some preliminary microplane assumptions.

5.2.1 Microplane coordinate system

In a general three-dimensional case the microplane outward unit normal vector $\mathbf{n}^\ell$ (5.2), associated to microplane ℓ, defines its spatial orientation on the discretized unit microsphere (Fig. 5.2).

$$\mathbf{n}^\ell = \left\{ n_1^\ell \quad n_2^\ell \quad n_3^\ell \right\}^{\mathbf{T}} \qquad \textbf{where} \quad \ell = 1,2,..n_p \tag{5.2}$$

The related microplane tangential unit vectors $\mathbf{m}^\ell$ and $\mathbf{k}^\ell$, defined as

$$\mathbf{m}^\ell = \left\{ m_1^\ell \quad m_2^\ell \quad m_3^\ell \right\}^{\mathbf{T}} \quad \textbf{and} \quad \mathbf{k}^\ell = \left\{ k_1^\ell \quad k_2^\ell \quad k_3^\ell \right\}^{\mathbf{T}} \qquad \textbf{where} \quad \ell = 1,2,..n_p , \tag{5.3}$$

are chosen in such way such that

$$\mathbf{k}^\ell = \mathbf{m}^\ell \times \mathbf{n}^\ell , \tag{5.4}$$

forming a local orthogonal coordinate system associated to microplane ℓ (Fig. 5.4).
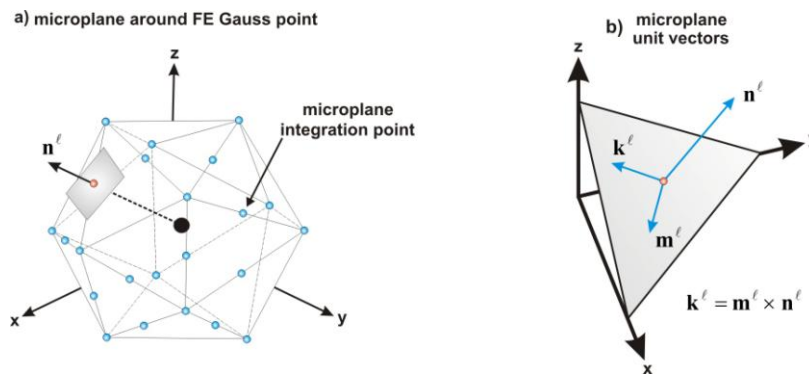
Figure 5.4 Microplane local coordinate system**: a)** microplanes and **b)** microplane unit vectors

5.2.2 Microplane strain components

The kinematic constraint principle allows to calculate the stain vector $\mathbf{e}^\ell$ from the macroscopic strain tensor $\boldsymbol{\varepsilon}$ as (Pivonka, Ožbolt, Lackner & Mang, 2004)

$$\mathbf{e}^\ell = \boldsymbol{\varepsilon} \cdot \mathbf{n}^\ell. \tag{5.5}$$

$\mathbf{e}^\ell$ can be further split into its normal component $\mathbf{e}_N^\ell$ as

$$\mathbf{e}_N^\ell = (\mathbf{e}^\ell \cdot \mathbf{n}^\ell)\, \mathbf{n}^\ell = e^\ell\, \mathbf{n}^\ell, \tag{5.6}$$

in which e^ℓ denotes the norm of the stain vector $\mathbf{e}_N^\ell$, and its tangential component $\mathbf{e}_T^\ell$ as

$$\mathbf{e}_T^\ell = \mathbf{e}^\ell - \mathbf{e}_N^\ell. \tag{5.7}$$

By substituting Eq. (5.5) into Eq. (5.6), the microplane normal component $\mathbf{e}_N^\ell$ is related to $\boldsymbol{\varepsilon}$ (Pivonka, Ožbolt, Lackner & Mang, 2004) through the second-order projection tensor $\mathbf{N}^\ell$ (5.8).

$$\mathbf{e}_N^\ell = (\mathbf{n}^\ell \cdot \boldsymbol{\varepsilon} \cdot \mathbf{n}^\ell)\, \mathbf{n}^\ell = (\mathbf{n}^\ell \otimes \mathbf{n}^\ell : \boldsymbol{\varepsilon})\, \mathbf{n}^\ell = (\mathbf{N}^\ell : \boldsymbol{\varepsilon})\, \mathbf{n}^\ell \tag{5.8}$$

Similarly, by inserting Eq. (5.5) into Eq. (5.7), the microplane strain component $\mathbf{e}_T^\ell$ can be also obtained from the macroscopic strain tensor $\boldsymbol{\varepsilon}$. In this case, the macro-micro transition is defined through the third-order projection tensor $\mathbf{T}^\ell$ given as

$$\mathbf{e}_T^\ell = \mathbf{n}^\ell \cdot \boldsymbol{\varepsilon} - (\mathbf{n}^\ell \cdot \boldsymbol{\varepsilon} \cdot \mathbf{n}^\ell)\, \mathbf{n}^\ell = (\mathbf{n}^\ell \cdot \mathbf{I} - \mathbf{n}^\ell \otimes \mathbf{n}^\ell \otimes \mathbf{n}^\ell) : \boldsymbol{\varepsilon} = \mathbf{T}^\ell : \boldsymbol{\varepsilon} \tag{5.9}$$

in which $\mathbf{I}$ denote the fourth-order unit tensor. Furthermore, the length $e_N^\ell = \mathbf{N}^\ell : \boldsymbol{\varepsilon}$ of $\mathbf{e}_N^\ell$ (normal to the microplane) can be decomposed as

$$e_N^\ell = e_V^\ell + e_D^\ell, \tag{5.10}$$

where e_V^ℓ denotes the volumetric part, given by

$$e_V^\ell = (1/3)\mathbf{1} : \boldsymbol{\varepsilon} = \mathbf{V}^\ell : \boldsymbol{\varepsilon}, \tag{5.11}$$

and e_D^ℓ denotes the deviatoric part defined as

$$e_D^\ell = e_N^\ell - e_V^\ell = \mathbf{N}^\ell : \boldsymbol{\varepsilon} - \mathbf{V}^\ell : \boldsymbol{\varepsilon} = \mathbf{D}^\ell : \boldsymbol{\varepsilon}. \tag{5.12}$$

In these expressions $\mathbf{V}^\ell$ and $\mathbf{D}^\ell$ are microplane second order projection tensors while $\mathbf{1}$ denotes the second order unit tensor.

Note that e_V^ℓ (5.11) does not depend on the microplane orientation (5.2). As a consequence, for a given Gauss point at which the macroscopic strain tensor $\boldsymbol{\varepsilon}$ is projected onto the surrounding microplanes, the volumetric strain components e_V^ℓ can be assumed as constant (5.13).

$$e_V^\ell = e_V = \text{const.} \tag{5.13}$$

Mention also that the tangential microplane strain vector $\mathbf{e}_T^\ell$ (5.9) can be decomposed into two (arbitrary) perpendicular strain components that lie on the microplane ℓ. It is important to point out that these tangential components may be interpreted as *shear microplane strain components*, usually denoted as $\mathbf{e}_M^\ell$ and $\mathbf{e}_K^\ell$. In accordance with the given share strains signature, the strain vector $\mathbf{e}_T^\ell$ can be furthermore decomposed as

$$\mathbf{e}_T^\ell = \mathbf{e}_M^\ell + \mathbf{e}_K^\ell, \tag{5.14}$$

where the part $\mathbf{e}_M^\ell$ is defined with

$$\mathbf{e}_M^\ell = (\mathbf{M}^\ell \cdot \mathbf{e}_T^\ell)\, \mathbf{M}^\ell = (\mathbf{M}^\ell \cdot \mathbf{T}^\ell : \boldsymbol{\varepsilon})\, \mathbf{M}^\ell = e_M^\ell\, \mathbf{M}^\ell \qquad \text{where} \quad \mathbf{M}^\ell = \frac{1}{2}(\mathbf{m}^\ell \otimes \mathbf{n}^\ell + \mathbf{n}^\ell \otimes \mathbf{m}^\ell), \tag{5.15}$$

while the part $\mathbf{e}_K^\ell$ with

$$\mathbf{e}_K^\ell = (\mathbf{K}^\ell \cdot \mathbf{e}_T^\ell)\, \mathbf{K}^\ell = (\mathbf{K}^\ell \cdot \mathbf{T}^\ell : \boldsymbol{\varepsilon})\, \mathbf{K}^\ell = e_M^\ell\, \mathbf{K}^\ell \qquad \text{where} \quad \mathbf{K}^\ell = \frac{1}{2}(\mathbf{k}^\ell \otimes \mathbf{n}^\ell + \mathbf{n}^\ell \otimes \mathbf{k}^\ell). \tag{5.16}$$

Tensors $\mathbf{M}^\ell$ and $\mathbf{K}^\ell$ are first-order projection tensors (Pivonka, Ožbolt, Lackner & Mang, 2004). Resuming, for a given FE Gauss point, the macroscopic strain tensor $\boldsymbol{\varepsilon}$ is projected on surrounding microplanes and then decomposed into the microplane volumetric e_V^ℓ, deviatoric e_D^ℓ and shear strain component $\mathbf{e}_M^\ell$ and $\mathbf{e}_K^\ell$, illustrated in Fig. 5.5.
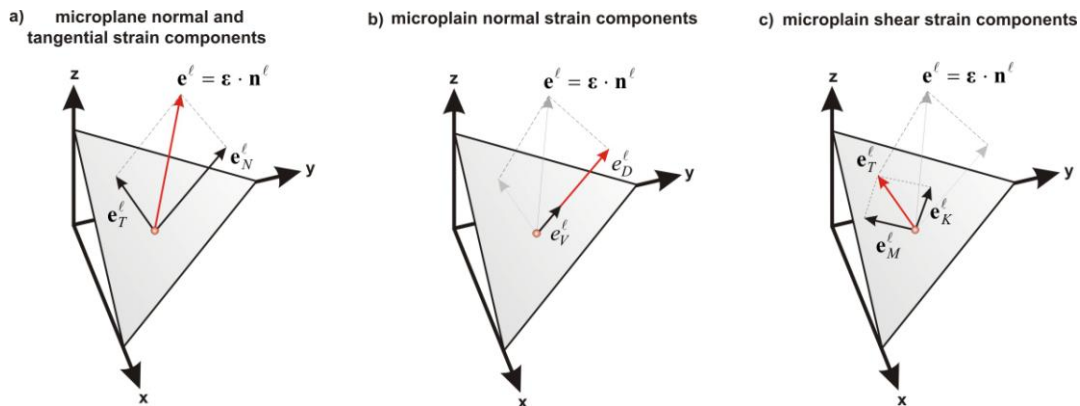
Figure 5.5 Microplane strain components: **a)** vectors and decompositions of **b)** normal and **c)** tangential components

5.2.3 *Microplane stress components*

For each microplane strain component (Fig. 5.5) an appropriate microplane stress component is obtained via microplane secant modules (Pivonka, Ožbolt, Lackner & Mang, 2004). Subsequently, the microplane stresses s_V, s_D^ℓ, s_M^ℓ and s_K^ℓ are calculated from e_V, e_D^ℓ, e_M^ℓ and e_K^ℓ, through the volumetric C_V, deviatoric C_D and shear microplane modules C_M and C_K, respectively (5.17).

$$s_V = C_V\, e_V$$
$$s_D^\ell = C_D\, e_D^\ell$$
$$s_M^\ell = C_M\, e_M^\ell \quad \text{and} \quad s_K^\ell = C_K\, e_K^\ell$$

(5.17)

In the proposed numerical formulation, the microplane *s-e* relationships are defined by means of microplane modules proposed by Ožbolt and Bažant (1996). Except for the region of volumetric compression, there are based on the *Mazar scalar damage theory* and defined with:

$$C_V = E_{V,0}(1-\omega_V),$$
$$C_D = E_{D,0}(1-\omega_D),$$
$$C_M = E_{M,0}(1-\omega_M) \quad \text{and} \quad C_K = E_{K,0}(1-\omega_K).$$

(5.18)

$E_{V,0}$, $E_{D,0}$, $E_{M,0}$ and $E_{K,0}$ are initial material modules (related to the state in which the material was undamaged) while ω_V, ω_D, ω_M and ω_K are the concrete *integrity parameters* related to the material damage at the microplane level. The integrity parameters (scalar values) are functions of microplane volumetric e_V, deviatoric e_D^ℓ and shear strain components $\mathbf{e}_M^\ell$ and $\mathbf{e}_K^\ell$ as:

$$\omega_V = 1 - e^{-\left|e_V/e_1\right|^m} \qquad \text{if} \qquad e_V \geq 0,$$
$$\omega_D = 1 - e^{-\left|e_D^\ell/e_1\right|^m} \qquad \text{if} \qquad e_D^\ell \geq 0,$$
$$\omega_D = 1 - e^{-\left|e_D^\ell/e_2\right|^n} \qquad \text{if} \qquad e_D^\ell < 0,$$

(5.19)

and

$$\omega_M = 1 - e^{-\left|e_T^\ell/e_5\right|^k} \quad \text{and} \quad \omega_K = 1 - e^{-\left|e_K^\ell/e_5\right|^k}.$$

(5.20)

The parameters e_1, e_2, e_3, e_4, e_5, m, n and k, are empirical parameters determined from the uniaxial compressive and tensile experiments. Note that e_5 is equal to e_3 if $e_V \geq 0$. On the other hand, if $e_V < 0$, e_5 is equal to $e_3 - e_4 e_V$. As one can note, the microplane shear components (5.20) depend on the volumetric strain components e_V through the empirical parameter e_5. This dependency introduces an additional scalar kinematic condition and

describes the microscopic frictional behavior on aggregate surface. Obviously, this is due to the influence of compression to the frictional behaviour. Now, in order to cover the complete range of possible deformations, the *s-e* relationship for volumetric compression is assumed as

$$C_V = E_{V,0}\left[\left(1+\left|\frac{e_V}{a}\right|\right)^{-p}+\left|\frac{e_V}{b}\right|^{q}\right]. \tag{5.21}$$

a, *b*, *p* and *q* are also empirical parameters but independent from the type of concrete under consideration. Namely, in this case there is no damage, so the scalar damage value ω_V is set equal to zero. Finally, the full range of microplane modules, given in Eq. (5.22) and Eq. (5.23), are obtained by introducing Eq. (5.19) and Eq. (5.20) into Eq. (5.18) and adding to them Eq. (5.21) for volumetric compression.

$$C_V = \begin{cases} E_{V,0}\exp\left[-\left|e_V/e_1\right|^{m}\right] & \text{if} \quad e_V \geq 0 \\ E_{V,0}\left[\left(1+\left|e_V/a\right|\right)^{-p}+\left|e_V/b\right|^{q}\right] & \text{if} \quad e_V < 0 \end{cases}$$

$$C_D = \begin{cases} E_{D,0}\exp\left[-\left|e_D^{\ell}/e_1\right|^{m}\right] & \text{if} \quad e_D^{\ell} \geq 0 \\ E_{D,0}\exp\left[-\left|e_D^{\ell}/e_2\right|^{n}\right] & \text{if} \quad e_D^{\ell} < 0 \end{cases} \tag{5.22}$$

$$C_M = \begin{cases} E_{M,0}\exp\left[-\left|e_M^{\ell}/e_3\right|^{k}\right] & \text{if} \quad e_M^{\ell} \geq 0 \\ E_{M,0}\exp\left[-\left|e_M^{\ell}/(e_3-e_4 e_V)\right|^{k}\right] & \text{if} \quad e_M^{\ell} < 0 \end{cases}$$

$$C_K = \begin{cases} E_{K,0}\exp\left[-\left|e_K^{\ell}/e_3\right|^{k}\right] & \text{if} \quad e_K^{\ell} \geq 0 \\ E_{K,0}\exp\left[-\left|e_K^{\ell}/(e_3-e_4 e_V)\right|^{k}\right] & \text{if} \quad e_K^{\ell} < 0 \end{cases} \tag{5.23}$$

Note that the microplane relationships s_M^{ℓ}-e_M^{ℓ} and s_K^{ℓ}-e_K^{ℓ} (5.23) have the same functions which are assumed to be symmetric (Fig. 5.6c). Also, according to the Eq. (5.21), when the concrete body is under volumetric compression, there is no material damage (Fig. 5.6a).
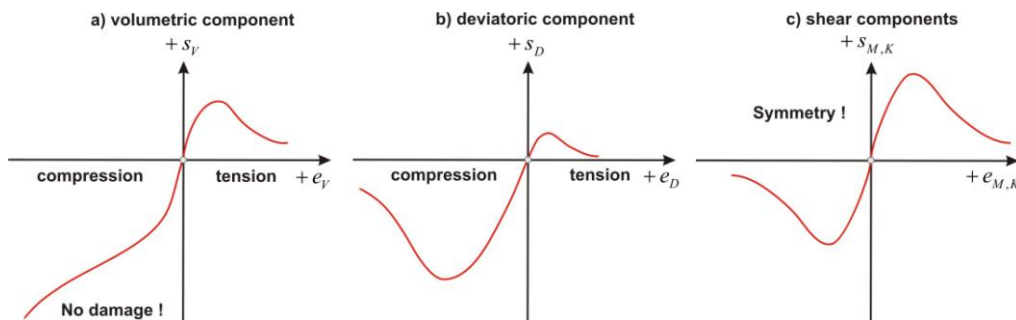
Figure 5.6 Qualitative illustration of the microplane stress-strain relationships (virgin load)

5.2.4 Macroscopic stress tensor

After retrieving the microplane stress components (5.17), the macroscopic stress tensor $\boldsymbol{\sigma}$ (2.92) is obtained by invoking the *principle of virtual work* (Kuhl & Ramm, 1998). In this case, the macroscopic internal work W^{macro} is approximated by the scalar product of macroscopic stress tensor $\boldsymbol{\sigma}$ and virtual variations $\delta\boldsymbol{\varepsilon}$, multiplied by the microsphere surfaces area (5.24).

$$W^{macro} = \frac{4\pi}{3}\boldsymbol{\sigma} : \delta\boldsymbol{\varepsilon} \tag{5.24}$$

On the other hand, the microscopic virtual work W^{micro} is obtained by adding the virtual work done by normal component s_N:

$$s_N\,\delta e_N = (s_V + s_D)\delta e_N\,, \tag{5.25}$$

to the tangential virtual work s_T:

$$s_T\,\delta e_T = (\sqrt{s_M^2 + s_K^2})\,\delta e_T\,, \tag{5.26}$$

and integrating the obtained sum over the domain of a unit sphere S (5.27).

$$W^{micro} = \int_S \left[s_N\delta e_N + s_T\delta e_T \right]dS \tag{5.27}$$

The equivalency of the stress work at the macro (5.24) and micro level (5.27) is defined by

$$\boldsymbol{\sigma} : \delta\boldsymbol{\varepsilon} = \frac{3}{4\pi}\int_S \left[s_N\delta e_N + s_T\delta e_T \right]dS\,, \tag{5.28}$$

or by decomposing s_N and s_T, as

$$\boldsymbol{\sigma} : \delta\boldsymbol{\varepsilon} = \frac{3}{4\pi}\int_S \left[(s_V + s_D)\,\delta e_N + s_M\delta e_M + s_K\delta e_K \right]dS\,. \tag{5.29}$$

For a discrete approximation of the unit sphere (Fig. 5.2), the microscopic virtual work W^{micro} is obtained by integration over the microplane area dS^{ℓ}. Since it is assumed that all microplanes have equal surface area, the RHS of Eq. (5.29) can be rewritten in discrete form. With a number n_m of microplanes used for the unit hemisphere discretization (Fig. 5.2), the microscopic stress works W^{micro} is defined as the sum of microplane contributions (5.30).

$$\boldsymbol{\sigma} : \delta\boldsymbol{\varepsilon} = 2\frac{3}{4\pi} \sum_{\ell=1}^{n_m} \underbrace{\left\{ \int_{S^\ell} \left[\ (s_V^\ell + s_D^\ell) \cdot \delta e_N^\ell + s_M^\ell \cdot \delta e_M^\ell + s_K^\ell \cdot \delta e_K^\ell \ \right] \mathrm{d}S^\ell \right\}}_{\text{Half of the total number of microplains}} \tag{5.30}$$

Since the strain component variations are associated to the variation of $\boldsymbol{\varepsilon}$ via

$$\delta e_N^\ell = \mathbf{N}^\ell : \delta\boldsymbol{\varepsilon},$$
$$\delta e_M^\ell = (\ \mathbf{M}^\ell \cdot \mathbf{T}^\ell) : \delta\boldsymbol{\varepsilon}, \tag{5.31}$$
$$\delta e_K^\ell = (\ \mathbf{K}^\ell \cdot \mathbf{T}^\ell) : \delta\boldsymbol{\varepsilon},$$

the macroscopic stress tensor $\boldsymbol{\sigma}$ (2.92) can be calculated by (Pivonka et al., 2004)

$$\boldsymbol{\sigma} = \sum_{\ell=1}^{n_m} \left\{ \frac{3}{2\pi} \int_{S^\ell} (s_V^\ell + s_D^\ell) \cdot \mathbf{N}^\ell \mathrm{d}S^\ell + \frac{3}{2\pi} \int_{S^\ell} s_M^\ell \, \mathbf{M}^\ell \cdot \mathbf{T}^\ell \mathrm{d}S^\ell + \frac{3}{2\pi} \int_{S^\ell} s_K^\ell \, \mathbf{K}^\ell \cdot \mathbf{T}^\ell \mathrm{d}S^\ell \right\}. \tag{5.32}$$

The former Eq. denotes the macroscopic state of stress at the FE Gauss point i.e. continuum point (*Chapter 2 – 2.1 Introduction*). To stress out an important fact, the former Eq. should be rewritten in indicial notation. For this purpose, the volumetric strain component is expressed as

$$e_V = \frac{\varepsilon_{kk}}{3}, \tag{5.33}$$

the deviatoric strain components as

$$e_D^\ell = n_i^\ell \, n_j^\ell \, \varepsilon_{ij} - e_V, \tag{5.34}$$

and the shear stain components as

$$e_M^\ell = m_i^\ell \, n_j^\ell \, \varepsilon_{ij} \qquad \text{and} \qquad e_K^\ell = k_i^\ell \, n_j^\ell \, \varepsilon_{ij}. \tag{5.35}$$

By substituting these relations into Eq. (5.31), Eq. (5.30) can be rewritten as

$$\sigma_{ij} = \sum_{\ell=1}^{n_m} \left\{ \frac{3}{2\pi} \int_{S^\ell} \left[n_i^\ell n_j^\ell s_V + n_i^\ell n_j^\ell s_D^\ell + \frac{1}{2}(m_i^\ell n_j^\ell + m_j^\ell n_i^\ell) \, s_M^\ell + \frac{1}{2}(k_i^\ell n_j^\ell + k_j^\ell n_i^\ell) \, s_K^\ell \right] \mathrm{d}S^\ell \right\}. \tag{5.36}$$

The given integrals are linear in stress and thus appropriate for *incremental stress analyses* which are required for non-linear problems but also for problems in which the material under consideration possess memory of its initial (virgin) state (*path-dependence*). Furthermore, Carol and Bažant (1997) suggest that the term $n_i n_j$ (placed next to the deviatoric stress component s_D) should be replaced by $n_i n_j - \delta_{ij}/3$. The magnitude of the new term $-\delta_{ij}/3$ is proportional to the difference between the tensile and compressive deviatoric strength. Bažant shows

that the new term has no effect in the elastic response and that its presence can be evident only in inelastic region. For this region the absence of the term can produce negative energy dissipation which is especially evidenced during closed strain cycles. Obviously, the pathological behavior breaches the restriction imposed by the *Second Law of Thermodynamics* (*Chapter 2 – 2.4 Thermodynamic restrictions*). However, in the proposed numerical formulation, the additional term $-\delta_{ij}/3$ is suppressed by setting the ratio of initial deviatoric and volumetric microplane modules to be less than one. Furthermore, in order to abide by the thermodynamic restriction, the shear microplane strength is assumed to be greater than the deviatoric compressive strength (Ožbolt, Li & Kožar, 2001). Finally, note that the term absence is also compensated by the shear resistance dependency on volumetric strain.

5.2.5 *Microplane tangent stiffness*

Ožbolt and Bažant (1992) demonstrated that the components of the tangent stiffness tensor C_{ijkl}^{m} can be calculated by substituting Eq. (5.33), Eq. (5.34), Eq. (5.35) and the incremental form of Eq. (5.18) into the incremental form of Eq. (5.36). Accordingly, C_{ijkl}^{m} arias as

$$C_{ijkl}^{\mathrm{m}} = \sum_{\ell=1}^{n_m} \left\{ \frac{3}{2\pi} \int_S \left[\begin{array}{l} n_i^\ell n_j^\ell n_r^\ell n_s^\ell C_D + \dfrac{1}{3} n_i^\ell n_j^\ell \delta_{rs}(C_V - C_D) + \ldots \\[2mm] \qquad \ldots + \dfrac{1}{4}(m_i^\ell n_j^\ell + m_j^\ell n_i^\ell)\,(m_r^\ell n_s^\ell + m_s^\ell n_r^\ell)\,C_M + \ldots \\[2mm] \qquad\qquad \ldots + \dfrac{1}{4}(k_i^\ell n_j^\ell + k_j^\ell n_i^\ell)\,(k_r^\ell n_s^\ell + k_s^\ell n_r^\ell) C_K \end{array} \right] \mathrm{d}S^\ell \right\}, \quad (5.37)$$

and enables to form the incremental relationship

$$\mathrm{d}\sigma_{ij} = C_{ijkl}^{\mathrm{m}}\,\mathrm{d}\varepsilon_{kl}, \tag{5.38}$$

which is necessary for non-linear analysis.

5.3   **Microplane stress tensor**

The very good performance of the microplane model for lies behind its conceptual simplicity. Namely, it is based on the possibility to retrieve direct physical meaning from the microplane stress components. Particularly, with various microplane spatial orientations, the normal and shear microplane components can be easy related to physical phenomena such as microstructure aggregate friction and strength or material yield limit at the three-dimensional microstructural level. However, it ought to be pointed out that the physical interpretation is justified only if the microplane stresses are true stresses (Cauchy stress). As already discussed (*Chapter 2 – 2.2.5 Cauchy's stress theory*), PK2 is not quite suitable for this purpose. Note that this is a valid topic only if the expected macroscopic strains are relatively large. On the other hand, if the generated strains do

not cause the relevant presence of non-linear terms in the strain-displacement matrix **B** (3.76), the 2nd Piola-Kirchhoff stress tensor will be reduced to a Cauchy stress tensor **σ** (5.39).

$$\mathbf{F} \approx \mathbf{I} \quad ; \quad \boldsymbol{\sigma} \approx S \qquad \text{where} \qquad \boldsymbol{\sigma} = \frac{1}{\det \mathbf{F}} \mathbf{F} \, S \, \mathbf{F}^{\mathrm{T}}. \tag{5.39}$$

On the other hand, if the macroscopic strains are relatively large, the presence of PK2 is inevitable due to the fact that the force equilibrium at the current configuration is related to stresses in the reference configuration (*two-point tensor*). This is the case of the numerical investigation under consideration. To approach the problem by regarding large-strain generalization of the microplane model, some findings by Bažant et al. (2000a) will be paraphrased hereafter.

To illustrate the mentioned stress differences, a comparison between PK2 (2.95) and the Cauchy stress tensor (2.92), generated from the same deformation on a single microplane, will be performed. For the sake of simplicity, suppose a deformation without material rotation. In this case, the material rotation matrix **R** will be equal to identity matrix **I** and the stress and strain tensor will be coaxial. Furthermore, assume that the local microplane axes have the same direction as the main orthogonal stress components. The spatial position of the considered microplane is defined by the angle of 45 degrees lying (Fig. 5.7). For this scenario, the deformation gradient matrix **F** (2.37) collects only principal stretch values such that (Shabana, 2008)

$$\mathbf{F} = \begin{bmatrix} \lambda_1 & 0 & 0 \\ 0 & \lambda_2 & 0 \\ 0 & 0 & \lambda_3 \end{bmatrix} = \mathbf{U}. \tag{5.40}$$

The deformation produces a true Cauchy stress tensor **σ** with only diagonal components Eq. (5.41).

$$\boldsymbol{\sigma} = \begin{bmatrix} \sigma_1 & 0 & 0 \\ 0 & \sigma_2 & 0 \\ 0 & 0 & \sigma_3 \end{bmatrix} \tag{5.41}$$

Since $S = J \, \mathbf{F}^{-1} \, \boldsymbol{\sigma} \, \mathbf{F}^{-\mathrm{T}}$, the given deformation gradient **F** (5.40), together with the related Cauchy stress tensor **σ** (5.42), produce PK2 filled only by diagonal components as

$$S = \begin{bmatrix} \dfrac{\sigma_1 \lambda_2 \lambda_3}{\lambda_1} & 0 & 0 \\ 0 & \dfrac{\sigma_2 \lambda_3 \lambda_1}{\lambda_2} & 0 \\ 0 & 0 & \dfrac{\sigma_3 \lambda_1 \lambda_2}{\lambda_3} \end{bmatrix}. \tag{5.42}$$

The shear component S_{12} is equal to (Bažant et al., 2000a)

$$S_{12} = \frac{S_1 - S_2}{2} = \frac{\sigma_1\left(\frac{\lambda_2\lambda_3}{\lambda_1}\right) - \sigma_2\left(\frac{\lambda_3\lambda_1}{\lambda_2}\right)}{2},$$ (5.43)

while the component σ_{12} is different and equal to

$$\sigma_{12} = \frac{\sigma_1 - \sigma_2}{2}.$$ (5.44)

By analyzing the normal components, the PK2 component S_{octa} can be expressed as

$$S_{octa} = \frac{\sigma_1\left(\frac{\lambda_2\lambda_3}{\lambda_1}\right) + \sigma_2\left(\frac{\lambda_3\lambda_1}{\lambda_2}\right) + \sigma_3\left(\frac{\lambda_1\lambda_2}{\lambda_3}\right)}{3},$$ (5.45)

while the Cauchy stress component σ_{octa} is again different and equal to

$$\sigma_{octa} = \frac{\sigma_1 + \sigma_2 + \sigma_3}{3}.$$ (5.46)

Note that the Cauchy component σ_{octa} can be physically interpreted as hydrostatic pressure (5.46) which is an important data for pressure-sensitive material such as concrete. On the other hand, the normal PK2 component S_{octa} will describe the same result but only for relatively small strains (5.39). For relatively large strains, S_{octa} (5.45) will have no direct physical meaning.
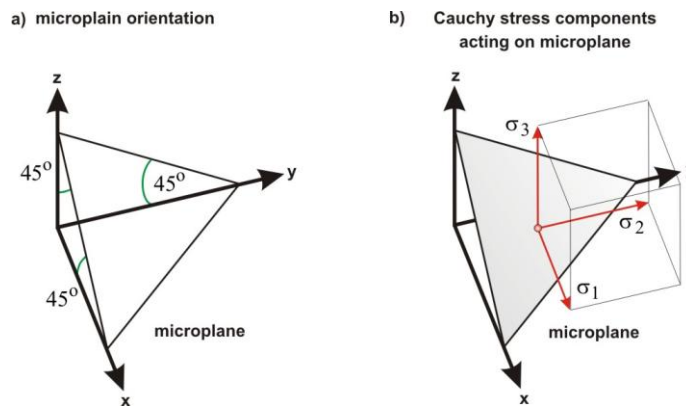
Figure 5.7 Considered microplane: **a)** spatial position and **b)** principal stress components

As discussed by Bažant et al. (2000a), with the strains growing tendency the PK2 components will progressively diverge from the corresponding components of the Cauchy stress tensor. This is especially evident in case of concentrated impact loadings (blast loading) where the factor of difference between **σ** and **S** can reach the value of two and even more.

Following the above-mentioned, the slip or stick frictional conditions can be hardly interpreted by adopting *S* (as well as the hardening and softening law on the microplane) and only the Cauchy true stress tensor **σ** will give real physical meaning. Nevertheless, due to the fact that the Cauchy stress tensor **σ** is not work conjugated to the here adopted Green-Lagrangian strain measure *E*, its essential form is not adequate for the constitutive description. Namely, for materials like concrete that retain information about deformation history, the constitutive description should be formulated in respect to the material state in the reference configuration. Therefore, the adequate stress tensor will be the true Cauchy stress tensor **σ** rotated back to the reference configuration (Bažant et al., 2000a). This is the formerly introduced *back-rotated Cauchy stress tensor s* (Belytschko, Liu & Moran, 2001). The backward rotation to the reference frame is carried out with the material rotation matrix **R** as

$$s = \mathbf{R}^{\mathrm{T}} \boldsymbol{\sigma} \, \mathbf{R}. \tag{5.47}$$

Note that when there is no material rotation (**R**=**I**), the back-rotated Cauchy stress tensor *s* is equal to the Cauchy stress tensor **σ**. The same principle (5.47) can be applied to Kirchhoff stress tensor (2.94), producing the *back-rotated Kirchhoff stress tensor* $\boldsymbol{\tau}_r$ (5.48).

$$\boldsymbol{\tau}_r = \mathbf{R}^{\mathrm{T}} J \boldsymbol{\sigma} \, \mathbf{R} \quad \text{where} \quad J \boldsymbol{\sigma} = \text{Kirchhoff stress tensor} \tag{5.48}$$

In this case, if **R**=**I** the back-rotated Kirchhoff stress tensor $\boldsymbol{\tau}_r$ will be equal to **σ**/*J*. The physical meaning of $\boldsymbol{\tau}_r$ can be simply drawn by dividing it by *J*. Since the tensor invariant are unaffected by rotation, for both tensors, i.e. *s* in Eq. (5.47) and $\boldsymbol{\tau}_r$ in Eq. (5.48), the physical meaning is not jeopardized.

For the numerical description covered by the thesis, the concrete pressure sensitivity is especially emphasized. For this reason the used stress tensor should refer to the initial configuration (5.46). Namely, such tensor has a clear physical meaning and makes the phenomenological interpretation of shear and normal microplane stress components possible (as well as of the hydrostatic pressure on the related microplane). Provided that the real pressure values on the microplanes can be assigned, the microplane material model will be able to simulate the complex concrete high-pressure ductile response and, on the other hand, it's low-pressure brittle failure (Bažant et al., 2000a).

In conclusion, the control of frictional effects, yield and strength material limit, and hardening or softening on the microplane level is easy when performed by a stress tensor that complies with the abovementioned requirements. So, the stress tensor that fulfills such conditions and is also adopted in the proposed numerical formulation is the back-rotated Cauchy stress tensor *s* (2.96).

5.4   Microplane strain tensor

To formulate the constitutive relations for concrete, a strain measure that will be work-conjugated to the discussed s and τ tensors should be found (2.100). Two problems arise from this task (Bažant et al., 2000a). The first problem is that the required strain measure should depend neither on the current deformation nor on the deformation path that leads to the current continuum state. In other words, the strain tensor that is work-conjugated to the back-rotated Cauchy stress tensor s (or to the back-rotated Kirchhoff stress tensor τ) will be *nonholonomic* (path-dependent). As showed by Bažant (1997), the appropriately strain tensor which is related to the back-rotated Cauchy stress tensor s (here denoted by e), can be obtained in an incremental form. The tensor derivation starts with the variational equivalence between the work of PK2, which is related to E (2.72), and the stress work performed by Cauchy true stress tensor σ that is conjugated to the unknown strain tensor e (5.49).

$$\delta e : \boldsymbol{\sigma} = \delta E : S \tag{5.49}$$

The back-rotated Cauchy stress tensor s can be introduced in Eq. (5.49) by expressing $\boldsymbol{\sigma}$ according to Eq. (5.47). Furthermore, PK2 tensor in the former Eq. can be represented in terms of $\boldsymbol{\sigma}$ through Eq. (5.39). Congruently, the given operations will produce the equivalence:

$$\delta e : \mathbf{R}^{\mathrm{T}} J \boldsymbol{\sigma} \mathbf{R} = \delta E : \mathbf{F}^{-1} \boldsymbol{\sigma} \, \mathbf{F}^{-\mathrm{T}} . \tag{5.50}$$

Following to the polar decomposition theorem, $\mathbf{F}$ can be in addition expressed as $\mathbf{RU}$ and, since $\mathbf{F}^{-1}=\mathbf{U}^{-1}\mathbf{R}^{\mathrm{T}}$ and $\mathbf{F}^{-\mathrm{T}}=\mathbf{RU}^{-1}$, the former expression can be than rewritten as (Bažant et al., 2000a)

$$\delta e : s = \delta E : \mathbf{U}^{-1} s \ \mathbf{U}^{-1} J \qquad \text{where} : s = \mathbf{R}^{\mathrm{T}} \boldsymbol{\sigma} \mathbf{R}, \tag{5.51}$$

or in indicial notation as

$$\delta e_{ij} \, s_{ij} = \delta E_{kl} \, Y_{ki} \, Y_{jl} \, s_{ij} \, J \qquad \text{where} : \mathbf{Y} = \mathbf{U}^{-1} . \tag{5.52}$$

This Eq. should be valid for all s and it will be true if:

$$\delta e_{ij} = Y_{jl} \, \delta E_{lk} \, Y_{ki} \, J . \tag{5.53}$$

Being

$$\delta E = \frac{\delta (\mathbf{UU})}{2}, \tag{5.54}$$

after replacing strain variations δ in Eq. (5.52) to differential d, such that

$$\mathrm{d} e_{ij} = Y_{jl} \, \mathrm{d} E_{lk} \, Y_{ki} \, J , \tag{5.55}$$

the incremental strain tensor de (Bažant et al., 2000a) can be obtained as follows (5.56).

$$d\boldsymbol{e} = \mathbf{U}^{-1} d\boldsymbol{E} \ \mathbf{U}^{-1} J = (J/2) \ \mathbf{U}^{-1} (d\mathbf{U} \ \mathbf{U} + \mathbf{U} \ d\mathbf{U}) \mathbf{U}^{-1} = (J/2) \ \mathbf{U}^{-1} (\mathbf{U}^{-1} d\mathbf{U} + d\mathbf{U} \ \mathbf{U}^{-1})$$

$$d\boldsymbol{e} = J \operatorname{sym}(\mathbf{U}^{-1} d\mathbf{U}) \tag{5.56}$$

If the principal strain axes do not rotate ($\mathbf{R}=\mathbf{I}$), the integration of the former Eq. will produce

$$\boldsymbol{e} = \int \begin{bmatrix} \lambda_2 \lambda_3 \, d\lambda_1 & 0 & 0 \\ 0 & \lambda_3 \lambda_1 \, d\lambda_2 & 0 \\ 0 & 0 & \lambda_1 \lambda_2 \, d\lambda_3 \end{bmatrix}, \tag{5.57}$$

where the RHS cannot be explicitly integrated if the stretch axes are not fixed. In other words, the derived strain tensor $\boldsymbol{e}$ is nonholonomic i.e. path-depended. Similarly, the variational equality

$$\delta \boldsymbol{\xi} : \boldsymbol{\tau} = \delta \boldsymbol{E} : \boldsymbol{S}, \tag{5.58}$$

will lead to the incremental strain tensor $d\boldsymbol{\xi}$ work conjugated to $\boldsymbol{\tau}$ (5.59).

$$d\boldsymbol{\xi} = \mathbf{U}^{-1} d\boldsymbol{E} \ \mathbf{U}^{-1} = (1/2) \ \mathbf{U}^{-1} (d\mathbf{U} \ \mathbf{U} + \mathbf{U} \ d\mathbf{U}) \mathbf{U}^{-1} = (1/2) \ \mathbf{U}^{-1} (\mathbf{U}^{-1} d\mathbf{U} + d\mathbf{U} \ \mathbf{U}^{-1})$$

$$d\boldsymbol{\xi} = \operatorname{sym}(\mathbf{U}^{-1} d\mathbf{U}) \tag{5.59}$$

In contrast to Eq. (5.56), $d\boldsymbol{\xi}$ is explicitly integrable and as such it is path-independent (5.60).

$$\boldsymbol{\xi} = \int \begin{bmatrix} d\lambda_1/\lambda_1 & 0 & 0 \\ 0 & d\lambda_2/\lambda_2 & 0 \\ 0 & 0 & d\lambda_3/\lambda_3 \end{bmatrix} = \begin{bmatrix} \ln \lambda_1 & 0 & 0 \\ 0 & \ln \lambda_2 & 0 \\ 0 & 0 & \ln \lambda_3 \end{bmatrix} \tag{5.60}$$

Note that the generate strain measure coincides with the previously introduced (2.75) logarithmic Henky strain tensor $\boldsymbol{H}$ (*Chapter 2 – 2.2.4.2 Material strain tensors*). The path-independency of $\boldsymbol{\xi}$ is preserved if the principal strain axes do not rotate ($\mathbf{R}=\mathbf{I}$). However, due to the fact that the principal strain axes usually rotate (eigenvectors of $\boldsymbol{\xi}$), the derived strain measure is not suitable for the formulation of the constitutive relations for concrete under impact load. Also, for materials like concrete which suffer damage phenomena, the requirement for preserving the memory about its virgin state plays a redundant importance for the constitutive description of such materials. The aforementioned can be summarized by quoting Bažant et al. (2000a).

"...The path-dependence destroys memory of the initial virgin state of the material..."

Furthermore, the second problem, representing a hindrance to the quest for a suitable strain measure, is the necessity for physical interpretations of strain components on differently oriented microplanes (Fig. 5.5). Particularly, the generalization of the microplane model for finite strain produces the need for physical interpretation of normal $\mathbf{e}_N$ and tangential $\mathbf{e}_T$ strain components. To obtain the generalization, the microplane strain components should meet the following requirements:

1st Requirement: *The normal strain component* $\mathbf{e}_N^\ell$ *must uniquely describe the stretching of the material line segment that is normal to microplane in the initial configuration.*

2nd Requirement: *The tangential strain components* $\mathbf{e}_M^\ell$ *and* $\mathbf{e}_K^\ell$ *must uniquely describe the change of angles between two initially orthogonal material line segments on the microplane.*

In other words, the microplane strain should be independent on the starching of the material line segment that lies on the initial microplane. An example of the requirement can be illustrated by analyzing the strain components on a microplane defined with the unit normal vector $\mathbf{n}=\left\{1/\sqrt{2} \quad 1/\sqrt{2} \quad 0\right\}^{\mathrm{T}}$. In this case, the Henky normal strain component H_N is

$$H_N = n_i\, n_j\, H_{ij} = \frac{H_{11} + H_{22}}{2} = \frac{1}{2}(\ln \lambda_1 + \ln \lambda_2) = \ln \sqrt{\lambda_1 \lambda_2}\,. \tag{5.61}$$

Let's compare the former strain component H_N with the normal component E_N (5.62) related to the Green-Lagrangian strain tensor $\boldsymbol{E}$ (2.73). The comparison will be appropriately justified later on.

$$E_N = n_i\, n_j\, E_{ij} = \frac{E_{11} + E_{22}}{2} = \frac{1}{4}(\lambda_1^2 + \lambda_2^2 - 2) \tag{5.62}$$

As Malvern proved (1969), the Green-Lagrangian strain tensor $\boldsymbol{E}$ produces a stretching E_N in the normal direction given by

$$E_N = \frac{1}{2}(\lambda_N^2 - 1). \tag{5.63}$$

At this point the notation Ξ should be introduced in order to represent the ratio of the principal stretching axes λ_1/λ_2. By bearing the given notation, λ_1 can be related to the normal stretching value λ_N through

$$\lambda_1 = \lambda_N \sqrt{\frac{2}{1 + \Xi^2}}\,. \tag{5.64}$$

Substituting Eq. (5.64) into Eq. (5.61), the Henky stretching value H_N, for the normal direction $\mathbf{n}$ of the given microplane, can be calculated as

$$H_N = \ln(\lambda_1 \sqrt{\Xi}) = \ln\left(\sqrt{\frac{2\Xi}{1 + \Xi^2}}\, \lambda_N\right). \tag{5.65}$$

An important conclusion can be drawn by comparing Eq. (5.62) and Eq. (5.65). The Henky normal component H_N depends on the stretching value λ_N but also on the ratio Ξ. Respect to the 1st requirement, Henky strain measure evidently breaches the prescribed condition. However, it would be a valid strain measure if the influence of Ξ is irrelevant. Well, according to Bažant et al. (2000a), it is not.

On the other hand, Eq. (5.65) illustrates that the normal stretching value E_N is immune to the ratio Ξ. Pursuant to the 1st requirement; this fact justifies the consideration of E and gives it seniority over other strain measures considered for the development of microplane constitutive relations.

After identifying E as an appropriated candidate for the constitutive definition, it should be also determine if the shear strain components fit into the 2nd requirement. For this purpose, assume a microplane on which the shear strains γ_{xy} and γ_{xz} are related to local microplane axes by subscripts x, y and z. These shear strains should uniquely define the shear angles θ_{xy} and θ_{xz} according to the 2nd requirement. Malvern demonstrated (1969) that the shear angles can be calculated from the strain components as:

$$\theta_{xy} = \arctan\left(\frac{(1+2E_x)\,(1+2E_y)}{4E_{xy}^2} - 1 \right)^{-1/2} \quad \text{and} \quad \theta_{xz} = \arctan\left(\frac{(1+2E_x)\,(1+2E_z)}{4E_{xz}^2} - 1 \right)^{-1/2} . \quad (5.66)$$

As the shear angles are here expressed only in terms of strain components, as well as the request contained in the 1st requirement, the Green-Lagrange strain tensor E fulfill also the 2nd requirement. In the case of Henky strain measure H, the shear angles are not expressed in terms of strain components on the related microplane (Bažant et al., 2000a). For this purpose, the shear angles are connected with the share angels on other microplanes and to stretches in other directions. It follows that the Henky strain measure fails to fulfill the conditions prescribed by the 1st and 2nd requirement. Concluding, it seems that the Green-Lagrangian strain tensor (2.73) is an appropriate choice for the microplane model applied to replicate the concrete response under high-energy impact loadings. In fact, according to the 1st and 2nd requirement, the components of E are sufficient to uniquely define the deformation on the microplane. However, being the metric of the Green-Lagrangian tensor quadratic, and the equilibrium conditions on the microplane linear, the work-conjugacy becomes a problem which should be examine (Bonet & Wood, 1997).

According to the abovementioned, an inevitable question should be answered: May the Green-Lagrangian strain tensor E be used and related to the back-rotated Cauchy stress tensor s ? If yes, possible side effects should be examined.

5.4.1 Unique correspondence to conjugate pairs

For a non-conjugated stress-strain pairs, the unique compliance with the conjugate constitutive law should be investigated (Bažant et al., 2000a). The non-conjugated law, which is here under consideration, can be formulated by introducing the tensorial function ψ with E as an argument (5.67).

$$s = \psi(E) \tag{5.67}$$

The law must be tested for correspondence with the conjugate constitutive law given by

$$S = \varphi(E), \tag{5.68}$$

in which φ denotes another tensorial function. The problem can be now formulated as follows. The non-conjugated law in Eq. (5.67) is admissible if the tensorial function ψ is uniquely related to the tensorial function φ, provided that this relation does not involve any material rotation (5.69).

$$\varphi(\boldsymbol{E}) \xleftrightarrow{\ \mathbf{R}=?\ } \psi(\boldsymbol{E}) \tag{5.69}$$

The requisite is examined by expressing the conjugate law in Eq. (5.68) in terms of $\boldsymbol{s}$. Substituting Eq. (5.47) in Eq. (5.39); the given definition (5.67) may be formulated by expressing $\boldsymbol{\sigma}$ in terms of φ as

$$\boldsymbol{\sigma} = J^{-1}\,\mathbf{F}\,\varphi(\boldsymbol{E})\,\mathbf{F}^{\mathrm{T}}. \tag{5.70}$$

According to Eq. (2.51), and by recalling that $\mathbf{U} = \sqrt{\mathbf{I}+2\boldsymbol{E}} = \mathbf{U}(\boldsymbol{E})$, the former Eq. can be rewritten as

$$\boldsymbol{\sigma} = J^{-1}\,\mathbf{R}\,\mathbf{U}(\boldsymbol{E})\,\varphi(\boldsymbol{E})\,\mathbf{U}(\boldsymbol{E})\mathbf{R}^{\mathrm{T}}. \tag{5.71}$$

The tensor $\boldsymbol{s}$ is obtained by multiplying Eq. (5.71) by $\mathbf{R}^{\mathrm{T}}$ from the left and by $\mathbf{R}$ from right side (5.72).

$$\boldsymbol{s} = J^{-1}\,\mathbf{U}(\boldsymbol{E})\,\varphi(\boldsymbol{E})\,\mathbf{U}(\boldsymbol{E}) \quad \text{where} \quad \psi(\boldsymbol{E}) = J^{-1}\,\mathbf{U}(\boldsymbol{E})\,\varphi(\boldsymbol{E})\,\mathbf{U}(\boldsymbol{E}) \tag{5.72}$$

It is now clear that the correspondence to conjugate constitutive law is satisfied:

$$\varphi(\boldsymbol{E}) = \mathbf{U}^{-1}(\boldsymbol{E})\,J\,\psi(\boldsymbol{E})\,\mathbf{U}^{-1}(\boldsymbol{E}) \tag{5.73}$$

since the given relation (5.73) uniquely defines the relation between the tensorial functions φ and ψ and it is not affected by material rotation (5.69).

5.4.2 Micro-macro constrains

After having tested the compliance with the conjugate constitutive law, the conjugacy between the micro and macro constraints should be also examined. For this purpose, the chronology of computations necessary for obtaining the macroscopic stress tensor, are here resumed. (i) On the basis of the macroscopic train tensor $\boldsymbol{E}$, the microplane strain components (Fig. 5.5) are calculated according to the kinematic constrains condition. (ii) The non-conjugated microplane stress components are calculated in accordance with the microplane constitutive laws (5.17). (iii) The macroscopic stress tensor is obtained following to the principle of virtual work (5.29).

The third step directly implies that the macroscopic strain components $\boldsymbol{E}$ and the microplane strain components $\mathbf{e}$ are conjugated to the Cauchy stress tensor $\boldsymbol{\sigma}$. The mentioned apparently introduces an additional kinematic condition. In other words, the microplane strain components are not only the projection of the macroscopic strain tensor but they are also the projection of the strain tensor on the microplane. It can be said that the

additional condition is a "*ghost*" kinematic condition due to the fact that the microplane can have only one kinematic constrain. Actually, such constrain can be trivially disproved. Namely, if the microplane strain components are defined by the projection of the macroscopic strain tensor E then, by definition, the microplane strain components will be obtained by projecting the strain tensor e that lies on that microplane. In short (Bažant et al., 2000a):

"...If the kinematic micro-macro constraint is imposed for one type of strain measure, then the kinematic constraint automatically holds for any type of strain measure..."

In summary, from the perspective of work-conjugacy, an appropriate strain measure for the adopted stress tensor s is the e strain tensor (5.57). However, the nonholonomic property of e reflects its path-dependency and makes it unusable for materials like concrete that retain the information on their initial state (virgin state). Furthermore, the tendency to preserve the strain objectivity on the microplane rejects the work-conjugate strain tensors as possible strain measure. The requirement to fully and uniquely describe the stretch of a material line segment (initially normal to the microplane), and to retain the true shear angle, is met only by the Green-Lagrangian strain tensor E (2.73).

In conclusion, in order to preserve the physical meaning of the microplane stress components, and to dispose with an objective microplane strain measure (immune to deformations on other microplanes), it can be deduced that a compromise is inevitable. Congruently, in the proposed numerical formulation the constitutive description is based on the back-rotated Cauchy stress tensor s and the Green-Lagrangian strain tensor E which are not work-conjugated. However, only in this manner the microplane model simplicity and its conceptual clarity can be preserved. On the other hand, it should be pointed out that even if the non-conjugated stress-strain pairs are used, their admissibility can be justified by testing the unique correspondence condition to another work-conjugate law and the unique micro-macro cinematic transition. As already discussed, those requirements have been met.

5.5 Ψ - discontinuity function

Based on the original Bažant and Prat's (BP) model (1987 & 1988), the formulation adopted in the present numerical investigation is enriched with the so-called *relaxed kinematic constraint principle* (Ožbolt, Li & Kožar, 2001). Namely, the original model displays pathological behavior for dominating tensile damage (tensile softening). For this type of loading, the pathological behaviour was evidenced by an unrealistic lateral extension (negative Poisson ration). For the purpose of illustrating the extended version of the model, which corrects the mentioned non-physical prediction, the basis of the original BP model will be hereafter presented.

5.5.1 BP model - pathological behavior

As Jirásek showed (1993), the pathological behavior of the BP model lies in the split of the normal microplane components into their volumetric and deviatoric parts rather than into microplane kinematic constraint. To illustrate the reason of this pathological expansion, which has been identified in concrete subject to tension loadings, consider a simple example where a two-dimensional specimen is loaded in a uniaxial tension (Fig. 5.8a). For the sake of simplicity, assume a plane stress analysis for a linear elastic material response and two microplanes (*x* and *y*) which are coaxial with the global rectangular coordinate axes (Ožbolt, Li & Kožar, 2001).
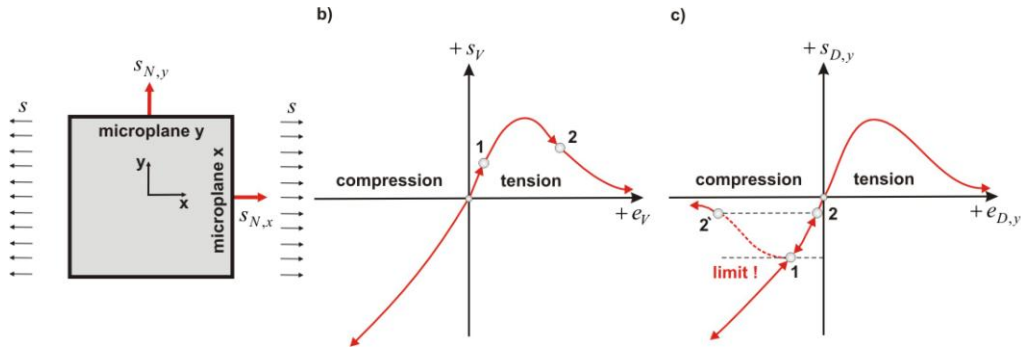
Figure 5.8 Microplane in uniaxial tension: **a)** load, **b)** volumetric and **c)** deviatoric stress-strain components

Furthermore, focus on the microplane perpendicular to the loading direction where the lateral expansion is expected. For the given scenario, the BP model requires the normal stress component to be split into its volumetric and deviatoric part as

$$s_{N,y} = s_V + s_{D,y}, \tag{5.74}$$

and the microplanes strain component to be split accordantly as

$$e_{N,y} = e_V + e_{D,y}. \tag{5.75}$$

Note that the condition

$$s_y = s_{N,y} = 0 \tag{5.76}$$

should be fulfilled. Approximately at point 1 in Fig. 5.8b the volumetric strain component is given by

$$e_V = (1/3)(1 - 2\upsilon)\, e_x, \tag{5.77}$$

and the deviatoric strain components by

$$e_{D,y} = -(1/3)(1 - \upsilon)\, e_x. \tag{5.78}$$

If $e_x > 0$ the deviatoric strain $e_{D,y}$ and deviatoric stress $s_{D,y}$ on the *y* microplane will be negative denoting compression state. Now, suppose that the given loading causes the vertical crack opening (crack state). In that case e_x will tend to infinity and the volumetric s_V and deviatoric s_D stresses will drop to 0.

In the BP model the volumetric s_V and deviator s_D stresses (for virgin load) are calculated by secant stiffness modules for volumetric C_V and deviator C_D components (5.22), respectively. With regard to the crack state, let's check when the condition (5.76) is fulfilled. According to Eq. (5.74) and Eq. (5.75) the crack state is preserved if one of the following conditions is satisfied (5.79).

$$C_D = 0 \qquad \text{or} \qquad e_{D,y} = 0 \tag{5.79}$$

The conditions simply reflect that the deviatoric component on the *y* microplane is subject to softening (Ožbolt, Li & Kožar, 2001). The Fig. 5.8c illustrates this situation with the dotted line indicating the deviatoric limit. Note that the BP model requires that the deviatoric compressive strength should be approximately 10 times greater than the volumetric tensile strength. According to that, the fulfillment of the second condition in (5.79) ensures the equality in (5.76). On the other hand, the deviatoric strain component $e_{D,y}$ is not subject to softening, and the model replicates lateral expansion (5.80).

$$e_{N,y} = e_V \tag{5.80}$$

5.5.2 Regularizing condition

To avoid the pathological behavior of the BP model, it can be demonstrated that an appropriate relationship between $C_{D,y}$ and C_V is necessary. By introducing s_V and s_D from the microplane constitutive equations in Eq. (5.17) into Eq. (5.74) and Eq. (5.75), and denoting that

$$\eta = \frac{C_{D,y}}{C_V}, \tag{5.81}$$

the condition in Eq. (5.82) can be obtained (Ožbolt, Li & Kožar, 2001).

$$\eta = \frac{-e_V}{e_{D,y}} \tag{5.82}$$

η can be rewritten by taking into account Eq. (5.77) and Eq. (5.78), which gives

$$\eta = \frac{1 - 2\upsilon}{1 + \upsilon}. \tag{5.83}$$

It follows that, in order to satisfy Eq. (5.82), η should be constant for any level of damage (5.84).

$$C_{D,y} = \eta\, C_V \tag{5.84}$$

The connection between the secant stiffness moduli refers that the condition (5.79) is fulfilled only when $C_{D,y}$ is proportional to C_V during the entire history of deformation which is characterized by damage. In conclusion, only an appropriate s_D-e_D relationship that satisfies (5.79) will lead to a realistic solution for concrete under

uniaxial tension. For other constitutive description, the BP model will predict certain lateral expansion or even the situation in which the normal stress components $s_{N,y}$ will never reach zero since $e_x \rightarrow +\infty$ (Ožbolt, Li & Kožar, 2001).

5.5.3 *Effective microplane strain components*

In order to remove the pathological behavior from the BP model, the discontinuity nature of the strain field should be taken into account. A possible solution is the improvement of the microplane kinematic condition by adding an additional constraint to the microplane strain components. Mention that there are other possibilities but they produce side effects at the microplane level, perceived as the non-negative energy dissipation (Bažant et al., 2000a). The proposed numerical formulation is based on retaining and expanding the microplane kinematic condition.

The main idea of the original BP model improvement lies in the extended description of the strain field, by introducing the concept of *effective microplane strain components* (Ožbolt, Li & Kožar, 2001). The theoretical modification perturbs the assumption originally introduced by Bažant and Prat (1987), and so, it is reasonable to interpret the model alteration as an improvement. Namely, instead of calculating the microplane stress components from the microplane strain data for dominate tensile load (obtained by projecting the macroscopic stress tensor E), the microplane stresses are calculated on the base of the so-called effective microplane strain components.

Except for microplane volumetric strain, the effective strain components are redefined as components of the projected macroscopic strain tensor E multiplied by a pre-defined function ψ. In this case, the model corrects the deviatoric microplane strain component e_D as

$$e_D = (n_i n_j E_{ij} - e_V)\, \psi. \tag{5.85}$$

Similarly, the tangential strain components are now calculated via

$$e_M = m_i\, n_j\, E_{ij}\, \psi\,, \qquad \text{and} \qquad e_K = k_i\, n_j\, E_{ij}\, \psi\,. \tag{5.86}$$

As mentioned, the model enrichment is based on the relaxed kinematic concept. Now, the prefix "relaxed" can be explained as follows. For dominated tensile loading, accompanied by discrete crack openings, the function ψ describes the innate discontinuous character of strain field by introducing *strain relaxations*. Due to the fact that the dominate tension loading can obtain any direction, for each microplane around the given FE Gauss point, the value ψ^{ℓ} is uniquely dedicated and defined across the interval

$$1 \geq \psi^{\ell} \geq 0. \tag{5.87}$$

Since ψ marks discontinuity in the strain field, it is called the *discontinuity function*. Its selection is influenced by the microplane volumetric stress-strain relationship and by the maximal principal stress σ_1 (tension stresses). Whit such assumptions, ψ allow the smooth transition from the dominant tensile load to dominant compressive load. The procedure is discussed as follow.

5.5.3.1 Strain relaxation – deviatoric components

At the initial material virgin state (even for small tensile load) the concrete integrity can be viewed as an isotropic elastic continuum (Ožbolt, Li & Kožar, 2001). By increasing tension load, the concrete integrity starts to decrease (stiffness degradation). At the microstructural level, a bunch of microcracks arise which can consequently lead to their local accumulation and finally, to material rupture evidenced at the macro-scale as a crack extension. The continuum theory predicts this state as a localization of strains at the crack trajectory.

In order to describe the stress behavior at the crack state, assume a plane damaged by horizontal tensile loading (Fig. 5.9). The damage evolution is directly related to the strain value in load direction (damage direction). By increasing lateral strains, which are denoted in Fig. 5.9 by the red arrow (direction 1), the stresses in the same direction start to decrease. In this case, the strain components oriented perpendicularly to the damage direction (direction 2) have decreased in a nearly elastic manner. After the material rupture, the three-dimensional stress state is reduced to a uniaxial stress-strain state.
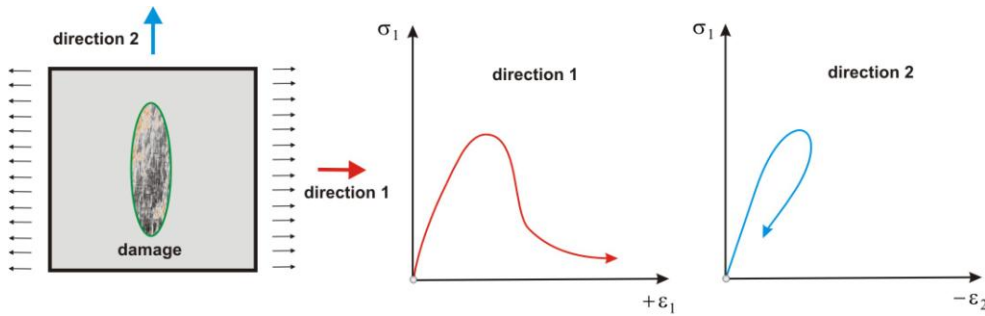
Figure 5.9 Influence of damage orientation on stress (macroscopic loading and unloading)

This is an important mechanism that should be incorporated in every material model for quasi-brittle material. In order to introduce the mechanism in the concept of relaxed kinematic constrain, an objective criteria is required for evidencing dominant tensile load. For this purpose, imagine a material volume segment loaded by tension in one, two or all three directions. In this case, the Green-Lagrangian volumetric strain component E_V and the principal stress s_I of the back-rotated Cauchy stress tensor s are positive. Thus, it seems reasonable to assume that dominate tensile load exists if (Ožbolt, Li & Kožar, 2001):

$$e_V > 0 \qquad \text{and} \qquad s_I > 0, \tag{5.88}$$

where e_V and s_I are invariant macroscopic tensor properties. Indeed, the invariant property makes Eq. (5.88) even more adequate criteria for dominate tensile load. Moreover, in the elastic range of material response, the principal stress can evidence the presence of tensile load. On the other hand, the condition (5.88) survives even if the volume segment is fully cracked. In such case, the total volumetric strain is positive and the principal stress drops close to zero. Furthermore, the total volumetric strain (for the cracked material) is approximately equal to a non-elastic volumetric strain which additionally indicates that (5.88) can be uses as an indicator of dominant tensile load.

After identifying the need to invoke the discontinuity function ψ, its value should be appropriately defined. As previously demonstrated in Eq. (5.84) for tensile load, the secant modulus C_D should be proportional to the secant modulus C_V. According to Eq. (5.84) and Eq. (5.18), the deviatoric stress component for virgin load is calculated as

$$s_D = C_D\, e_D\, \mathrm{e}^{-\left|\frac{e_V}{e_1}\right|^m}, \tag{5.89}$$

where e_D represents the total microplane deviatoric strain. By applying the effective microplane strain concept, the former expression can be rewritten as

$$s_D = C_D\, e_{D,eff}, \tag{5.90}$$

in which $e_{D,eff}$ denotes the effective strain and is calculated through the discontinuity function by

$$e_{D,eff} = e_D \psi \qquad \psi = \mathrm{e}^{-\left|\frac{e_V}{e_1}\right|^m}. \tag{5.91}$$

The same concept can be applied to the microplane secant modulus giving

$$s_D = C_{D,eff}\, e_D, \tag{5.92}$$

where $C_{D,eff}$ represents the effective secant modulus and is calculated by

$$C_{D,eff} = C_D \psi. \tag{5.93}$$

The effective deviatoric secant modulus $C_{D,eff}$ is proportional to C_V and varies from $C_{D,0}$ (in the initial virgin state) to zero (crack state). In order to preserve the discussed proportionality given in Eq. (5.84), the discontinuity function ψ must be of the same type as the function that controls the microplane volumetric secant modulus C_V (5.21).

It can be conclude that the discontinuity function ψ applied to the microplane deviatoric strain component enables the material relaxation in the direction perpendicular to the principal damage direction. Therefore, one may say that the mechanism illustrated in Fig. 5.9 has been replicated. Also, note that for the general three-

dimensional case, where the damage can move towards any direction, the various microplane orientations can easily trap the principal damage direction. Namely, as the discontinuity function is prescribed for each microplane separately, the microplane which is perpendicular to the crack surface has the negative deviatoric strain and will be unloaded (5.94).

$$e_D = e_N - e_V \quad , \quad e_N \to 0 \quad , \quad e < 0 \tag{5.94}$$

By contrast, the microplane which is parallel to the crack surface has positive deviatoric strain:

$$e_D = e_N - e_V \quad , \quad e_N > e_V \quad , \quad e_N > 0 \implies e_D > 0, \tag{5.95}$$

and is loaded in tension. Depending on loading or unloading case, the deviator microplane strain components need or need not be multiplied by the discontinuity function ψ. In this manner, even for complex three-dimensional damage evolution, the microplane model can replicate the anisotropic damage behavior at the concrete microstructural level.

5.5.3.2 Strain relaxation – what about volumetric components ?

According to Eq. (5.85) and Eq. (5.86), the question why the volumetric strain components are not split into their effective and non-effective part, seems valid. Principally, there are four important reasons for that. (i) As already introduced in Eq. (5.13), the volumetric strain components are invariant in respect to the microplane orientation. (ii) The static constraint on the volumetric stress component has been fulfilled whereas $e_V \to \infty$ when $s_V \to 0$. (iii) Its originality should be preserved due to its role for macroscopic tensile damage identification. (iv) The information about the volumetric strain component is useful for monitoring of the stress-strain patch in case of concrete under cycling loading.

Furthermore, according to Eq. (5.93), the microplane negative deviatoric strain component indicates that the microplane orientation (5.2) is orthogonal to the damage direction. If the damage increases, the deviatoric stress and strain in the direction of damage evolution should relax and consequently reach zero. In order to reproduce this effect artificially, the discontinuity function for the deviatoric strain component is conditionally assumed as (Ožbolt, Li & Kožar, 2001):

$$\psi = e^{-\left| f(s_I)\frac{e_V}{e_1} \right|^m} \quad \textbf{if} \quad e_D < 0 \ \textbf{and} \ e_V > 0 \ \textbf{and} \ s_I > s_{I,\min}, \tag{5.96}$$

$$\psi = 0 \qquad \text{if} \quad e_D \geq 0,$$

in which $s_{I,\min}$ denotes small negative limit value of the maximum principal stress. In principle, ψ in Eq. (5.96) has the same form as the microplane stress-strain relationship for volumetric tension (5.19). The difference is evidenced in the introduced function $f(s_I)$ which reflects the smoothed transition from the discontinuous state (at the tensile crack opening) to the continuous one in which the crack is closing, producing compression at the crack surface (Fig. 5.10).
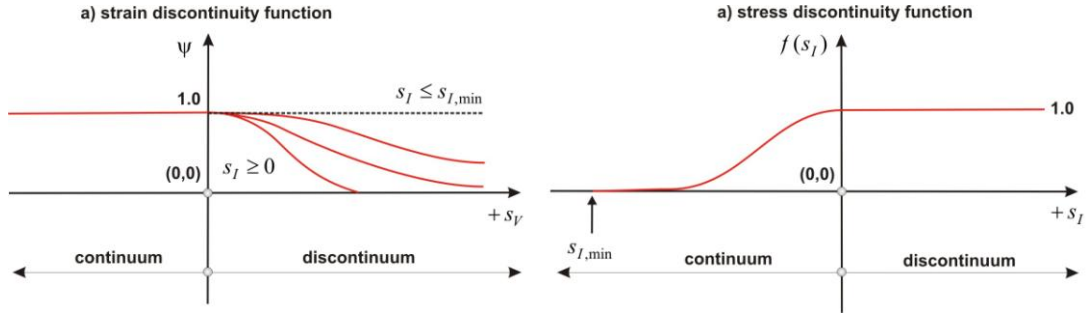
Figure 5.10 Microplane discontinuity function: **a)** strain discontinuity and **b)** stress discontinuity function

Based on experimental cyclic test data, the function $f(s_I)$ is here adopted as:

$$
\begin{aligned}
f(s_I) &= 1 && \text{if} && s_I > 0 \ , \\
f(s_I) &= 0 && \text{if} && s_I < s_{I,\min} \ , \\
f(s_I) &= 1 - \sin\left(\frac{\pi}{2}\left|\frac{s_I}{s_{I,\min}}\right|\right) && \text{if} && s_{I,\min} \le s_I \le 0 \ .
\end{aligned}
\tag{5.97}
$$

In conclusion, for microplanes closely oriented towards the damage direction, the strain value perpendicular to the crack surface reaches infinity while the appropriate microplane stresses are reduced to zero. This unloading scenario can be summarized as follows (5.98).

$$
e_V \rightarrow +\infty \;\; \Rightarrow \;\; (s_V, s_D, s_T(s_M, s_K)) \rightarrow 0 \quad \text{and} \quad e_D \rightarrow +\infty \quad \text{with} \quad \psi = 1
\tag{5.98}
$$

5.5.3.3 *Strain relaxation – shear components*

In order to numerically trap the concrete behavior under high confining pressure (which is obviously important in high-energy impact loading), the shear microplane strain components should be influenced by the microplane volumetric strain (5.23). For this purpose, note that the independency of shear components $\mathbf{e}_M^\ell$ and $\mathbf{e}_K^\ell$ specifies that there is no co-axiality between their microplane stress components. Now, in the case of tension loading accompanied by the crack state (positive normal stresses), the shear resistance should be reduced to zero. On the other hand, for negative normal stress, caused by compression loading, the microplane share resistance should be activated, which can be physically interpreted as the microstructural frictional effect (concrete aggregate interlocking). This is a typical situation in which the concrete is under pure compression, or shear compression softening, where the microplanes shear persistence lies in the mainly normal compressive stress. In this case, it is convenient to model concrete as a continuum filled by cracks (Ožbolt, Li & Kožar, 2001). However, in case of dominant tensile damage, the shear stress and strain microplane components should be reduced to zero. The aforementioned situations can be numerically reflected by the shear discontinuity function here assumed as

$$\psi = e^{-\left| f(s_I) \frac{e_V}{e_1} \right|^m} \qquad \text{if} \qquad e_V > 0 \quad \text{or} \quad s_I > s_{I,\min}, \tag{5.99}$$

$$\psi = 1 \qquad\qquad \text{if} \qquad \text{else}.$$

Once again, the introduced discontinuity function is influenced by function $f(s_I)$, enabling the smoothed continuum-discontinuum transition (5.97). This is an almost crucial improvement of the BP microplane model, due to the fact that under high-energy impacts loading, the presence of shear failure mode is inevitable. This fact is especially evidenced in experiments in which a plain concrete beam is tested on relatively high impact loadings (Sukontasukkul & Mindess, 2003).

5.6   Cyclic loading

The presence of cyclic loading in a general triaxial case is incorporated in the adopted microplane model by loading-unloading rules attributed to each uniaxial stress-strain microplane relationship. Namely, the virgin loading for the ℓ microplane is reached if:

$$e^{\ell} \Delta e^{\ell} \qquad \text{and} \qquad (e^{\ell} - e^{\ell}_{\max})\,(e - e^{\ell}_{\min}) \geq 0, \tag{5.100}$$

in which $e^{\ell}_{\max}$ and $e^{\ell}_{\min}$ denote the maximal and minimal strain value that has been attained so far. For other situations, the microplane unloading or reloading case is activated when the microplane stress-strain relationship is reconstructed in an incremental form by

$$ds = C_{cy}de, \tag{5.101}$$

where C_{cy} represents the unloading-reloading tangent moduli given by

$$C_{cy} = C_{cy,0}\alpha + s\left(\frac{1-\alpha}{e - e^*}\right). \tag{5.102}$$

The strain component e^* in Eq. (5.102) is calculated according to the total strain value e by

$$e_1 = e_p - \frac{s_p}{C_0} + \beta(e - e_p) \qquad \text{if} \qquad e > e_p, \tag{5.103}$$

$$e_1 = e_p \qquad\qquad\qquad \text{if} \qquad e \leq e_p,$$

in which s_p and e_p denote the positive ($s_p{}^+$) or negative ($s_p{}^-$) peak stress, and ($e_p{}^+$) and ($e_p{}^-$) are the corresponding positive and negative peak strains. The parameter α in Eq. (5.102) and the parameter β in Eq. (5.103) are empirically chosen and usually assumed as constant between 1 and 0. For each microplane, C_0 represents its initial elastic stiffness moduli. A sample of loading-unloading-reloading rules is illustrated in Fig. 5.11. It can be see that, in the region of volumetric compression (Fig. 5.11a), the loading-unloading modulus is defined by the initial elastic volumetric modulus $C_{V,0}$ (virgin state). On the other hand, the stress-strain relation in the tension quadrant is controlled by Eq. (5.102).
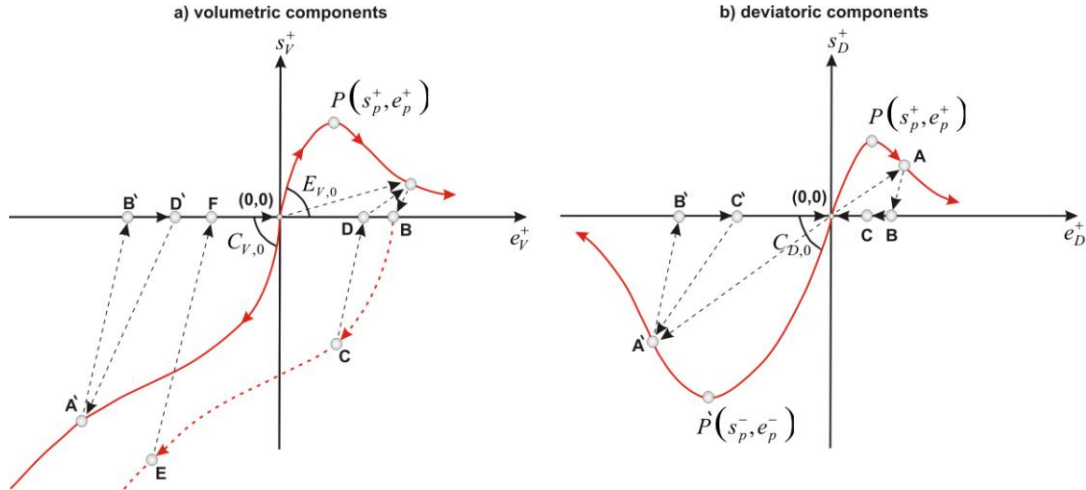
Figure 5.11 Loading-unloading-reloading rules for: **a)** volumetric and **b)** deviatoric microplane components

Following the letters in Fig. 5.11, an example of a typical load cycle, composed of the virgin loading tension, unloading in compression and reloading in tension, can be given as (Ožbolt, Li & Kožar, 2001)

$$(0,0) \rightarrow P \rightarrow A \rightarrow B \rightarrow C \rightarrow D \rightarrow A \rightarrow B \rightarrow E \rightarrow F \rightarrow (0,0) \rightarrow A.$$

Another one could be

$$(0,0) \rightarrow A' \rightarrow B' \rightarrow D' \rightarrow A',$$

or even

$$(0,0) \rightarrow A' \rightarrow B' \rightarrow (0,0) \rightarrow P \rightarrow A \rightarrow B \rightarrow E \rightarrow F \rightarrow (0,0) \rightarrow A,$$

which denotes the virgin loading in compression, unloading and then reloading in tension (Fig. 5.11a). Similar rules can be applied for the description of cycling loading attributed to deviatoric compression and tension (Fig. 5.11b). The cycling rules for shear microplane components are almost the same as for the deviatoric component (Fig. 5.11a). However, in order to reproduce the effect evidenced in bond cyclic experiment (where the loading in one direction causes the decreasing of share strength and stiffness in the opposite direction), the share microplane components are adapted through the stiffness moduli C_M and C_K multiplied by an additional damage function given as

$$\omega_s = e^{-1.2\left(\frac{\Lambda}{\Lambda_0}\right)^{1.1}}. \tag{5.104}$$

In this Eq. Λ denotes dissipation of the accumulated shear energy while Λ_0 represents the area under the monotonic microplane shear stress-strain curve. This empirical damage function has been proposed by Eligehausen, Popov and Bertero (1983), and is based on an evaluated number of experimental bond cycle test data.

5.7   Anisotropy

Considering the origin of material anisotropy, the *initial* and *damage induced anisotropy* should be distinguished. The first one is a consequence of the material structure in the initial virgin state. The second one is caused by damage localization in a particular direction (Fig. 5.10) and its evolution is influenced by loading (Kuhl, Ramm & de Borst, 2000). At the numerical implementation level, both situations can be very elegantly incorporated into the microplane material model (Ožbolt, Li & Kožar, 2001). Indeed, the damage induced anisotropy is automatically taken into account by various microplanes orientations in which the stress-strain dependency is uniquely defined as the function of damage (5.18). The initial material anisotropy can be incorporated in two different ways.

5.7.1 $\Omega(\mathbf{n})$ – *material weak direction*

The initial anisotropy can be incorporated by considering the function $\Omega(\mathbf{n})$ depending on the microplane normal direction (5.2) in respect to the material weak direction $\mathbf{w}$. The function $\Omega(\mathbf{n})$ is represented as a statistical distribution of the weak direction frequency attributed to the microplane normal vector $\mathbf{n}^{\ell}$ (Fig. 5.12). Particularly, if the microplane normal vector is parallel to the weak direction, $\Omega(\mathbf{n})$ is equal to 1 and if the vector $\mathbf{n}^{\ell}$ is perpendicular to $\mathbf{w}$, $\Omega(\mathbf{n})$ is equal to 0.
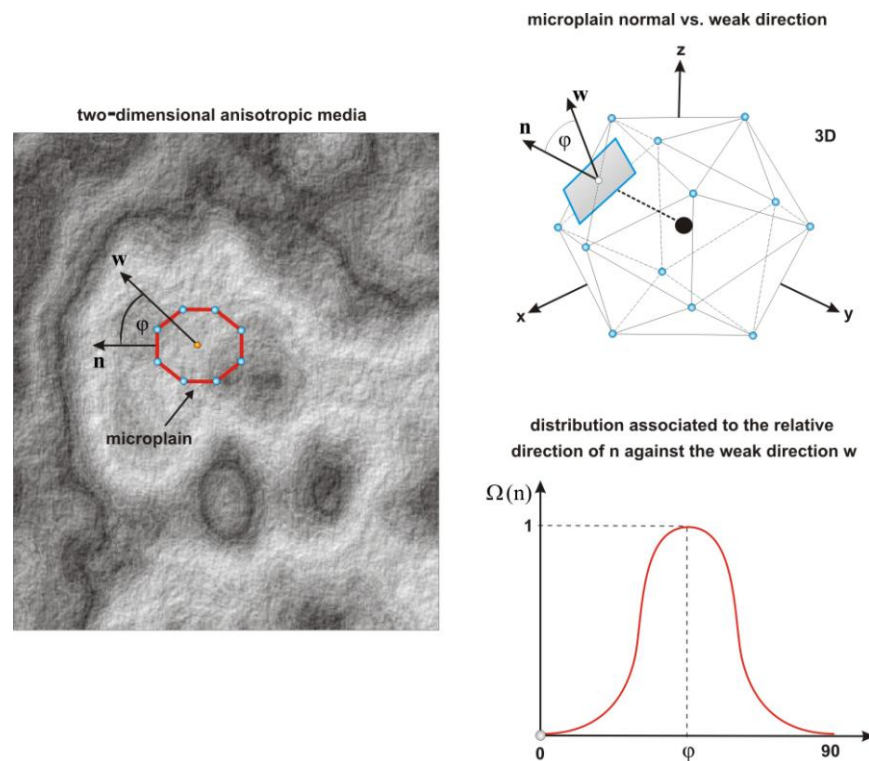
Figure 5.12 Material anisotropy viewed as a weak direction defined with angle φ

Once the material weak direction **w** is known, the function $\Omega(\mathbf{n})$ can be introduced in Eq. (5.36) from where the macroscopic stress tensor **σ** is calculated. As the volumetric stress components does not depend on the microplane orientation (denoting volumetric isotropy), Eq. (5.36) can be rewritten as

$$\sigma_{ij} = \sum_{\ell=1}^{n_m} \left\{ s_V \delta_{ij} + \frac{3}{2\pi} \int_{S^\ell} \left[n_i^\ell n_j^\ell s_D^\ell + \frac{1}{2}(m_i^\ell n_j^\ell + m_j^\ell n_i^\ell) s_M^\ell + \frac{1}{2}(k_i^\ell n_j^\ell + k_j^\ell n_i^\ell) s_K^\ell \right] \Omega(\mathbf{n}^\ell) \, \mathrm{d}S^\ell \right\}. \quad (5.105)$$

Mention that the weak point of the strategy is the difficulty to identify the function $\Omega(\mathbf{n})$ in the experimental tests. However, in the proposed numerical formulation the function is defined empirically as

$$\Omega(\mathbf{n}) = (n_i w_i)^\gamma, \quad (5.106)$$

where w_i is the component of the weak direction **w** and γ is the parameter ≥ 1 (Ožbolt, Li & Kožar, 2001).

5.7.2 Anisotropy by microplane orientation

The second strategy is based on defining the uniaxial microplane constitutive description for different types of microplane orientations (Prat & Gens, 1994). The strategy modifies Eq. (5.22) and Eq. (5.23) by extending their dependency to the microplane normal direction **n** (5.107).

$$
\begin{aligned}
C_V &= C_V \ (e_V, \mathbf{n}) \\
C_D &= C_D \ (e_V, e_D, \mathbf{n}) \\
C_M &= C_M \ (e_M, e_V, s_V, \mathbf{n}) \\
C_K &= C_K \ (e_K, e_V, s_V, \mathbf{n})
\end{aligned}
\qquad (5.107)
$$

In contrast with the previous strategy, the volumetric anisotropy is here replicated by setting the microplane volumetric modules as a function of microplane orientation (5.2). The passage from micro to macro scale is the same as discussed earlier (*5.1.1 Microplane strain components*).

5.8   Strain rate sensitivity

In order to develop a numerical formulation able to realistically capture the concrete acute failure under high-energy impact loading (but also low-impact loading), the *strain rate sensibility effect* should be included in the concrete constitutive description. Namely, experiments confirm that the response of concrete structures is directly related to loading rate (Bentur, Mindess & Banthia, 1986; Sukontasukkul & Mindess, 2003). As discussed by Ožbolt et al. (2006), there are mainly three different effects that govern the mechanical behavior of concrete exposed to external loading.

(i) *At a relatively low-loading rate, like static or quasi-static loading rate, the concrete response is manifested as the bulk material creeping between the cracks.*

(ii) *With a smooth margin of transition, by increasing the loading rate the material response is governed by the rate dependency of the growing microcracks.*

(iii) *At high-impact loading, the material response is under dominant influence of inertial forces, which can significantly change the stress and strain state at the crack tip.*

Basically, all three failure mechanisms are always present but their contributions to concrete cracking vary with loading rate. It can be deduced that the concrete cone of failure (Fig. 5.13) varies and depends on the deformation rate.

> *With the present numerical formulation the author intends to numerically replicate, and subsequently investigate, the transition between the abovementioned three effects that govern the concrete failure.*

Numerous theoretical and experimental researchers, motivated by the importance of strain rate effect, have developed a variety of strategies aimed to quantitatively describe its manifestation (Bažant et al., 2000b). A lot of proposed models were based on different stress-displacement relationships, similar to the *spring-dashpot models* of *viscoelasticity*. However, in the proposed numerical formulation, the model for rate dependency is based on the energy activation theory of bond ruptures (Krausz & Krausz, 1988). The adopted model can reproduce the rate dependency of the crack propagation across a wide range of loading rates (Ožbolt & Reinhardt, 2001; Ožbolt, Rah & Meštrović, 2006).
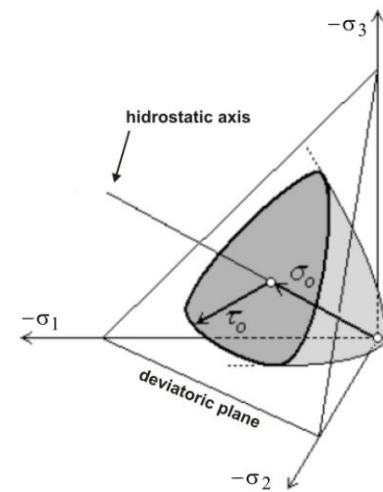
Figure 5.13 Concrete cone of failure

The rate dependency model is here implemented in the thermodynamically consistent M2-O microplane model for concrete (Ožbolt, Rah & Meštrović, 2006). On the basis of the previously mentioned effects (that govern the concrete failure process), the introduced rate dependency model enables to numerically reconstruct the first two. Indeed, the proposed numerical formulation is sensitive to the rate dependency related to formation of microcracks and to the creep of concrete between the microcracks. The third effect is not included in the model since it is not a part of the constitutive law (inertial forces). It emerges automatically from the dynamic equilibrium equation due to the direct interaction of the constitutive law with the activation of inertial forces.

In contrast with the model proposed by Bažant et al. (2000b), where the initial concrete elasticity modulus is manipulated by a pre-defined viscoelastic model, the rate dependency softening and hardening are here controlled by the formation of microcracks. With such physical background, the adopted concept is reasonable since the concrete microcracks start to grow immediately upon the implication of loads.

In order to represent the rate dependency caused by the creep of concrete between the microcracks, the *generalized Maxwell model* for concrete is adopted (Ožbolt & Reinhardt, 2001). Considering the duration of load, the first rate dependency effect (**i**) is manifested in relatively short loading times (impact loadings) and the second one, in relatively long loading times associated to creep fracture interactions (static loading).

After introducing the basic concepts related to strain rate effect, the model for simulating the rate dependency is hereafter presented. For this purpose, assume a concrete body smeared with parallel cohesive cracks. In this case, the rate of macroscopic strain $d\varepsilon/dt$ can be expressed as

$$\frac{d\varepsilon}{dt} = \frac{\dot{w}}{s_{cr}} + \frac{\dot{\sigma}}{E}.$$

(5.108)

In this Eq. ε denotes the macroscopic strain, normal to the direction of parallel microcracks, s_{cr} represents the spacing of the assumed parallel cracks and the term dw/dt is the crack opening ratio where w indicates the crack aperture. By validly assuming that the elastic strain ratio $(d\sigma/dt)/E$ can be neglected in respect to the crack opening ration dw/dt (Ožbolt, Rah & Meštrović, 2006), the former Eq. (5.108) can be simplified such that

$$\frac{d\varepsilon}{dt} \approx \frac{\dot{w}}{s_{cr}} .$$

(5.109)

Having introduced this reasonable simplification, the influence of strain rate effect may be applied to the stress-strain constitutive relationship. Accordingly, the macroscopic stress components $\sigma(\varepsilon)$ are related to the macroscopic strain components ε via the constitutive material description enriched by the rate-of-deformation $d\varepsilon/dt$ (5.110).

$$\sigma(\varepsilon) = \sigma^0(\varepsilon)\underbrace{\left[1 + c_2 \ln\left(\frac{2\dot{\varepsilon}}{c_1}\right)\right]}_{\text{strain rate influence}}$$

(5.110)

The parameters c_1 and c_2 are material constant obtained by fitting test data (Bažant et al., 2000b). Note that the macroscopic stress $\sigma(\varepsilon)$ are the product of the originally obtained stress $\sigma(\varepsilon)^0$ multiplied by a correctional factor that reflects the influence of the rate-of-deformation (5.110).

Resume, for the given microplane strain components, the microplane stress components are obtained through the microplane uniaxial constitutive definition (5.17). At this scale of observation, the microplane stresses do not depend on the rate-of-deformation. Namely, to preserve the tensors objectivity, it is seems reasonable to assume that the microplane stress components are unaffected by the previously defined principle (5.110). In this case, the rate-of-deformation is measured at the macroscopic level, with a scalar quantity associated to the macroscopic Green-Lagrangian strain tensor *E* (5.111).

$$\dot{\gamma} = \sqrt{\frac{1}{2}\dot{E}_{ij}\dot{E}_{ij}} \tag{5.111}$$

Measuring the rate-of-deformation at the microplane level would be inappropriate due to the fact that individual microplanes possess different strain rate which will consequently lead to a subjective strain rate measure.

Chapter 6

Contact mechanics

6.1 Introduction

In order to numerically simulate the free fall drop weight experiment, as well as any other mechanical interaction, contact between different FE discretizations has to be considered. For this purpose, resume that the non-linear nature of contact phenomenon will requires the incremental solution to reproduce body deformation path. Mention also that in each time increment Δt the contact simulation brings two different tasks. (i) Since the contact event is evident in mesh boundary interactions and, on the other hand, the introduced equation of motion cannot recognize contact events, an exterior procedure is needed to monitor the deformation path and to notify if contact occurs. (ii) By identifying and localizing mesh contact regions, the description of forces over the contact interfaces should be given according to the principles of *contact mechanics*. Basically, these two procedures can be classified as *contact detection* and *contact resolution stage* (Fig. 6.1). Since the computational stages are principally different, i.e. the first one involves only kinematical aspect of contact while the second one involves the mechanical aspects; it is convenient to discuss them separately.

According to the abovementioned, the current chapter addresses the issue of an adequate modifications for Eq. (4.30), needed to include the presents of contact forces. The here discussed contact resolution stage will be principally valid for an arbitrary result previously obtained in the contact detection stage. The contact detection stage will be discussed in the next chapter.
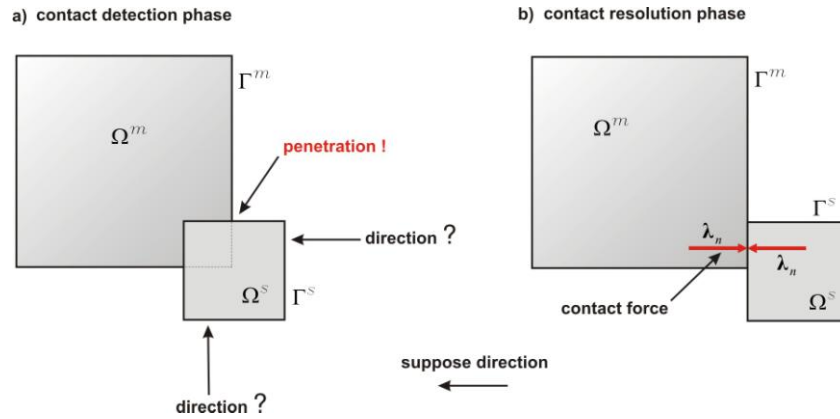
Figure 6.1 Numerical treatment of contact: **a)** contact detection and **b)** contact resolution phase

Each contact problems involve a number n_b of solids for which the upper index κ can be used to represent the bodies geometrical and mechanical data association ($\kappa=1..n_b$). However, since the main attention is here dedicated to numerically investigate the concrete response by simulating the free fall drop weight experiment (Fig. 1.1), it is reasonable to simplify the description by considering only two bodies that are further indicated as the body m and s ($\kappa=m,s$).

Under these circumstances, the pre-defined force field b^κ induces the motion of bodies and generates the deformation path completely defined with the reference configuration at time t_n and current configuration at time t_{n+1}. During the deformation history, the domains Ω^κ bounded by Γ^κ can occasionally come into contact and thus produce the contact boundary interface Γ_c (Fig. 6.2). Note that the contact interface dimension is one order below the space dimension. Therefore, in case of two-dimensional problems Γ_c is a curve, and in case of three-dimensional problems, Γ_c is a surface. Mention also that the contact surface Γ_c is usually unknown in advance and has to be determined in an iterative fashion (non-linear problem).

6.2   Strong formulation

By definition, the contact problem arises from the classical body deformation analysis (3.3) by adding the *contact displacements constraints* to introduce a restriction over the displacement solution space. Namely, since two material points cannot occupy the same space at the same time, the displacement field that causes penetrations between bodies must be forbidden. Furthermore, the solution space restriction will be additionally influenced by the physical property over the contact surface Γ_c. In other words, the tangential displacements will depend on an adopted frictional constitutive behavior.

In order to obtain the FE approximation of displacement field **u** for bodies under collision, the strong problem formulation should be considered. The formulation was originally introduced by Signorini (1933) and it is therefore also known as the *Signorini problem*.
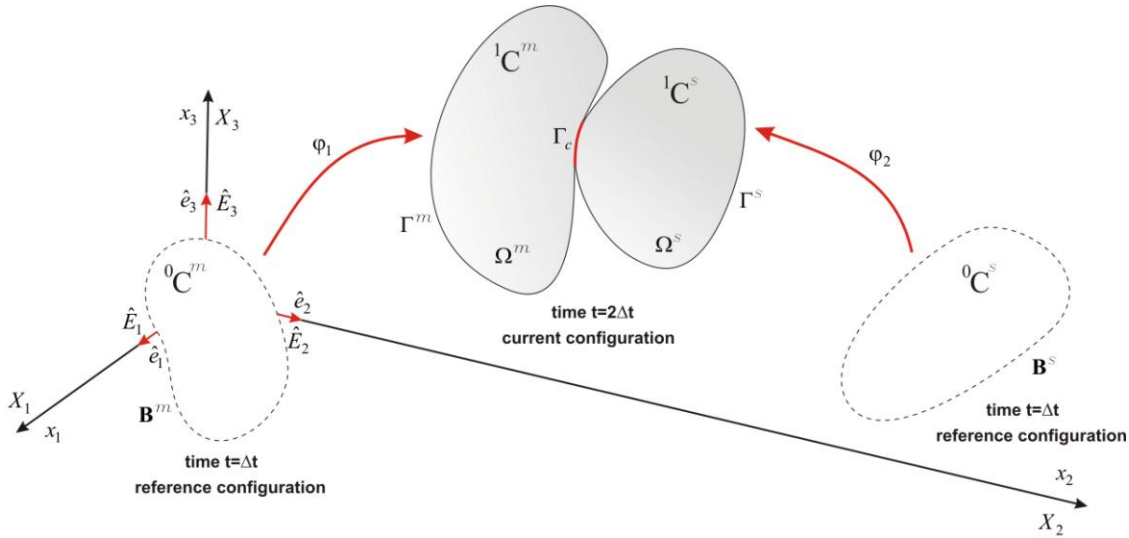
Figure 6.2 Deformation path characterized by mechanical interaction (contact on boundary Γ_c)

6.2.1 Signorini problem

The governing differential equations for bodies in contact/impact are principally the same as the previously introduced in (3.3). However, the key differences lie in the additional *kinematic* and *kinetic conditions*, defined on the contact interface Γ_c (Fig. 6.2). Resume, due to the fact that the body domain should not be interpenetrated (not allowed physical penetrations); the so-called impenetrability contact condition must be fulfilled (kinematic condition). Furthermore, to characterize the contact response, the physical behaviour of Γ_c should be also taken into account (kinetic condition). By enriching the earlier given strong form (3.3) with the mathematical description of the mentioned conditions, the strong form for contact problem can be formulated as follows (Signorini problem):

$$\text{find} \quad u \in \Re^3 \quad \text{such that:}$$

$$\rho^\kappa b_i^\kappa + \sigma_{ij,j}^\kappa = 0 \quad \text{in} \quad \Omega^\kappa,$$

$$\text{respect to:}$$

$$\sigma_{ij}^\kappa = f(\varepsilon_{ij}^\kappa, \dot{\varepsilon}_{ij}^\kappa, \text{ect.}),$$

$$\varepsilon_{ij}^\kappa = f(u_i^\kappa),$$

$$\text{and subject to:}$$

$$t_i^\kappa = \sigma_{ji}^\kappa n_j^\kappa = \bar{t}_i^\kappa \quad \text{on} \quad \Gamma_t^\kappa,$$

$$u_i^\kappa = \bar{u}_i^\kappa \quad \text{on} \quad \Gamma_u^\kappa,$$

and additionally to:

$$g_i^\kappa \geq 0, \tag{6.1a}$$

$$t_i^\kappa \leq 0 \quad \text{on} \quad \Gamma_c, \tag{6.1b}$$

$$g_i^\kappa t_i^\kappa = 0, \tag{6.1c}$$

where:

$$\Gamma^\kappa = \Gamma_t^\kappa \cup \Gamma_u^\kappa \qquad \text{and} \qquad \Gamma_t^\kappa \cap \Gamma_u^\kappa = \notin.$$

By considering a number of bodies in the pre-defined force field b^κ, the possible mechanical interactions are now introduced via additional boundary contact conditions (6.1). Particularly, if the negative gap value g_i indicates the magnitude of non-physical penetrations, then the first *impenetrability contact condition* (6.1a) states that no penetration is allowed (6.2).

$$g_i^\kappa = \begin{cases} > 0 & \text{no contact} \\ = 0 & \text{contact} \\ < 0 & \text{penetration} \end{cases} \tag{6.2}$$

The second so-called *intensility contact condition* (6.1b) describes the compressive character of normal traction, and states that only compressive stresses can occur on Γ_c. The so-called *complementarity contact condition* (6.1c) combines the impenetrability (6.1a) and intensility conditions (6.1b) by describing the unique product between them. This condition is also known as the *unitary contact condition* and expresses the fact that contact forces do not produce mechanical work (Belytschko, Liu & Moran, 2001). In other words, if there is no contact, no compressive traction can occur. By contrast, if there are no compressive stresses, the gap value must be positive.

6.2.2 Karush-Kuhn-Tucker constraints

The conditions (6.1) are also known as *Karush-Kuhn-Tucker conditions* of optimality (KKT). The conditions are required in the weak form of equilibrium (3.15) and lead to the so-called *weak inequalities* or *variational inequalities principle* (Wriggers, 2002). The KKT conditions can be also approximately fulfilled by appropriately controlling the impenetrability condition (6.1a). In the proposed numerical formulation the KKT conditions are fulfilled artificially by means of an adequate description of the related numerical algorithm. However, since the numerical description lies in the geometrical approximation of bodies, the impenetrability condition cannot be exactly fulfilled and certain tolerance value is needed to measure the non-physical penetration. Note the importance of the computational stage for contact detection and the influence of the earlier discussed computational round-off error (*Chapter 4 - 4.3.1 Assumption, approximations and errors*).

6.2.3 Frictional constraints

As a real contact event is always accompanied by a certain amount of frictional energy dissipation, the phenomenological description of friction should be given. As already mentioned, the frictional behavior imposes an additional restriction on the displacement solution space. Particularly, depending on frictional properties over Γ_c, the particles in contact can be subject to *stick* or *slip contact condition* (Wriggers, 2002). The skipping between them is quantitatively described by a pre-defined friction models. In the proposed numerical formulation, the Coulomb frictional model is used to reproduce the dissipative nature of tangential contact forces. Accordingly, the functional relation Φ between the normal $\mathbf{t}_N$ and the tangential component $\mathbf{t}_T$ of traction vector $\mathbf{t}$ are obtained through the frictional coefficient μ. For this purpose, the tangential velocity $\mathbf{v}_T$ between the particle in contact and the consistency parameter for slip ζ are needed (Kloosterman, 2002). The frictional constraints can be now formulated as follows (6.3).

$$\Phi := \|\mathbf{t}_T\| - \mu\|\mathbf{t}_N\| \leq 0 \tag{6.3a}$$

$$\mathbf{v}_T + \zeta\,\mathbf{t}_T = 0 \tag{6.3b}$$

$$\zeta \geq 0 \tag{6.3c}$$

$$\Phi \cdot \zeta = 0 \tag{6.3d}$$

Mention that the friction coefficient μ is here assumed as constant while for some other constitutive descriptions it can be set as a function of velocity and/or pressure. The condition in Eq. (6.3b) and Eq. (6.3c) induces the tangential traction as work opposite to the slip direction. Similarly to Eq. (6.1c), Eq. (6.3d) represents the frictional complementary condition. In other words, there is no slip contact condition if the tangential traction has not reached its local minimum. On the other hand, if the slip condition is activated, Φ has reached its maximum i.e. zero.

As mentioned earlier (*Chapter 4 – 4.3.1 Assumption, approximations and errors*), the obstacle in numerical contact simulation lies in an unsmoothed response of bodies under collision. In fact, the velocity field v_N, normal to the interface Γ_c is always a discontinuous function of time. As such, it is difficult to be captured numerically. However, sufficiently small time steps Δt will able to flow through the solution process without significantly lose the normal velocity feature. On the other hand, by assuming frictional contact behaviour, the tangential velocities $\mathbf{v}_T$ becomes also discontinuous function of time. In this case, the discontinuous nature of v_T is manifested through the switching between *stick* and *slip* contact condition (Belytschko, Liu & Moran, 2001). In a general case, the discontinuous nature of tangential displacements is significantly lower than the discontinuous behavior of normal velocities. Consequently, the discontinuous nature of tangential velocity will be automatically preserved if the assumed time step Δt can preserve the normal velocity feature.

6.2.4 Continuity constraint

Assume a displacement filed which is not continuously differentiable; i.e. its derivatives are discontinuous along a certain number of surfaces. In this case, the considered domain Ω must be subdivided in sub-domains Ω_e (FE) in which the displacement function should be at least C^1 (*Chapter 3 – 3.2.4 Finite element approximation*). Note that the situation reflects the contact condition along the boundary Γ_c (the so-called material interface). As a consequence, since the strains are first derivative of displacements, the continuous property of stress filed should be obviously also preserved (Fig. 6.3).
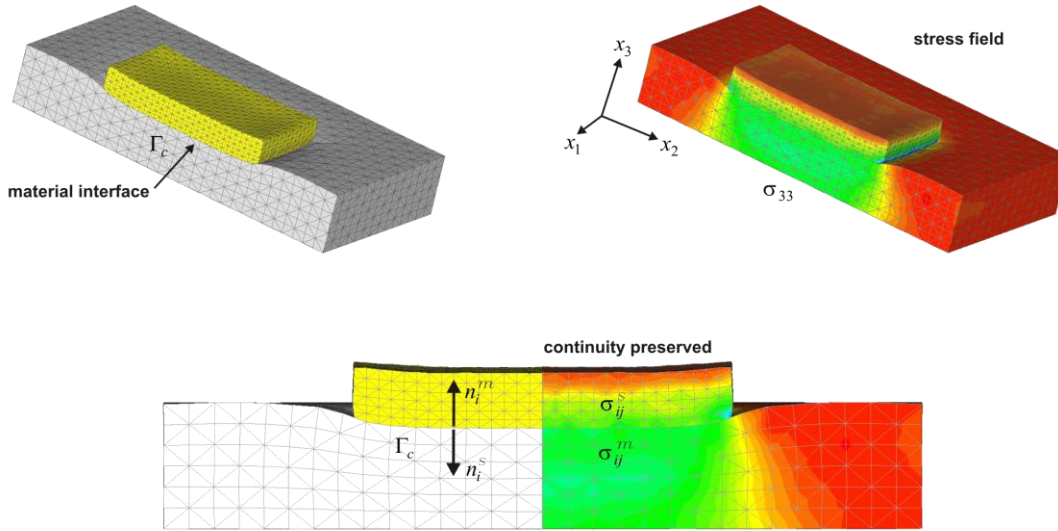
Figure 6.3 Continuity condition preserved by the program code based on the proposed numerical formulation

The continuity condition can be expressed by applying the divergence theorem to each FE domain Ω_e (Belytschko, Liu & Moran, 2001). The procedure gives the jump $[[\mathbf{n}\,\mathbf{u}]]$ in the displacement field $\mathbf{u}$ as

$$[[\mathbf{n}\,\mathbf{u}]] = [[\,n_i\,u_i\,]] = n_i^m u_i^m + n_i^s u_i^s\,, \tag{6.4}$$

and the jump $[[\mathbf{n}\,\boldsymbol{\sigma}]]$ in the stress field $\boldsymbol{\sigma}$ as

$$[[\mathbf{n}\,\boldsymbol{\sigma}]] = [[\,n_i\,\sigma_{ij}\,]] = n_i^m \sigma_{ij}^m + n_i^s \sigma_{ij}^s\,. \tag{6.5}$$

The vectors $\mathbf{n}^m$ and $\mathbf{n}^s$ denote the outward normal vectors on body m and s, respectively (Fig. 6.3). In order to preserve the continuity of $\mathbf{u}$, the condition in Eq. (6.4) should vanish on Γ_c. However, as the stress field emerges from the constitutive description (which is connected to displacements through the strain definition), it is reasonable to suppose that continuity of $\boldsymbol{\sigma}$ will preserve the displacement filed continuity. Accordingly, the continuity constraint can be reduced to

$$[[\mathbf{n}\,\boldsymbol{\sigma}]] = [[\,n_i\,\sigma_{ij}\,]] = n_i^m \sigma_{ij}^m + n_i^s \sigma_{ij}^s = 0. \tag{6.6}$$

6.3   Weak formulation

To gradually introduce the contact restrictions (6.1) into the dynamic equilibrium Eq. (4.30), suppose at the moment that deformation path of bodies B^κ (κ=1,2) does not involve any mechanical interactions. Thus, by including inertial forces through the *D'Alabert's principle*, the dynamic equilibrium Eq. becomes

$$\sigma_{ij,j}^\kappa + \rho^\kappa f_i^\kappa = \rho^\kappa \ddot{u}_i^\kappa. \tag{6.7}$$

Furthermore, according to the previously discussed procedure (*Chapter 3 – 3.2.3 Weak form*), the weak form of the former strong expression is obtained as

$$\sum_{\kappa=1}^{2} \left\{ \int_{\Omega^\kappa} \delta u_i^\kappa \, \rho^\kappa \ddot{u}_i^\kappa \, \mathrm{d}\Omega^\kappa + \int_{\Omega^\kappa} \delta u_{i,j}^\kappa \, \sigma_{ij}^\kappa \, \mathrm{d}\Omega^\kappa - \int_{\Omega^\kappa} \delta u_i^\kappa \, b_i^\kappa \, \mathrm{d}\Omega^\kappa - \int_{\Gamma_t^\kappa} \delta u_i^\kappa \, \bar{t}_i^\kappa \, \mathrm{d}\Gamma_t^\kappa \right\} = 0, \tag{6.8}$$

where δu represents an arbitrary test function with the property that allows δu to disappear from the boundary part Γ_t which is subject to traction boundary conditions (3.3e). Now, suppose that the deformation path causes mechanical interaction i.e. contact on Γ_c. In order to introduce this scenario into the weak form (6.8), the displacement solution space must be restricted by excluding those displacements that violates the abovementioned contact constraints over Γ_c. For this purpose, the variation of the so-called *contact energy functional* Π_c is introduced in Eq. (6.8) as

$$\sum_{\kappa=1}^{2} \left\{ \int_{\Omega^\kappa} \delta u_i^\kappa \, \rho^\kappa \ddot{u}_i^\kappa \, \mathrm{d}\Omega^\kappa + \int_{\Omega^\kappa} \delta u_{i,j}^\kappa \, \sigma_{ij}^\kappa \, \mathrm{d}\Omega^\kappa - \int_{\Omega^\kappa} \delta u_i^\kappa \, b_i^\kappa \, \mathrm{d}\Omega^\kappa - \int_{\Gamma_t^\kappa} \delta u_i^\kappa \, \bar{t}_i^\kappa \, \mathrm{d}\Gamma_t^\kappa \right\} + \delta \Pi_c = 0. \tag{6.9}$$

The structure of the functional Π_c depends on the method adopted to enforce the contact constraints. Among many different strategies used for this purpose (Wriggers, 2002), the **Lagrange multipliers method** (LM) is found to be the most suitable for the here proposed numerical formulation.

6.3.1 Lagrange multipliers method

From the mechanical point of view, Lagrange multipliers λ can be seen as force necessary to separate bodies after the non-physical penetration (6.2) has been detected. In other words, LM denotes reaction force due to the contact constraint. In terms of energy, the contact event is here described by introducing the artificial contact energy functional Π_c, stored on the interface Γ_c (often called "parasite" contact energy). In this case, Π_c is defined by the LM work performed on the forbidden gap value g (6.2). The structure of Π_c follows by decomposing the total work of λ into its normal λ_N and tangential part λ_T. At this point, it is important to note

that the measure of *g* is relatively performed from the position where the particles intersect the boundary before penetrating inside the domain. By visualizing this trajectory, it follows that the gap vector **g** can be decomposed into its normal $\mathbf{g}_N$ and tangential part $\mathbf{g}_T$ (Fig. 6.4). It is clear that if the particle trajectory is perpendicular to Γ_c, *g* will be equal to g_N.
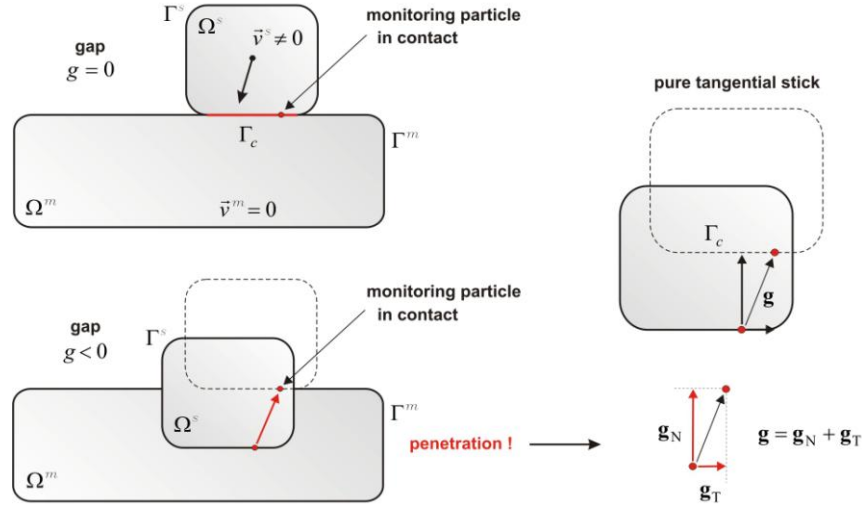
Figure 6.4 Two-dimensional gap components (contact with pure tangential stick)

The contact energy functional Π_c can be formulated as

$$\Pi_c(\lambda, g) = \int_{\Gamma_c} (\boldsymbol{\lambda}_N \cdot \mathbf{g}_N + \boldsymbol{\lambda}_T \cdot \mathbf{g}_T) \, d\Gamma_c.$$

(6.10)

In accordance with Eq. (6.8), the former functional is introduced into the weak statement by invoking its stationary value. Since the functional argument is the contact force *λ* and the related gap value *g*, the variation leads to the following contribution (6.11).

$$\delta\Pi_c(\lambda, g) = \int_{\Gamma_c} (\boldsymbol{\lambda}_N \cdot \delta\mathbf{g}_N + \boldsymbol{\lambda}_T \cdot \delta\mathbf{g}_T) \, d\Gamma_c + \int_{\Gamma_c} (\delta\boldsymbol{\lambda}_N \cdot \mathbf{g}_N + \delta\boldsymbol{\lambda}_T \cdot \mathbf{g}_T) \, d\Gamma_c$$

(6.11)

The first integral represents the virtual work performed by normal and tangential *λ* component, while the second one introduces the enforcement of the contact constraints. To introduce simplicity, the discussion is currently restricted only to the stick contact case, ignoring eventual tangential slip motion (Fig. 6.4). Therefore, the terms $\boldsymbol{\lambda}_N \cdot \delta\mathbf{g}_T$ and $\delta\boldsymbol{\lambda}_N \cdot \mathbf{g}_T$ describe the pure tangential stick case in which the tangential slip $\mathbf{g}_T$ is reduced to zero. As a consequence, $\boldsymbol{\lambda}_T$ becomes tangential reaction force. Note that the tangential traction vector $\mathbf{t}_T$ has to be determined from the adopted constitutive definition of friction. In particular, the tangential contact constraints are here included artificially by monitoring the tangential motion of FE nodes over Γ_c. The related

procedure will be discussed later. At the moment, the mentioned strategy allows to simplify the contact integral by ignoring tangential components (6.12).

$$\delta \Pi_c(\lambda, g) = \int_{\Gamma_c} (\boldsymbol{\lambda}_N \cdot \delta \mathbf{g}_N + \delta \boldsymbol{\lambda}_N \cdot \mathbf{g}_N) \, d\Gamma_c \tag{6.12}$$

Resuming, Eq. (6.12) only enforces the impenetrability contact constraint (6.2). The assumption is here required for further considerations. Therefore, it is assumed that the contact forces acts on the normal gap component $\mathbf{g}_N$ which is defined perpendicularly to the boundary Γ_c. Consequently, g has to be determined according to the *minimum distance problem*.

6.3.2 Gap & minimum distance function

Consider bodies $\boldsymbol{B}^m \subset \mathfrak{R}^3$ and $\boldsymbol{B}^s \subset \mathfrak{R}^3$ with $\Omega^m \cap \Omega^s \subset \not\in$ in their reference configuration. If bodies establish contact, the condition (6.1a) can be rewritten in terms of particle coordinates $\mathbf{x}^\kappa$ in the current configuration. Subsequently, with regard to particles interacting on boundaries Γ^m and Γ^s, the impenetrability contact condition can be express as

$$g = (\mathbf{x}^s - \mathbf{x}^m) \cdot \mathbf{n}^m \geq 0, \tag{6.13}$$

in which $\mathbf{n}^m$ represents the normal outward unit vector on Γ^m. Supposing that $\Gamma_c \subset \Gamma^m \cap \Gamma^s$ is a convex region (at least locally), to each point on Γ^s the minimum distance function d relates a point $\mathbf{x}^m$ on Γ^m via

$$d = \min_{\mathbf{x}^m} \left\| \mathbf{x}^s - \mathbf{x}^m \right\| = \left\| \mathbf{x}^s - \overline{\mathbf{x}}^m \right\|. \tag{6.14}$$

The related gap value g_N is given by (Zienkiewicz & Taylor, 2002)

$$g_N = (\mathbf{x}^s - \overline{\mathbf{x}}^m) \cdot \overline{\mathbf{n}}^m \geq 0, \tag{6.15}$$

where the unit normal vector $\overline{\mathbf{n}}^m$ is defined as

$$\overline{\mathbf{n}}^m = -\frac{\mathbf{x}^s - \overline{\mathbf{x}}^m}{\left\| \mathbf{x}^s - \overline{\mathbf{x}}^m \right\|}. \tag{6.16}$$

It should be pointed out that the distance function d (6.14) is sometimes locally non-differentiable. The property depends on the boundaries in contact. In particular, it may happen that the projection of point $\mathbf{x}^s$ is not unique. However, in practical applications such discontinuities do not have great influence. Indeed, the non-differentiable property can be by-passed by appropriate numerical techniques (Wriggers, 2002).

As the weak form (6.12) requires first variation of g_N, and the gap value is a function of displacements (6.15), the first variation will produce (Parisch, 1989):

$$\delta g_N = (\mathbf{x}^s - \overline{\mathbf{x}}^m) \cdot \delta \overline{\mathbf{n}}^m + (\delta \mathbf{u}^s - \delta \overline{\mathbf{u}}^m) \cdot \overline{\mathbf{n}}^m. \tag{6.17}$$

Since $\delta \mathbf{n}$ is perpendicular to $\mathbf{n}$ (orthogonality), the first term on the RHS is equal to zero (Wriggers, 2002). The other term, associated to particles with coordinates $\mathbf{x}^s$ and $\overline{\mathbf{x}}^m$, indicates the admissible variations of particles displacements.

6.3.3 Variational formulation

In order to retrieve the FE approximation of displacement field for bodies under contact/impact, the variational formulation of the constrained Eq. of motion is needed. For this purpose, assume that the contact surface Γ_c is known in the reference configuration. In such case, the *active set of contact constraints* will be known, enabling to form the constrained weak form of equilibrium within Δt. Therefore, according to Eq. (6.9) and Eq. (6.12), the frictionless variational formulation becomes

$$\sum_{\kappa=1}^{2} \left\{ \int_{\Omega^\kappa} \delta u_i^\kappa \rho^\kappa \ddot{u}_i^\kappa \, d\Omega^\kappa + \int_{\Omega^\kappa} \delta u_{i,j}^\kappa \sigma_{ij}^\kappa \, d\Omega^\kappa - \int_{\Omega^\kappa} \delta u_i^\kappa b_i^\kappa \, d\Omega^\kappa - \int_{\Gamma_t^\kappa} \delta u_i^\kappa \bar{t}_i^\kappa \, d\Gamma_t^\kappa \right\} + \dots$$

$$\dots + \int_{\Gamma_c} (\lambda_{Ni} (\delta u_i^s - \delta \overline{u}_i^m)) \, d\Gamma_c + \int_{\Gamma_c} (\delta \lambda_{Ni} g_{Ni}) \, d\Gamma_c = 0, \tag{6.18}$$

where δu_i are test functions which are set to vanish on boundaries $d\Gamma_u$ where the displacements are prescribed. The given weak form defines the deformation mapping functions φ^κ (2.9), such that Eq. (6.18) is satisfied for all $\delta u^\kappa \in \mathcal{P}$ where

$$\mathcal{P} = \left\{ (\delta u_i^m, \delta u_i^s) \in \mathcal{V}^h \mid \left[\delta u_i^s - \delta \overline{u}_i^m \right] \cdot \overline{n}_i^m \geq 0 \right\}, \tag{6.19}$$

in which the space $\mathcal{V}^h$ is the same as the one previously introduced in Eq. (3.23).

6.4 FE formulation

The FE simulation of contact events is related to many difficulties. The first obstacle arises from the spatial discretization that involves the approximation of original smoothed boundary with linear FE boundaries (Fig. 3.1). As a consequence, it may occur that for the FE edge which is defined by two penetrated nodes, the edge remain in contact even after the edge nodes are remove from it. Such issue gave origin to different strategies developed to reach an adequate solution (e.g. edge-edge contact element). The second obstacle is particularly

present in contact analysis accompanied with large deformation. Namely, due to the discrete FE environment, the normal vectors between elements cannot be continuously defined. In other words, the FE surfaces over Γ_c have non-unique normal vectors.

In order to overcome the mentioned difficulties, the so-called *smoothed contact description* can be applied. The principal idea is to replace the flat FE boundary by a smoothed surface approximation usually generated by *Bezier interpolations* (Wriggers, 2002). In this case, the contact constraints have to be satisfied on this smoothed Γ_c approximation. However, for the sake of simplicity, in the proposed numerical formulation the flat nature of FE boundaries is retained and the smoothed contact description is not considered.

6.4.1 Spatial discretization

Differently from the strong and weak form, in FE form the enforcement of contact constraints is carried out discretely. Namely, since the mesh boundaries are represented by finite number of flat surfaces, the contact constraints violations are measured only on specific locations. Commonly, the mesh boundary nodes are used for this purpose (Fig. 6.5). However, mentioned that expect the FE nodes, the element edges and surfaces can be also used to define mesh interaction.
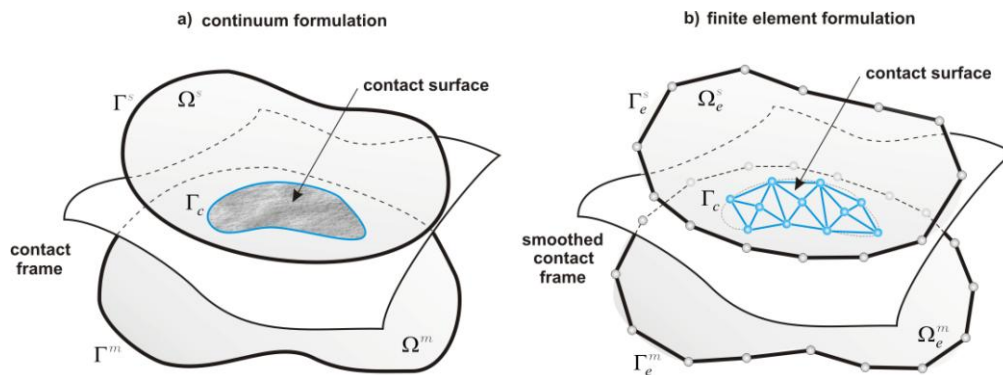
Figure 6.5 Contact surface between: **a)** two continuum bodies and **b)** two bodies approximated by FE

In FE analysis the element nodes, edges and surfaces are universally denoted as *finite element design objects*. Obviously, the interaction between different design objects is possible. It follows that the most robust description of contact will be obtained by taking into account the interaction between all design objects. On the other hand, the related contact description becomes complicated and it usually required only in cases of continuum fragmentation problems. The need is evident since the number of design objects that can interact in between rapidly grows during mesh fragmentation. However, to retain simplicity and due to the fact that the fragmentation process is here avoided, the proposed numerical formulation evidence meshes interaction only in FE nodes. Indeed, as the concrete fracturing process is here modeled by the formerly discussed smeared cracking concept (*Chapter 5 – 5.1 Introduction*), the strategy is well justified.

_____

There is another important consequence on using FE for contact analysis. To evidence it, emphasize that the real contact surface is approximated by flat tetrahedral elements (Fig. 3.2). Under this circumstance, the following important question should be answer.

How fine should be discretized the boundaries of bodies in contact, in order to reproduce real interface behavior, as well as the contact surface geometry?

Well, it is obvious that by increasing the number of design objects over Γ_c, the result will lead to a better description of interface phenomena. On the other hand, it is also well-known that the procedure dramatically increases the computational time. Therefore, the problem is usually solved by an engineering estimation, making a compromise between these extremes. The aforementioned serves as the argument to justify the interface discretization used in the later presented numerical examples (*Chapter 10 – Numerical examples*).

Before proceeding it is opportune to introduce some typical notations used for the contact analysis and permits to simplify the description of the contact resolution stage (Fig. 6.1). For this purpose, consider two bodies in contact. The related FE discretizations are often referred to as *master* and *slave discretizations*. According to that, the spatial discretization of a concrete body will be referred to as a master discretization (*master body*). The body that induces impact load will be denoted as *slave body* (e.g. impact hammer). Note the correspondence with the earlier introduced notations m and s.

Furthermore, consider the FE nodes on the boundary Γ_c where the contact constraints violations are evidenced (Fig. 6.5). In the proposed numerical formulation the registered violations are discretely treated by adopting the so-called *node-to-segment contact resolution strategy*. In this case, for a given slave node that breaches the prescribed contact conditions (6.1), the node-to-segment strategy involves the activation of contact constraints fulfillment in a set of boundary nodes on the master body. Particularly, for a spatial discretization performed by linear tetrahedral element (*Chapter 3 – 3.3 Linear tetrahedral element*), each slave node is related to three master nodes that describe a flat triangular boundary surface. At this point, note that each boundary surface can be hit with more than one slave node. The nodes that are involved in the contact form one *contact element* and are usually denoted as *contact element nodes*. Also, during the contact element assimilation, it is a usual practice to denote the slave node as the *contractor node* and the related master surface, as the *target surface*.

Finally, it should be pointed out that for contact analysis with FE, the contact constraints are not satisfied in advance. Namely, as earlier mentioned, the contact surface Γ_c is not known a priori. It arises from the contact constraint fulfillment prescribed upon FE nodes. Consequently, it can be said that the contact problem in the FE environment is retroactive.

6.4.1.1 Contact surface parameterization

In order to obtain the FE approximation of a displacement field for bodies in contact/impact, the discrete nature of mechanical interaction in the FE environment should be examined. For this purpose, a uniquely local coordinate system is defined for each target surface. In other words, the parameterization of the real continuous surface, originally described by curvilinear coordinates, is introduced (Fig. 6.6).
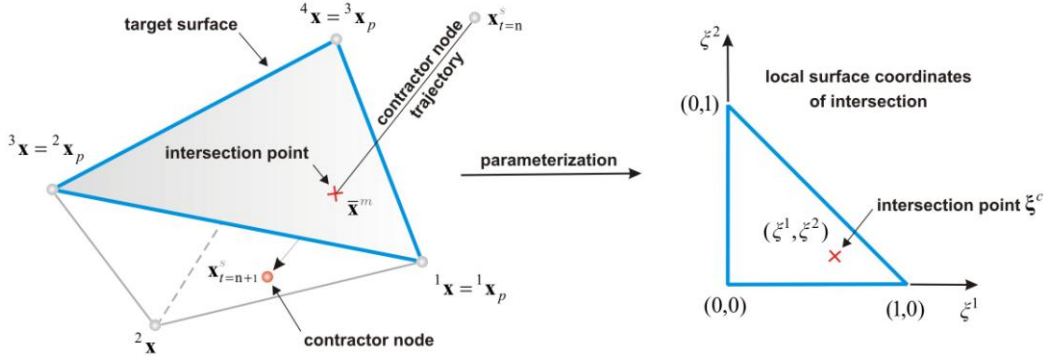
Figure 6.6 Target surface parameterization: **a)** intersection point in global and **b)** local coordinates

The parameterization enables to relate an arbitrary intersection point $\bar{\mathbf{x}}^m$ on the target surface to local surface coordinates $\boldsymbol{\xi}=\{\xi^1,\xi^2\}^{\mathrm{T}}$. According to Eq. (3.62), the relationship is carried out by the element nodal coordinates $^c\mathbf{x}_p$ and respective nodal shape functions N_c^p as

$$\bar{\mathbf{x}}^m = \sum_{c=1}^{3} N_c^p(\xi^1,\xi^2)\,{}^c\mathbf{x}_p, \tag{6.20}$$

where c stands for quantities related to nodes on target surface ($c=1,2,3$). In order to describe the geometry of each target surface, the tangent vectors at a position $\boldsymbol{\xi}=\{\xi^1,\xi^2\}^{\mathrm{T}}$ are given as

$$\bar{\mathbf{a}}_\alpha = \frac{\partial\,^i\mathbf{x}}{\partial\xi^1} \qquad \text{and} \qquad \bar{\mathbf{a}}_\beta = \frac{\partial\,^i\mathbf{x}}{\partial\xi^2}. \tag{6.21}$$

The corresponding unit vectors are specified as

$$\mathbf{a}_\alpha = \frac{\bar{\mathbf{a}}_\alpha}{\left\|\bar{\mathbf{a}}_\alpha\right\|} \qquad \text{and} \qquad \mathbf{a}_\beta = \frac{\bar{\mathbf{a}}_\beta}{\left\|\bar{\mathbf{a}}_\beta\right\|}, \tag{6.22}$$

and the unit normal vector as

$$\mathbf{n} = \frac{\bar{\mathbf{a}}_\alpha \times \bar{\mathbf{a}}_\beta}{\left\|\bar{\mathbf{a}}_\alpha \times \bar{\mathbf{a}}_\beta\right\|}. \tag{6.23}$$

The metric of the target surface can be defined by components of the *covariant metric tensor* $m_{\alpha\beta}$ (Kloosterman, 2002; Wriggers, 2002) which are given by the dot product of the basic vectors in Eq. (6.22) as

$$m_{\alpha\beta} = \bar{\mathbf{a}}_\alpha \cdot \bar{\mathbf{a}}_\beta .$$

(6.24)

Similarly, the components of the *contravariant metric tensor* $m^{\alpha\beta}$ are determined by

$$m^{\alpha\beta} = (m_{\alpha\beta})^{-1},$$

(6.25)

which provides the transition between complementary tangential systems via

$$\bar{\mathbf{a}}^\alpha = m^{\alpha\beta}\, \bar{\mathbf{a}}_\beta .$$

(6.26)

Since contact problems always involves a non-linear load-displacement curve (even for small deformation of elastic solids), the given geometrical quantities are necessary to obtain the linearized form of Π_c in Eq. (6.18). The procedure is discussed hereafter.

6.4.1.2   *Consistent tangent stiffness matrix*

To derive the consistent contact tangent matrix, the relationship between δg_{N} and $\delta \xi$ must be determined. For this purpose consider the gap function

$$\mathbf{x}^s - \bar{\mathbf{x}}^m(\xi) - g_{\mathrm{N}}\,\bar{\mathbf{n}}^m = \mathbf{x}^s - \sum_{c=1}^{3} N_c^p(\xi)\, {}^c\mathbf{x}_p - g_{\mathrm{N}}\,\bar{\mathbf{n}}^m = 0,$$

(6.27)

in which $\mathbf{x}^s$ denotes the coordinates of a penetrated node while $\bar{\mathbf{x}}^m(\xi)$ denotes the coordinates of a point on the target plain (Fig. 6.6). According to the former Eq., the relationship between δg_{N} and $\delta \xi$ is obtained via (Wriggers, 2002)

$$\bar{\mathbf{n}}^m \delta g_{\mathrm{N}} + \bar{\mathbf{a}}_\alpha \delta \xi^1 + \bar{\mathbf{a}}_\beta \delta \xi^2 = \delta \mathbf{x}^s - \sum_{c=1}^{3} N_c^p(\xi)\, {}^c\mathbf{x}_p - g_{\mathrm{N}}\delta \bar{\mathbf{n}}^m ,$$

(6.28)

from where it follows that

$$(\bar{\mathbf{n}}^{m\mathrm{T}}\bar{\mathbf{n}}^m)\delta g_{\mathrm{N}} = \bar{\mathbf{n}}^{m\mathrm{T}}\left(\delta \mathbf{x}^s - \sum_{c=1}^{3} N_c^p(\xi)\, {}^c\mathbf{x}_p - g_{\mathrm{N}}\delta \bar{\mathbf{n}}^m \right),$$

(6.29)

or in a matrix notation:

$$\delta g_{\mathrm{N}} = \delta \hat{\mathbf{x}}^{\mathrm{T}}\, \hat{\mathbf{U}}_c ,$$

(6.30)

where

$$
\hat{\mathbf{U}}_c = \begin{Bmatrix} -N_1^p(\xi)\,\overline{\mathbf{n}}^{\,m} \\ -N_2^p(\xi)\,\overline{\mathbf{n}}^{\,m} \\ -N_3^p(\xi)\,\overline{\mathbf{n}}^{\,m} \\ \overline{\mathbf{n}}^{\,m} \end{Bmatrix}
\quad \text{and} \quad
\delta\hat{\mathbf{x}} = \begin{Bmatrix} \delta^1\mathbf{x}_p \\ \delta^2\mathbf{x}_p \\ \delta^3\mathbf{x}_p \\ \delta\mathbf{x}^s \end{Bmatrix}.
\tag{6.31}
$$

Evidently the vector $\hat{\mathbf{U}}_c$ performs the distribution of contact influence across the contact element nodes (Zienkiewicz & Taylor, 2002). Assuming frictionless contact conditions, the variation of the contact integral in Eq. (6.10) may be now written as

$$
\delta\Pi_c = \begin{bmatrix} \delta\hat{\mathbf{x}} & \delta\lambda_{\mathrm{N}} \end{bmatrix} \begin{Bmatrix} \lambda_{\mathrm{N}}\hat{\mathbf{U}}_c A_c \\ g_{\mathrm{N}} A_c \end{Bmatrix},
\tag{6.32}
$$

where A_c denotes the contact surface area i.e. area of integration. The consistent contact tangent matrix arises from the linearization of the variational form of the contact integral in Eq. (6.12). The linearization produces (Zienkiewicz & Taylor, 2002):

$$
\Delta(\delta\Pi_c) = (\delta g_{\mathrm{N}}\Delta\lambda_{\mathrm{N}} + \delta\lambda_{\mathrm{N}}\Delta g_{\mathrm{N}} + \lambda_{\mathrm{N}}\Delta(\delta g_{\mathrm{N}}))A_c,
\tag{6.33}
$$

in which the gap value Δg_{N} can be now obtained according to Eq. (6.29), by simply replacing the variation δ with Δ. Furthermore, the linearized term $\Delta(\delta g_{\mathrm{N}})$ follows from Eq. (6.17) as

$$
\Delta(\delta g_{\mathrm{N}}) = -\delta\overline{\mathbf{u}}_{,\gamma}^{\,m} \cdot \Delta\xi^\gamma + (\delta\mathbf{u}^s - \delta\overline{\mathbf{u}}^{\,m}) \cdot \Delta\overline{\mathbf{n}}^{\,m},
\tag{6.34}
$$

where $\delta\overline{\mathbf{u}}_{,\gamma}^{\,m}$ denotes the differentiation with respect to ξ^γ, where $\gamma=1,2$ (Wriggers, 2002). Due to the fact that the normal vector is perpendicular to the tangent vectors (6.21), it follows that

$$
\Delta\overline{\mathbf{n}}^{\,m} = \Delta\frac{\overline{\mathbf{a}}_\alpha \times \overline{\mathbf{a}}_\beta}{\left\| \overline{\mathbf{a}}_\alpha \times \overline{\mathbf{a}}_\beta \right\|} = -\overline{\mathbf{a}}_\alpha\, m^{\alpha\beta}(\Delta\overline{\mathbf{a}}_\beta \cdot \overline{\mathbf{n}}^{\,m}) = -m^{\alpha\beta}\left[\mathbf{a}_\alpha \otimes \overline{\mathbf{n}}^{\,m} \right]\Delta\overline{\mathbf{a}}_\beta,
\tag{6.35}
$$

in which the linearized tangent vectors are defined as

$$
\Delta\overline{\mathbf{a}}_\alpha = \Delta\mathbf{u}_2 - \Delta\mathbf{u}_1 \quad \text{and} \quad \Delta\overline{\mathbf{a}}_\beta = \Delta\mathbf{u}_3 - \Delta\mathbf{u}_1.
\tag{6.36}
$$

Following the earlier introduced notations, $\Delta\mathbf{u}_c$ denotes the incremental displacement vector of nodes on the target surface ($c=1,2,3$). For flat target surface, the linearized terms in Eq. (6.35) and Eq. (6.36) lead to the linearized gap variation, such that (Wriggers, 2002)

_____

$$\Delta(\delta g_{\mathrm{N}}) = -\Delta\xi^{\gamma}\,\delta\overline{\mathbf{u}}_{,\gamma}^{m}\cdot\overline{\mathbf{n}}^{m} - m^{\alpha\beta}(\delta\mathbf{u}^{s} - \delta\overline{\mathbf{u}}^{m})\cdot\left[\mathbf{a}_{\alpha}\otimes\overline{\mathbf{n}}^{m}\right]\Delta\overline{\mathbf{a}}_{\beta}\,, \tag{6.37}$$

in which the linearization of ξ is given by

$$\Delta\xi^{\alpha} = m^{\alpha\beta}\left[(\Delta\mathbf{u}^{s} - \Delta\overline{\mathbf{u}}^{m})\cdot\overline{\mathbf{a}}_{\beta}\right] + g_{\mathrm{N}}\overline{\mathbf{n}}^{m}\cdot\Delta\overline{\mathbf{a}}_{\beta}\,. \tag{6.38}$$

The vectors $\Delta\mathbf{u}^{s}$ and $\Delta\overline{\mathbf{u}}^{m}$ represent the incremental displacement vectors for slave node and the closets point on the target surface, respectively. Finally, the linearization of the contact contribution $\delta\Pi_{c}$ in Eq. (6.18) can be obtained by combining Eq. (6.37) and Eq. (6.38). Accordingly, the contribution of one contact element to the total tangent stiffness matrix will produce a symmetric matrix as (Wriggers, 2002)

$$\mathbf{K}_{\mathrm{T}}^{c} = -\begin{bmatrix} \mathbf{N}_{1}\otimes\mathbf{T}_{1} + \mathbf{N}_{2}\otimes\mathbf{T}_{2} + \mathbf{T}_{1}\otimes\mathbf{N}_{1} + \mathbf{T}_{2}\otimes\mathbf{N}_{2} + \ldots \\[2mm] \ldots + g_{N}\left[m^{11}\mathbf{N}_{1}\otimes\mathbf{N}_{1} + m^{12}\left[\mathbf{N}_{1}\otimes\mathbf{N}_{2} + \mathbf{N}_{2}\otimes\mathbf{N}_{1}\right] + m^{22}\mathbf{N}_{2}\otimes\mathbf{N}_{2}\right] \end{bmatrix}, \tag{6.39}$$

where

$$\mathbf{N}_{\alpha} = \begin{Bmatrix} -N_{1,\alpha}^{p}\,\overline{\mathbf{n}}^{m} \\ -N_{2,\alpha}^{p}\,\overline{\mathbf{n}}^{m} \\ -N_{3,\alpha}^{p}\,\overline{\mathbf{n}}^{m} \\ 0 \end{Bmatrix} \quad\text{and}\quad \mathbf{T}_{\alpha} = \begin{Bmatrix} -N_{1}^{p}\,\overline{\mathbf{a}}_{\beta}\,m^{\alpha\beta} \\ -N_{2}^{p}\,\overline{\mathbf{a}}_{\beta}\,m^{\alpha\beta} \\ -N_{3}^{p}\,\overline{\mathbf{a}}_{\beta}\,m^{\alpha\beta} \\ \overline{\mathbf{a}}_{\beta}\,m^{\alpha\beta} \end{Bmatrix}. \tag{6.40}$$

With the linearized form of the contact contribution in Eq. (6.18), the incremental loadings can be related to incremental displacements through (Zienkiewicz & Taylor, 2002)

$$\Delta(\delta\Pi_{c}) = \begin{bmatrix} \delta\hat{\mathbf{x}}^{\mathrm{T}} & \delta\lambda_{\mathrm{N}} \end{bmatrix}\begin{bmatrix} \lambda_{\mathrm{N}}\mathbf{K}_{\mathrm{T}}^{c} & \hat{\mathbf{U}}_{c} \\ \hat{\mathbf{U}}_{c} & 0 \end{bmatrix}\begin{Bmatrix} \Delta\hat{\mathbf{x}} \\ \Delta\boldsymbol{\lambda}_{\mathrm{N}} \end{Bmatrix}. \tag{6.41}$$

Evidently, the LM method introduces an additional unknown for each contact element. Therefore, the system of Eq. (6.41) will linearly increase with increasing the number of contacts. From the perspective of computational effort, this property makes the LM method improper for practical applications. However, apart this inconvenient property, note that the method enable to enforce the contact conditions exactly and unconditionally. This is not the case for other techniques. Namely, an alternative strategy, that will bypass this negative side effect, could be the he *penalty regularization technique* (Wriggers, 2002). In this case, the contact conditions are satisfied conditionally but without increasing the number of DOF in the system. It should be also mentioned that the LM method produces zeros on a part of the diagonal of the tangent matrix. However, the *perturbed Lagrangian method* can be adopted to avoid division by zero (Zienkiewicz & Taylor, 2002). Finally, note that the contact tangent matrix is associated to local DOF. Therefore, in order to affect a set of global DOF, the assembling operator **A** is invoked (3.38).

6.4.1.3 Note on contact interface velocity

To illustrate an important fact, consider particles *A* and *B* attached to body *a* and *b*, respectively. Assume that the velocity vector of body *b* define a collision trajectory with the standstill body *a*. Furthermore, imagine relatively small time increments d*t*. Upon the occurrence of the first contact (particles lying on each other on Γ_c), it is reasonable to expect that the velocity of the particle *B* will gradually decrease. On the other hand, due to the transfer of kinetic energy, the velocity of the particle *A* will gradually increase. Resume that the particles are in contact. At this point, one may ask: *How is it possible that two material points, which are in contact, have different velocities?* Well, at the micromechanical level the particles are not continuously in contact as can be presupposed by observing the macroscopic level. Actually, once the velocity of particle *a* reach the velocity of particle *b* (Fig. 6.7a), the velocities of both particles decrease continuously but with different fluctuations around the average velocity (Fig. 6.7b). This behaviour of velocities on Γ_c is present due to the influence of inertial forces on the contact surface. Indeed, the oscillatory behavior can vary in frequency and depends on the mechanical and kinematical properties of bodies under impact.
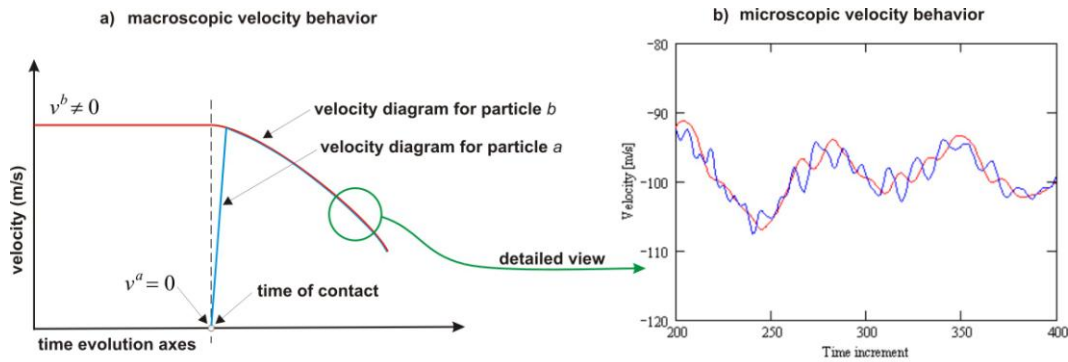
Figure 6.7 Change in velocity due to impact: **a)** macroscopic point of view and **b)** microscopic point of view

Mention that the proposed three-dimensional numerical formulation predicts this scenario. As will be later presented (*Chapter 10 – 10.3.2.2 Contact force, force equilibrium and reactions*), the evaluated contact forces suffer high-frequency oscillations, which is directly caused by the character of particles velocities on Γ_c.

Furthermore, an additional observation can be made. As the velocities of particles on Γ_c are locally different (Fig. 6.7b), the time evolution causes continuous separations and reestablishes interactions. Obviously, the occasional separation of particles leads to no contact forces. As the particles separation is not simultaneous, the fluctuation of the total contact force is reasonable. However, due to this complex interface behavior, there aren't experimental observations that could confirm this scenario which is here predicted numerically. Therefore, since the fluctuations cannot be validated, the later presented results should be viewed as a qualitative description of the discussed phenomenon.

6.4.1.4   Contact force interpolation

Even for discretizations in which the mesh nodes over Γ_c coincide in their initial configurations, large sliding contact will cause relatively large tangential displacement and produce *non-matching* meshes over Γ_c. As a consequence, the difference between discretizations of Γ_c can harm the earlier discussed continuity requirement prescribed for the stress field (6.6). Basically, the requirement will be met if the contact forces on the mesh boundaries Γ_c are balanced (Fig. 6.3). In order to activate the forces equilibrium between non-matching meshes, the interpolation of Lagrange multipliers should be considered. It is evident that the contact force interpolation in Eq. (6.30) is performed consistently with Eq. (3.61) and Eq. (3.62). Therefore, at a certain point on the target surface, $\boldsymbol{\lambda}$ can be interpolated as (isoparametric property)

$$\boldsymbol{\lambda} \approx \sum_{c=1}^{3} N_c^p(\boldsymbol{\xi})\,\boldsymbol{\lambda}_c\,, \tag{6.42}$$

where $\boldsymbol{\lambda}_c$ denotes the contact force vector associated to target plane node c. As may be perceived, for the here adopted FE the contact force is linearly distributed across the surface Γ_c. However, Eq. (6.42) is efficient only if the discretizations are not significantly different (Fig. 6.3). In an extreme case, the differences among mesh boundaries will produce not coinciding force fields $\boldsymbol{\lambda}$ on both side of Γ_c. In this case, that requirement for equilibrium cannot be satisfy. Thus, the used approximation is reasonable only if the expected displacements are relatively small. However, for large tangential displacement (e.g. penetration and body perforation problems), the remeshing procedure can be use to progressively adapt the meshes interface, compensating the non-matching meshes. Note also that there are other strategies that can be use for bypass the non-matching deviations. Particularly, the so-called *mortar method* (Wriggers, 2002) is based on introducing an additional discretization; for the purpose of separately interpolate the contact forces field between the bodies. The performance of the strategy is evident in the Taylor and Papadopoulos patch test (Crisfield, 2000).

6.4.1.5   FE form of equilibrium

In order to introduce the impenetrability contact condition into the discrete Eq. (4.13), the variational form of the contact energy functional should be discretized. Accordingly, the first term in Eq. (6.12), which represents the contribution of virtual work done by contact forces, is approximated as

$$\boldsymbol{\lambda}_{\mathrm{N}}\,\delta\mathbf{g}_{\mathrm{N}} \approx \left\{\delta\mathbf{u}^c\right\}^{\mathrm{T}}\mathbf{G}^{\mathrm{T}}\boldsymbol{\lambda}_{\mathrm{N}}\,. \tag{6.43}$$

In this Eq. $\delta\mathbf{u}^c$ collects the displacement variations as

$$\left\{\delta\mathbf{u}^c\right\} = \left\{ \delta^1 u_1^m \quad \delta^1 u_2^m \quad \delta^1 u_3^m \quad \dots \quad \delta^3 u_1^m \quad \delta^3 u_2^m \quad \delta^3 u_3^m \quad \delta u_1^s \quad \delta u_2^s \quad \delta u_3^s \right\}^{\mathbf{T}}, \tag{6.44}$$

and the so-called *contact displacement matrix* **G** arises in accordance with Eq. (6.31) as

$$
-\begin{bmatrix}
N_1^p(\xi) & 0 & 0 & N_2^p(\xi) & 0 & 0 & N_3^p(\xi) & 0 & 0 & -1 & 0 & 0 \\
0 & N_1^p(\xi) & 0 & 0 & N_2^p(\xi) & 0 & 0 & N_3^p(\xi) & 0 & 0 & -1 & 0 \\
0 & 0 & N_1^p(\xi) & 0 & 0 & N_2^p(\xi) & 0 & 0 & N_3^p(\xi) & 0 & 0 & -1
\end{bmatrix}. \tag{6.45}
$$

The matrix components are related to local DOF and can be translated into global notation by the assembling operator **A** (3.38). Note that the matrix components are unknown *a-priori*. Namely, during the deformation path evolution, **G** will vary due to the variations in contact position ξ. In such case, an external procedure is needed to monitor the nodal displacements and to adequately adapt **G** as contact occurs (*Chapter 7 – Contact detection*). It is important to note that the contact forces $\{\mathbf{G}^T \cdot \boldsymbol{\lambda}_N\}$ should not be viewed as a part of external forces. As the force value depends on deformation (i.e. displacements), it is part of internal forces. The second term in Eq. (6.12) denotes the weak form of impenetrability constraint. The related FE expression can be written as

$$
\mathbf{g}_N = \mathbf{G}\{\mathbf{u} + \mathbf{X}\} = \mathbf{0}, \tag{6.46}
$$

in which **u** represents the incremental nodal displacements while **X** represents the coordinates vector in the reference configuration. The equation can be literally interpreted as follows. After adding the displacement vector **u** to material coordinates **X**, no mesh interpenetration can occur ($\mathbf{g}_N = \mathbf{0}$). The final form of the constrained Eq. of motion can be obtained by introducing the contact force approximation (6.43) into Eq. (4.13) and demanding the fulfillment of the impenetrability condition (6.46). The procedure will give:

$$
\mathbf{M}\ddot{\mathbf{u}} + \mathbf{C}\dot{\mathbf{u}} + \mathbf{F}^{in} + \mathbf{G}^T\boldsymbol{\lambda}_N = \mathbf{F}^{ex}(t), \tag{6.47a}
$$

$$
\mathbf{G}\{\mathbf{u} + \mathbf{X}\} = \mathbf{0}. \tag{6.47b}
$$

Eq. (6.47a) denotes the force equilibrium in contact and the second one (6.47b) ensures the fulfillment of impenetrability condition (6.2). However, since the temporal discretization is not yet involved, Eq. (6.47) represents the semi-discrete Eq. of motion. Analogically to Eq. (6.41), the LM method introduces $\boldsymbol{\lambda}_N$ as an additionally unknown which can be determined by solving Eq. (6.47a) and Eq. (6.47b) simultaneously. It should be mentioned that the RHS of Eq. (6.47a), i.e. external force vector, is here assumed equal to zero. Namely, the presence of forces on the LHS arises from the second Newton law, as a consequence of change in linear momentum in time when contact occurs. Accordingly, Eq. (6.47a) can be rewritten as

$$
\mathbf{M}\ddot{\mathbf{u}} + \mathbf{C}\dot{\mathbf{u}} + \mathbf{F}^{in} = -\mathbf{G}^T\boldsymbol{\lambda}_N. \tag{6.48}
$$

It will be interesting to see the contribution of forces on the LHS in reaching equilibrium state with contact forces on the RHS (*Chapter 10 – 10.3.2.2 Contact force, force equilibrium and reactions*).

_____

6.4.2 Temporal discretization

In order to obtain the fully discrete Eq. of motion, the dependent variables should be approximated by an appropriated time integration technique. For this purpose, note that all the assumptions and approximations discussed earlier (*Chapter 4 – 4.3.1 Assumption, approximations and errors*) are also valid for the here considered FE contact/impact description. Furthermore, in order to gradually discuss the numerical description of friction, it is opportune to introduce a short observation on λ. In contrast to the above assumptions (6.12), the arbitrary direction of contact force λ will be further considered. Accordingly, depending on the spatial orientations of a particular target surface (6.22), the total magnitude of λ will be split into its normal λ_N and tangential component λ_T (6.49).

$$\lambda = \lambda_N + \lambda_T \tag{6.49}$$

6.4.2.1 Implicit time integration

Resume that for events which are here under consideration (impact and blast loadings), the deformation history is "trapped" in a relatively short period of time (*Chapter 1 – 1.1 Motivation*). For this purpose, to evidence some inappropriate properties of the implicit time integration, and to justify the here adopted explicit time integration, a briefly discussion on the first one is introduced. At the moment, mention also that the original form of the explicit time integration is inappropriate as well. However, there are assumptions that introduce the needed modifications and will be discussed later on.

According to the Newmark single-step methods, which can reproduce both explicit and implicit time integration, the dependent variables in Eq. (6.47) are discretized in time as

$$\mathbf{M}\,\ddot{\mathbf{u}}_{n+1} + \mathbf{C}\,\dot{\mathbf{u}}_{n+1} + \mathbf{K}\,\mathbf{u}_{n+1} + \mathbf{G}_{n+1}^{\mathrm{T}}\,\lambda_{n+1} = \mathbf{0}, \tag{6.50a}$$

$$\mathbf{G}_{n+1}\left\{\mathbf{u}_{n+1} - \mathbf{u}_n + \mathbf{X}_n\right\} = \mathbf{0}. \tag{6.50b}$$

The system of Eq. determinates the unknown displacement vector $\mathbf{u}_{n+1}$ and force vector λ_{n+1} at the end of the time increment Δt. In order to obtain these vectors, the second order direct time integration operators are here assumed as (Carpenter, Taylor & Katona, 1991)

$$\begin{aligned}
\mathbf{u}_{n+1} &= \mathbf{q}_0 + b_0\,\Delta\ddot{\mathbf{u}}_{n+1}, \\
\dot{\mathbf{u}}_{n+1} &= \mathbf{q}_1 + b_1\,\Delta\ddot{\mathbf{u}}_{n+1}, \\
\ddot{\mathbf{u}}_{n+1} &= \mathbf{q}_2 + b_2\,\Delta\ddot{\mathbf{u}}_{n+1},
\end{aligned} \tag{6.51}$$

where

$$\mathbf{q}_0 = \mathbf{u}_n + \Delta t\, \dot{\mathbf{u}}_n + \frac{1}{2}\Delta t^2\, \ddot{\mathbf{u}}_n\,,$$

$$\mathbf{q}_1 = \dot{\mathbf{u}}_n + \Delta t\, \ddot{\mathbf{u}}_n\,, \tag{6.52}$$

$$\mathbf{q}_2 = \ddot{\mathbf{u}}_n\,.$$

The integration constants are given as functions of integration parameters β and γ (6.53).

$$b_0 = \frac{1}{2}\Delta t^2 \beta \tag{6.53a}$$

$$b_1 = \Delta t\, \gamma \tag{6.53b}$$

$$b_2 = 1 \tag{6.53c}$$

The integration operator corresponds to the *Beta-2 method*, which is a subset of the *generalized Beta-m method* (Carpenter, Taylor & Katona, 1991). Furthermore, by substituting Eq. (6.51) into Eq. (6.50), the incremental Eq. of motion can be rewritten in compact form as

$$\begin{bmatrix} \left[b_2\,\mathbf{M} + b_0\,\mathbf{K}_T \right] & \mathbf{G}_{n+1}^{T} \\ b_0\mathbf{G}_{n+1} & \mathbf{0} \end{bmatrix} \begin{Bmatrix} \Delta\ddot{\mathbf{u}}_{n+1} \\ \Delta\boldsymbol{\lambda}_{n+1} \end{Bmatrix} = \begin{Bmatrix} -\left\{ \mathbf{M}\mathbf{q}_2 + \mathbf{K}_T\,\mathbf{q}_0 \right\} \\ -\mathbf{G}_{n+1}\left\{ \mathbf{q}_0 + \mathbf{X} \right\} \end{Bmatrix}. \tag{6.54}$$

By assuming $\beta = 0$ and $\gamma = 0.25$, which corresponds to the *constant-average-acceleration method* (also known as trapezoidal rule), the system of Eq. is integrated in an implicit manner. Now, from the perspective of the thesis subject, the inappropriate properties follow from (6.54). Namely, note that during the solution process, the zero on the matrix diagonal can lead to division by zero. However, this is a minor problem which can be bypassed by the *perturbed Lagrangian method* (Wriggers, 2002).
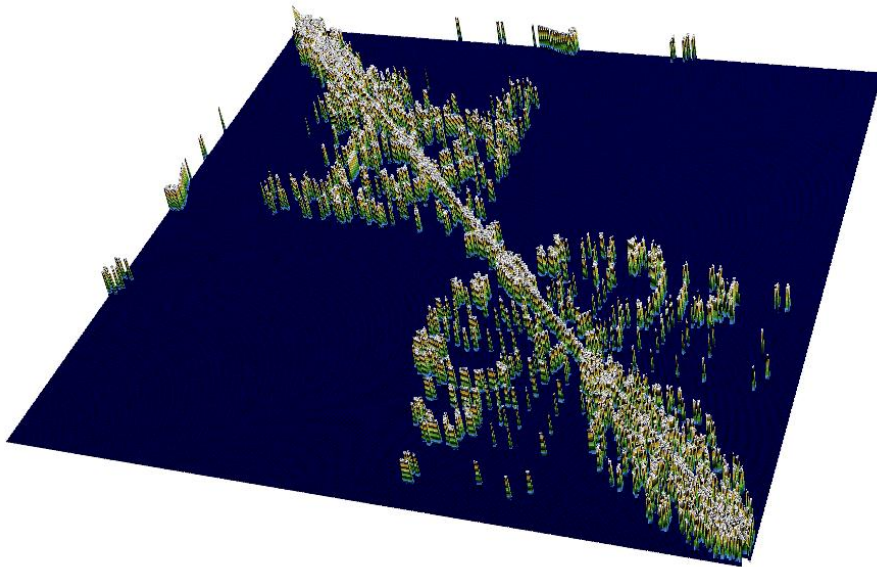

Figure 6.8 Spectral view of coefficient matrix obtained by implicit time integration

Furthermore, the assumed parameters of integration will produce a non-symmetric coefficient matrix (6.54). The matrix skew property will influence the solution strategy needed to obtaining the unknown vectors $\mathbf{u}_{n+1}$ and $\boldsymbol{\lambda}_{n+1}$. However, as a main obstacle, note that the contact constraints contributions (introduced by $\mathbf{G}$) considerably increase the bandwidth of the matrix (Fig. 6.8). As a consequence, the implicit time integration will requires a considerable amount of memory space and CPU time. On the other hand, due to the fact that highly non-linear events will require considerable number incremental steps, the uncoupled system of Eq. is here needed. For this purpose, the explicit time integration is further considered.

6.4.2.2   Explicit time integration

By setting $\beta = 0$ and $0 \le \gamma \le 1$ the integration of Eq. (6.54) becomes explicit giving

$$\underbrace{\begin{bmatrix} \begin{bmatrix} b_2\,\mathbf{M} + \mathbf{0} \end{bmatrix} & \mathbf{G}_{n+1}^{\mathrm{T}} \\ \mathbf{0} & \mathbf{0} \end{bmatrix}}_{\text{singular matrix}} \begin{Bmatrix} \Delta\ddot{\mathbf{u}}_{n+1} \\ \Delta\boldsymbol{\lambda}_{n+1} \end{Bmatrix} = \begin{Bmatrix} -\{\mathbf{M}\,\mathbf{q}_2 + \mathbf{K}_{\mathrm{T}}\,\mathbf{q}_0\} \\ -\mathbf{G}_{n+1}\{\mathbf{q}_0 + \mathbf{X}\} \end{Bmatrix}. \tag{6.55}$$

Note that integration parameter β in Eq. (6.53a) reduce the integration constant b_0 to zero. Consequently, the explicit solution strategy produces a singular coefficient matrix. Obviously, the influence excludes its admissibility. However, by introducing appropriated assumptions, an alternative explicit procedure can be obtained. The procedure is discussed hereafter.

6.4.2.3   Forward incremental Lagrange multipliers method

It can be demonstrated that the contact forces $\boldsymbol{\lambda}_{n+1}$ directly influence the forward difference term $\Delta\ddot{\mathbf{u}}_{n+1}$ but acts one time step too late with respect to terms $\mathbf{u}_n, \dot{\mathbf{u}}_n$ or $\ddot{\mathbf{u}}_n$. Additionally, note that the forward difference term $\Delta\ddot{\mathbf{u}}_{n+1}$ is not present in the second order incremental equation

$$\mathbf{u}_{n+1} = \mathbf{u}_n + \Delta t\,\dot{\mathbf{u}}_n + \frac{1}{2}\Delta t^2\ddot{\mathbf{u}}_n + \beta\Delta\ddot{\mathbf{u}}_{n+1}, \tag{6.56}$$

since for explicit integration $\beta = 0$. Therefore, the contact forces $\boldsymbol{\lambda}_{n+1}$ have no influence on incremental displacements $\mathbf{u}_{n+1}$. However, an alternative procedure can be obtained by relating displacement constraint at time n+1 to LM at time n. The procedure is known as the *forward incremental Lagrangian multipliers method* and allows to rewrite Eq. (6.50) as (Carpenter, Taylor & Katona, 1991)

$$\mathbf{M}\,\ddot{\mathbf{u}}_n + \mathbf{C}\dot{\mathbf{u}}_n + \mathbf{F}_n^{in} + \mathbf{G}_{n+1}^{\mathrm{T}}\,\boldsymbol{\lambda}_n = \mathbf{0}, \tag{6.57a}$$

$$\mathbf{G}_{n+1}\{\mathbf{u}_{n+1} - \mathbf{u}_n + \mathbf{X}_n\} = \mathbf{0}. \tag{6.57b}$$

For the explicit time integration the adapted incremental solution strategy will be obtained by substituting the central difference approximations for velocities (4.17) and accelerations (4.18) into Eq. (6.57). To determinate the unknown incremental displacement $\mathbf{u}_{n+1}$, the strategy produce four computational steps. At the end of each time increment Δt, the incremental displacement vector $\Delta\mathbf{u}_n = \mathbf{u}_{n+1} - \mathbf{u}_n$ is calculated by summing the contributions of displacements values obtained in the so-called *displacement predictor* and *displacement corrector stage*.

The first stage requires to assume that there are not mechanical interactions between FE meshes at the beginning of a time increment Δt. In other words, by temporarily ignoring the influence of contact, the computation start with the contact predictor stage where the nodal displacements $\mathbf{u}_{n+1}^{D}$ are calculated with respect to the classical explicit displacement update (6.58).

$$\mathbf{u}_{n+1}^{D} = \underbrace{\left[\mathbf{M} + \frac{\Delta t}{2}\mathbf{C} \right]^{-1}}_{\text{diagona matrix}} \Delta t^{2} \left\{ \underbrace{\mathbf{F}_{n}^{ex} - \mathbf{F}_{n}^{in}}_{\mathbf{0}} \right\} + \frac{\Delta t}{2}\mathbf{C}\left\{ \mathbf{u}_{n-1} \right\} + \mathbf{M}\left\{ 2\mathbf{u}_{n} - \mathbf{u}_{n-1} \right\}. \tag{6.58}$$

The computation proceeds by activation of the so-called *global contact detection algorithm*. The procedure is discussed hereafter and it basically consists on identifying possible non-physical penetration of boundary FE nodes (Fig. 6.6). For those contractor nodes that violate the impenetrability constraint (6.2), and penetrate in a forbidden mesh domain, the local detection strategy is activated. The strategy should localize the position of contact ξ which is needed for to calculation of the contact displacement matrix $\mathbf{G}_{n+1}$ (6.45). Once the detection procedures are executed, the correction of the previously calculated displacement field (6.58) is performed by adding the contact displacement contribution (Carpenter, Taylor & Katona, 1991). For this purpose, the contact forces $\boldsymbol{\lambda}_n$, i.e. Lagrange multipliers, are determined for each contact element according to Eq. (6.59).

$$\boldsymbol{\lambda}_{n} = \left\{ \begin{matrix} \lambda_{1} \\ \lambda_{2} \\ \lambda_{3} \end{matrix} \right\} = \left[\Delta t^{2}\mathbf{G}_{n+1}\mathbf{M}^{-1}\mathbf{G}_{n+1}^{\mathrm{T}} \right]^{-1}\mathbf{G}_{n+1}\left\{ \mathbf{u}_{n+1}^{D} - \mathbf{u}_{n} + \mathbf{X}_{n} \right\} \tag{6.59}$$

In order to correct the non-physical event (penetration), the contact displacement vector $\mathbf{u}_{n+1}^{C}$ is calculated in the third computational step by distributing the contact forces from Eq. (6.59) among the contact element nodes (Fig. 6.6). Depending on the position of contact ξ the contact displacements are calculated through the contact displacement matrix $\mathbf{G}_{n+1}$ as

$$\mathbf{u}_{n+1}^{C} = -\Delta t^{2}\mathbf{M}^{-1}\mathbf{G}_{n+1}^{\mathrm{T}}\boldsymbol{\lambda}_{n}. \tag{6.60}$$

At the end of the time interval Δt, the total nodal displacements $\mathbf{u}_{n+1}$ are calculated as

$$\mathbf{u}_{n+1} = \mathbf{u}_{n+1}^{C} + \mathbf{u}_{n+1}^{D}. \tag{6.61}$$

Resuming, depending on the adopted time integration technique, the predictor and displacement correction stage can be performed both simultaneously and separately. The first procedure will lead to a coupled system of equations and the second one to the uncoupled system of equations. Due to the discussed difficulties, the proposed numerical formulation is based on the explicit time integration. However, like every explicit time integration technique, the illustrated modified strategy is also conditionally stable. In order to avoid numerical instability, the time increment Δt must be smaller than the critical time increment Δt_{cr} (4.33). Note also that all the consequences of the introduced assumptions and approximations are still present as it was earlier disused (*Chapter 4 – 4.3.1 Assumption, approximations and errors*).

6.4.2.4 High-frequency numerical damping

Mention that the Beta-2 integration method has been introduced here on purpose. Namely, it allows high-frequency numerical damping, which is expected to be necessary for numerical simulations of impact loadings. Its implementation is very simple which additionally justifies its use. It is carried out by replacing the term Δt^2 in Eq. (6.59) and Eq. (6.60) with $\Delta t^2 (\beta_0 + 0.5)$, where $0 \leq \beta_0 \leq 0.5$ (Carpenter, Taylor & Katona, 1991). It the later presented numerical examples (*Chapter 10 – Numerical examples*), the parameter β_0 was set to 0.45.

6.5 Gauss-Seidel iteration

In order solve Eq. (6.58), Eq. (6.59), Eq. (6.60) and Eq. (6.61), the effective iteration strategy developed by Carpenter, Taylor and Katona (1991) is here implemented and so briefly discussed. For this purpose, consider a number n_c of contact constraint violations. By introducing the upper index i for indicates the particular violation, the components of matrix $\mathbf{G}_{n+1}$ (6.45) and vector $\boldsymbol{\lambda}_n$ (6.59) can be related to a particular violation as $\mathbf{G}_{n+1}^{i}$ and $\boldsymbol{\lambda}_n^{i}$. According to the given notations, Eq. (6.59) can be expressed as

for $i = 1, 2, .., n_c$

$$\sum_{j=1}^{n_c} \Delta t^2 \, \mathbf{G}_{n+1}^{i} \mathbf{M}^{-1} \left[\mathbf{G}_{n+1}^{j} \right]^{T} \boldsymbol{\lambda}_n^{j} = \mathbf{G}_{n+1}^{i} \left\{ \mathbf{u}_{n+1}^{D} - \mathbf{u}_n + \mathbf{X}_n \right\}. \tag{6.62}$$

The solution strategy proposes by Carpenter et al. (1991) is based on the Gauss-Seidel iterative strategy. The iterative cycles from iterations k to $k+1$ is illustrated in Eq. (6.63).

for $i = 1, 2, .., n_c$

$$^{k,k+1}\mathbf{g}^i = \begin{Bmatrix} ^{k,k+1}g_1^i \\ ^{k,k+1}g_2^i \\ ^{k,k+1}g_3^i \end{Bmatrix} = \mathbf{G}_{n+1}^i \left\{ \mathbf{u}_{n+1}^D - \mathbf{u}_n + \mathbf{X}_n \right\} - \dots$$

$$\dots \sum_{j=1}^{n_c} \Delta t^2 \, \mathbf{G}_{n+1}^i \, \mathbf{M}^{-1} \left[\mathbf{G}_{n+1}^j \right]^{\mathrm{T}} {}^k\boldsymbol{\lambda}_n^j - \sum_{j=1}^{i-1} \Delta t^2 \, \mathbf{G}_{n+1}^i \, \mathbf{M}^{-1} \left[\mathbf{G}_{n+1}^j \right]^{\mathrm{T}} {}^{k+1}\boldsymbol{\lambda}_n^j \tag{6.63a}$$

$$\Delta\boldsymbol{\lambda}^i = \left[\Delta t^2 \, \mathbf{G}_{n+1}^i \, \mathbf{M}^{-1} \left[\mathbf{G}_{n+1}^i \right]^{\mathrm{T}} \right]^{-1} \cdot {}^{k,k+1}\mathbf{g}^i \tag{6.63b}$$

$$^{k+1}\boldsymbol{\lambda}_n^i = {}^k\boldsymbol{\lambda}_n^i + \Delta\boldsymbol{\lambda}^i \tag{6.63c}$$

However, the presented strategy is not yet suitable for numerical implementation. Namely, note that Eq. (6.63a) contains the contact contribution coupling between *i*-th and *j*-th displacement constraints. For this reason, an appropriate expression should be obtained by combining Eq. (6.59) and Eq. (6.60). In this case, the value of the contact displacement at the beginning of the iteration step *k* can be expressed as

$$^k\mathbf{u}_{n+1}^C = -\sum_{j=1}^{n_c} \Delta t^2 \, \mathbf{M}^{-1} \left[\mathbf{G}_{n+1}^j \right]^{\mathrm{T}} {}^k\boldsymbol{\lambda}_n^j, \tag{6.64}$$

and, at the end of the iteration, as

$$^{k+1}\mathbf{u}_{n+1}^C = -\sum_{j=1}^{n_c} \Delta t^2 \, \mathbf{M}^{-1} \left[\mathbf{G}_{n+1}^j \right]^{\mathrm{T}} {}^{k+1}\boldsymbol{\lambda}_n^j, \tag{6.65}$$

giving the difference between them as

$$\Delta\mathbf{u}^C = {}^{k+1}\mathbf{u}_{n+1}^C - {}^k\mathbf{u}_{n+1}^C. \tag{6.66}$$

By substituting Eq. (6.63c) into Eq. (6.64) and Eq. (6.65), the former Eq. become

$$\Delta\mathbf{u}^C = \sum_{j=1}^{n_c} \Delta\mathbf{u}_j^C \tag{6.67}$$

where $\quad \Delta\mathbf{u}_j^C = -\Delta t^2 \, \mathbf{M}^{-1} \left[\mathbf{G}_{n+1}^j \right]^{\mathrm{T}} \Delta\boldsymbol{\lambda}^j.$

From iteration *k* to *k*+1, the displacement vector $^{k,k+1}\mathbf{u}_{n+1}^C$ will be given as

$$^{k,k+1}\mathbf{u}_{\mathrm{n+1}}^{\mathrm{C}} = {}^{k}\mathbf{u}_{\mathrm{n+1}}^{\mathrm{C}} + \sum_{j=1}^{i-1}\Delta\mathbf{u}_{j}^{\mathrm{C}}. \tag{6.68}$$

Furthermore, by substituting Eq. (6.64) and Eq. (6.67) into the former Eq., the displacement vector $^{k,k+1}\mathbf{u}_{\mathrm{n+1}}^{\mathrm{C}}$ can be now expressed as

$$^{k,k+1}\mathbf{u}_{\mathrm{n+1}}^{\mathrm{C}} = -\sum_{j=1}^{n_c}\Delta t^{2}\,\mathbf{M}^{-1}\Big[\mathbf{G}_{\mathrm{n+1}}^{j}\Big]^{\mathrm{T}}\,{}^{k}\boldsymbol{\lambda}_{n}^{j} - \sum_{j=1}^{i-1}\Delta t^{2}\mathbf{M}^{-1}\Big[\mathbf{G}_{\mathrm{n+1}}^{j}\Big]^{\mathrm{T}}\,{}^{k+1}\boldsymbol{\lambda}_{\mathrm{n}}^{j}. \tag{6.69}$$

Apart the incremental displacement vector in Eq. (6.67), the incremental force vector $\Delta\boldsymbol{\lambda}^{i}$ can be obtained by substituting Eq. (6.69) into Eq. (6.63a). The procedure will result in

$$\Delta\boldsymbol{\lambda}^{i} = \Big[\Delta t^{2}\mathbf{G}_{\mathrm{n+1}}^{i}\mathbf{M}^{-1}\Big[\mathbf{G}_{\mathrm{n+1}}^{i}\Big]^{\mathrm{T}}\Big]^{-1}\cdot\mathbf{G}_{\mathrm{n+1}}^{i}\Big\{{}^{k,k+1}\mathbf{u}_{\mathrm{n+1}}^{\mathrm{C}} + \mathbf{u}_{\mathrm{n+1}}^{\mathrm{D}} - \mathbf{u}_{\mathrm{n}} + \mathbf{X}_{\mathrm{n}}\Big\}. \tag{6.70}$$

Concluding, the Gauss-Seidel solution strategy (6.63) can be reformulated as follows (6.71).

$$\text{for } i = 1,2,..,n_c$$

$$^{k,k+1}\mathbf{g}^{i} = \mathbf{G}_{\mathrm{n+1}}^{i}\cdot\Big\{\mathbf{u}_{\mathrm{n+1}}^{\mathrm{C}} + \mathbf{u}_{\mathrm{n+1}}^{\mathrm{D}} - \mathbf{u}_{\mathrm{n}} + \mathbf{X}_{\mathrm{n}}\Big\} \tag{6.71a}$$

$$\Delta\boldsymbol{\lambda}^{i} = \Big[\Delta t^{2}\mathbf{G}_{\mathrm{n+1}}^{i}\mathbf{M}^{-1}\Big[\mathbf{G}_{\mathrm{n+1}}^{i}\Big]^{\mathrm{T}}\Big]^{-1}\cdot{}^{k,k+1}\mathbf{g}^{i} \tag{6.71b}$$

$$^{k+1}\boldsymbol{\lambda}_{\mathrm{n}}^{i} = {}^{k}\boldsymbol{\lambda}_{\mathrm{n}}^{i} + \Delta\boldsymbol{\lambda}^{i} \tag{6.71c}$$

$$\Delta\mathbf{u}_{i}^{\mathrm{C}} = -\Delta t^{2}\,\mathbf{M}^{-1}\Big[\mathbf{G}_{\mathrm{n+1}}^{i}\Big]^{\mathrm{T}}\Delta\boldsymbol{\lambda}^{i} \tag{6.71d}$$

$$^{k,k+1}\mathbf{u}_{\mathrm{n+1}}^{\mathrm{C}} \xleftarrow{\ \text{update}\ }\Big\{{}^{k,k+1}\mathbf{u}_{\mathrm{n+1}}^{\mathrm{C}} + \Delta\mathbf{u}_{i}^{\mathrm{C}}\Big\} \tag{6.71e}$$

The benefit of using the Gauss-Seidel iteration strategy is shown by the fact that all the needed computations are performed at local FE level. The property is especially attractive since in the adopted explicit integration technique (4.30) the computation of dynamic displacements is here also free of any global matrix. Furthermore, as demonstrated by Carpenter, Taylor and Katona (1991), the convergence of the strategy is affected only by the difference between the masses of contractor node and related target surface nodes. Particularly, if the target nodes are not so massive, the convergence is slower. However, in case where the masses are not extremely different, the convergence rate is almost linear.

The converged state is reached when

$$\left\| \Delta \boldsymbol{\lambda} \right\| \le \varepsilon \left\| {}^{k+1}\boldsymbol{\lambda}_n \right\|, \tag{6.72}$$

where ε denotes a pre-defined tolerance value. Note that from the point of view of numerical implementation, the iterative strategy in Eq. (6.71) can be elegantly incorporated in any explicit FE contact analysis. The pseudo code in Box 6.1 is given to support the statement.

```
! Gauss-Seidel iteration loop
! ***************************
2       DO Penetration = 1, No_Penetrations

                CALL Gauss_Seidel_GAP (Penetration)

                CALL Gauss_Seidel_LAGRANGE (Penetration)

                CALL Gauss_Seidel_FRICTION (Penetration)

                CALL Gauss_Seidel_UPDATE_LAGRANGE (Penetration)

                CALL Gauss_Seidel_CONTACT_DISPLACEMENT (Penetration)

           END DO

           CALL Gauss_Seidel_CONVERGENCE ; IF (GS_convergence="NO") GOTO 2

           ELSE RETURN
```

Box 6.1 Subroutines for the reproduction of the Gauss-Seidel iteration strategy

Evidently, the given algorithm enables to resolve each contact constraint violation separately. This is due to the fact that the system of Eq. is now uncoupled. Observe also that there is an anticipated subroutine that deals with the frictional behavior on the contact interface (`Gauss_Seidel_FRICTION`). Namely, the contact kinematic conditions are here resolved separately by prescribing displacement constraints to prevent overlapping and to control contact sliding. Particularly, the surface force conditions, i.e. normal (6.1b) and tangential force limit (6.3a), are laid down and controlled in case of violation of the constitutive law.

6.6   Contact force restrictions

The algorithm in (6.71b) leads to the contact surface reaction $\boldsymbol{\lambda}$ that will satisfy the contact impenetrability constraint by pulling the contractor node to the position of intersection with the target surface (Fig. 6.6). However, once the impenetrability condition is satisfied (6.2), the surface contact force conditions may be violated. Therefore, the normal component of contact forces should be always compressive. On the other hand, depending on the type of the adopted frictional constitutive model, there is a certain limit prescribed to the tangential force component as well.

6.6.1 Contact reaction – normal component

During the Gauss-Seidel iterative fashion, the coordinates of contact elements nodes are progressively updated (6.71e). Consequently, the gap value will vary in each iterative cycle (6.71a). According to that, mention that there are situations in which the iterative procedure will put the contractor node outside the penetrated domain (g>0). In that case, the next iteration loop will tends to pull back the node to the position of intersection, provoking tensile contact reaction. Obviously, this scenario is not physical and the node under consideration should be released from contact (Fig. 6.9).
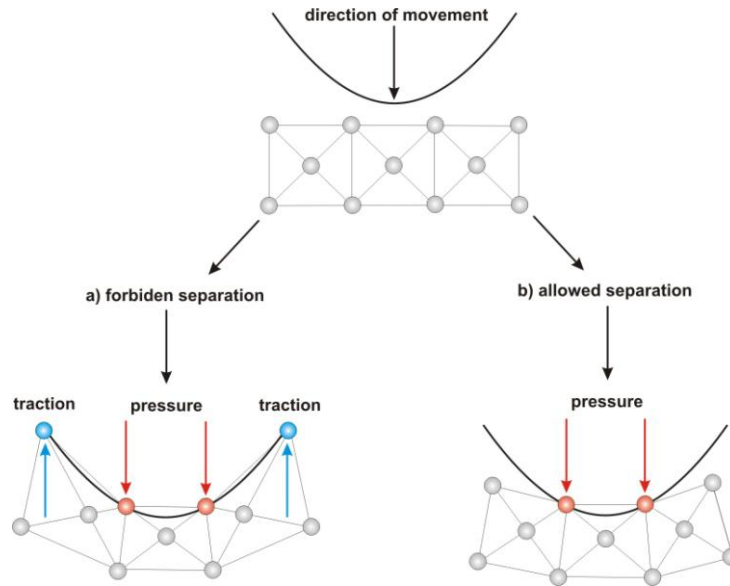

Figure 6.9 Numerical consequence on: **a)** forbidden nodal separation and **b)** allowed nodal separation

It follows that the contact force components should be progressively monitored to include the nodal separation in the above algorithm (6.71). For this purpose, note that λ in Eq. (6.71b) is given in respect to global rectangular axes. In order to test the normal component λ_N for tension, λ should be transformed into local coordinates of the belonging target surface. For this purpose, since the target surfaces are here always flat, the normal component λ_N can be defined as

$$\lambda_N = (\lambda \cdot \overline{\mathbf{n}}^m)\lambda. \tag{6.73}$$

The contractor node related to Eq. (6.73) can be now tasted for separation. Namely, if the force λ_N denotes tension, the nodal separation is simply reproduced by setting λ_N equal to zero. The procedure is equal for all nodes in contact and can be summarize as follow (6.74).

$$\text{for } i = 1,2,..,n_c$$

$$\text{if } \quad \lambda_N^i > 0 \quad \text{then} \quad \lambda_N^i = 0. \tag{6.74}$$

6.6.2 Contact reaction – tangential component

Apart the normal reaction force λ_N (6.74), the allowed limit of its tangential component λ_T is also prescribed by the assumed frictional constitutive model. Particularly, the Coulomb frictional model is here employed to differentiate the stick from the slip contact condition (Fig. 6.5). Similarly to Eq. (6.73), to perform the tangential check force limit, the force component λ_T should be obtained from λ and the related target surface vectors (6.21). The computation involves basic vector algebra as

$$\lambda_T = (\lambda \cdot \mathbf{m}) \cdot \mathbf{m} + (\lambda \cdot \mathbf{k}) \cdot \mathbf{k}, \qquad (6.75)$$

where the projection vectors $\mathbf{m}$ and $\mathbf{k}$ are given by

$$\mathbf{m} = \frac{\overline{\mathbf{a}}_\alpha}{\left\| \overline{\mathbf{a}}_\alpha \right\|} \qquad \text{and} \qquad \mathbf{k} = \frac{\overline{\mathbf{a}}_\beta - (\overline{\mathbf{a}}_\beta \cdot \mathbf{m}) \cdot \mathbf{m}}{\left\| \overline{\mathbf{a}}_\beta - (\overline{\mathbf{a}}_\beta \cdot \mathbf{m}) \cdot \mathbf{m} \right\|}. \qquad (6.76)$$

Once the force component λ_T is known, the tangential force correction is introduced behind Eq. (6.71b). The computational procedure is graphically illustrated in Fig. 6.10.
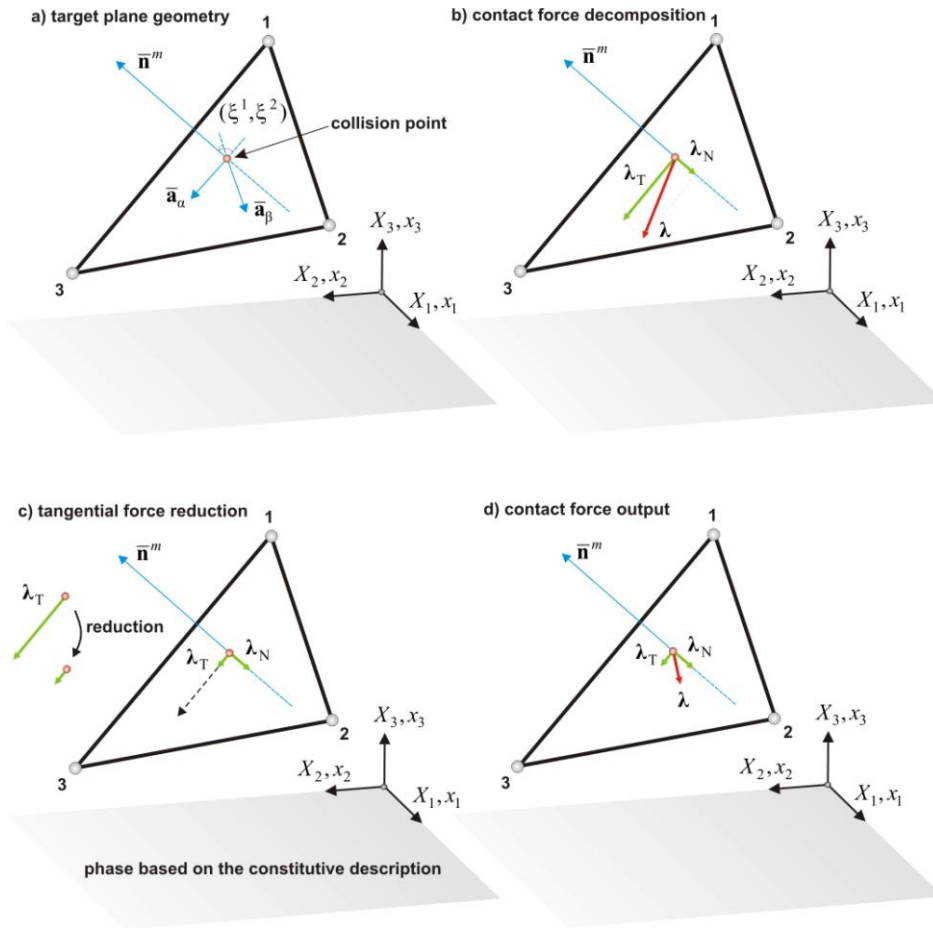

Figure 6.10 Illustration of computational steps needed for nodal displacement relaxation

In other words, after calculating the contact force vector $\boldsymbol{\lambda}$, in the computational step (6.71b), the obtained force is decomposed into its normal $\boldsymbol{\lambda}_N$ and tangential part $\boldsymbol{\lambda}_T$ according to (6.73) and (6.75), respectively (Fig. 6.10b). The computation proceeds with checking the nodal tendency for contact separation (6.74). This is reasonable since the tangential force $\boldsymbol{\lambda}_T$ in the Coulomb frictional model depends on $\boldsymbol{\lambda}_N$. Furthermore, it is clear that if the node establishes tension load, further checking will not be required since the node will be released from contact. On the other hand, if the tensile force is not present, the tangential force components have to be tested for eventual sliding contact condition. At the numerical implementation level, the given qualitative description can be restated in algorithm form as

$$\text{for } i = 1,2,..,n_c$$

$$\text{if } \quad \lambda_{N_n}^i > 0 \quad \text{then} \quad \lambda_{N_n}^i = 0$$

$$\text{if } \quad \left\| \lambda_{T_n}^i \right\| > \mu \left\| \lambda_{N_n}^i \right\| \quad \text{then} \quad \lambda_{T_n}^i = \mu \left\| \lambda_{N_n}^i \right\| \frac{\lambda_{T_n}^i}{\left\| \lambda_{T_n}^i \right\|},$$

$$\tag{6.77}$$

which is activated for each contractor node after the computation step in Eq. (6.71b). Note that if the tangential force component $\boldsymbol{\lambda}_T$ has been modified (according to the assumed frictional constitutive description), a new respective contact force $\boldsymbol{\lambda}$ should be computed before moving onto the next iterative cycle (Fig. 6.10d).

Finally, it ought to be mentioned that during the Gauss-Seidel iteration cycles the components of the displacement constraint matrix $\mathbf{G}_{n+1}$ (6.45) are not alternated. However, if the numerical simulation is characterized by large slings, the matrix components will vary due to the sliding of contactor nodes along target surfaces. For this purpose, even if a very small time increment Δt is adopted, which will consequently produce a relatively small incremental nodal displacements, it would be convenient to calculate $\mathbf{G}_{n+1}$ at the beginning of each Gauss-Seidel iteration process or at the beginning of each time increment.

6.6.3 Numerical example

In order to test the above numerical algorithm, a numerical experiment is conducted by simulating a collision event between two elastic spheres. The spheres under consideration are identical from the geometrical, kinematical and mechanical point of view, except that the velocity vectors are characterized by opposite directions. The sticking and sliding contact conditions are induced by setting the friction coefficient μ equal to ∞ and 0, respectively. In order to magnify the influence of contact, the spheres trajectory is set to be eccentric. The numerical results are shown in Fig. 6.11.
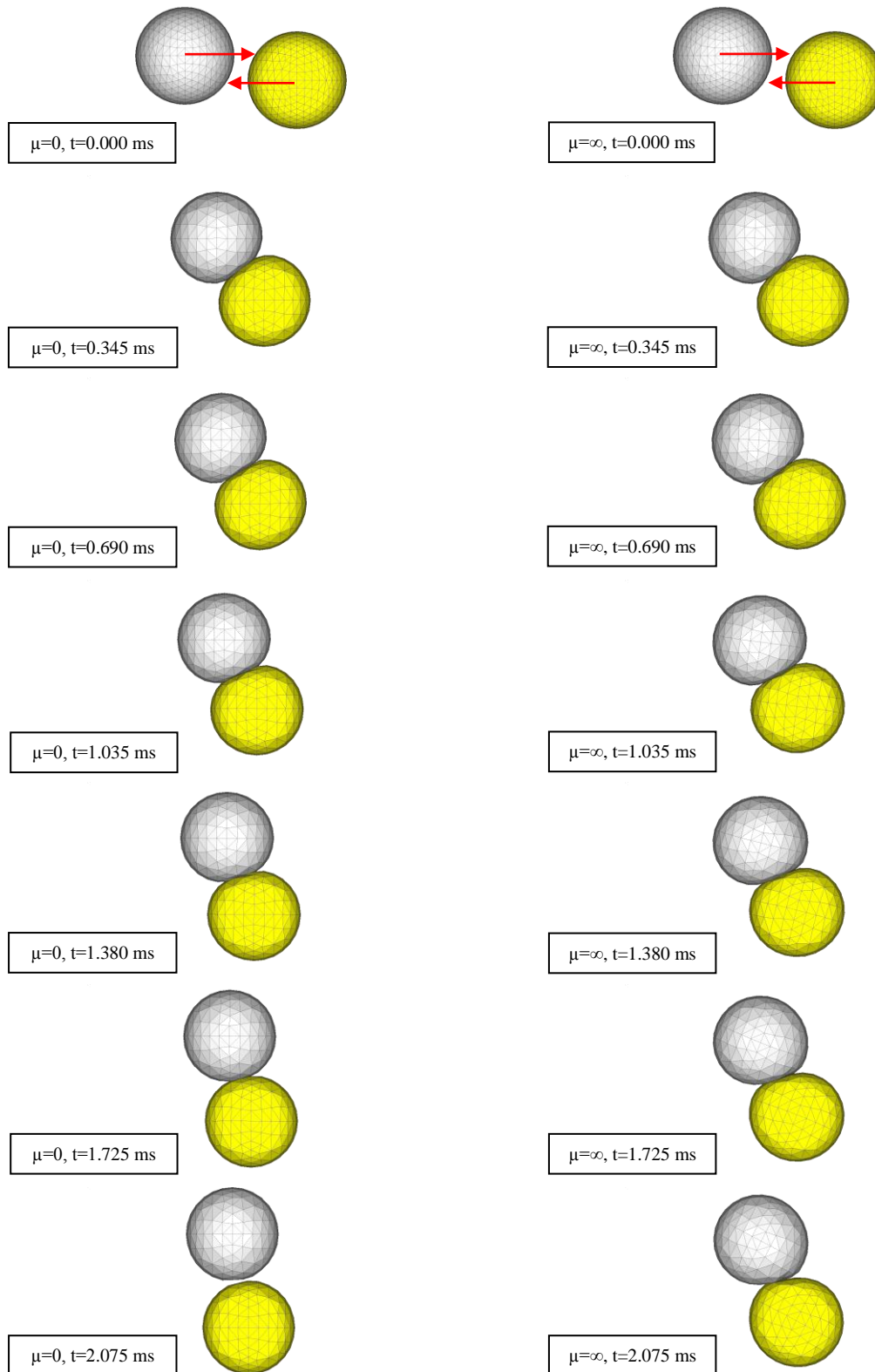
Figure 6.11 Numerical simulation of spheres under collision: **a)** left column μ=0 and **b)** right column μ=∞

Evidently, the collision response is highly influenced by the presence of friction. Namely, the left column of Fig. 6.11 illustrate the collision response in which it was assumed that μ=0. In that case, the sliding contact condition was activated, leading to a repulsive collision response without the presence of spheres rotations. The explanation to that is the following: since there is not any tangential force, and the straight line of normal contact forces almost passes through the spheres centers (relatively small displacements), the collision response cannot involve angular momentum. At the energetical level, the numerical simulation predicts the correct transformation of energies without the presence of entropy. As shown in Fig. 6.12, after the spheres separation had occurred, the balance of energies was satisfied. However, some minor difference arose as a consequence of numerical approximation.
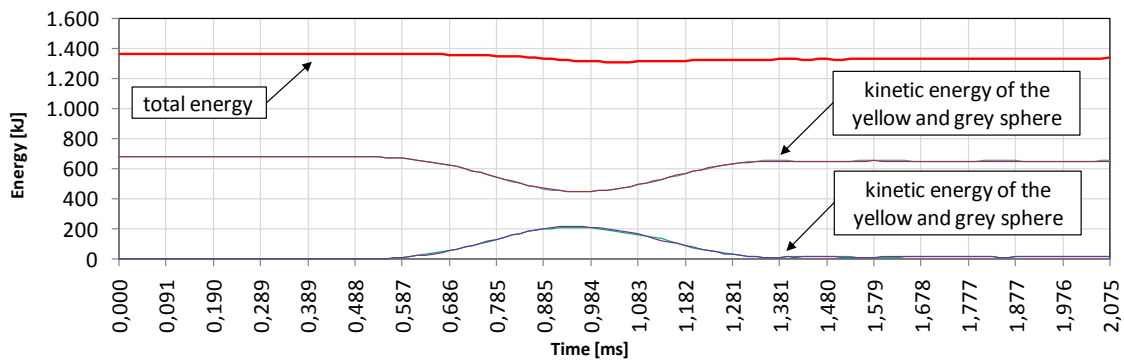

Figure 6.12 Mechanical energies vs. time (μ=0)

On the other hand, when the frictional coefficient μ was set equal to ∞, the presence of tangential forces caused the spheres to rotate around their centers (inertial effect). Indeed, it can be seen that the spheres in the left column separated from each other while, for the same time increment, those in the right one were still in contact. The numerical simulation also predicted correctly the dissipative nature of friction forces since the sphere velocities after impact did not return to their initial value (Fig. 6.13). It is also interesting no note that the presence of friction causes the sphere to suffer more deformations.
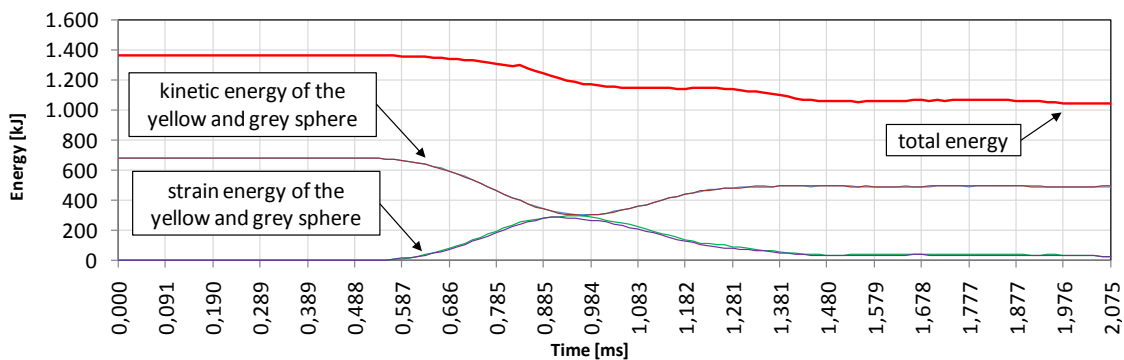

Figure 6.13 Mechanical energies vs. time (μ=∞)

Fig. 6.12 and Fig. 6.13 are qualitatively validated and prove to be in a good compliance with the numerical predictions available in the literature (Cirak & West, 2005).

Chapter 7

Contact detection

7.1 Introduction

Differently from the analytical treatment of contact problems (*Hertzian contact*), the contact constraints in numerical analysis are satisfied retroactively. Namely, the enforcement procedure is invoked after their violations have been detected. Consequently, the ability to identify contact constraints violations immediately becomes a requirement. For this purpose, a set of computational procedure forms the so-called *contact detection stage*. In particular, as the contact constrains violations in FE environment are measured discretely, the related set of computational procedure is used to localize such violations by focusing the respective search on FE nodes. Indeed, it is a common practice to hierarchically split the contact detection stage into *global* and *local detection phase*. The global detection phase serves to determine if the FE boundary nodes interpenetrated any discretizational domain and, if so, to obtain the nodes ID. After that, in the local detection phase a detailed search is performed to approximate the time and position when the contactor node hit the target surface. The procedures enable the assembling of contact elements by paring contractor nodes with nodes on the belonging target surfaces.

The contact constraint enforcement is here based on the assumption that only nodal displacements $\mathbf{u}^D$ (6.58) are present at the beginning of each time increment Δt. Therefore, the respective force field does not include the presence of contact forces $\{\mathbf{G}^T \cdot \boldsymbol{\lambda}\}$. The side effect is that the impenetrability constraint violations are then temporary allowed. However, the contact constraint enforcements are still retroactively satisfied (*Chapter 6 – 6.4.2.3 Forward incremental Lagrange multipliers method*).

The contact detection stage should lead to the unknown collision time t_c (located between two neighboring time steps) in which the violation of impenetrability contact constraint begins (Fig. 7.1). As the initial nodal position at the beginning of each time increment Δt is known, t_c will lead to the position on the target surface where the violation occurs (Fig. 6.6).
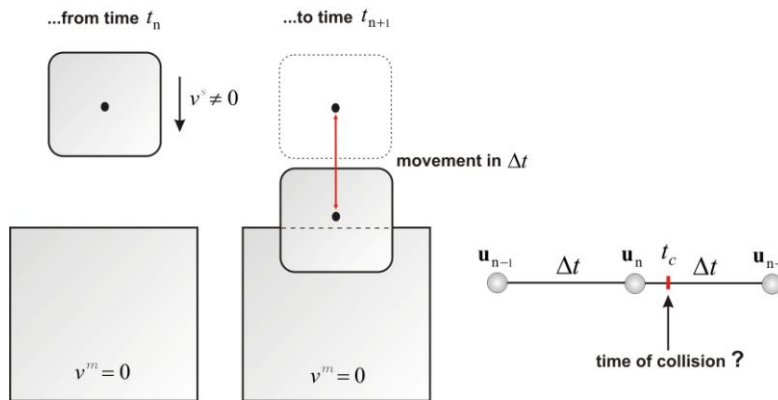

Figure 7.1 Collision detection viewed from the perspective of time stepping (incremental analysis)

It is important to note that the contact detection stage require presupposing nodal velocities between times steps t_n and t_{n+1}. Particularly, in the proposed numerical formulation, it is assumed that at the beginning of each contact detection stage, the nodal velocities are constant inside Δt. The assumption is reasonable since the adopted explicit time integration requires relatively small time increments. Mention that the exact computation of t_c will not significantly improve the numerical prediction (Carpenter, Taylor & Katona, 1991).

Before proceeding, an important fact should be underlined. Since the physical event under consideration is trapped in a very small period of time (*Introduction – Note on experimental observations*), and a considerable number of time increments is inevitable in order to reproduce the non-linear response, the adopted time increment Δt will be particularly small ($\Delta t \ll$ 1ms). The consideration will introduce difficulties for the computation of t_c. Furthermore, the global detection phase will also suffer some consequences due to the relatively small nodal movements between time t_n and t_{n+1}. Namely, a relatively small nodal movement can occasionally result in a seemingly permanent proximity of contractor nodes to target surfaces. As a consequence, the possibility to detect nodal penetrations will be very difficult due to the presence of computational round-off errors (*Chapter 4 – 4.3.1 Assumption, approximations and errors*).

Nevertheless, as the analysis proceeds, the contractor node will move away from the target surface. In a certain moment, it will emerge from the region occupied by round-off errors. In such moment, it will be computationally visible and detected by the global detection procedure. Note also that in this case the related magnitude of **g** will be greater than the magnitude of surrounding contractor nodes that regularly report the violation of impenetrability contact condition (6.2).

Mention that the abovementioned scenario, in which one non-detected penetration is carried through time, could produce dramatic consequences on the numerical simulation. In fact, once the earlier nonregistered penetration has been detected, the jump in gap value will be considerable (comparing it with neighboring gap vectors). As a consequence, a grater contact force will be needed to satisfy the impenetrability constraint (6.59). Consequently, by disposing of convergence state, the following time increment will register a relatively enormous presence of inertial forces. The local significant difference between inertial forces will cause the divergence of the solution process.

In order to overcome these problems, the presence of computational round-off errors should be minimized. For this purpose, it is recommended that the variables contained in the contact detection stage (both in global and local phase) are classified as *double precision* (REAL 8), or even *quad precision variables* (REAL 16). In the program code developed in accordance with the proposed numerical formulation, the double precision statement is used for variables declaration. Additionally, some external computational procedures are incorporated to monitor and appropriately resolve the still possible no detected penetrations.

7.2   FE surfaces that are candidates for mechanical interaction

Since the considered mechanical interactions occur across the body external boundaries Γ^κ, the eventual presence of internal boundaries is here ignored. Under this circumstance, it is obvious that, in the three-dimensional FE environment, the list of *boundary nodes* and *boundary surfaces* is necessary to perform the contact analysis (Fig. 7.1). Before presenting the strategy aimed to obtain such data, it should be clarified why for each discretization both data are needed.

According to the previous Chapter, the numerical treatment of contact phenomena starts by attributing the boundary nodes on one mesh as potential contractor nodes, and the boundary surfaces on the other mesh as potential target surfaces. In order to form a contact element, the contractor nodes identified in the global detection phase are paired with belonging three nodes on the target surface (Fig. 6.6), recognized in the local detection phase. After the contact detection and contact resolution stage has been performed, and before proceeding with the next time increment, the associations of contractor nodes and target surfaces are switched between the meshes. In this case, a new contact detection and contact computing stage is performed.
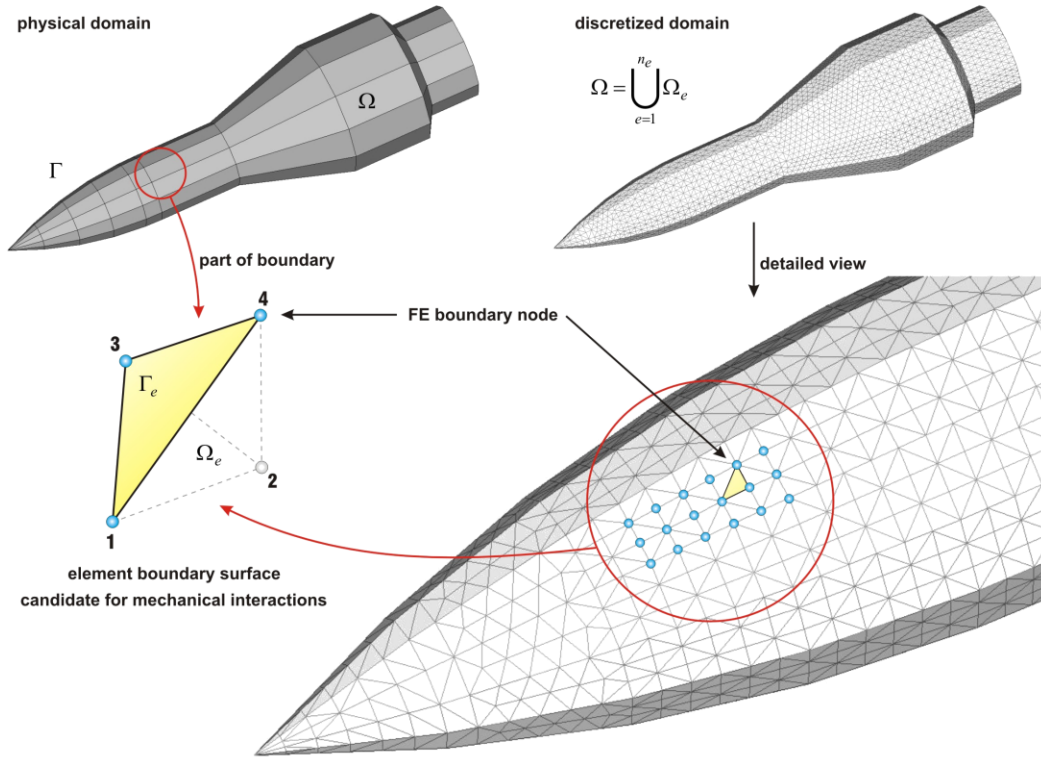
Figure 7.2 Target surfaces and contractor nodes on boundary elements (objects subject to mechanical interactions)

Namely, the switching of attributes between target surfaces and contractor nodes is here introduced due to the fact that the contact constraint violations are measured by monitoring the contractor nodes and not surfaces. In other words, since the meshes under interaction can have different nodal density over Γ_c (Fig. 6.3), this strategy will ensure that all non-physical nodal penetrations have been removed. On the other hand, even if the meshes have equal nodal density over Γ_c (perfect nodal pairing), large sliding analysis will leads to an inevitable non-matching interface. In this case, the switching between contact detection attributes is necessary to evidence the not allowed penetrations on both meshes. In short, if there are two bodies under collision, the computational stage related to contact detection and contact resolution phases is performed twice in each time increment (*two-pass algorithm*).

As the boundary element surfaces are here defined by three boundary nodes (Fig. 7.2), it follows that by knowing the list of boundary surfaces, the list of boundary nodes will be automatically defined. Note that the needed data are hidden in the so-called *mesh topology matrix* (7.1).

$$
\texttt{Topology\_Mtx} =
\begin{bmatrix}
nd1_{e=1} & nd2_{e=1} & nd3_{e=1} & nd4_{e=1} \\
nd1_{e=2} & nd2_{e=2} & nd3_{e=2} & nd4_{e=2} \\
\vdots & \vdots & \vdots & \vdots \\
nd1_{e=n_e} & nd2_{e=n_e} & nd3_{e=n_e} & nd4_{e=n_e}
\end{bmatrix}
\begin{matrix}
\leftarrow \text{nodes on element \#1} \\
\leftarrow \text{nodes on element \#2} \\
\\
\leftarrow \text{nodes on element \# } n_e
\end{matrix}
\qquad (7.1)
$$

The notations $nd1_e$,.., $nd4_e$ stand for nodes ID on the e element. The nodal combinations that will define each boundary surface can be found by identifying what is common for these surfaces. In other words, it should be recognize what makes them different from the interior surfaces? Well, in order to preserve the continuum assumption, the internal elements will divide surfaces while the boundary surfaces will remain undivided. In this sense, the nodal combinations that define boundary surfaces will be unique. According to that, the three nodes that lie on a particular boundary surfaces can be extracted from matrix `Topology_Mtx` (7.1) according to the concept illustrated in Box 7.1.

```
! for a given FE spatial discretization form a list of boundary surfaces
! **********************************************************************

DO Consider_Element = 1, Number_of_Elements

nd1 = Topology_Mtx (Consider_Element, 1)
nd2 = Topology_Mtx (Consider_Element, 2)
nd3 = Topology_Mtx (Consider_Element, 3)
nd4 = Topology_Mtx (Consider_Element, 4)

        DO Permutation = 1, 4

             SELECT CASE (Permutation)
             CASE (1): SETnd1 = nd1 ; SETnd2 = nd2 ; SETnd3 = nd3
             CASE (2): SETnd1 = nd2 ; SETnd2 = nd3 ; SETnd3 = nd4
             CASE (3): SETnd1 = nd1 ; SETnd2 = nd2 ; SETnd3 = nd4
             CASE (4): SETnd1 = nd1 ; SETnd2 = nd3 ; SETnd3 = nd4
             END SELECT

           DO Other_Element = 1, Number_of_Elements

              IF Consider_Element = Other_Element CYCLE ; Count_nd = 0

                 TESTnd1 = Topology_Mtx (Other_Element, 1)
                 TESTnd2 = Topology_Mtx (Other_Element, 2)
                 TESTnd3 = Topology_Mtx (Other_Element, 3)
                 TESTnd4 = Topology_Mtx (Other_Element, 4)

              IF SETnd1 = TESTnd1 OR SETnd1=TESTnd2 OR SETnd1=TESTnd3 OR SETnd1=TESTnd4 THEN

                 Count_nd = Count_nd + 1

              IF SETnd2 = TESTnd1 OR SETnd2=TESTnd2 OR SETnd2=TESTnd3 OR SETnd2=TESTnd4 THEN

                 Count_nd = Count_nd + 1

              IF SETnd3 = TESTnd1 OR SETnd3=TESTnd2 OR SETnd3=TESTnd3 OR SETnd3=TESTnd4 THEN

                 Count_nd = Count_nd + 1

              IF (Count_nd = 3) EXIT LOOP

           END DO: Other_Element

            IF (Count_nd /= 3) THEN SETnd1 , SETnd2 , SETnd3 are nodes on boundary surface
!           ***********************************************************************
        END DO: Permutation

END DO: Consider_Element
```

Box 7.1 Pseudo-code delivered to retrieve the list of elements boundary surfaces (target surfaces)

7.3   Global detection

At the beginning of any time increment, the mesh boundaries are separated due to the previously fulfillment of the impenetrability contact condition (6.2). Furthermore, according to the adopted explicit time integration technique (6.58), the computation of the next continuum configuration begins by calculating the incremental nodal displacement $\Delta \mathbf{u}^D$. After adding the displacement vector $\Delta \mathbf{u}^D$ to material coordinate vector $\mathbf{X}_n$, it is reasonable to expect that a particular boundary nodes can be found inside some discretized domain. In order to remove these nodes from such non-physical positions, the forces needed to separate the bodies should be calculated. However, in order to form contact element nodal pairs, and before proceeding to the related Eq. (6.59), the ID of penetrated nodes must be obtained in the global detection stage.

7.3.1 Note on robustness and efficiency

Since the time increment necessary to numerically simulate the concrete response under impact loading will be relatively small ($\Delta t <\!\!< 1$ms), and the geometry of the already formed contact interface can be rather complex, the issue of robustness of global contact detection arises automatically.

Furthermore, note that one undetected penetration, or even worse; one wrongly detected penetration can lead to numerical divergence. Therefore, the robustness issue can be viewed as a crucial requirement for the contact detection stage. For illustration, consider the case in which 100 nodes violate the impenetrability condition in each time increment. Additionally, assume that 15000 time increments are needed to perform the complete numerical analysis. In such case, the computational procedures used for global detection must register 1500000 forbidden node penetrations! Evidently, the fact immediately gives rise to the computational algorithm robustness requirement.

It should be mentioned that the abovementioned scenario is more than possible. Indeed, typical industrial FE contact simulation requires an even larger number of nodes in order to adequately describe the contact force field. Consequently, the computational efficiency requirement arises as well. Evidently, the global detection phase has to be fast and reliable at the same time.

Since the contact interface Γ_c is unknown in advance (and may significantly vary in time); it follows that the global detection phase mast be performed across all boundaries in each time increment. Only in this manner some possible hidden contact regions can be revealed. However, for an arbitrary spatial discretization, the primitive loop over all boundary nodes candidate for penetration would be quite expensive and inappropriate for practical applications. Mention that the requirements of videogames industry (car racing and combat competitions) and the SF film industry (the cloth of master Joda in the remake of the Star Wars trilogy), led to few very efficient global detection strategies that are also used in numerical FE contact/impact simulations.

In order to numerically reproduce the free fall drop weight experiment (Fig. 1.1) or concrete penetration (Fig. 1.3), the proposed numerical formulation uses a primitive but robust global detection strategy. The strategy is based on the previously discussed geometrical description of the tetrahedral finite elements (*Chapter 3 – 3.3.1 Geometrical description*). Before illustrating the adopted strategy, mention that with the aim of ensuring its efficiency, some external procedures have been delivered for the purpose of speeding up the search of nodal contact impenetrability violations (6.2). The procedures are incorporated into the delivered program code and are later briefly presented.

7.3.2 Detection strategy

In order to identify mesh boundaries involved in contact, the procedure adopted here follows from the known *point in polygon test*. The procedure is based on the fact that the barycentric coordinates ξ of a point P are positive if the point is inside the element domain Ω_e (*Chapter 3 – 3.3.1 Geometrical description*). In this case, the sum of barcentric coordinates is equal to 1 and $0 \leq \xi_n \leq 1$.

The procedure can be formulated as follow. After adding the incremental displacements $\Delta \mathbf{u}^D$ (6.58) to coordinate vector $\mathbf{X}_n$, a check loop is performed for each slave boundary nodes. The procedure consists on calculating the slave node barcentric coordinates for elements in the computational loop. If for an element in the loop the barcentric coordinates are in accordance with Eq. (3.42), the penetration is detected. In other words, for a boundary node with coordinates $\{ \; x_1^c \; x_2^c \; x_3^c \; \}^{\mathrm{T}}$, the penetration check will involve the computational loop over a number of elements n_e as:

$$\text{for } e = 1,2,..,n_e$$

$$\xi_n(x_1, x_2, x_3) = (\alpha_n^e + x_1^c \, \beta_n^e + x_2^c \, \gamma_n^e + x_3^c \, \delta_n^e) \quad \text{where} \quad n = 1,2,3,4, \tag{7.2}$$

where the coefficients $\alpha_n^e, \beta_n^e, \gamma_n^e$ and δ_n^e, are given in Eq. (3.54), (3.55), (3.56) and (3.57), respectively. The strategy can be also reformulated in terms of region volumes (Fig. 3.3). Moreover, the volume terminology brings a benefit since the range check of barcentric coordinate can be here suppressed. The volumes V_n are defined by pairing three element nodes with the coordinates of the node candidate for penetration. The computations are performed according to Eq. (3.40) where the coordinates of the penetrated node and the coordinates of element node cyclically switch. If all volumes are positive, the point will be inside Ω_e. Note that the strategy is very simple and robust but inefficient. Namely, due to the frequent request for contact detection (and numerous necessary looping procedures), the illustrated loop is inappropriate for practical computations. However, some speedup aspects will be discussed later.

To perform the search for possible nodal penetrations, except the mesh topology matrix (7.1), the nodal coordinate matrix `Coord_Mtx` should be given as well. For a typical three-dimensional spatial discretization, the matrix structure can be represented as follow (7.3).

$$\texttt{Coord\_Mtx} = \begin{bmatrix} X_{1,n=1} & X_{2,n=1} & X_{3,n=1} \\ X_{1,n=2} & X_{2,n=2} & X_{3,n=2} \\ \vdots & \vdots & \vdots \\ X_{1,n=n_n} & X_{2,n=n_n} & X_{3,n=n_n} \end{bmatrix} \begin{matrix} \leftarrow \text{coordinates of node \#1} \\ \leftarrow \text{coordinates of node \#2} \\ \\ \leftarrow \text{coordinates of node \#}n_n. \end{matrix} \tag{7.3}$$

The matrixes (7.1) and (7.2) are obtained from the commercial mesh generation program FEMAP. The topology matrix (7.1) and the nodal coordinate matrix (7.3) are given in accordance with the spatial discretization performed by linear tetrahedral elements. The matrix uniquely defines the three-dimensional finite element discretization and contains information needed for the adopted global detection procedure. However, it should be pointed out that the local detection phase will not involve only the geometrical aspects of meshes but also the kinematical aspects of nodal movement between times steps t_n and t_{n+1}.

It is easy to demonstrate that the computations of volumes in Eq. (3.40), which are illustrated in Fig. 3.3, involves the computation of some terms that are repeating. For this purpose, the optimizing algorithm, that will avoid repeated calculations, is given in Box 7.2.

```
! identify the boundary nodes that interpenetrate into an FE mesh
! **************************************************************

DO Consider_Node = 1, Number_of_Nodes

sx = Coord_Mtx(List_of_Boundary_Nodes(Consider_Node),1)

sy = Coord_Mtx(List_of_Boundary_Nodes(Consider_Node),2)

sz = Coord_Mtx(List_of_Boundary_Nodes(Consider_Node),3)


        DO Consider_Element = 1, Number_of_Elements

           x2xs = Coord_Mtx(Topology_Mtx(Consider_Element,2),1) - sx
           x3xs = Coord_Mtx(Topology_Mtx(Consider_Element,3),1) - sx
           x4xs = Coord_Mtx(Topology_Mtx(Consider_Element,4),1) - sx
           y2ys = Coord_Mtx(Topology_Mtx(Consider_Element,2),2) - sy
           y3ys = Coord_Mtx(Topology_Mtx(Consider_Element,3),2) - sy
           y4ys = Coord_Mtx(Topology_Mtx(Consider_Element,4),2) - sy
           z2zs = Coord_Mtx(Topology_Mtx(Consider_Element,2),3) - sz
           z3zs = Coord_Mtx(Topology_Mtx(Consider_Element,3),3) - sz
           z4zs = Coord_Mtx(Topology_Mtx(Consider_Element,4),3) - sz

           V =x2xs*(y3ys*z4zs-y4ys*z3zs)+y2ys*(x4xs*z3zs-x3xs*z4zs)+z2zs*(x3xs*y4ys-x4xs*y3ys)

           IF ( V < -tolerance ) CYCLE

           xsx1 = sx - Coord_Mtx(Topology_Mtx(Consider_Element,1),1)
           ysy1 = sy - Coord_Mtx(Topology_Mtx(Consider_Element,1),2)
           zsz1 = sz - Coord_Mtx(Topology_Mtx(Consider_Element,1),3)
```

```
        x3x1 = Coord_Mtx(Topology_Mtx(Consider_Element,3),1) - &
                       & Coord_Mtx(Topology_Mtx(Consider_Element,1),1)

        x4x1 = Coord_Mtx(Topology_Mtx(Consider_Element,4),1) - &
                       & Coord_Mtx(Topology_Mtx(Consider_Element,1),1)

        y3y1 = Coord_Mtx(Topology_Mtx(Consider_Element,3),2) - &
                       & Coord_Mtx(Topology_Mtx(Consider_Element,1),2)

        y4y1 = Coord_Mtx(Topology_Mtx(Consider_Element,4),2) - &
                       & Coord_Mtx(Topology_Mtx(Consider_Element,1),2)

        z3z1 = Coord_Mtx(Topology_Mtx(Consider_Element,3),3) - &
                       & Coord_Mtx(Topology_Mtx(Consider_Element,1),3)

        z4z1 = Coord_Mtx(Topology_Mtx(Consider_Element,4),3) - &
                       & Coord_Mtx(Topology_Mtx(Consider_Element,1),3)

        V =xsx1*(y3y1*z4z1-y4y1*z3z1)+ysy1*(x4x1*z3z1-x3x1*z4z1)+zsz1*(x3x1*y4y1-x4x1*y3y1)

        IF ( V < -tolerance ) CYCLE

        x2x1 = Coord_Mtx(Topology_Mtx(Consider_Element,2),1) - &
                       & Coord_Mtx(Topology_Mtx(Consider_Element,1),1)

        y2y1 = Coord_Mtx(Topology_Mtx(Consider_Element,2),2) - &
                       & Coord_Mtx(Topology_Mtx(Consider_Element,1),2)

        z2z1 = Coord_Mtx(Topology_Mtx(Consider_Element,2),3) - &
                       & Coord_Mtx (Topology_Mtx(Consider_Element,1),3)

        V =x2x1*(ysy1*z4z1-y4y1*zsz1)+y2y1*(x4x1*zsz1-xsx1*z4z1)+z2z1*(xsx1*y4y1-x4x1*ysy1)

        IF ( V < -tolerance ) CYCLE

        V =x2x1*(y3y1*zsz1-ysy1*z3z1)+y2y1*(xsx1*z3z1-x3x1*zsz1)+z2z1*(x3x1*ysy1-xsx1*y3y1)

        IF ( V < -tolerance ) CYCLE

        No_Penetrations = No_Penetrations + 1

        Penetration_List(No_Penetrations)=List_of_Boundary_Nodes(Consider_Node) EXIT LOOP
 !      ***********************************************************************************
     END DO: Consider_Element
 END DO: Consider_Node
```

Box 7.2 Pseudo-code delivered to identify if boundary mesh nodes interpenetrate in any FE domain

Note that the aspect of computational efficiency is additionally improved by the function CYCLE (Box. 7.2). Indeed, for the first noticed negative volume, the function enables the jump from the current computational loop to the next one, and thus accelerates the search. Furthermore, due to the computational round-off errors, the test of volume sign is performed by assuming a minimum tolerance value which is set as negative value close to zero. Namely, the computed volume for the node-surfaces proximity can be easily below zero. Since the surface under consideration can lie on the mesh boundary, the situation should not be interpreted as a problem *a-priori*. In this case, the gap value *g* is close to zero, denoting no contact (6.2). However, if the

penetrated node lies on the interior surface (between two internal element faces) the detection procedure may fail to identify the penetration. This is the reason why a certain tolerance is needed to check the sign of calculated volumes. The same situation occurs if the contractor node falls on the internal element edge. As in case of node-surface proximity, these situations can be accounted for taking into account low tolerance while checking the related volume sign. Finally, mention that the strategy presented in Box 7.2 is valid only if the node numbering convention is respected (Fig. 3.2).

7.3.3   Speed-up of global detection

Even for the improved global contact detection (Box 7.2), it is easy to agree that the computational loop is still rather expensive. In order to minimize necessary computations, and to preserve the robustness of the strategy, two simple modifications are presented below.

The first modification arises from the fact that relatively small time increments Δt must be adopted in order to reproduce the deformation path caused by high-energy impact loading. The mentioned makes the assumption of relatively small incremental displacements valid. So, after adding the displacement vector $\Delta \mathbf{u}^D$ to coordinate vector $\mathbf{X}_n$, the forbidden penetrations will always be registered in the proximity of mesh boundaries. Consequently, the strategy given in Box 7.2 can be simply improved by replacing the list of elements in the loop `Consider Element` (which denotes the list of elements in the whole discretization) with the list of elements situated only on the mesh boundary (boundary layer elements). By dramatically decreasing the number of computational loops, the modification will considerably contribute to the acceleration of the global contact detection phase (Fig. 7.3).
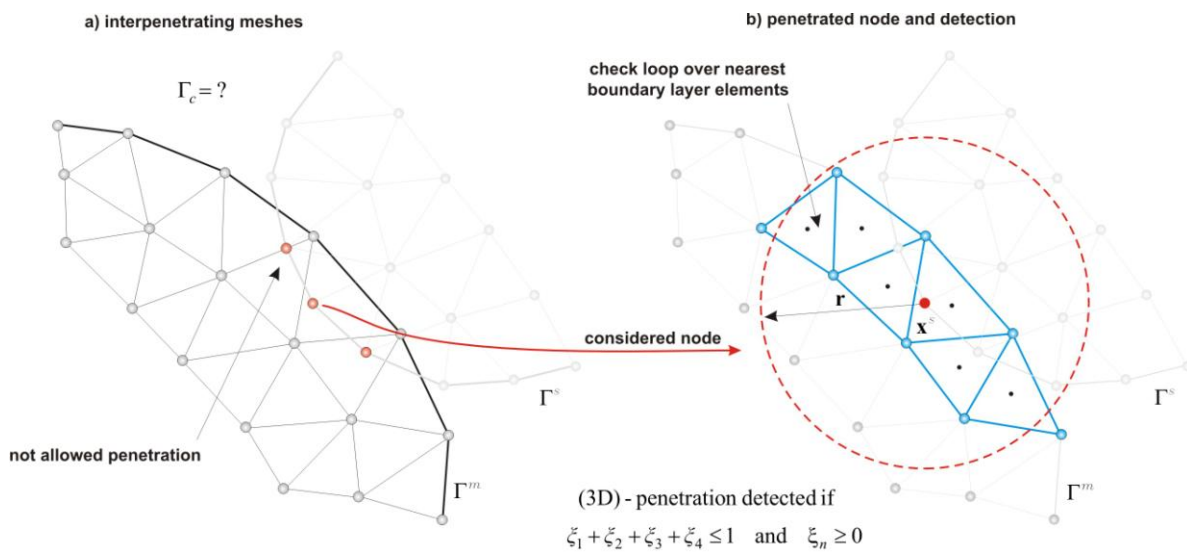

Figure 7.3 Identifications of not allowed nodal penetrations (test by local coordinates or volume sing)

The computational loop in Box 7.2 can be further accelerated by specifying the radius **r** for volume testing. In this case, instead of performing the loop check over all elements, the loop procedure is performed over a number of boundary elements that are situated inside the radius **r** (Fig. 7.3b). Considering that the computation of distance between two points is evidently much cheaper than the volume computations (7.2), it is reasonable to calculate the barycenter coordinates of all elements on the mesh boundary and then the distance between that retrieved coordinates and the boundary node candidates for penetration. If the distance is smaller than the pre-defined tolerance value **r** (Fig. 7.3b), the penetration check will be carried out by volume computations (Box 7.2). As a benefit, for a node candidate for penetration, the check loop will be performed only over the nearest elements on the boundary layer, improving the efficiency of the strategy.

7.4 Local detection

Resume, after identifying the ID of a boundary node that penetrates into a forbidden spatial discretization (now classified as contractor node), a detailed check should be performed in order to find an adequate target surface needed to perform the contact element assimilation. The related computations form the local contact detection phase.

7.4.1 Surfaces that are candidates for contact assimilation

The most robust way to find possible contact pairs would be to check every contractor node against every boundary surface with a pre-defined quantitative measure for contact pair assimilation. However, even for simplest criteria of contact pair assembly, it is evident that the given description is quite expensive and consequently inappropriate for practical applications.
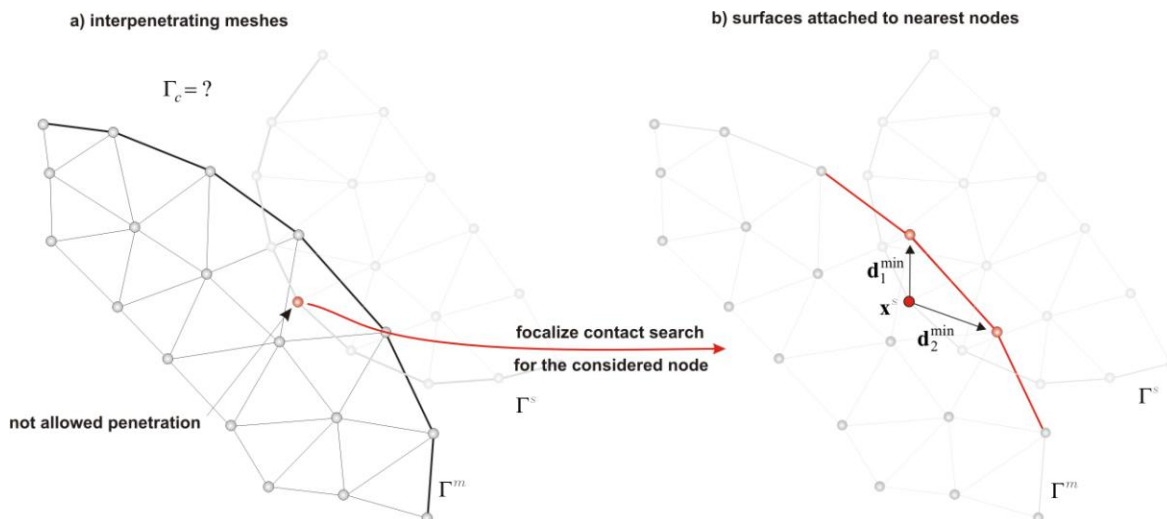

Figure 7.4 Set of candidate surfaces as plains attached to the boundary nodes nearest to the penetrated node

However, according to the assumption of relatively small incremental displacements, the contact element assimilation can be focused only on certain number of boundary surfaces around each contractor node. This is possible since the small nodal movement implies no interaction with more distant surfaces. The list of surfaces that are candidates for contact assimilation can be obtained as follow. The first step is to determine the number of boundary nodes nearest to the contractor node in question. Note that, due to the large number of nodes on the mesh boundaries, the procedure should be performed carefully. Otherwise, it could badly harm the computational efficiency. For this purpose, Box 7.3 contains an optimized pseudo-code delivered for this purpose.

```
! for a given penetrated node find a certain number of nearest boundary nodes
! ***************************************************************************

DO Penetration = 1, No_Penetrations

Node_Distance_Vec = 0.0
Node_Number_Vec = 0

mx = Coord_Mtx(Penetration_List(Penetration),1)
my = Coord_Mtx(Penetration_List(Penetration),2)
mz = Coord_Mtx(Penetration_List(Penetration),3)

        DO Boundary_Node = 1, Number_of_Boundary_Nodes

            sx = Coord_Mtx(List_of_Boundary_Nodes(Boundary_Node),1)
            sy = Coord_Mtx(List_of_Boundary_Nodes(Boundary_Node),2)
            sz = Coord_Mtx(List_of_Boundary_Nodes(Boundary_Node),3)

            Node_Distance_Vec(Boundary_Node)=((mx-sx)**2.0+(my-sy)**2.0+(mz-sz)**2.0)**0.5

            Node_Number_Vec(Boundary_Node)=List_of_Boundary_Nodes(Boundary_Node)

        END DO: Boundary_Node

                DO Near_Node = 1, Number_of_Near_Nodes

                    Minimal_Distance = MINVAL(Node_Distance_Vec)

                  DO Boundary_Node = 1, Number_of_Boundary_Nodes

                     IF (Node_Distance_Vec(Boundary_Node)=Minimal_Distance) THEN

                     Nearest_Node_List(Penetration,Near_Node)=Node_Number_Vec(Boundary_Node)
!                    ***************************************************************************

                     Node_Distance_Vec(Boundary_Node)=1.0D+30 ; EXIT LOOP

                     END IF

                  END DO: Boundary_Node

                END DO: Near_Node

END DO: Penetration
```

Box 7.3 Pseudo-code delivered to find nearest boundary nodes to the penetrated node (contractor node)

Once the nearest boundary nodes are identified, the list of candidate surfaces will be determined for each penetrated node by a check loop over all boundary surfaces. The check loop will consist on storing that boundary surfaces that contains at least one nearest boundary nodes.

However, mention that a smaller number of nearest nodes may produce a list of candidate surfaces not accurate enough to trap the contact pair assimilation. Indeed, such situations may lead to wrong assimilation of contact pairs and cause the collapse of the entire numerical simulation. Such scenario is particularly evident in penetration and perforation problems in which, due to the complex time evolution of Γ_c (Fig. 3.4), the contact interface requires a refined discretization.

Before proceeding with the adopted local contact detection strategy, it should be pointed out that the related computations will be based only on the geometrical properties (static projection) and/or kinematical properties (dynamic projection) of nodes on the meshes boundaries.

7.4.2 Closest point strategy

The simplest strategy for pairing contractor nodes with belonging target surface nodes arises from the earlier discussed minimum distance function d (*Chapter 6 – 6.3.2 Gap & minimum distance function*). However, due to its static projection nature, the strategy is not suitable for frictional contact simulations, and it is used here only when the other two implemented strategies (later discussed) fail to identify the contact pairs.
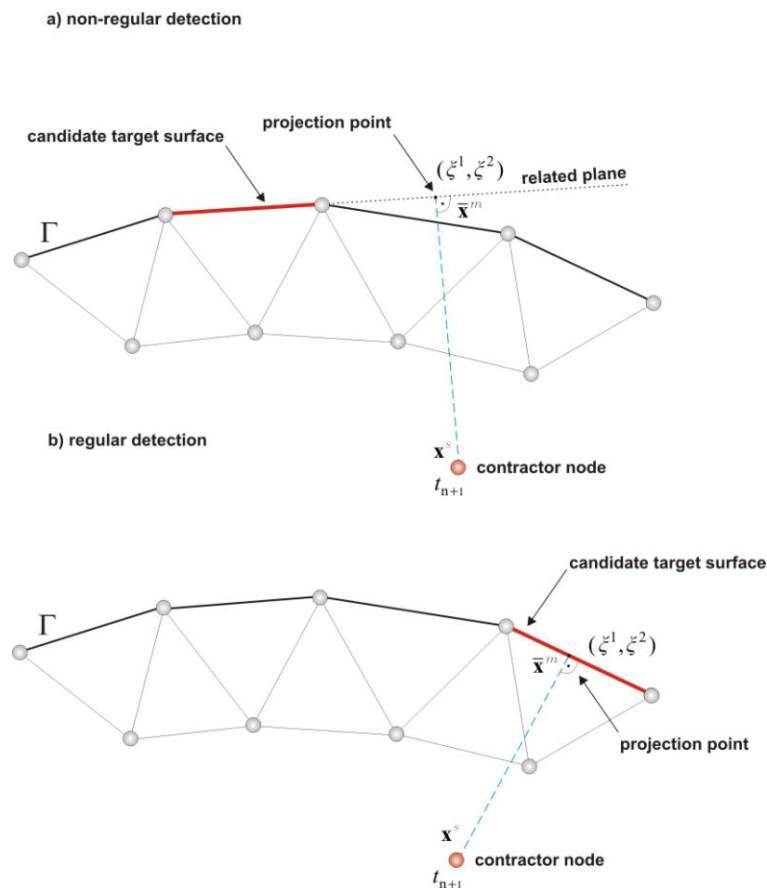

Figure 7.5 Illustration of the closest point strategy: **a)** non-regular and **b)** regular contact detection

Indeed, the combination of different strategies is well justified since the result of the local detection phase is important as the global one. However, the presents of other detection procedures can be also justified by taking into account the fact that each detection procedure operates within a short period of time. Under this circumstance, it is highly sensitive to computational round-off errors (Fig. 7.1). On the other hand, note also that penetration and perforation problems (Fig. 3.4) produce a very challenging environment for local contact detections, evidencing the requirement for few detection procedures.

According to Fig. 7.5, the *closest point strategy* consists on performing a set of successive perpendicular projections of each contractor node over a list of related nearest boundary surfaces (earlier obtained according to Box 7.3). For this purpose, it is assumed that the boundary surface that contains the closest projection is the most suitable for contact element assimilation (Fig. 7.5). Since for the adopted FE the tangent vectors that define the spatial orientation of element surface do not depend on the coordinates $\xi = \{\xi^1, \xi^2\}^T$, the closest form of the minimal distance function d (6.14) can be written as (Wriggers, 2002)

$$\left\{ \mathbf{x}^s - \overline{\mathbf{x}}^m(\xi) \right\} \cdot \overline{\mathbf{a}}_\alpha = \left\{ \mathbf{x}^s - \sum_{c=1}^3 N_c^p(\xi^1, \xi^2) \, {}^c\mathbf{x}_p \right\} \cdot \overline{\mathbf{a}}_\alpha = 0, \tag{7.4}$$

which can be solved directly for ξ^1 and ξ^2 (7.5).

$$\begin{bmatrix} \overline{\mathbf{a}}_\alpha \cdot \overline{\mathbf{a}}_\alpha & \overline{\mathbf{a}}_\alpha \cdot \overline{\mathbf{a}}_\beta \\ \overline{\mathbf{a}}_\beta \cdot \overline{\mathbf{a}}_\alpha & \overline{\mathbf{a}}_\beta \cdot \overline{\mathbf{a}}_\beta \end{bmatrix} \begin{Bmatrix} \xi^1 \\ \xi^2 \end{Bmatrix} = \begin{Bmatrix} (\mathbf{x}^s - {}^1\mathbf{x}) \cdot \overline{\mathbf{a}}_\alpha \\ (\mathbf{x}^s - {}^1\mathbf{x}) \cdot \overline{\mathbf{a}}_\beta \end{Bmatrix} \tag{7.5}$$

Nevertheless, note that the minimum distance requirement is necessary but it is not sufficient to report the contact element found. Being the perpendicular projections performed on plains defined by boundary surfaces, the projection point ξ can fall outside the boundary surface (as illustrated in Fig. 7.5b). Therefore, in order to ensure that the projection point is inside the boundary surface, the compliance of the local projection coordinates ξ must be checked (7.6).

$$\xi^1 + \xi^2 = 1 \quad \text{and} \quad \xi^n \geq 0 \quad \text{where} \quad n = 1,2 \tag{7.6}$$

Finally, the global coordinates of a projection can be obtained by

$$\overline{\mathbf{x}}^m = \begin{bmatrix} 1 & 1 & 1 & 1 \\ {}^1x_{p,1} & {}^2x_{p,1} & {}^3x_{p,1} & x_1^s \\ {}^1x_{p,2} & {}^2x_{p,2} & {}^3x_{p,2} & x_2^s \\ {}^1x_{p,2} & {}^2x_{p,3} & {}^3x_{p,3} & x_2^s \end{bmatrix} \cdot \begin{Bmatrix} 1 - \xi^1 - \xi^2 \\ \xi^1 \\ \xi^2 \\ 0 \end{Bmatrix}, \tag{7.7}$$

where the notation ${}^c x_{p,n}$ is in accordance to Eq. (6.20) and denotes the coordinates component n, of the target surface node c that lies on the mesh boundary (Fig. 6.6).

7.4.3 Trajectory intersection strategy

A more efficient local detection strategy, and also more appropriate for frictional contact analysis, is the *trajectory intersection strategy*. The strategy is based on the assumption that the mesh that contains candidate target surfaces does not suffer nodal displacements obtained in Eq. (6.58). The assumption can be supported by the earlier introduced assumption that the incremental nodal displacements $\Delta \mathbf{u}^D$ are relatively small due to the adopted small time increment Δt.

For the sake of illustration, consider a contractor node moving from time t_n to time t_{n+1} (Fig. 7.6). The line segment that connects the neighboring temporal positions defines the node trajectory. The trajectory intersection strategy chooses the target surface which will be crossed by the contract node trajectory from the list of candidate surfaces (Fig. 7.6).
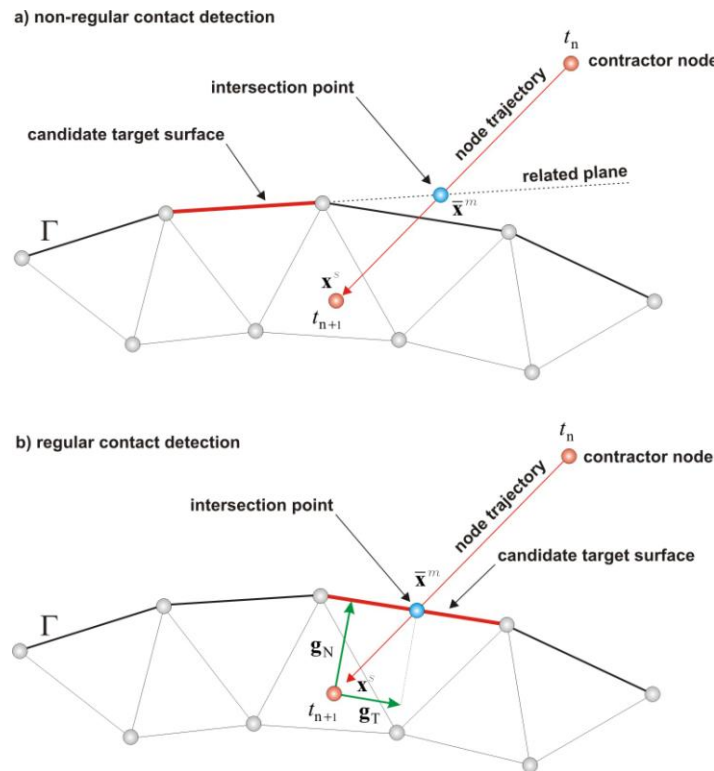

Figure 7.6 Illustration of the trajectory intersection strategy: **a)** non-regular and **b)** regular contact detection

At the numerical implementation level, the strategy requires the computation of the intersection parameter T which defines the global rectangular coordinates of intersection (7.8).

$$
\begin{aligned}
\bar{x}_1^m &= (x_{1,\Delta t}^s) \cdot T + x_{1,t=n}^s &, \quad x_{1,\Delta t}^s &= x_{1,t=n+1}^s - x_{1,t=n}^s \\
\bar{x}_2^m &= (x_{2,\Delta t}^s) \cdot T + x_{2,t=n}^s &, \quad x_{2,\Delta t}^s &= x_{2,t=n+1}^s - x_{2,t=n}^s \\
\bar{x}_3^m &= (x_{3,\Delta t}^s) \cdot T + x_{3,t=n}^s &, \quad x_{3,\Delta t}^s &= x_{3,t=n+1}^s - x_{3,t=n}^s
\end{aligned}
\tag{7.8}
$$

For the given set of coordinates ${}^{c}\mathbf{x}_{p}$, each of them associated to the target surface nodes through index c, and coordinates vectors $\mathbf{x}^{s}_{t=n}$ and $\mathbf{x}^{s}_{t=n+1}$, associated contractor node in time t_n and t_{n+1}, the intersection parameter T arises as a value that satisfies

$$\left\| \begin{bmatrix} \left[x^{s}_{1,\Delta t} \cdot T + x^{s}_{1,t=n} \right] - {}^{1}x_{p,1} & \left[x^{s}_{2,\Delta t} \cdot T + x^{s}_{1,t=n} \right] - {}^{1}x_{p,2} & \left[x^{s}_{3,\Delta t} \cdot T + x^{s}_{1,t=n} \right] - {}^{1}x_{p,3} \\ ({}^{2}x_{p,1} - {}^{1}x_{p,1}) & ({}^{2}x_{p,2} - {}^{1}x_{p,2}) & ({}^{2}x_{p,3} - {}^{1}x_{p,3}) \\ ({}^{3}x_{p,1} - {}^{1}x_{p,1}) & ({}^{3}x_{p,2} - {}^{1}x_{p,2}) & ({}^{3}x_{p,3} - {}^{1}x_{p,3}) \end{bmatrix} \right\| = 0, \qquad (7.9)$$

and can be explicitly calculated as shown in Box 7.4.

```
! procedure for calculate the intersection parameter T
! ****************************************************

LOWER(1 ) = -Px1*Cz1*Py2      ;      UPPER(1 ) =  Cx0*Py2*Pz3
LOWER(2 ) =  Px1*Cy1*Pz2      ;      UPPER(2 ) = -Px1*Cz0*Py3
LOWER(3 ) = -Px3*Cz1*Py1      ;      UPPER(3 ) =  Px2*Cy0*Pz1
LOWER(4 ) =  Px3*Cz1*Py2      ;      UPPER(4 ) = -Cx0*Pz2*Py3
LOWER(5 ) =  Px3*Cy1*Pz1      ;      UPPER(5 ) = -Px2*Cy0*Pz3
LOWER(6 ) = -Px3*Cy1*Pz2      ;      UPPER(6 ) =  Px1*Pz2*Py3
LOWER(7 ) =  Px1*Cz1*Py3      ;      UPPER(7 ) = -Cx0*Py2*Pz1
LOWER(8 ) = -Px1*Cy1*Pz3      ;      UPPER(8 ) = -Cx0*Py1*Pz3
LOWER(9 ) =  Px2*Cz1*Py1      ;      UPPER(9 ) =  Cx0*Pz2*Py1
LOWER(10) = -Px2*Cz1*Py3      ;      UPPER(10) =  Cx0*Pz1*Py3
LOWER(11) = -Px2*Cy1*Pz1      ;      UPPER(11) = -Px1*Py2*Pz3
LOWER(12) =  Px2*Cy1*Pz3      ;      UPPER(12) =  Px2*Py1*Pz3
LOWER(13) = -Cx1*Pz1*Py3      ;      UPPER(13) =  Px2*Cz0*Py3
LOWER(14) =  Cx0*Py2*Pz3      ;      UPPER(14) = -Px2*Cz0*Py1
LOWER(15) = -Cx1*Pz2*Py1      ;      UPPER(15) = -Px2*Pz1*Py3
LOWER(16) =  Cx1*Pz2*Py3      ;      UPPER(16) =  Px1*Cy0*Pz3
LOWER(17) =  Cx1*Py1*Pz3      ;      UPPER(17) =  Px3*Cy0*Pz2
LOWER(18) =  Cx1*Py2*Pz1      ;      UPPER(18) = -Px3*Cy0*Pz1
LOWER(19) = -Cx1*Py2*Pz3      ;      UPPER(19) = -Px3*Pz2*Py1
LOWER(20) = -Px1*Cz0*Py3      ;      UPPER(20) = -Px3*Cz0*Py2
LOWER(21) =  Px2*Cy0*Pz1      ;      UPPER(21) =  Px3*Cz0*Py1
LOWER(22) = -Cx0*Pz2*Py3      ;      UPPER(22) =  Px3*Py2*Pz1
LOWER(23) = -Px2*Cy0*Pz3      ;      UPPER(23) = -Px1*Cy0*Pz2
LOWER(24) = -Cx0*Py2*Pz1      ;      UPPER(24) =  Px1*Cz0*Py2
LOWER(25) = -Cx0*Py1*Pz3
LOWER(26) =  Cx0*Pz2*Py1
LOWER(27) =  Cx0*Pz1*Py3
LOWER(28) =  Px2*Cz0*Py3      ! NOTATIONS
LOWER(29) = -Px2*Cz0*Py1      ! *********
LOWER(30) =  Px1*Cy0*Pz3      ! Px1,Py1,Pz1 ->coordinates of #1 target surface node (time tn)
LOWER(31) =  Px3*Cy0*Pz2      ! Px2,Py2,Pz2 ->coordinates of #2 target surface node (time tn)
LOWER(32) = -Px3*Cy0*Pz1      ! Px3,Py3,Pz3 ->coordinates of #3 target surface node (time tn)
LOWER(33) = -Px3*Cz0*Py2      ! Cx0,Cy0,Cz0 ->coordinates of contractor node       (time tn)
LOWER(34) =  Px3*Cz0*Py1      ! Cx1,Cy1,Cz1 ->coordinates of contractor node       (time tn+1)
LOWER(35) = -Px1*Cy0*Pz2
LOWER(36) =  Px1*Cz0*Py2

        T = SUM(UPPER) / SUM(LOWER)
!       **************************

! * WARNING * -> TRAJECTORY IN PLANE (T=NaN)

            IF (ABS(SUM(LOWER))<=tolerance) TRAJECTORY_TYPE = "PARALLEL"

! * WARNING * -> TRAJECTORY PARALLEL WITH PLANE (T=oo)

            IF (ABS(T)>1.0D+20)             TRAJECTORY_TYPE = "PARALLEL"
```

Box 7.4 Terms needed for calculating the trajectory intersection parameter T (note the warnings)

However, even though the global coordinates of intersection are determined (7.8), the computation is not yet over. Formerly obtained coordinates are again given as coordinates of intersection between the contractor node trajectory and the plain defined by tangent vectors on the candidates' surface (6.21). In other words, if the intersection point falls outside the target plain area, the considered target surface must be rejected as a candidate for contact element assembling (Fig. 7.6). Thus, in order to ensure the validity of the candidate surface the global coordinates of intersection $\overline{\mathbf{x}}^m$ are translated to the local surface coordinates $\boldsymbol{\xi}=\{\xi^1,\xi^2\}^{\mathrm{T}}$ (7.7). Then, the candidate surface is reported as target surface provided that the allowed range of local coordinates is respected (7.6).

7.4.4 Continuous collision detection strategy

The most robust local detection procedure, here primarily invoked, is the continuous *collision detection strategy*. Namely, after gathering a list of potential interaction surfaces for a given contractor node, the strategy establishes the time of contact t_c and the position $\boldsymbol{\xi}$ where the contractor node hits the surfaces. The amount of non-physical penetration can be then easily obtained. Evidently, the strategy is based on the geometrical and kinematical properties of nodes involved in contact. Particularly, by assuming that the nodal velocities $\mathbf{v}_c$ do not change between time t_n and t_{n+1}, the strategy will reveal if and when the contractor node hits the candidate boundary surface (Fig. 7.7).
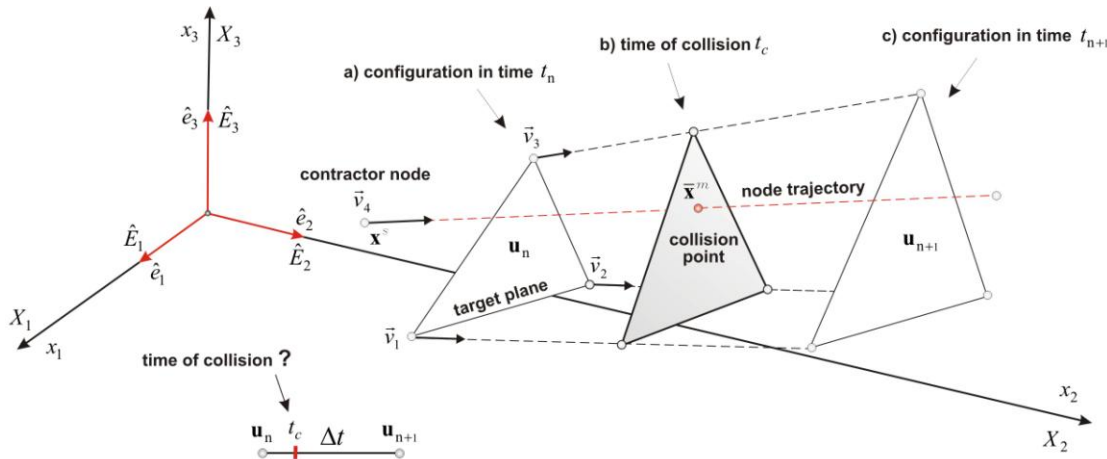

Figure 7.7 Illustration of the continuous collision detection strategy (movement of nodes from time t_n and t_{n+1})

The idea is based on the fact that at the time of collision t_c, the four nodes are coplanar. Provot (1997) showed that for four points defined by the position vectors $\mathbf{x}_n$ and constant velocities $\mathbf{v}_n$, the time t_c at which the points are coplanar satisfy

$$(\mathbf{x}_{21}+t_c\mathbf{v}_{21})\times(\mathbf{x}_{31}+t_c\mathbf{v}_{31})\cdot(\mathbf{x}_{41}+t_c\mathbf{v}_{41})=0, \tag{7.10}$$

where

$$\mathbf{x}_{ij} = \mathbf{x}_i - \mathbf{x}_j \quad \text{and} \quad \mathbf{v}_{ij} = \mathbf{v}_i - \mathbf{v}_j. \tag{7.11}$$

Since the nodal coordinate vectors $\mathbf{x}_n$ and velocities $\mathbf{v}_n$ at a time t_n are known (reference frame), in order to solve Eq. (7.10) the monomial form of the polynomial is needed. By extending the differences in Eq. (7.11) to Eq. (7.10), and grouping the outcome by means of t_c, the solution is obtained by 188 additions and 192 multiplications. From the perspective of efficiency, it is obvious that this computation requires considerable computational effort. Namely, note that the local detection phase is the most frequently applied computational stage in every contact/impact analysis. However, the polynomial can be computed by only 50 additions and 48 multiplications (Hutter & Fuhrmann, 2007), provided that the coefficients are grouped and rewritten as dot- and cross-products (7.12).

$$a_3 = \mathbf{v}_{21} \cdot \mathbf{v}_{31} \times \mathbf{v}_{41} \tag{7.12a}$$

$$a_2 = \mathbf{x}_{21} \cdot \mathbf{v}_{31} \times \mathbf{v}_{41} - \mathbf{v}_{41} \cdot \mathbf{x}_{31} \times \mathbf{v}_{21} - \mathbf{v}_{21} \cdot \mathbf{x}_{41} \times \mathbf{v}_{31} \tag{7.12b}$$

$$a_1 = \mathbf{v}_{41} \cdot \mathbf{x}_{21} \times \mathbf{x}_{31} - \mathbf{x}_{21} \cdot \mathbf{x}_{41} \times \mathbf{v}_{31} - \mathbf{x}_{41} \cdot \mathbf{x}_{31} \times \mathbf{v}_{21} \tag{7.12c}$$

$$a_0 = \mathbf{x}_{41} \cdot \mathbf{x}_{21} \times \mathbf{x}_{31} \tag{7.12d}$$

Furthermore, each cross-product occurs twice thus it can be calculated only once. Now, the time in which the points are coplanar represents the real roots of the cubic polynomial in time

$$P(t_c) = a_3 \cdot t_c^3 + a_2 \cdot t_c^2 + a_1 \cdot t + a_0. \tag{7.13}$$

Note that there are many strategies aimed to reach the solution of the former polynomial. However, in the proposed numerical formulation the so-called companion matrix $\mathbf{M}_c$ is used for this purpose (7.14).

$$\mathbf{M}_c = \begin{bmatrix} 0 & 0 & \dfrac{-a_0}{a_3} \\ 1 & 0 & \dfrac{-a_1}{a_3} \\ 0 & 1 & \dfrac{-a_2}{a_3} \end{bmatrix} \tag{7.14}$$

The roots of the polynomial (7.13) are equal to the eigenvalues of $\mathbf{M}_c$ (7.14). Note that the eigenvalues should be found by means of a procedure coherent with the *double precision* statement used to specify the involved variables. Note also that being the matrix (7.14) non-symmetric; its eigenvalues can obtain imaginary components. Obviously, the imaginary results are instantly discarded. Finally, since the co-planarity condition is necessary but not sufficient for detecting the point-surface interaction, the appropriate time result is the lowest one between the remaining.

Chapter 8

Adaptive finite elements

8.1 Introduction

As high-energy impact loading can occasionally result in penetration of one body into another (or even cause body perforation), the related numerical description must take into consideration possible dramatically changes in geometry of FE. Indeed, the shape of finite elements may degenerate rapidly, what in extreme type of loading can occasionally even lead to almost flat three-dimensional finite elements. In fact, with relatively large concentration of displacements at the impact area, the nearest FE evidence distortional behavior. It is easy to deduce that the problem arises as a consequence of the Lagrangian description of motion (*Chapter 2 – 2.2.1 Kinematics of finite strain*). To avoid element degradations, the so-called *Arbitrary Lagrangian Eulerian formulation* (ALE) is developed to overcome this inappropriate FE behavior (Belytschko, Liu & Moran, 2001). However, due to complexity of ALE formulation, the proposed numerical formulation is based on the Lagrangian description of motion and deals differently with this undesired FE shape degradation. Particularly, the numerical description of concrete subject to penetration is given by the *adaptive finite element strategy* (known as remeshing procedure).

By knowing the convergence state at the end of each time increment Δt, the finite elements distortion (degradations) is quantified and tested in order to establish whether it exceeds the pre-defined tolerance value. If so, the mesh adaptation algorithm is activated. The basics of the mesh adaptation are given by a brief chronological presentation of the related procedures.

8.2   Remeshing criteria

In order to evidence the need for remeshing, a quantitative measure of element distortion must be introduced. For this purpose, due to its simplicity, robustness and reliability, the *element collapse ratio* has been incorporated in the delivered program code. It consists in calculating the parameter χ_e as a ratio between the longest $L_{\max}^e$ and shortest element edge $L_{\min}^e$ in the spatial configuration (8.1).

$$\chi_e = \frac{L_{\max}^e}{L_{\min}^e} \tag{8.1}$$

For linear tetrahedral elements (Fig. 3.2), it is a common practice to tune the procedure in the following manner. If the parameter χ_e is grater than 10, the procedure declares element *e* unsuitable for the next time increment and attributes distortional behavior to it (Fig. 8.1).
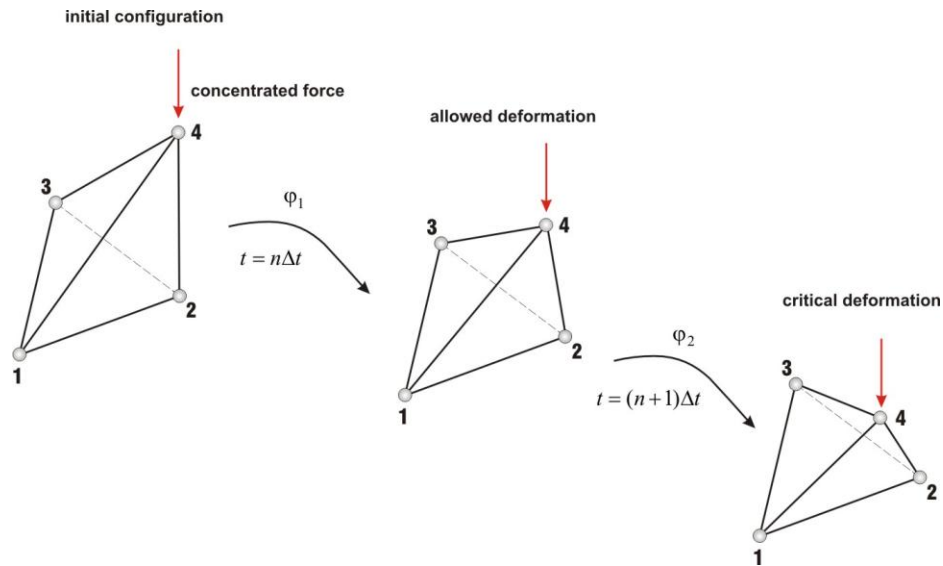

Figure 8.1 Progressive element degradation due to concentrated force (remeshing needed for χ>10)

At the numerical implementation level, the computation of parameter χ_e can be simply and efficiently incorporated (Box 8.1). However, in order to perform the continuous monitoring of elements shape degradation, the procedure must be activated at the end of each time increment.

```
! for a given tetrahedral discretization test mesh elements for distortion
! *************************************************************************

DO Consider_Element = 1, Number_of_Elements

        x1 = Coord_Mtx(Topology_Mtx(Consider_Element,1),1)
        x2 = Coord_Mtx(Topology_Mtx(Consider_Element,2),1)
        x3 = Coord_Mtx(Topology_Mtx(Consider_Element,3),1)
        x4 = Coord_Mtx(Topology_Mtx(Consider_Element,4),1)

        y1 = Coord_Mtx(Topology_Mtx(Consider_Element,1),2)
        y2 = Coord_Mtx(Topology_Mtx(Consider_Element,2),2)
        y3 = Coord_Mtx(Topology_Mtx(Consider_Element,3),2)
        y4 = Coord_Mtx(Topology_Mtx(Consider_Element,4),2)

        z1 = Coord_Mtx(Topology_Mtx(Consider_Element,1),3)
        z2 = Coord_Mtx(Topology_Mtx(Consider_Element,2),3)
        z3 = Coord_Mtx(Topology_Mtx(Consider_Element,3),3)
        z4 = Coord_Mtx(Topology_Mtx(Consider_Element,4),3)

        Lenght(1) = ( ((x1-x2)**2.0) + ((y1-y2)**2.0) + ((z1-z2)**2.0) ) ** 0.50
        Lenght(2) = ( ((x2-x3)**2.0) + ((y2-y3)**2.0) + ((z2-z3)**2.0) ) ** 0.50
        Lenght(3) = ( ((x3-x1)**2.0) + ((y3-y1)**2.0) + ((z3-z1)**2.0) ) ** 0.50
        Lenght(4) = ( ((x4-x1)**2.0) + ((y4-y1)**2.0) + ((z4-z1)**2.0) ) ** 0.50
        Lenght(5) = ( ((x4-x2)**2.0) + ((y4-y2)**2.0) + ((z4-z2)**2.0) ) ** 0.50
        Lenght(6) = ( ((x4-x3)**2.0) + ((y4-y3)**2.0) + ((z4-z3)**2.0) ) ** 0.50


        rate = ( MAXVAL(Lenght(:)) / MINVAL(Lenght(:)) )
!       *************************************************


        IF ( rate > tolerance ) REMESHING_STATUS="YES" & EXIT LOOP
END DO: Consider_Element
```

Box 8.1 Pseudo-code for calculation of tetrahedral elements collapse ratio (activated at the end of each increment)

Since the remeshing procedure involves two spatial discretizations, one before and one after remeshing, it is opportune to distinguish them. For this purpose, the spatial discretization and the related mechanical fields are here characterized as "old" and "new", related to the time at which the remeshing process is carried out. Therefore, after the need for remeshing has been detected (REMESHING_STATUS="YES" in Box 8.1), the contact/impact analysis is temporarily frozen and the procedure for generating the new spatial discretization is invoked. Basically, each remeshing procedure can be hierarchically divided in two phases. The first one involves the generation of the deformed boundary (Box 7.1), and the second one, the generation of a new spatial discretization over the constructed deformed boundary.

Mention that the remeshing process can occasionally keep some elements from the old mesh, and generate new elements elsewhere. Actually, this is a common practice and it is employed here, as well. The benefit of this practice is especially evident when the discretization under consideration describes a quasi-brittle material which establishes cracking and damage phenomena. The statement is discussed late on (*8.4 Path-dependency vs. remeshing*). Additionally, since the discretization occasionally changes form one increment to another, it is opportune to consider eventual mesh adaptations in spatial regions of particular interest (refinement procedure). The procedure is discussed in the following section.

8.3   Refinement criteria

Since the numerical simulation of concrete penetration and perforation events are the main topic of the current Chapter, it should be pointed out that the inevitable remeshing procedure enables to address possible mesh refinements around zones of special interest. Actually, it can be said that the refinement procedure is here somehow inevitable. To support the statement, assume a rigid object that tends to completely penetrate into the concrete mass. In this case, it is reasonable to presuppose that the initial spatial discretization will not be able to accurately describe the shape of the penetrated body. Therefore, progressive mesh adaptations are needed to numerically reproduce Γ_c (Fig. 6.5).

However, apart the abovementioned geometrical need for refinement, the mechanical aspect should be taken into account as well. Indeed, from the historical point of view, the FE refinement procedures arise as a consequence of the need to measure the numerical error caused by FE approximation. Particularly, as was suggested by Zienkiewicz and Zhu (1987), the absolute scalar error ζ_e can be obtained from the generalized form of the classical energy error norm (8.2).

$$\zeta_e^2 = \int_{\Omega_e} \left\| (\boldsymbol{\sigma}^h - \boldsymbol{\sigma}^r)(\dot{\boldsymbol{\varepsilon}}^h - \dot{\boldsymbol{\varepsilon}}^r) \right\| d\Omega_e \tag{8.2}$$

In Eq. (8.2) $\boldsymbol{\sigma}^h$ and $\dot{\boldsymbol{\varepsilon}}^h$ are the stress and strain rates, obtained as FE solution, while $\boldsymbol{\sigma}^h$ and $\dot{\boldsymbol{\varepsilon}}^r$ are the related so-called *reconstruction variables*. In order to measure the solution error, the reconstruction variables are obtained by the *Superconvergent Path Recovery* (Zienkiewicz & Zhu, 1992). Basically, after the error distribution over the spatial discretization is known, the refinement procedure is invoked to increase the number of elements (*h refinement procedure*) or the order of interpolation functions (*p refinement procedure*), or even both of them (*ph refinement procedure*), in zones with errors. However, the briefly illustrated FE error estimator is here not considered. The refinement procedure is presented here only because of geometrical aspects of the FE degradation and not because of the presence of errors in the state variable field (displacements).

It is easy to deduce that, in the numerical simulations of penetration and perforation problems, the mesh zones of interest will be the interface surface Γ_c (zones under refinement). On the other hand, by taking into account the three-dimensional environment for remeshing and refinement procedure, it is obvious that the related procedure will be so complex that should be addressed with special attention. For this purpose, the further discussion will be focused only on a certain type of problems, avoiding generalization. Namely, the perforation problems will be excluded from the further discussion and the penetration problems will be limited to concrete block under impact of shaped objects such as steel anchors and nails.

So far, the reasons for introducing remeshing and refinement procedure have been justified. Now, once the need for remeshing has been identified, the refinement procedure must identify spatial regions which will be refined (Fig. 8.1 & Box 8.1). For this purpose, note that from the chronological point of view, the refinement procedure will precedes the remeshing procedure. Namely, as a result of the refinement procedure, a set of points on and inside the deformed boundary will be retrieved and used to define the locations where the new nodes should be generated. In other words, the refinement procedure will locally prescribe the new mesh property and in this sense introduce restrictions into remeshing.

In order to focus the mesh refinement to specific zones, a quantitative needed to identify the regions of interest should be defined. Since the refinement zones are unknown *a priory*, the related measure must be objective. Indeed, the procedure should include the entire spatial discretization in order to be able to localize the zone of interest. For this purpose, the domain space subject to refinement (Ω_r) can be seen as the union of old domains Ω_e which are mostly affected by deformations.

According to Eq. (2.46), it can be deduced that the determinant of the deformation gradient matrix $\mathbf{F}$ (2.37), i.e. the *Jacobian of deformation J*, will be adequate to quantify the state of FE deformation. In order to check if the element domain Ω_e should be added to Ω_r, the element *Jacobian of deformation* is compared to predefined threshold value ε_r. If $J_e > \varepsilon_r$, the space occupied by the element e will be considered for further refinement. In the later presented numerical example (*Chapter 10 – Numerical examples*), ε_r was set to be depended on the maximal *Jacobian of deformation* (8.3).

$$\varepsilon_r = \det \mathbf{F}_{\max} = \max \left\{ \det \mathbf{F}_e \right\} \tag{8.3}$$

The space region Ω_r subject to refinement was obtained by performing a check loop over all elements in the discretization. Particularly, for those finite elements for which J_e was greater than ε_r multiplied by the scaling coefficient δ (8.4), the element region Ω_e was added to Ω_r. The scaling coefficient δ is here set to 0.85.

$$\begin{aligned} &\text{for } e = 1,2,..,n_e \\ &\det \mathbf{F}_e > \varepsilon_r \cdot \delta \quad \rightarrow \quad \text{refinement over } \Omega_e \end{aligned} \tag{8.4}$$

It should be pointed out that the procedure can form space regions Ω_r that are not connected between each other. In this case, each Ω_r should be treated separately. Indeed, once the regions for refinement are discovered (here the contact regions between the concrete block and steel anchor), the procedure for inserting refinement points should be loop over the number of space regions Ω_r. After that, the remeshing procedure will use such points to allocate new mesh nodes.

The strategy for prescribing new nodal positions follows from the geometry of old elements stored in the list for refinement (8.4). However, since the procedure is already present in the commercial program code FEMAP, which is here used to perform remeshing procedure; it will be only briefly discussed.

Basically, after defining the region for refinement (union of space region Ω_e of those elements for which J_e exceeds the pre-defined criteria value), the program locally produces a new discretization according to the three-dimensional *Delaunay triangularization*. The local discretization is performed by setting a greater value of the so-called *element density parameter*, compared to its value in the same region in the old discretization. However, it should be pointed out that the procedure will progressively decrease the volume of finite elements in Ω_r. Namely, as the incremental analysis goes on, the number of elements in Ω_r will increase and the spatial region Ω_r not evidently. As a consequence, the volume of FE in Ω_r will decrease. In this case, the problem of possible element collapsing arises. To avoid too small elements, the minimum element volume value that should not be traverse (V_{min}), is specified. Therefore, the abovementioned procedure (8.4) is modified by excluding those elements that already reach such margin (8.5).

$$\text{for } e = 1,2,..,n_e$$

$$\text{if } (\det \mathbf{F}_e > \varepsilon_r \cdot \delta \quad \text{and} \quad V_e > V_{min}) \rightarrow \quad \text{refinement over } \Omega_e$$

(8.5)

Note that the volume restriction will not cause the smallest element to resist the refinement procedure. Indeed, since the number of small elements will increases with the evolution of the analysis and, being excluded from refinement (8.5), they will form their own greater spatial region. The region formed by small elements accumulation can be then again remeshed. The possibilities of a described procedure, which is developed and implemented in the delivered program code, are illustrated in Fig. 8.2.
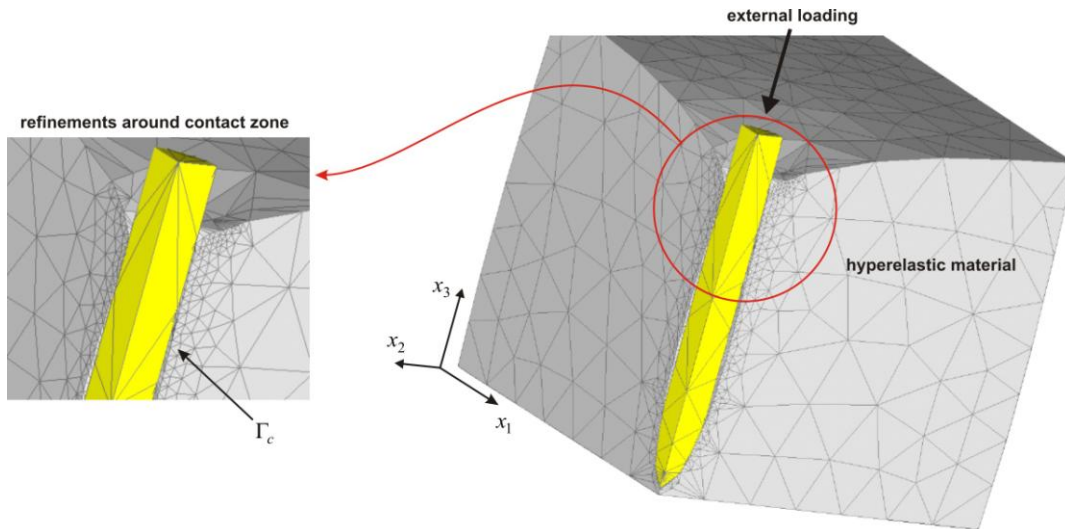

Figure 8.2 Numerical result of a typical penetration problem reproduced by continuous mesh adaptations

By progressive inserting new nodes in the old discretization, the illustrated adaptive finite element strategy allows numerical discretization of very large concentrated displacements (near perforation). Furthermore, it can be observed that the strategy clearly predicts the contact surface Γ_c as the zone of interest. Indeed, by further reduction of the scaling coefficient δ (8.5), the accuracy of the retrieved solution will increase and even a more expanded region will be refined. Consequently, the region under consideration will not be any region but the one that will suffer grater deformations. Therefore, in the case of concrete fracturing, it is expected that the strategy will identify cracks trajectory and follow the cracks accordingly by increasing the number of elements around them. However, since the developed procedure requires considerable computation effort, due to continuous mesh generations and other related complexities, it was not tested yet for this purpose.

For a spatial discretization performed by linear tetrahedral elements, the determinant of the deformation gradient matrix $\mathbf{F}$, which is here used to define the refinement criteria (8.5), can be calculated as

$$\det \mathbf{F} = \left| \begin{bmatrix} \sum_{n=1}^{4} \dfrac{dN_n}{dx_1}\,{}^n u_1 & \sum_{n=1}^{4} \dfrac{dN_n}{dx_2}\,{}^n u_1 & \sum_{n=1}^{4} \dfrac{dN_n}{dx_3}\,{}^n u_1 \\[2ex] \sum_{n=1}^{4} \dfrac{dN_n}{dx_1}\,{}^n u_2 & \sum_{n=1}^{4} \dfrac{dN_n}{dx_2}\,{}^n u_2 & \sum_{n=1}^{4} \dfrac{dN_n}{dx_3}\,{}^n u_2 \\[2ex] \sum_{n=1}^{4} \dfrac{dN_n}{dx_1}\,{}^n u_3 & \sum_{n=1}^{4} \dfrac{dN_n}{dx_2}\,{}^n u_3 & \sum_{n=1}^{4} \dfrac{dN_n}{dx_3}\,{}^n u_3 \end{bmatrix} + \mathbf{I} \right|. \tag{8.6}$$

At the numerical implementation level, the determinant of the deformation gradient matrix $\mathbf{F}$ can be calculated as is illustrated in Box 8.2.

```
! for a given tetrahedral discretization form a spatial region for refinement
! ****************************************************************************

DO Consider_Element = 1, Number_of_Elements

        x1 = Coord_Mtx(Topology_Mtx(Consider_Element,1),1)
        x2 = Coord_Mtx(Topology_Mtx(Consider_Element,2),1)
        x3 = Coord_Mtx(Topology_Mtx(Consider_Element,3),1)
        x4 = Coord_Mtx(Topology_Mtx(Consider_Element,4),1)

        y1 = Coord_Mtx(Topology_Mtx(Consider_Element,1),2)
        y2 = Coord_Mtx(Topology_Mtx(Consider_Element,2),2)
        y3 = Coord_Mtx(Topology_Mtx(Consider_Element,3),2)
        y4 = Coord_Mtx(Topology_Mtx(Consider_Element,4),2)

        z1 = Coord_Mtx(Topology_Mtx(Consider_Element,1),3)
        z2 = Coord_Mtx(Topology_Mtx(Consider_Element,2),3)
        z3 = Coord_Mtx(Topology_Mtx(Consider_Element,3),3)
        z4 = Coord_Mtx(Topology_Mtx(Consider_Element,4),3)

        dN1dx = ( y2*(z4-z3) - y3*(z4-z2) + y4*(z3-z2) ) * ( 1.0d+0 / Element_Volume )
        dN1dy = (-x2*(z4-z3) + x3*(z4-z2) - x4*(z3-z2) ) * ( 1.0d+0 / Element_Volume )
        dN1dz = ( x2*(y4-y3) - x3*(y4-y2) + x4*(y3-y2) ) * ( 1.0d+0 / Element_Volume )
```

```
        dN2dx = (-y1*(z4-z3) + y3*(z4-z1) - y4*(z3-z1) ) * ( 1.0d+0 / Element_Volume )
        dN2dy = ( x1*(z4-z3) - x3*(z4-z1) + x4*(z3-z1) ) * ( 1.0d+0 / Element_Volume )
        dN2dz = (-x1*(y4-y3) + x3*(y4-y1) - x4*(y3-y1) ) * ( 1.0d+0 / Element_Volume )

        dN3dx = ( y1*(z4-z2) - y2*(z4-z1) + y4*(z2-z1) ) * ( 1.0d+0 / Element_Volume )
        dN3dy = (-x1*(z4-z2) + x2*(z4-z1) - x4*(z2-z1) ) * ( 1.0d+0 / Element_Volume )
        dN3dz = ( x1*(y4-y2) - x2*(y4-y1) + x4*(y2-y1) ) * ( 1.0d+0 / Element_Volume )

        dN4dx = (-y1*(z3-z2) + y2*(z3-z1) - y3*(z2-z1) ) * ( 1.0d+0 / Element_Volume )
        dN4dy = ( x1*(z3-z2) - x2*(z3-z1) + x3*(z2-z1) ) * ( 1.0d+0 / Element_Volume )
        dN4dz = (-x1*(y3-y2) + x2*(y3-y1) - x3*(y2-y1) ) * ( 1.0d+0 / Element_Volume )

        F(1,1) = ( dN1dx * Displacements_Vec ( Element_dof(Consider_Element,1 ) ) ) + &
                 ( dN2dx * Displacements_Vec ( Element_dof(Consider_Element,4 ) ) ) + &
                 ( dN3dx * Displacements_Vec ( Element_dof(Consider_Element,7 ) ) ) + &
                 ( dN4dx * Displacements_Vec ( Element_dof(Consider_Element,10) ) ) + 1.0d+0

        F(1,2) = ( dN1dy * Displacements_Vec ( Element_dof(Consider_Element,1 ) ) ) + &
                 ( dN2dy * Displacements_Vec ( Element_dof(Consider_Element,4 ) ) ) + &
                 ( dN3dy * Displacements_Vec ( Element_dof(Consider_Element,7 ) ) ) + &
                 ( dN4dy * Displacements_Vec ( Element_dof(Consider_Element,10) ) )

        F(1,3) = ( dN1dz * Displacements_Vec ( Element_dof(Consider_Element,1 ) ) ) + &
                 ( dN2dz * Displacements_Vec ( Element_dof(Consider_Element,4 ) ) ) + &
                 ( dN3dz * Displacements_Vec ( Element_dof(Consider_Element,7 ) ) ) + &
                 ( dN4dz * Displacements_Vec ( Element_dof(Consider_Element,10) ) )

        F(2,1) = ( dN1dx * Displacements_Vec ( Element_dof(Consider_Element,2 ) ) ) + &
                 ( dN2dx * Displacements_Vec ( Element_dof(Consider_Element,5 ) ) ) + &
                 ( dN3dx * Displacements_Vec ( Element_dof(Consider_Element,8 ) ) ) + &
                 ( dN4dx * Displacements_Vec ( Element_dof(Consider_Element,11) ) )

        F(2,2) = ( dN1dy * Displacements_Vec ( Element_dof(Consider_Element,2 ) ) ) + &
                 ( dN2dy * Displacements_Vec ( Element_dof(Consider_Element,5 ) ) ) + &
                 ( dN3dy * Displacements_Vec ( Element_dof(Consider_Element,8 ) ) ) + &
                 ( dN4dy * Displacements_Vec ( Element_dof(Consider_Element,11) ) ) + 1.0d+0

        F(2,3) = ( dN1dz * Displacements_Vec ( Element_dof(Consider_Element,2 ) ) ) + &
                 ( dN2dz * Displacements_Vec ( Element_dof(Consider_Element,5 ) ) ) + &
                 ( dN3dz * Displacements_Vec ( Element_dof(Consider_Element,8 ) ) ) + &
                 ( dN4dz * Displacements_Vec ( Element_dof(Consider_Element,11) ) )

        F(3,1) = ( dN1dx * Displacements_Vec ( Element_dof(Consider_Element,3 ) ) ) + &
                 ( dN2dx * Displacements_Vec ( Element_dof(Consider_Element,6 ) ) ) + &
                 ( dN3dx * Displacements_Vec ( Element_dof(Consider_Element,9 ) ) ) + &
                 ( dN4dx * Displacements_Vec ( Element_dof(Consider_Element,12) ) )

        F(3,2) = ( dN1dy * Displacements_Vec ( Element_dof(Consider_Element,3 ) ) ) + &
                 ( dN2dy * Displacements_Vec ( Element_dof(Consider_Element,6 ) ) ) + &
                 ( dN3dy * Displacements_Vec ( Element_dof(Consider_Element,9 ) ) ) + &
                 ( dN4dy * Displacements_Vec ( Element_dof(Consider_Element,12) ) )

        F(3,3) = ( dN1dz * Displacements_Vec ( Element_dof(Consider_Element,3 ) ) ) + &
                 ( dN2dz * Displacements_Vec ( Element_dof(Consider_Element,6 ) ) ) + &
                 ( dN3dz * Displacements_Vec ( Element_dof(Consider_Element,9 ) ) ) + &
                 ( dN4dz * Displacements_Vec ( Element_dof(Consider_Element,12) ) ) + 1.0d+0

        detF = F(1,1) * (F(2,2) * F(3,3) - F(2,3) * F(3,2)) - &
               F(1,2) * (F(2,1) * F(3,3) - F(3,1) * F(2,3)) + &
               F(1,3) * (F(2,1) * F(3,2) - F(2,2) * F(3,1))


            IF (detF > detF_margin) CALL RIFINEMENT_DOMAIN (Consider_Element)
!           *****************************************************************


    END DO: Consider_Element
```

Box 8.2 Computation of deformation gradient matrix for the linear tetrahedral element (*J* - refinement measure)

In order to illustrate the proposed refinement procedure, a set of pictures is shown in Fig. 8.3. The given example is obtained by the delivered program code and illustrates the time evolution of mesh density caused by remeshing and refinement procedures. It is easy to agree that the procedures are inevitable for penetration problems. Namely, observe that the in the initial state the mesh region at the front side of the anchor is poorly discretized. As the numerical simulation proceeds, it will be adapted to handle the deformations properly. Note also that the rest of the discretization remains unchanged (zones of lower interest). The benefit of the illustrated strategy is that the computational efficiency can be preserved as long as possible.
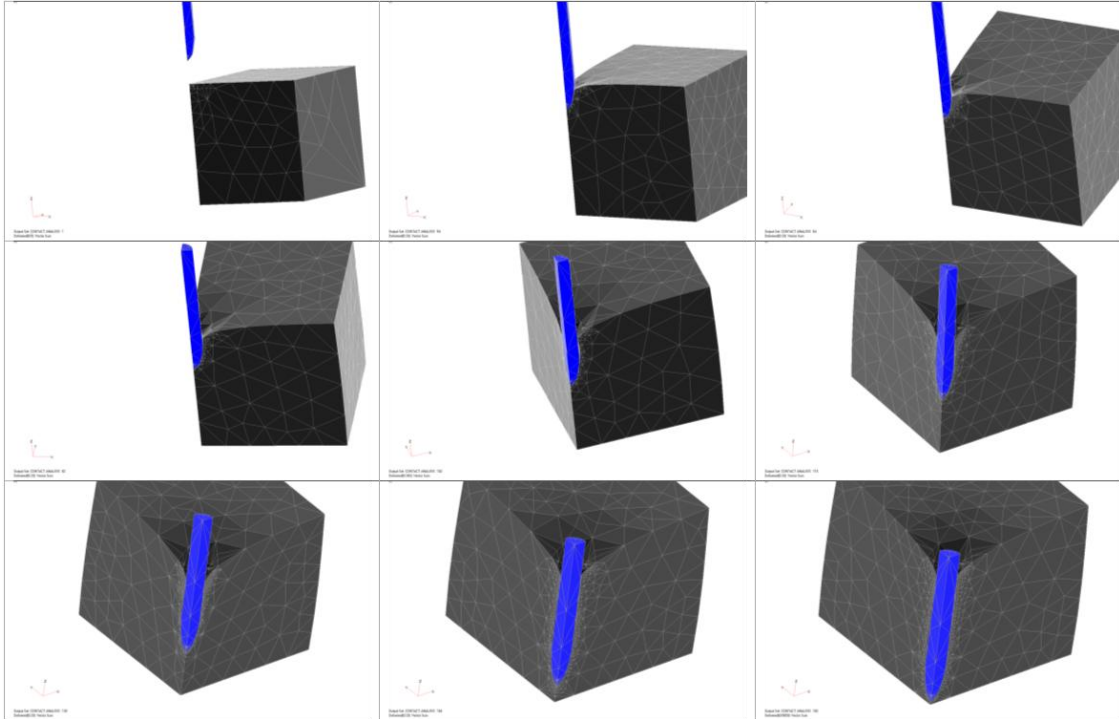
Figure 8.3 Sequences of anchor penetration into a hyperelastic block (progressive refinements around contact)

Besides the remeshing and refinement procedures, there is another subject-related procedure which should be carefully considered in order to fully accomplish the mesh adaptation task. Namely, before proceeding to the next increment of the analysis, the mentioned procedure is expected to copy the mechanical fields from the old discretization to the new one. It should be pointed out that the mapping procedure for non-linear material is challenging task and should be discussed in more details.

8.4   Path-dependency vs. remeshing

Since the remeshing procedure generates a new discretization that is free of any mechanical fields, it is clear that the mechanical information can be preserved only by mapping the mechanical fields from the old discretization to the new one. Several methods have been developed for this purpose (Zienkiewicz, Taylor & Zhu; 2000), but only few are found to be suitable and are employed in the delivered program code. Namely,

due to different materials behaviors, the mapping generalization is not possible. On the other hand, since the remeshing and refinement procedure always produces significant difference between old and new discretization, the mapping procedure is far away from being trivial. Indeed, the projection of old mechanical fields over the new discretization can never exactly reflect the so far reached mechanical state and it will always introduce a certain artificial diffusion of the field in transition. In case of materials like concrete, that suffer damage phenomenon and stain localizations, the artificial diffusion makes the problem even more challenging. Before proceeding with the discussion related to field mapping, some typical notations used in mapping procedures ought to be introduced.

The mechanical fields that are subject of transportation from the old to new discretization are denoted as *state variables*. However, the variables that are needed in the adopted microplane material model are here denoted as *damage variables* (*Chapter 5 – 5.2.3 Microplane stress components*). The reason why such difference is emphasized lies in the nature of damage variables which is more discrete compared to the much smoother fields of state variables (e.g. displacement). In fact, during the transportation of fields from old discretization to the new one, the state and damage variables should be treated separately in order to minimize artificial diffusions and preserve, as much as possible, their original state.

It is common practice to relate all computational procedures necessary for the mapping of a particular mechanical field to the so-called *transfer operator* T. In this case, the relation between the old and new mesh data can be represented as

$$(\sigma^{new}, \varepsilon^{new}, \text{ect.}) = \mathsf{T}(\sigma^{old}, \varepsilon^{old}, \text{ect.}). \tag{8.7}$$

In order to transport all mechanical fields contained in the old discretization, note that the transfer operator T should operate on two types of variables. Namely, by considering one finite element and all related mechanical fields, it can be deduce that the first type of variables will be the vector fields stored in the element nodes (displacements, velocities, accelerations, ect.) and the second one, the tensor fields stored in the FE Gauss point (stress, strain, ect.). In other words, two types of transfer operators will be needed to fully map the old fields into the new discretization. The first is here denoted by T_1, and it is associated to the mesh Gauss point data, while the second one T_2 is associated to the mesh nodal data. Note that T_1 contains two sub-operators since it maps the state and damage variables, for which different mapping procedures are needed.

8.4.1 Transfer operators T_1 & T_2

The difficulties related to the transfer operator T_1, used for the mapping of mesh Gauss point data, arise from the discontinuity of the fields in transition. Namely, with the spatial discretization performed by linear tetrahedral elements, the stress and strain fields inside element domains Ω_e will be constant (*Chapter 3 – 3.3.3.1 Internal force vector*). Therefore, σ and ε are discontinuous over element boundaries. The fact that discontinuity in the old and new discretization cannot be the same implies that exact mapping solutions do not exist (Fig. 8.4).
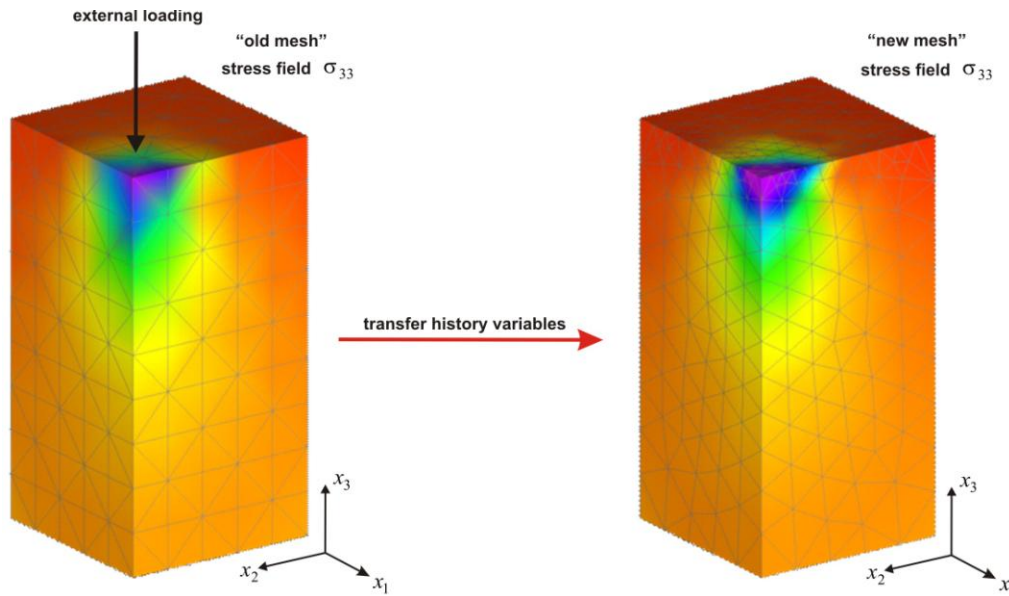
Figure 8.4 Mapping of the stress filed σ_{33} from the old discretization to the new one (note the qualitative accordance)

The related error can be quantified by taking into account two aspects. The first one states that the sum of energetic quantities $\{\boldsymbol{\sigma}_e \cdot V_e\}$ in the old and in the new discretization should coincide. Such requirement can be formulated as

$$\underline{\boldsymbol{\sigma}}^{old}_{e=1} \cdot V^{old}_{e=1} + \underline{\boldsymbol{\sigma}}^{old}_{e=2} \cdot V^{old}_{e=2} + \ldots + \underline{\boldsymbol{\sigma}}^{old}_{e=n_e} \cdot V^{old}_{e=n_e} = \underline{\boldsymbol{\sigma}}^{new}_{e=1} \cdot V^{new}_{e=1} + \underline{\boldsymbol{\sigma}}^{new}_{e=2} \cdot V^{new}_{e=2} + \ldots + \underline{\boldsymbol{\sigma}}^{new}_{e=n_e} \cdot V^{new}_{e=n_e}. \tag{8.8}$$

and it can be only approximately satisfied since the discretizations are *a priori* different and the constant stress and strain fields in each tetrahedral element produce field jumps over the elements boundaries. However, note that the condition in Eq. (8.8) is necessary but not sufficient to ensure the correspondence of fields. In order to ensure the spatial distribution of state variables $\boldsymbol{\sigma}$ and $\boldsymbol{\varepsilon}$, the deflection of old and new iso-surfaces should be minimized as much as possible. Nevertheless, this requirement is difficult to quantify and to incorporate into any transfer operator. Namely, the minimum departure of iso-surfaces should arise as a consequence of an appropriated mapping procedure.

8.4.1.1 *Shape function transfer – operator* T_1

In order to illustrate the transfer operator used for mapping stress and stain fields, imagine a new mesh M1 immersed into the old discretization M2. In this case, the mesh boundaries coincide while the rest of interior nodes will be rarely with equal coordinates. Namely, as mentioned earlier, the remeshing procedure will cause that the number of nodes on the old and new boundary will be different but they will still describe the same boundary. As a consequence, the number of elements will also vary. Particularly, it is common practice to progressively increase the number of elements at each remeshing stage. In this way, it is easier to meet the second abovementioned requirement (i.e. the minimum departure of iso-surfaces).

The projection of the old quantity q^{M1} onto the new quantity q^{M2} can be summarized as follows (Wriggers, 2002). (i) The quantity q^{M1} is projected onto the element nodes by element interpolation functions (3.60). The obtained state is here denoted as $\Lambda_{q,N}^{M1}$ (Fig. 8.5a). (ii) A search procedure is invoked to find the positions of new mesh nodes in the old mesh. (iii) After pairing each new node with one old element, the quantity q^{M1} is projected from old nodes onto the new mesh nodes. The projections are again performed by element interpolation functions (3.60). (iv) The new quantity q^{M2} is obtained by interpolation of the nodal values q^{M1} to the new element Gauss point (denoted as $\Lambda_{q,G}^{M2}$). The described transfer procedure is graphically illustrated in Fig. 8.5.
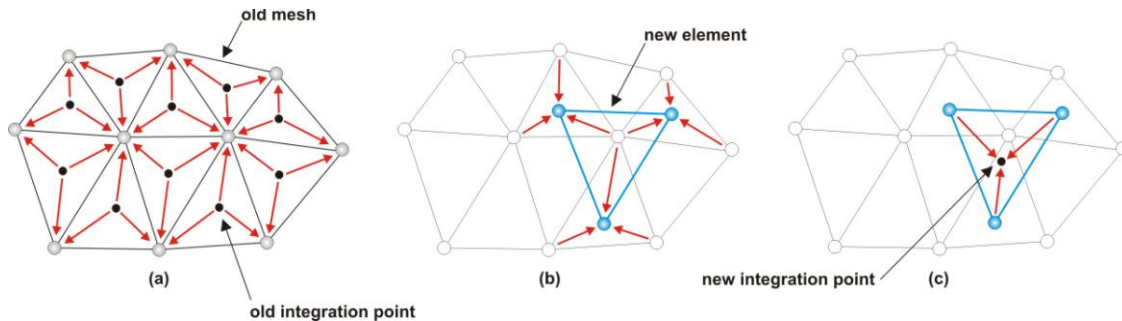
Figure 8.5 T_1 transfer: **(a)** from old Gauss point to old nodes, **(b)** to new nodes and finally; **(c)** to new Gauss points

Note that the discontinuous character of the state variable q in the old discretization is replaced by an approximated continuous field in the new discretization. As a consequence, the given procedure introduces an artificial diffusion in the reconstructed mechanical field. In other words, the transfer procedure will cause that the pick stress value in a particular zone in the old discretization will be smoothed over a certain number of elements in the new discretization. However, the eventual side-effects of the introduced artificial diffusion are here minimized by increasing the density of FE in the new discretization at zone of special interest (contact surface). Since the described procedure involves element interpolation function, the procedure is named *shape function transfer operator* (SFT) and is often given in compact form as (Gharehbaghi & Khoei, 2008)

$$
\begin{array}{ccc}
\text{Gauss points} & & \text{Nodal points} \\[2em]
\Lambda_{q,\mathrm{G}}^{\mathrm{M1}} & \xrightarrow{\text{old mesh-M1}} & \Lambda_{q,\mathrm{N}}^{\mathrm{M1}} \\[1em]
& (q^{\mathrm{M1}}) = \mathsf{T}_1(q^{\mathrm{M2}}) & \downarrow \\[1em]
\Lambda_{q,\mathrm{G}}^{\mathrm{M2}} & \xleftarrow{\text{new mesh-M2}} & \Lambda_{q,\mathrm{N}}^{\mathrm{M2}}
\end{array}
\tag{8.9}
$$

The signatures $\Lambda_{q,\mathrm{N}}^{\mathrm{M1}}$ and $\Lambda_{q,\mathrm{N}}^{\mathrm{M2}}$ denote the state of variable q in the old and new mesh nodes, respectively. Similarly, $\Lambda_{q,\mathrm{G}}^{\mathrm{M1}}$ and $\Lambda_{q,\mathrm{G}}^{\mathrm{M2}}$ denote the state variable in the old and new FE Gauss points, respectively. Mention that in the delivered program code, the illustrated transfer operator does not copy only the stress and strain fields but also the mesh density. Indeed, a few test transfer procedures have demonstrated that the density distribution suffers minor artificial diffusion and that possible side effects can be therefore easily ignored.

8.4.1.2   *Closest point transfer – operator* T_2

In order to preserve the discrete nature of cracking, the artificial diffusion introduced by the shape function transfer operator cannot be allowed or it should be at least minimized as much as possible. Therefore, a more appropriated transfer procedure is used for the mapping of damage variables. The procedure consists in taking the data from the closest Gauss point to the new one (Fig. 8.6).
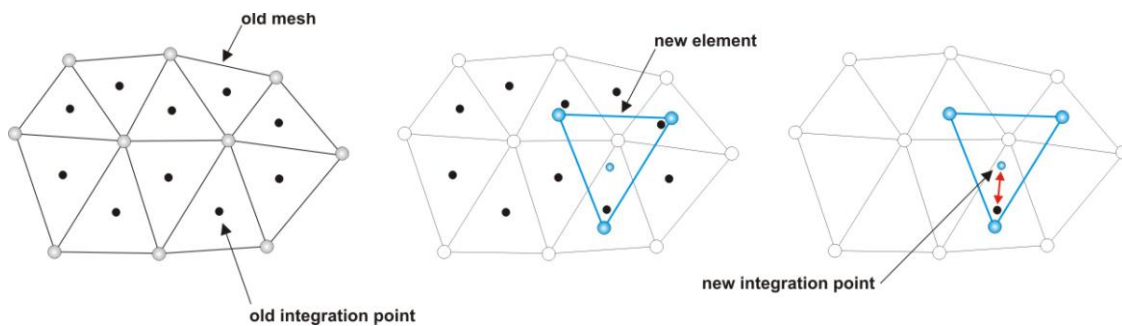
Figure 8.6 Illustration of the closest point transfer procedure T_2 in two-dimensional FE environment

Beside its simplicity, some comparative studies demonstrated that the procedure is suitable for the transfer of damage variable. Namely, it preserves the size of damage and does not introduce any damage diffusion. However, it should be mentioned that the strategy introduces some minor stress oscillations. On the other hand, once the computation has been resumed, the induced oscillations decrease in time due to equilibrium iterations (*Chapter 10 – Numerical examples*).

8.4.2 *Transfer operator* T_3

The transfer operator procedure dedicated to mapping of element nodal values (such as displacements), velocities or accelerations is a much easier and more accurate than the aforementioned two (T_1 & T_2). Indeed, since the element nodal values are linearly interpolated inside the element domain, which is obtained by pre-defined elements interpolation functions (3.61), the nodal fields are not characterized by jumps between the elements boundaries.

Before defining T_3, note that only the nodal displacement field should be transported. In fact, the calculation of the velocity and acceleration field by the reconstructed displacement field is reasonable since the related computational effort is much cheaper than the transportation of all nodal fields.

In principle, the transfer operator T_3 can be formulated as follows:

(i)   Find the old element in which the node n^{new} is located (Box. 7.2).

(ii)   Calculate the barcentric coordinates ξ of node n^{new} located in the now known old element.

(iii)   According to Eq. (3.61), from the displacement vectors $^n\mathbf{u}^{old}$ stored in nodes of the old element, calculate the displacement vector $\tilde{\mathbf{u}}$ for node n^{new}.

Based on the above instructions, T_3 can be formulated as

$$
\begin{array}{ll}
\text{Nodal points} & \\[2mm]
\Lambda_{u,N}^{M1} \qquad\qquad \rightarrow & \text{old mesh - M1} \\[2mm]
& \qquad\qquad \downarrow \\
(u^{M1}) = T_3(u^{M2}) & \underbrace{\left\langle \tilde{\mathbf{u}}^{new} = \sum_{n=1}^{4} N_n(\xi)\, {}^n\mathbf{u}^{old} \right\rangle} \\[2mm]
& \qquad\qquad \downarrow \\
\Lambda_{u,N}^{M2} \qquad\qquad \leftarrow & \text{new mesh - M2}
\end{array}
\tag{8.10}
$$

where Λ^{M1} and Λ^{M2} denote the displacement field in the old and new discretization, respectively, $\tilde{\mathbf{u}}^{new}$ denotes the displacement vector associated to the new mesh nodes and $^n\mathbf{u}^{old}$ the displacement vectors associated to the old mesh nodes. According to Eq. (3.43) and Eq. (3.61), the above described procedure can be translated into an efficient program code as illustrated in Box 8.3.

```
! copy old displacement field into the new discretization
! ****************************************************

DO New_Node = start_ID, end_ID

!     INITIALIZE
!     *****************************************
      LOOP = 0 ; INFO = "Na"
!     *****************************************
      New_Node_XYZ(1) = 1.0
      New_Node_XYZ(2) = New_Coord_Mtx(New_Node,1)
      New_Node_XYZ(3) = New_Coord_Mtx(New_Node,2)
      New_Node_XYZ(4) = New_Coord_Mtx(New_Node,3)
!     *****************************************

        5    DO Old_Element = start_ID, end_ID

                XYZ_Mtx(1,1) = 1.0
                XYZ_Mtx(1,2) = 1.0
                XYZ_Mtx(1,3) = 1.0
                XYZ_Mtx(1,4) = 1.0
                XYZ_Mtx(2,1) = Element_#1_Node_x_Coord_Vec(Old_Element)
                XYZ_Mtx(2,2) = Element_#2_Node_x_Coord_Vec(Old_Element)
                XYZ_Mtx(2,3) = Element_#3_Node_x_Coord_Vec(Old_Element)
                XYZ_Mtx(2,4) = Element_#4_Node_x_Coord_Vec(Old_Element)
                XYZ_Mtx(3,1) = Element_#1_Node_y_Coord_Vec(Old_Element)
                XYZ_Mtx(3,2) = Element_#2_Node_y_Coord_Vec(Old_Element)
                XYZ_Mtx(3,3) = Element_#3_Node_y_Coord_Vec(Old_Element)
                XYZ_Mtx(3,4) = Element_#4_Node_y_Coord_Vec(Old_Element)
                XYZ_Mtx(4,1) = Element_#1_Node_z_Coord_Vec(Old_Element)
                XYZ_Mtx(4,2) = Element_#2_Node_z_Coord_Vec(Old_Element)
                XYZ_Mtx(4,3) = Element_#3_Node_z_Coord_Vec(Old_Element)
                XYZ_Mtx(4,4) = Element_#4_Node_z_Coord_Vec(Old_Element)

                CALL SGESV(4,1,XYZ_Mtx,4,IPIV,New_Node_XYZ,4,INFO) ! LApack solver (Ax=b)

                Local(1) = New_Node_XYZ(1)
                Local(2) = New_Node_XYZ(2)
                Local(3) = New_Node_XYZ(3)
                Local(4) = New_Node_XYZ(4)

                IF (Local(1) < -tolerance) CYCLE
                IF (Local(2) < -tolerance) CYCLE
                IF (Local(3) < -tolerance) CYCLE
                IF (Local(4) < -tolerance) CYCLE

                Transfer_Mtx(1,1) = Old_Nodal_Value_Vec(Old_Element_dof_Vec(Old_Element,1))
                Transfer_Mtx(1,2) = Old_Nodal_Value_Vec(Old_Element_dof_Vec(Old_Element,4))
                Transfer_Mtx(1,3) = Old_Nodal_Value_Vec(Old_Element_dof_Vec(Old_Element,7))
                Transfer_Mtx(1,4) = Old_Nodal_Value_Vec(Old_Element_dof_Vec(Old_Element,10))
                Transfer_Mtx(2,1) = Old_Nodal_Value_Vec(Old_Element_dof_Vec(Old_Element,2))
                Transfer_Mtx(2,2) = Old_Nodal_Value_Vec(Old_Element_dof_Vec(Old_Element,5))
                Transfer_Mtx(2,3) = Old_Nodal_Value_Vec(Old_Element_dof_Vec(Old_Element,8))
                Transfer_Mtx(2,4) = Old_Nodal_Value_Vec(Old_Element_dof_Vec(Old_Element,11))
                Transfer_Mtx(3,1) = Old_Nodal_Value_Vec(Old_Element_dof_Vec(Old_Element,3))
                Transfer_Mtx(3,2) = Old_Nodal_Value_Vec(Old_Element_dof_Vec(Old_Element,6))
                Transfer_Mtx(3,3) = Old_Nodal_Value_Vec(Old_Element_dof_Vec(Old_Element,9))
                Transfer_Mtx(3,4) = Old_Nodal_Value_Vec(Old_Element_dof_Vec(Old_Element,12))

                New_Nodal_Value_Local_Vec = MATMUL(Transfer_Mtx, Local)

                INFO = "FOUND" ; EXIT LOOP

            END DO: Old_Element

        IF (INFO = "NaN") LOOP = LOOP + 1 AND tol = tol + 1.0d-03

        IF (LOOP >  50 ) CALL DEEPER_SEARCH(New_Node) ; IF (INFO = "NaN") GOTO 5

END DO: New_Node
```

Box 8.3 Computation procedure for the transfer of displacement filed from the old discretization to the new discretization

Chapter 9

FE program NACFAIL

9.1   Introduction

In order to test the proposed three-dimensional numerical formulation, the presented procedures are translated into a computational program code. For this purpose, the computer language FORTRAN95 was used. The code verification is performed by comparing the numerical predictions of a free fall drop weight experiment (Fig. 1.1 & Fig. 10.1) with the related experimental results taken from the literature (Bentur, Mindess & Banthia, 1986; Sukontasukku & Mindess, 2003).

The obtained program is named NACFAIL, which is an acronym and stands for:

Numerical **A**nalysis of **C**oncrete **Fa**ilure under **I**mpact **L**oadings,

and was used to obtain all the numerical examples contained in the thesis. The *pre-processing part* (mesh generation) and the *post-processing part* (results preview) were conducted in the commercial program package FEMAP v7.0.

9.2   NACFAIL structure

In order to summarize the computational steps presented in previous Chapters, the structure of the developed program code is hereafter described. For this purpose, the NACFAIL *kernel* is shown in Box 9.1. Note that due to the presence of non-linearity, the subroutines are executed in a repeated fashion. In this case, each computation cycle forms one time increment of the analysis. Obviously, the subroutines named `Initialize` are executed only once, i.e. at the beginning of the analysis. However, if the problem under consideration needs remeshing procedure, the `Initialize` subroutines will be executed once again to adapt the memory space necessary to allocate newly generated arrays.

```fortran
PROGRAM nacfail

        CALL Initialize_MODEL_PARAMETERS
        CALL Initialize_MESH_and_TOPOLOGY
        CALL Initialize_VECTOR_and_MATRIX
        CALL Initialize_MICROPLANE
        CALL Initialize_COLLISION_TRAJECTORY

2       CALL TRANSFER_OPERATORS

        CALL ELEMENTS_VOLUME
        CALL SHAPE_FUNCTIONS
        CALL GENERATE_B_mtx
        CALL INTERNAL_FORCE
        CALL INCREMENTAL_dt
3       CALL DIRECT_INTEGRATION (mesh_condition)

        CALL SET_CONTACT_PASS
4       CALL UPDATE_COORDINATES (pass)
        CALL GLOBAL_SEARCH (pass)
        CALL CLOSEST_NODES (pass)
        CALL CANDIDATES_SURFACES (pass)
        CALL LOCAL_SEARCH (pass)
        CALL CONTACT_CONSTRAINS (pass)
        CALL Gauss_Seidel (pass)                ; IF (pass="FIRST") GOTO 4

        CALL MESH_STABILITY (mesh_condition)    ; IF (mesh_condition="UNSTABLE") GOTO 3

        CALL INCREMENTAL_DISPLACEMENTS
        CALL DEFORMATION_GRADIENT
        CALL POLAR_DECOMPOSITION
        CALL STRAIN_TENSOR
        CALL STRESS_TENSOR
        CALL UPDATE_CONFIGURATIONS

        CALL PRINT_INCREMENT_OUTPUT

        CALL TEST_MESH_DISTORTION (remeshing)
        CALL FEMAP (remeshing)

        IF (INCREMENT="NEXT") GOTO 2

END PROGRAM nacfail
```

Box 9.1 List of subroutines that forms the kernel of NACFAIL (computer language FORTRAN90)

In accordance with the UL formulation (*Chapter 3 – 3.4 UL formulation*), at the beginning of each time increment, the previously obtained deformed configuration is set as the reference configuration for the current increment of the analysis. However, a few preliminary operations are needed if the remeshing procedure has been evidenced at the end of the previous time increment. In such a case, the computational steps contained in subroutine TRANSFER OPERATORS are performed to transfer the state variables (8.9), damage variables (Fig. 8.6) and nodal displacements (8.10) from old discretization to the new one (*Chapter 8 – 8.4 Path-dependency vs. remeshing*). Nevertheless, regardless of whether the remeshing procedure was activated or not, after subroutine TRANSFER OPERATORS, the meshes are set to their reference configurations (material coordinates).

The next set of computational steps begins with subroutine ELEMENTS VOLUME, where the elements volumes are calculated in their reference configuration (3.40). Furthermore, the element nodal shape functions (3.60) are determined in the subroutine SHAPE FUNCTIONS and used to generate the element strain-displacement matrixes **B** (3.74) in the subroutine GENERATE B mtx (*Chapter 3 – 3.3.3.1 Internal force vector*). According to Eq. (3.76) the internal force vector $\mathbf{F}^{in}$ is calculated in subroutine INTERNAL_FORCE. At this point, note that the computation of non-linear terms in Eq. (3.74) and Eq. (3.76) can be avoided since the time integration is performed explicitly (*Chapter 4 – 4.3.2.2 Explicit time integration*). Accordingly, the physical significance of the results is ensured if the adopted time increment Δt is smaller than the critical one which is for this purpose calculated in the next subroutine INCREMENTAL dt.

Following the adopted forward incremental Lagrange multiplies method (*Chapter 6 – 6.4.2.3 Forward incremental Lagrange multipliers method*), the program execution proceeds with the computation of the displacement vector $\mathbf{u}^D$ (6.58) in subroutine DIRECT INTEGRATION. The computations are performed by temporary neglecting the possible mechanical interactions. Namely, if the meshes interpenetrate, the enforcements of contact constraints are satisfied retroactively by identifying contact constraint violations in the following set of subroutines (contact detection). For this purpose, the list of boundary surfaces and boundary nodes is obtained in subroutine Initialize MESH and TOPOLOGY (*Chapter 7 – 7.2 FE surfaces that are candidates for mechanical interaction*).

As the contact description is numerically performed in compliance with the *two-pass algorithm*, the contact detection stage starts with subroutine SET CONTACT PASS, where the master and slave roles is attributed to meshes. Thereafter, the mesh node coordinates are updated in subroutine UPDATE COORDINATES, by adding the formerly calculated incremental displacements $\Delta\mathbf{u}^D$ to them. The contact detection stage begins with subroutine GLOBAL SEARCH, in which the violations of the contact impenetrability condition are identified (Box 7.2). Congruently with the procedure given in Box 7.3, in subroutine CLOSEST NODES, a list of nearest boundary nodes is attributed to each contractor node. From the obtained results, a list of candidates target surfaces is composed for each contractor node in subroutine CANDIDATES SURFACES. In order to pair one contractor node

with the belonging target surface, the continuous collision strategy is executed in subroutine LOCAL SEARCH (*Chapter 7 – 7.4 Local detection*). However, if the strategy fails to pair contact element nodes, which is possible due to computational round-off errors, the local detection phase will proceed with subroutines developed for trajectory intersection strategy (Fig. 7.6) and closest point detection strategy (Fig. 7.5). In subroutine CONTACT CONSTRAINS, the contact displacement matrix **G** (6.45) is generated for each contact element.

In the next set of subroutines, the contact displacement matrixes are used to enforce the contact constraints over Γ_c. The related subroutines are executed according to the Gauss-Seidel iterative fashion, and are contained in subroutine Gauss Seidel (*Chapter 6 – 6.5 Gauss-Seidel iteration*). Finally, with the convergence state obtained after a set of iterations, subroutines dedicated to contact procedures are executed once again if the string variable *pass* is set equal to "FIRST" (Box. 9.1). In particular, the contact procedures are executed again but with switching the master and slave body rules (two-pass algorithm).

At this point, at the end of the current time increment the displacement vector $\mathbf{u}_{n+1}$ is completely defined (6.61). However, possible mesh instabilities should be excluded by verifying if the Euclidian norm of the element displacement vector satisfies the requirement given in Eq. (4.35). The verification is carried out by corresponding computations contained in subroutine MESH STABILITY (*Chapter 4 – 4.3.2.2 Explicit time integration*). If a particular element fails to meet the prescribed condition, the incremental analysis will be repeated by adopting a smaller time interment Δt. In this case, the computation cycles are performed by decreasing the time increment Δt, until the condition in Eq. (4.35) is fulfilled with respect to all elements in the discretization. However, it should be mentioned that the condition is typically satisfied without the reductions of time increment. Namely, it is here introduced only to overcome possibly inconvenient nodal displacements which can be particularly evidenced in concrete penetration problems.

In the following set of subroutines (Box 9.1), the Cauchy stress tensors are calculated for the now known current configuration. The computation starts with subroutine INCREMENTAL DISPLACEMENTS where the incremental displacement vector $\Delta\mathbf{u}$ is calculated as $\Delta\mathbf{u}^D+\Delta\mathbf{u}^C$. The displacement vector $\Delta\mathbf{u}$ is further used to define incremental strain tensors. Since it is assumed that the constitutive definitions are given through the Green-Lagrangian strain tensor $\boldsymbol{E}$, the computation will proceed with subroutine DEFORMATION GRADIENT (*Chapter 2 – 2.2.2 Deformation gradient*). According to Eq. (2.37), the subroutine provides the matrix **F**, which maps the elements in the reference configuration to their positions in the current configuration. In order to obtain the right Cauchy-Green deformation tensor **C** (2.61), which is needed for the calculation of the Green-Lagrangian strain tensor $\boldsymbol{E}$, the polar decomposition theorem is further performed on the previously defined matrix **F.** The related procedures are contained in subroutine POLAR DECOMPOSITION, and are discussed at the beginning of the thesis (*Chapter 2 – 2.2.3 Multiplicative polar decomposition*). Once the element deformation

has been separated from the rigid body rotation, the required Green-Lagrangian strain tensor **E** (2.73) is calculated in the following subroutine named STRAIN TENSOR (*Chapter 2 – 2.2.4.1 Green-Lagrangian strain tensor*). As the here performed contact/impact analysis involves two different materials (i.e. two different constitutive laws), subroutine STRESS TENSOR splits the computation of stress tensors in two parts. In particular, the strain tensors attributed to the slave body are used in the hyperelastic constitutive model (*Chapter 2 – 2.2.8 Hyperelasticity*), and the strain tensors associated to the master body are used in the microplane material model as the macroscopic strain measure (*Chapter 5 – 5.2.2 Microplane strain components*). The execution ends with subroutine UPDATE CONFIGURATIONS, in which the update of stress fields and coordinates vectors are performed according to the Updated Lagrange formulation (*Chapter 3 – 3.4 UL formulation*).

At the end of the current time increment, subroutine PRINT INCREMENT OUTPUT (Box 9.1) summarizes the convergence status of contact forces in the screen output format. Beside other monitoring variables, at the end of a regular time increment of the contact/impact analysis, the NACFAIL screen output shows also the growing or decreasing tendency of involved mechanical energies (Fig. 9.1).

However, note that the incremental computation of the current time increment is not finished yet, since the meshes under consideration may suffer relatively large concentrated loading (penetration problems) that render them unsuitable as reference configurations for the next increment of the analysis (Fig. 8.1). As previously discussed, in order to avoid the degradation of FE geometry (*Chapter 8 – 8.2 Remeshing criteria*), the element distortional behavior in subroutine TEST MESH DISTORTION is quantified

Figure 9.1 NACFAIL screen output (incremental monitoring)

according to the criteria given in Eq. (8.1). If the remeshing procedure is needed, subroutine FEMAP activates the mesh generator FEMAP which will form a new spatial discretization for the so far obtained deformed boundary. Due to the peculiarity of the procedure, the related operations are discussed separately in the next

subtitle. Nevertheless, with or without remeshing, the next increment of the analysis begins with subroutine `TRANSFER OPERATORS` and proceeds as discussed earlier.

The subroutines that form NACFAIL *kernel* (Box 9.1), and other subroutines involved in the computations, are translated into a set of computational instructions by the Lahey/Fujitsu LF95 Compiler for 32-bit computational architecture.

9.3   Implementation of remeshing

In order to preserve the computational efficiency, which is especially required for penetration problems, the program user should not be involved in possible interventions caused by remeshing. For this purpose and since FEMAP has two useful properties, NACFAIL is joined with FEMAP in an exchanging communication cycles. Namely, FEMAP contains its own *basic script* enabling the manipulation of mesh generation, and second; there is the possibility of automatic run of the specific subroutine immediately after FEMAP activation. The benefit of these two program property are further explained.

If at the end of a certain time increment the subroutine `TEST MESH DISTORTION` (Box 9.1) evidences the need for remeshing, a calling statement in subroutine `FEMAP` runs the mesh generator (Box 9.2). In this case, the mesh generator creates a new discretization for the so far obtained deformed boundary.

```
! if the mesh elements are badly distorted, call FEMAP to automatically generate a new mesh
! ******************************************************************************************

IF (REMESHING_STATUS="YES") CALL SYSTEM ('C:\FEMAP\FEMAP.exe') ! see Box 8.1
```

Box 9.2 FORTRAN statement for the activation of FEMAP from NACFAIL (need for FEMAP.exe file address)

Note that before calling FEMAP, and after detecting the need for remeshing, NACFAIL should provide the information regarding the deformed boundary which is to be remeshed. For this purpose, there are two dedicated folders, through which NACFAIL and FEMAP communicate. The folders are named with respect to meshing time, as pre_REMESHING and post_REMESHING folder.

Furthermore, once the calling statement in Box 9.2 activates FEMAP, the coordinates of boundary nodes and the nodes on boundary plains will be already stored in the folder pre_REMESHING. At this point, it should be mention that the computations in NACFAIL are temporarily frozen and will be reactivated automatically when FEMAP is closed.

In order to automatically run FEMAP script files, which contains the program instructions for remeshing, in the FEMAP dialog window the address at which the related program script is located ought to be inserted (Fig. 9.2). Furthermore, the check box in the same dialog window (located next to "Run Program for New Model only"), should also be activated.
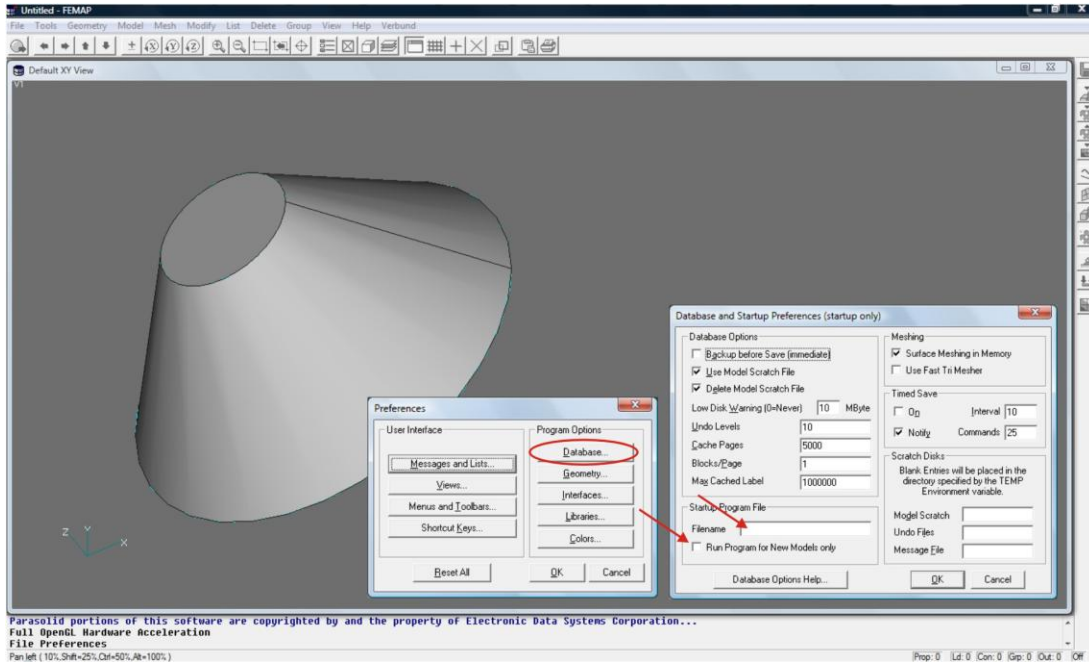

Figure 9.2 Dialog box for the setting of script automatic start immediately upon FEMAP launching

Until now, the preliminary operations for the remeshing automation were presented and now the chronological aspect of procedures used to guide FEMAP through the discretization process will be discussed. For this purpose, mention that the first task of program scripts that are executed with the FEMAP activation is to create a mesh boundary on the bases of files previously allocated by NACFAIL in the pre_REMESHING folder. In accordance with FEMAP basic script program language, the program structure delivered to obtain the mesh boundary is given in Box 9.3. At the end of the given basic script, there are further instructions for execution of remeshing.

```
! FEMAP script - form the mesh boundary based on the result of the procedure given in Box 7.1
! ********************************************************************************************

SUB Construct_Mesh_Boundary

Dim Line1      As Long
Dim Line2      As Long
Dim ret_val    As Long

Dim ival1      As Integer
Dim ival2      As Integer
Dim ival3      As Integer

Dim loc1       As esp_Coord
Dim loc2       As esp_Coord
Dim loc3       As esp_Coord
```

```
        OPEN "C:\Contact\pre_REMESHING\No_Planes_on_Boundary.txt" FOR Input As #1

             Line Input #1, st
             ret_val = esp_MiscParseInit(st)
             ret_val = esp_MiscParseInt(1,ival1)
             Plane_Number = ival1
             CLOSE #1

        OPEN "C:\Contact\pre_REMESHING\Planes_Nodaes_on_Boundary.txt" FOR Input As #1

             FOR i = 1 To Plane_Number

                  Line Input #1, st

                          ret_val = esp_MiscParseInit(st)

                          ret_val = esp_MiscParseInt(1,ival1)
                          ret_val = esp_MiscParseInt(2,ival2)
                          ret_val = esp_MiscParseInt(3,ival3)

                          ret_val = esp_CoordOnNode(ival1,loc1)
                          ret_val = esp_CoordOnNode(ival2,loc2)
                          ret_val = esp_CoordOnNode(ival3,loc3)

                          Line1    = esp_LineEndpoints(10,1,loc1,loc2)
                          Line2    = esp_LineEndpoints(10,1,loc1,loc3)

                          ret_val = esp_SurfRuled(Line1,Line2)

             NEXT i
             CLOSE #1
END SUB

ret_val = esp_FileProgramRun ( "C:\Contact\pre_REMESHING\Remeshing.PRG" )
```

Box 9.3 The given FEMAP script chooses the spatial region for further meshing on the basis of the list of boundary nodes

After obtaining the deformed boundary, the remeshing procedure can be summarized in a set of program scripts illustrated in Box 9.4. In accordance with the previously discussed subject of mesh refinement (*Chapter 8 – 8.3 Refinement criteria*), the generation of the new discretization begins with the script delivered for this purpose. The related basic script operates on coordinates of points on and inside the earlier retrieved domain, and will be used to define a part of the new mesh (restrictions for remeshing).

```
! FEMAP script – extension of the procedure in Box 9.3 – procedures for remeshing
! *****************************************************************************

ret_val = esp_FileProgramRun ( "C:\Contact\post_REMESHING\Refinement.PRG" )

ret_val = esp_FileProgramRun ( "C:\Contact\post_REMESHING\Meshing.PRG" )

ret_val = esp_FileProgramRun ( "C:\Contact\post_REMESHING\Import_Both_Discretization.PRG" )

ret_val = esp_FileProgramRun ( "C:\Contact\post_REMESHING\Renumber_Nodes.PRG" )

ret_val = esp_FileProgramRun ( "C:\Contact\post_REMESHING\Renumber_Elements.PRG" )

ret_val = esp_FileProgramRun ( "C:\Contact\post_REMESHING\Export_Discretization.PRG" )

ret_val = esp_FileProgramRun ( "C:\Contact\post_REMESHING\Export_Boundary_Conditions.PRG" )

CLOSE FEMAP
```

Box 9.4 Chronological execution of FEMAP script programs for mesh remeshing (note the renumbering necessity)

Once the zones of special interest have been defined (refinement zones), the next basic script gives FEMAP necessary instructions for the new mesh. It is important to note that after the mesh has been created, the other non-remeshed mesh (the anchor or nail mesh) should be imported together with the new one (concrete body). Namely, as a result of every remeshing procedure, the numbering of elements and nodes will not coincide with the related numbers in the old discretization. This is a side effect of every remeshing procedure. However, the importing of both meshes allows the renumbering of nodes and elements ID, preserving the identification continuity by avoiding ID repetitions.

In the last two basic scripts given in Box 9.4, the files containing the information on the newly generated discretization are put in post_REMESHING folder. After that, the last instructions force FEMAP to close and give NACFAIL the authorization to proceed with the next increment of the analysis. The computational cycle is considered closed when the txt files left by FEMAP are imported in NACFAIL, and the transfer of all mechanical fields is performed (Fig. 9.3).
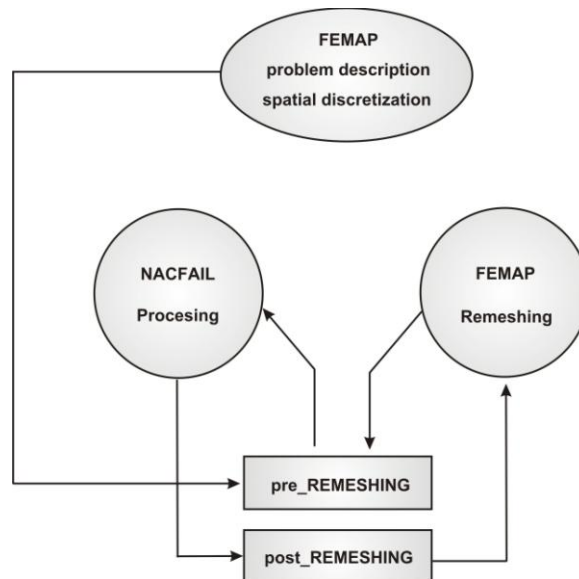
Figure 9.3 Communication between NACFAIL and FEMAP

Mention that it is possible to create program intercommunication (NACFAIL - FEMAP) such that the remeshing and refinement procedure are included for both meshes under collision. The mentioned possibility will allow the numerical simulation of relatively soft body. In that case, the continuous mesh adaptation will be more than required since large displacements at the front of impact are expected for both bodies. In such a case, a special attention must be paid to the renumbering of nodes and elements. Namely, note that there are three remeshing scenarios. The remeshing procedure can be performed for each discretization separately and for both discretizations simultaneously in the same time increment. However, due to the complexity of a needed procedure, which arises as a consequence of different remeshing possibilities, the remark is not yet included in NACFAIL.

9.4   Parallelization

In order to obtain an accurate solution, it is advisable to describe the collision event with a relatively dense mesh of finite elements (*Chapter 6 – 6.4.1 Spatial discretization*). On the other hand, it is also well known that by increasing the number of FE in the discretizations, the computational time effort will be tremendously affected. Therefore, it is opportune to briefly address some possibilities to speed-up the computations.

By examining the mathematical operations present in NACFAIL, it can be seen that only vector operations are performed. Indeed, there is a matrix inversion in Eq. (6.59) but, as the lumped mass matrix is here adopted, the mentioned computation is trivial since the matrix has a diagonal form. Being only vector operations spread over the entire program code, parallelization of the code by the use of OpenMP technique seems to be more reasonable. Basically, OpenMP parallelization consists in the distribution of a non-iterative computational loop, over a number of interconnected CPU cores. In order to illustrate the program implementation strategy, consider a DO loop which doesn't involve any iteration. The computation can be distributed over a number of CPU cores by adding the OpenMP instruction for parallelization (Box 9.5).

```
! distribute a non-iterative loop over a number of threads
! ********************************************************

! $OMP DO

     DO i = 1, 100

       variable = f(i)

     END DO

! $OMP END DO
```

Box 9.5 Algorithm for distribute a DO loop over a number of CPU cores

OpenMP parallelization is especially useful for the contact detection phase. Namely, by distributing the computational loop in Box 7.2 over a number of cores, the global detection phase can be significantly accelerate. On the other hand, the application of the OpenMP parallelization to the local search phase should be further considered. Resume, an appropriate target surface is determined for each penetrated node from the list of candidates' surfaces. Thus, the computations related to the identification of appropriate target surface will be distributed over a number of cores by dividing the list of candidate surfaces by the number of such cores. In order to choose the suitable one, note that the result of all loops should be unified to enable a unique check of contact element assimilation.

Chapter 10

Numerical examples

10.1 Introduction

Three-point bending experiment (Fig. 1.1) shows that the beam resistance and brittleness increase with an increase of loading rate (Sukontasukku & Mindess, 2003). In particular, under relatively low loading rates, it has been shown that the beam failure is due to bending, characterizing the so-called fracture mode I. On the other hand, by an increase in loading rate there is a transition from bending to shear mode of failure. However, due to the fact that fracture takes place in a rather short time period, the experiments at high loading rates are usually related to difficulties of measurement of mechanical properties. In this sense, the numerical analysis is performed for the following two reasons: (i) The first one is to investigate whether the proposed numerical formulation is able to reproduce correctly the experimental results and, if so, (ii) to investigate the response of concrete beam under different loading rates (e.g. energy distribution, failure modes, cracking rate, etc). For this purpose, the following numerical study is carried out by using the delivered program code NACFAIL. In order to evaluate the obtained numerical predictions, the next topic summarizes the basic concepts of concrete failure under impact load.

10.2 Preliminaries

Resume, the results of experimental investigations have shown that loading rate significantly influences the response of structures made of quasi-brittle materials (such as concrete). By comparing the concrete response under static or quasi-static load, with the response obtained at high loading rates (impact), it can be seen that the concrete nominal strength increases with increasing of loading rate.

As discussed earlier (*Chapter 5 – 5.8 Strain rate sensitivity*), the structural response depends on loading rate in terms of three different effects. (i) The first one is the creep of the bulk material between the cracks. (ii) The second one is the rate dependency of the growing micro-cracks. (iii) The last one emerges as the effect of structural inertia forces. Actually, at relatively high loading rates, the last one can significantly influence the state of stresses at the material level. However, each of the aforementioned effects is always present but the dominance of the first, the second or the third effect depends on the type of material and on loading rate. In case of quasi-brittle materials, which exhibit non-elastic strain localization and damage phenomenon, the first effect is important only at relatively low loading rates (creep-fracture interaction). The second one is important at medium loading rates, and the last one dominates the failure mechanism at relatively high loading rates (impact loadings).

Moreover, it is known that the failure mechanism depends on the loading rate, as well. If the loading rate falls inside the static or quasi-static loading region, a concrete beam loaded at the mid-span fails due to the dominating bending stresses (failure mode I). In this case, the failure process is governed by the first abovementioned effect. On the other hand, by increasing the loading rate, the so-called mixed failure mode will be induced. This mode of failure is characterized by a bending crack and two inclined share cracks. By further increase in the loading rate, the mixed mode of failure becomes more articulated. As a matter of fact, under relatively high impact load, the beam rupture is characterized by the pure share mode of failure (only lateral cracks). In order to numerically reproduce the mentioned modes of failure, and the transition modes, the concrete constitutive law is here influenced by the rate-of-deformation.

Currently, there are only a limited number of experimental studies engaged in the investigation of concrete failure mode as a function of loading rate (Bentur, Mindess & Banthia, 1986; Sukontasukku & Mindess, 2003; Ožbolt & Reinhardt, 2005; Saatci & Vecchio, 2009). Apart from the influence of loading rate, the experimental studies address problems such as rather complex energy transfer mechanism that occurs between the contact surfaces of bodies under collision (Comite Euro-International Du Beton, 1988). Indeed, the complex energy transformation mechanism implies that the high impact loading cannot be simply observed as an extreme case of strain rate. Furthermore, as observed by Bentur, Mindess and Banthia (1986), experiments may hardly satisfy the energy balance by measuring energies in the system. On the other hand, by assuming isothermal thermodynamical conditions, note that the numerical analysis should reveal the transformation of the impact kinetic energy into other mechanical energies.

According to the abovementioned, and due to the fact that the concrete failure process occurs in a very short period of time (Fig. 10.1), numerical studies are useful and necessary for a better understanding of concrete damage phenomena under impact loading (Dilger et al., 1978; Reinhardt, 1982; Curbach, 1987; CEB, 1988; Bažant & Gettu, 1992; Weerheijm, 1992; Ožbolt & Reinhardt, 2001, 2005; Saatci & Vecchio, 2009).

Mention that different constitutive relations were employed in the past studies to numerically reproduce the influence of loading rate on the structure response. Principally, most of these models were based on the spring-dashpot models of visco-elasticity. Some models cover only a limited range of loading rates, whereas others cover a more general range. The proposed FE formulation is based on the rate dependent microplane model for concrete (Ožbolt et al., 2001; Ožbolt et al., 2006; Bažant et al., 2000) and is based on the rate process theory of bond ruptures (Krausz & Krausz, 1988).
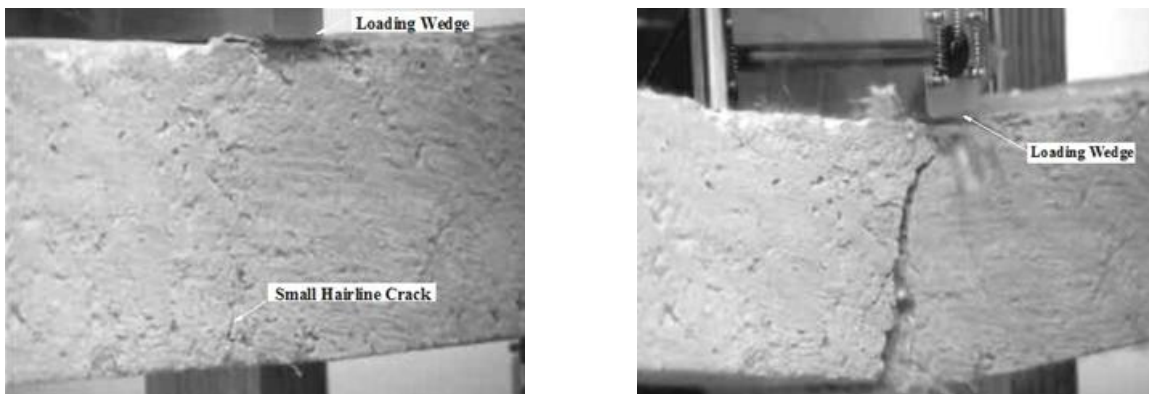
Figure 10.1 The time period between the first contact and the concrete beam rupture is around 1ms

It can be concluded that, due to the complexity of concrete response under impact load, the main purpose of the thesis is to check whether the proposed numerical formulation is able to realistically predict the rate dependent failure mechanism of plain concrete beam. If yes, the influence of the impact velocity on the response of the beam will be studied.

10.3 Plain concrete beam – impact analysis

The numerical experiment is conducted by three-dimensional FE simulation of the free fall drop weight experiment (Fig. 1.1). In order to numerically replicate different failure modes, the altitude of the dropping hammer is set as a variable. The investigated range of impact velocities implies very high strain rates but still smaller than those at which the dropping hammer would cause extreme local damage (crashing over the impact zone). For all dropping altitudes (Fig. 10.2), the beam under consideration is a simply supported beam and loaded by an impact hammer on its middle span.

The dropping hammer is assumed to be linear elastic with Young's modulus $E_h = 100000$ N/mm^2 and density $\rho_h = 8000$ kg/m^3. The length of the hammer is 600 mm and the cross-section area is 300×300 mm. On the contact interface Γ_c the frictional coefficient μ is assumed equal to 0.5. The dimensions of the beam are: length-height-width = $3000 \times 600 \times 300$ mm, while the mechanical properties are: Young's modulus $E_c = 30000$ N/mm^2, Poisson's ratio $\upsilon = 0.18$, uni-axial compressive strength $f_c = 45.0$ N/mm^2, tensile strength $f_t = 2.70$ N/mm^2, fracture energy $G_F = 0.10$ N/mm and density $\rho_c = 2300$ kg/m^3.
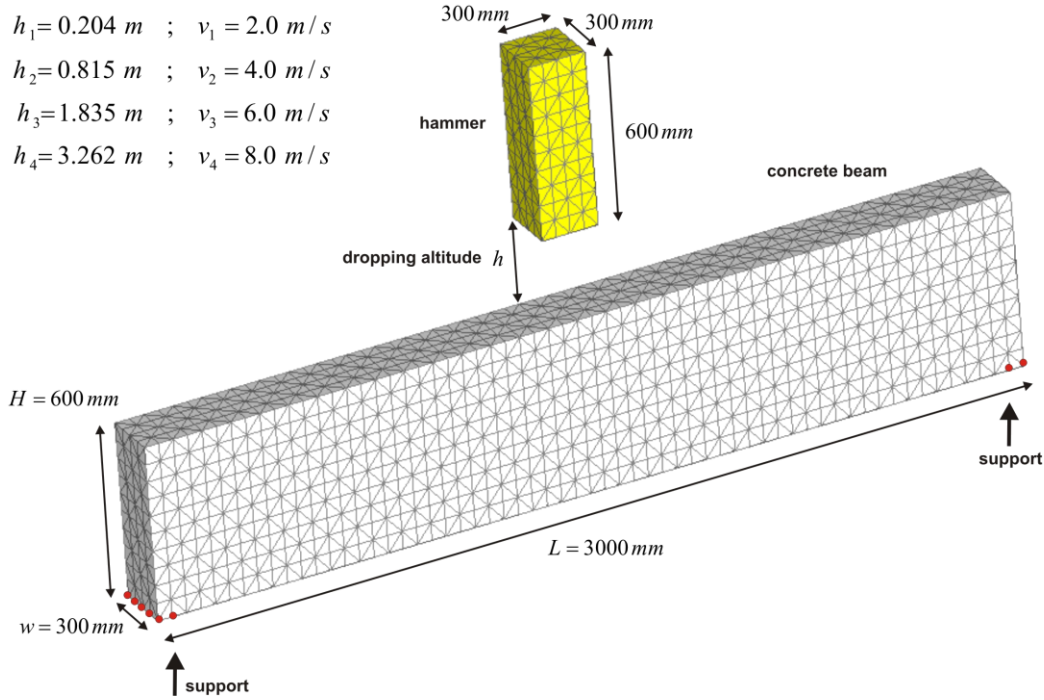
Figure 10.2 Spatial discretization of the free fall drop weight experiment (linear tetrahedral elements)

The numerical analysis is performed for quasi-static loading and for impact velocities of 2, 4, 6 and 8 m/s. Besides the static analysis, the altitudes that cause mentioned impact velocities are illustrated in Fig. 10.2. Mention that, since it is expect that the contact interface Γ_c will not change significantly in time, the adaptive finite elements strategy may be ignored here.

It ought to be pointed out that the non-unilateral contact/impact analysis provides a more realistic beam response. Namely, since the temporal variation of contact forces is a result of inertial properties of the contact interface Γ_c (Fig. 6.7), they can be numerically reproduced only by including the deformation property of both bodies under collision. On the other hand, with a unilateral contact description, the numerical simulation cannot capture the fluctuations of the contact forces. Furthermore, in order to enhance the contact accuracy, in each time increment a *two-pass algorithm* is introduced by switching the master and slave attribute between the meshes in contact.

10.3.1 Static analysis

Fig. 10.3 illustrates the beam failure for the currently considered type of loadings. The picture has been taken from the website of the Engineering research center ATLSS, at the Lehigh University in Bethlehem (Pennsylvania, USA). Note that the proportions of the beam in the experiment and the proportions of the discretized beam are almost identical (Fig. 10.2 & Fig. 10.3).

Figure 10.3 Plain concrete beam exposes in the three-point bending experiment under static loading conditions

In order to ensure static or quasi-static loading conditions, the loading rate is controlled by prescribing displacement vectors at nodes located over the contact surface Γ_c. Therefore, the presence of inertial forces is suppressed by gradual increase of nodes displacement. Thus, the force needed to produce the prescribed displacement is calculated.

According to the briefly discussed smeared cracking concept (*Chapter 5 – 5.1 Introduction*), the cracking trajectories are visible in terms of maximal principal strains (Fig. 5.3). In particular, the critical crack aperture w_{cr} is assumed to be 0.2 mm the average element size is equal to 50 mm. According to Eq. (5.1), it follows that the critical strain ε_r is equal to 0.004. For static loading conditions, the predicted mode of failure is illustrated in Fig. 10.4.

As documented by Sukontasukkul and Mindess (2003), the beams failure mode at static loading conditions primary fall in the flexural mode. The failure is characterized by a single crack, initiated at the bottom of the beam, where the tensile stresses are maximal. By increasing the loading magnitude, the crack propagates straight to the top of the beam surface (beam rupture). As expected, the numerically predicted beam failure mode is of type I (bending failure mode). It is easy to agree that the obtained result (Fig. 10.4) is congruent with the experimental observation (Fig. 10.3).
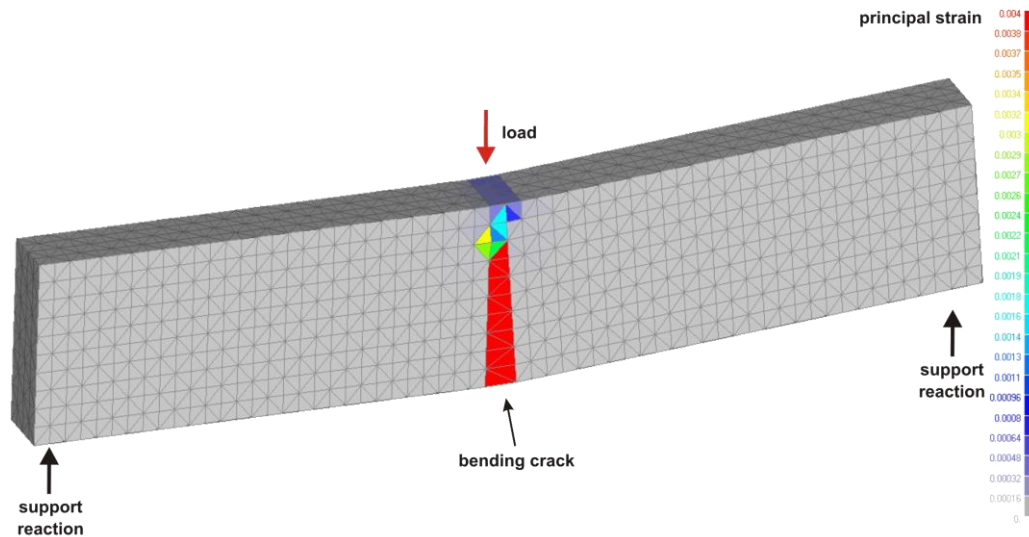
Figure 10.4 Failure mode at static analysis

It should be pointed out that no crack branching or temporal crack arrests are evidenced in the experimental investigations. Accordingly, as will be illustrated soon, the numerical analysis predicts almost linear increasing of the crack tip velocity, without branching or evolutional arrest.

Once the beam rupture takes place, the resistance decreases rapidly (quasi-brittle failure). The performed numerical analysis correctly predicts the mentioned beam behavior, which can be supported by Fig. 10.5 showing the calculated load-displacement curve at the beam mid-span.
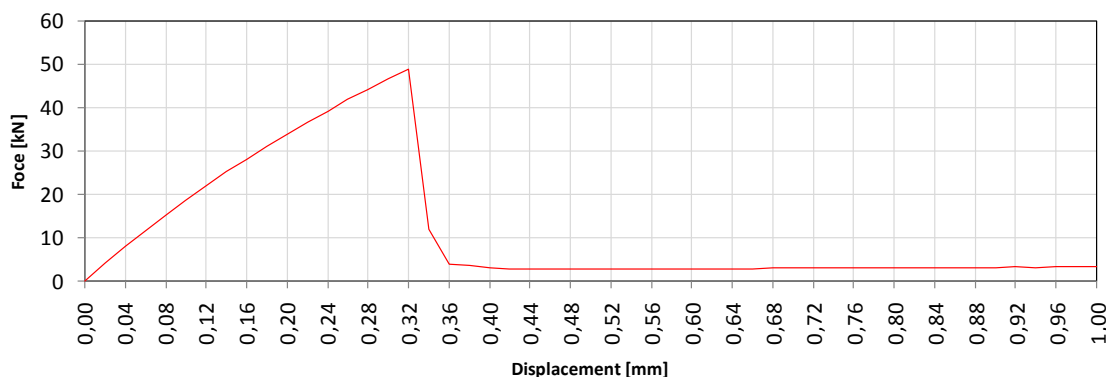
Figure 10.5 Load-displacement curve at the beam mid-span (static analysis)

10.3.2 Dynamic analysis

Apart from the static loading conditions, the response for dynamic loading is here tested. A set of numerical predictions of the free fall drop weight experiments are given. The numerical results are obtained by keeping the hammer mass constant and by varying the hammer dropping altitude, all according to the specifications given in Fig. 10.2.

10.3.2.1 Failure modes and energies transformation

Fig. 10.6, 10.7, 10.8 and 10.9 shows predicted failure modes in terms of maximal principal strains. Consider the time interval up to the moment when the contact beam-hammer contact force drops approximately to zero. Within this time period the relevant damage of the beam takes place. It can be seen that for impact velocity of 2 m/s dominates mode-I fracture. However, for impact velocity higher than 4 m/s dominates shear failure mode and for impact velocities between 2 m/s and 4 m/s there is a transition from bending to shear failure. Similar results were obtained by experimental investigations (Sukontasukku & Mindess, 2003). Note, that these "limit" impact velocities are valid only for the here investigated beam-hammer geometry and their mechanical properties. For other geometrical and mechanical properties, these limit velocities would change. However, the observed failure modes would principally be the same.
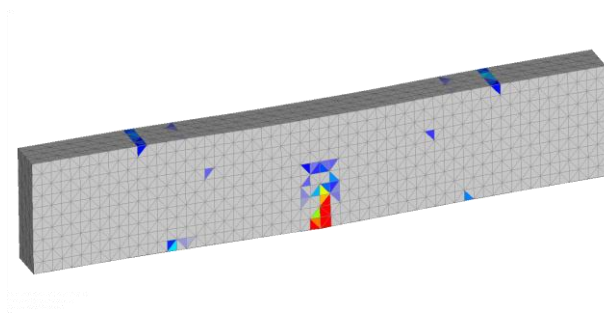
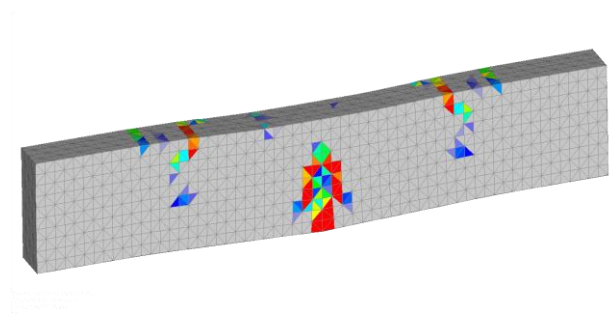**Figure 10.6** Failure mode at impact velocity of 2 m/s

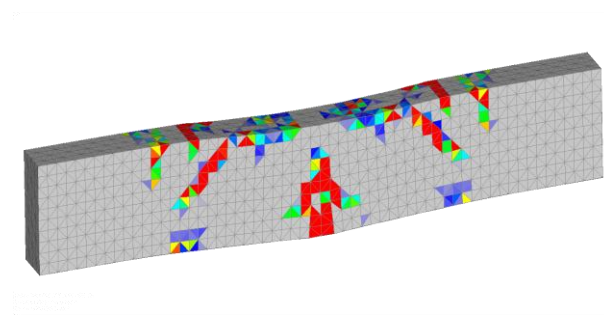**Figure 10.7** Failure mode at impact velocity of 4 m/s

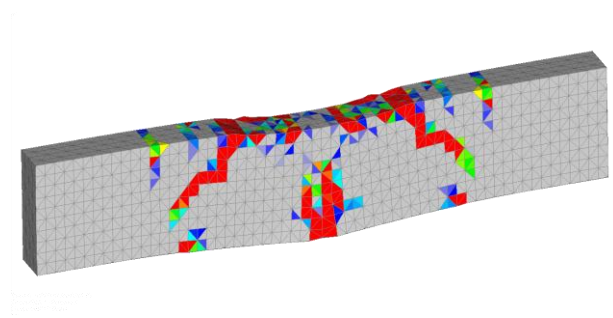**Figure 10.8** Failure mode at impact velocity of 6 m/s

Figure 10.9 Failure mode at impact velocity of 8 m/s

The numerically obtained shear crack inclination is in accordance with the typical experimental observations (Fig. 10.10 - the picture has been taken from the website of Faculty of Science and Technology at the University of Macau).

Figure 10.10 Typical share failure mode

Fig. 10.11, 10.12, 10.13 and 10.14 shows computed distributions of energy as a function of time. It can be seen that, because of relatively high stiffness of the hammer, its deformation energy is negligible compared the deformation energy of the beam. After approximately 0.30 ms the total kinetic energy of the hammer is transformed into deformational and kinetic energy of the beam. The figure shows that the total energy slightly decreases with time. For all loading rates the decrease is obvious only up to the point of transition of the total kinetic energy of the hammer into the beam (approximately up to $t = 0.30$ ms). The reason for this slight drop is the frictional energy between the beam and hammer, which is not included in the total energy plotted. The smaller part of the energy loss is caused by numerical error. The energy curves show that the sum of deformational and kinetic energy is equal to the total energy (isothermal conditions), what confirms that dynamic equilibrium is fulfilled.

10.3.2.2 Contact force, force equilibrium and reactions

The predicted mid-span impact loads and reactions are, as a function of time, plotted in Fig. 10.15 and Fig. 10.17, respectively. Comparing the peak load for quasi-static load (see Fig. 10.5) and impact load (Fig. 10.15), it can be seen that the impact load is much higher than the quasi-static peak (failure) load. With increase of impact velocity the impact load increases. Compared to the impact load, the reaction forces are relatively small. They are activated after the beam is already significantly damaged and impact load reduces almost to zero. This indicates that the load transfer takes place in a relatively small zone of the beam, close to impact zone, and that the impact load is almost entirely in equilibrium with inertia forces. Indeed, with increase of loading velocity, the zone of the load transfer tends to be smaller i.e. more localized (see predicted failure modes).
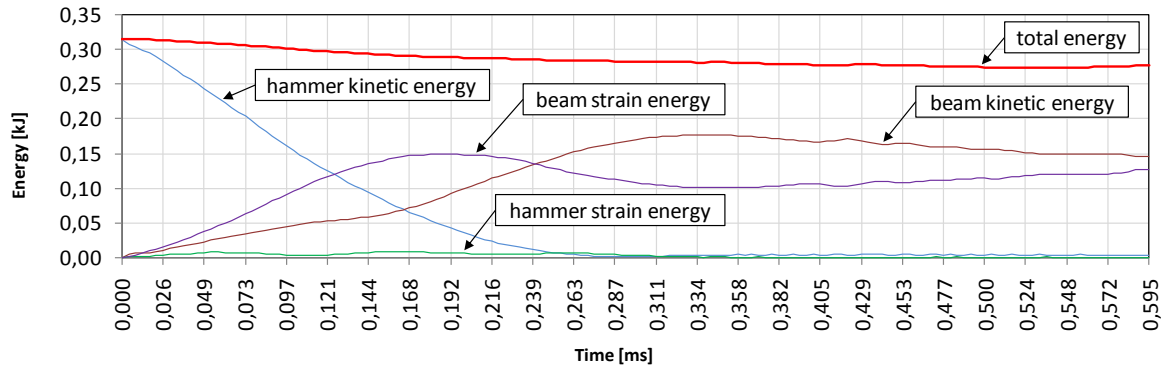
Figure 10.11 Predicted transformation of mechanical energies at impact velocity of 2 m/s
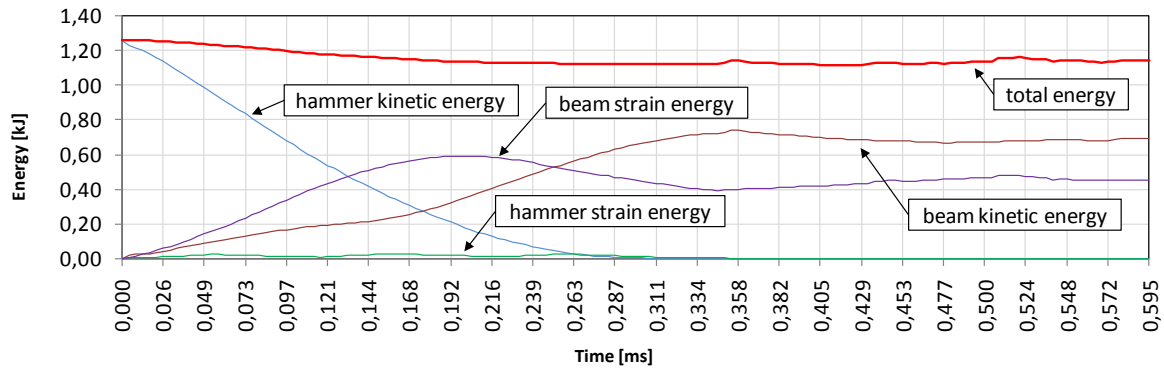

Figure 10.12 Predicted transformation of mechanical energies at impact velocity of 4 m/s
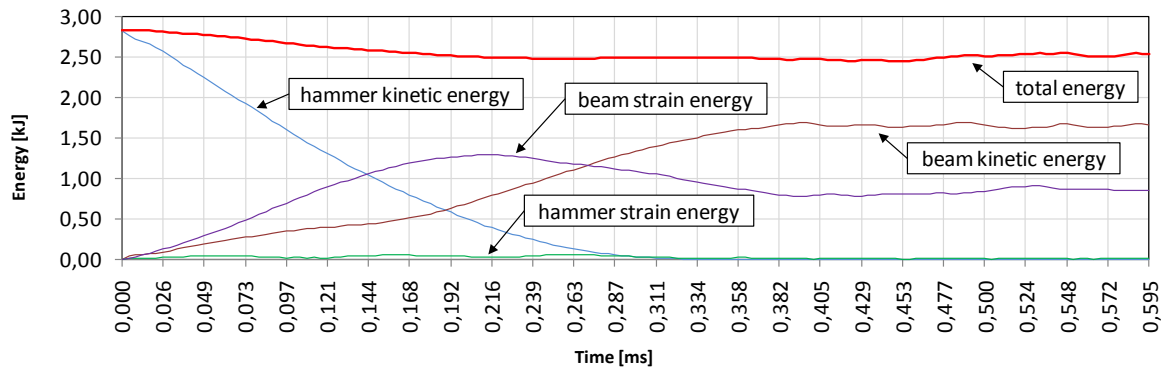

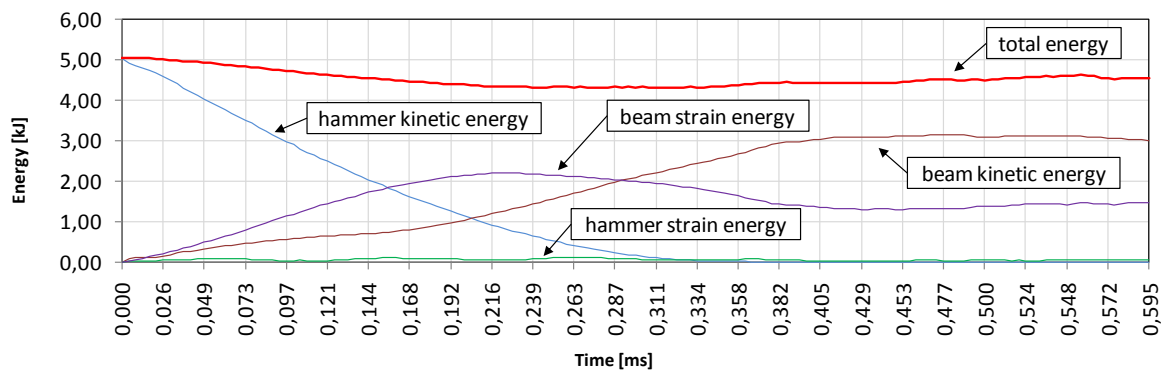**Figure 10.13** Predicted transformation of mechanical energies at impact velocity of 6 m/s

Figure 10.14 Predicted transformation of mechanical energies at impact velocity of 8 m/s

Resume, except the gravity field, there are no external forces acting upon the bodies under collision. Once the contact occurs, all forces present in Eq. (6.48) arise from the change of linear momentum (2nd Newton Law).
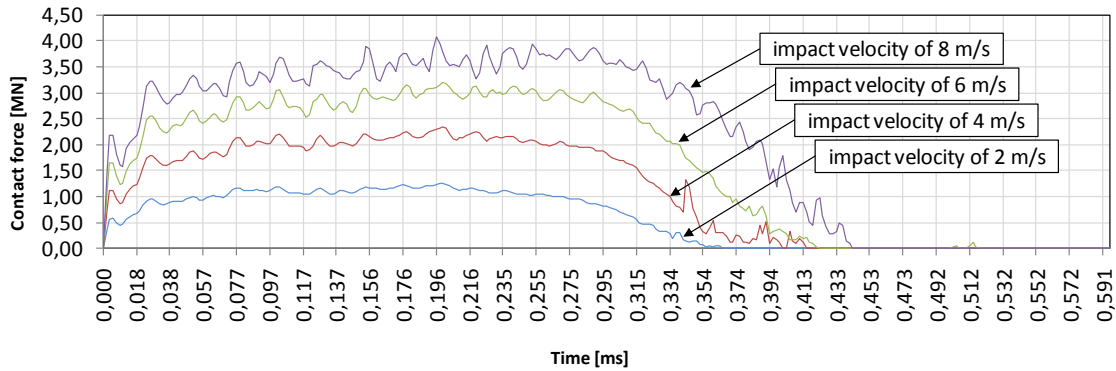

Figure 10.15 Predicted contact forces vs. time

As mentioned earlier (*Chapter 6 – 6.4.1.5 FE form of equilibrium*), observe that the numerical analysis can reveal the contribution of inertial, viscous damping and internal forces in reaching equilibrium state with contact forces. According to Eq. (6.48), for the case where the impact velocity was set equal to 8 m/s, the numerically predicted force components are plotted in Fig. 10.16.
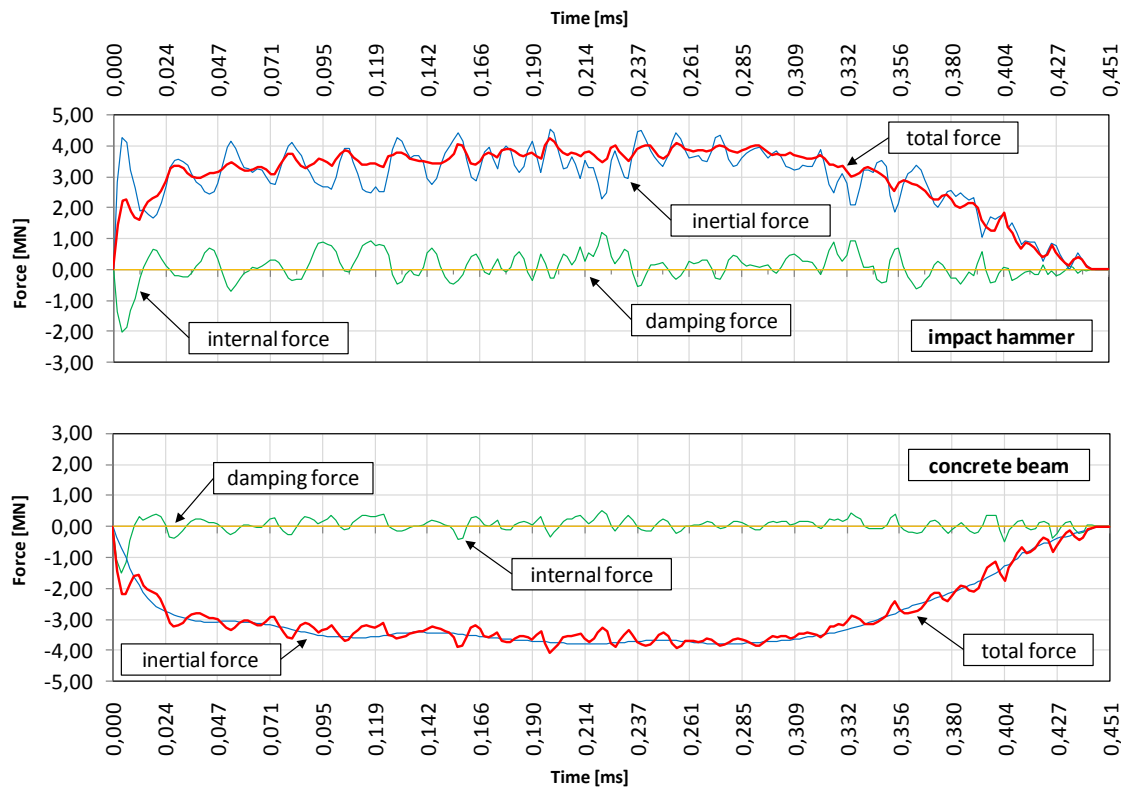

Figure 10.16 Contact force components in the direction of loading (impact velocity of 8 m/s)

Furthermore, it can also be seen that just after the impact of the hammer, the reactions start to act in direction opposite to the impact load (positive reactions). However, once the beam in the zone of impact is damaged, the left and the right part of the beam tend to be lifted up (negative reactions). The mechanism can be illustrated by taking into account the principal compressive stress waves.
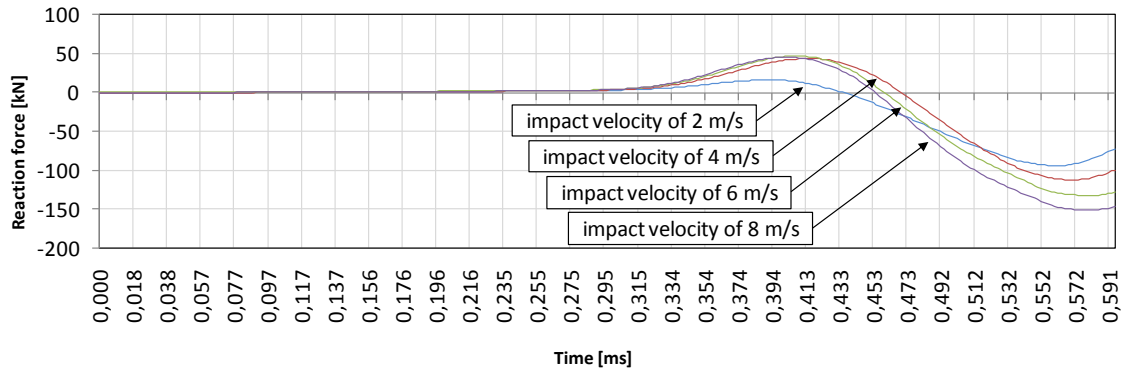

Figure 10.17 Predicted support reactions vs. time

10.3.2.3 Compressive stress waves

Figure10.18 illustrates the plot of sequence of distribution of principal compressive stress waves for the case of impact velocity of 2 m/s. It can be seen that after the beam is damaged in the mid bottom region, the compressive wave propagates under an angle of approximately 35 degree and reflects from the bottom beam surface into the left and the right regions of the beam ends by pushing these parts into direction that is opposite to the load direction (negative reaction). Note also that the velocity of wave propagation is calculated correctly. Namely, for the used concrete the loading wave speed can be calculated from the material properties giving $(E_c/\rho_c)^{0.5} = 3551$ m/s. Accounting for the beam geometry and the time predicted for the propagation of the loading wave from the top to the bottom of the beam (0.165 ms, Fig. 10.18d), it turns out the velocity of 3593 m/s, what agrees well with the loading wave velocity for the used concrete.

10.3.2.4 Propagation velocity of the bending crack tip

In Fig. 10.19 are shown velocities of bending-crack tip as a function of time. They are obtained from the evaluation of numerical results. The relative velocities are related to Rayleigh wave speed (maximal speed of crack propagation), which is for the used concrete $v_R = C_R(G_c/\rho_c)^{0.5} = 2{,}140$ m/s. The constant C_R depends on Poisson's ratio. For the simulated concrete it is equal to $C_R = 910$ (for crack velocity in m/s) and G_c is shear modulus of concrete. It is interesting to observe that after crack initiation, there is almost linear increase in velocity of the crack tip up to the maximal velocity of approximately $0.55v_R$.
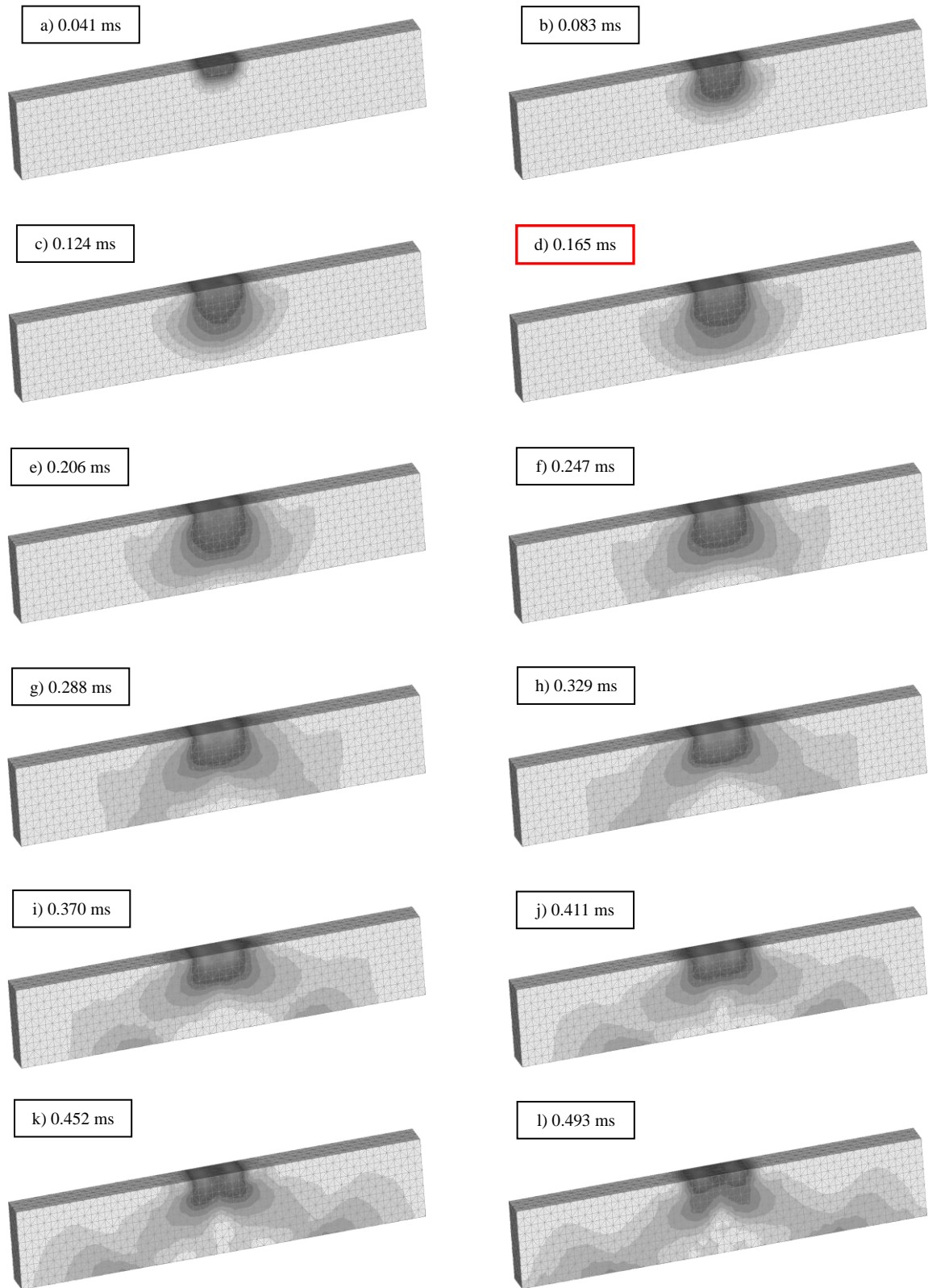
Figure 10.18 Sequences of propagation of principal compressive stresses waves for impact velocity of 2 m/s (bending failure)

This is in good agreement with theoretical prediction (Freund, 1972a; Freund, 1972b). From Fig. 10.19 can be seen that maximal crack speed only slightly increases with increase of impact velocity. According to theoretical solution for dynamic propagation of a single crack (Freund, 1972a; Freund, 1972b), for relative velocities greater than 0.5 crack branching of mode-I crack is possible. This is also confirmed by the results of the present study. Namely, Fig. 10.7, 10.8 and 10.9 show that after reaching relative velocity of 0.5, bending crack tends to branch into two inclined cracks.
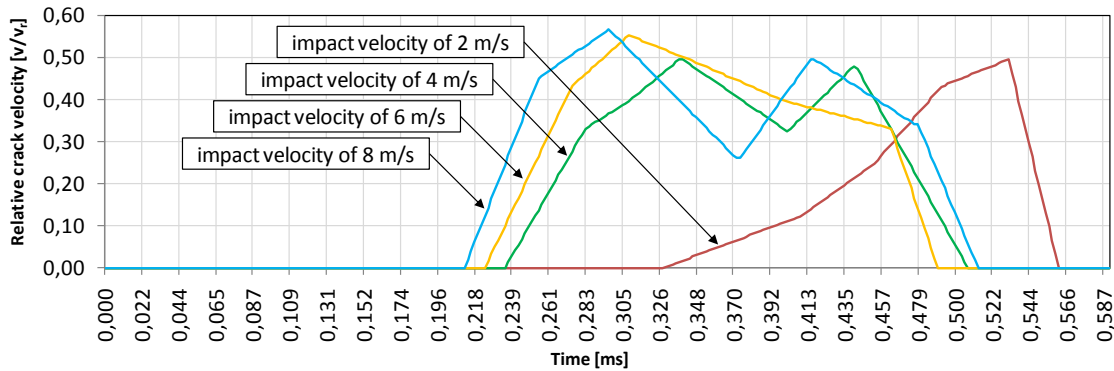

Figure 10.19 Relative velocity of the bending crack tip as a function of time

Furthermore, the evaluation of results indicates that the acceleration at the crack tip is very high, i.e., for a few orders of magnitude higher than the gravity constant. How realistic are such values is difficult to say because it is well known that standard numerical integration scheme, such as used here, often leads to not accurate estimation of acceleration. Mention that he results related to the dynamic crack propagation can be considered only as qualitative. To get more detailed view into the dynamic crack propagation, numerical analysis should be carried out with finer discretization of the cracking zone.

10.3.3 Concluding remarks

The comparison between numerical and experimental results (Sukontasukkul & Mindess, 2003), shows that the used numerical formulation is able to correctly capture the rate dependant failure mechanism of plain concrete beam. Similar as in the present study, the recent numerical studies (Ožbolt & Reinhardt, 2005a,b) show that for lower loading rates (bending failure) the rate sensitive response is controlled by local inertia forces at the crack tip. In numerical analysis this is accounted for by the rate dependent constitutive law of concrete. Furthermore, it is shown that for high and extremely high strain rates (shear failure mode), the structural inertia forces govern structural response and that the rate dependency at the constitutive level is much less important. The consequence is that the structural response is strongly dependent on the geometry of the structure. The same turns out to be the case in the present numerical study, what implies that, in contrary to lower loading rates, for higher loading rates bending reinforcement would have no or little effect on the failure mode that is of shear type.

10.4 Concrete block – penetration analysis

To test the presented FE adaptive procedure, the numerical experiment is conducted by simulating the impact event of a steel nail with the concrete block. Due to the complexity of the problem, a brief overview of necessary requirements concerning the numerical description are hereafter given.

10.4.1 Numerical requirements

Obviously, large displacements and finite strains are needed in order to realistically model the concrete behavior at the front of the nail. Dynamic analysis is required to predict the transformation of nail kinetic energy into strain energy of a concrete block. The cracking and damage phenomena are modeled with a smeared crack approach and the objectivity of the results is assured by the use of the crack band approach (Bažant & Oh, 1983). Before illustrating the result of the numerical simulation, there are two numerical aspects that should be separately addressed.

10.4.1.1 Critical time increment

The adaptive finite element procedure automatically entails further consideration of the critical time increment Δt_{cr}, that arises as a stability condition of the explicit time integration. Resume, in order to preserve the physical meaning of the numerical results, the adopted time step Δt must be smaller than the critical one Δt_{cr} (4.33).

Since the remeshing procedure changes the FE geometry *a-priori*, the temporal variations of Δt_{cr} should be taken into account. However, if no remeshing procedure is applied, the variations of Δt_{cr} will be still present but as a smoothed curve in time. Furthermore, apart from the geometrical property of FE mesh, Δt_{cr} is also influenced by the change in stiffness. In case of materials like concrete, the progressive stiffness degradation obviously causes changes of Δt_{cr}. However, the changes produced by stiffness degradation are smoother than the changes caused by the remeshing procedure and they usually cause less serious consequences on the numerical analysis. Namely, the remeshing procedure will occasionally cause jumps of Δt_{cr} that can transverse the adopted time step Δt and make it inadequate for proceeding with the numerical analysis.

Note that time step Δt should not be adapted with respect to the current Δt_{cr}. Namely, the adaptation will cause that the displacement vector $\mathbf{u}_n$ and the displacement vector $\mathbf{u}_{n-1}$ in Eq. (4.30) would be temporarily non-consistent. Such non-consistency could produce numerical instability, often viewed as the fluctuation of the total system energy, and lead to numerical divergence.
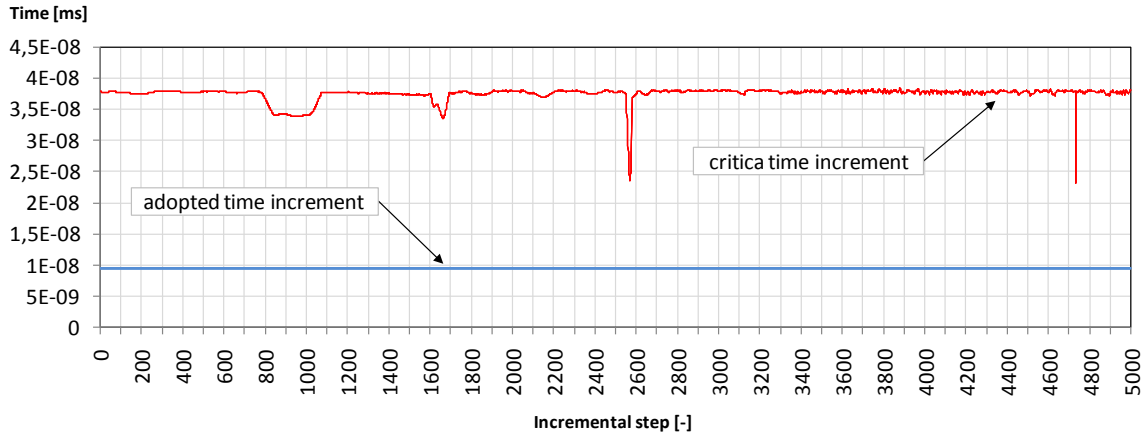
Figure 10.20 Progressive changes in Δt_{cr} and the adopted Δt for the numerical example given in Figure 10.22

The discussed inconvenient side effect of remeshing can be bypassed by assuming the first time increment Δt (calculated for the first mesh at the beginning of the numerical simulation) reasonably lower than any critical future time increment Δt_{cr}. Obviously, the exact prediction of the later generated Δt_{cr} is not possible, but it is possible to exclude eventual extreme values. For the sake of illustration, Fig. 10.20 shows changes in Δt_{cr} with respect to time increments of the analysis and the assumed time increment Δt that has allowed a correct execution of the computation.

10.4.1.2 Boundary conditions

The second numerical aspect is related to specification of boundary conditions. In order to simulate the penetration of the nail correctly, mention that it is common engineering practice to set a steel plate. The plate has an opening which allows the nail to pass through. Namely, the impact of the nail at concrete surface cause local damage in form of spalling of concrete boundary layer (Fig. 10.21). Therefore, the purpose of the steel plate is obvious. It should be also mentioned that the impact event without the steel plate can be treated numerically as well, provided that the continuum fragmentation is included, which enables the separation of elements from discretized concrete block. However, since the continuum fragmentation is here not yet included, an alternative is introduced.

Note also that at the numerical implementation level, the penetration scenario cannot be simulated only by assuming two bodies under mechanical interactions (concrete-nail). This is due to the fact that the mechanical interaction between the concrete block and the steel plate is present as well. An appropriated strategy will by the multi body contact analysis.

However, because of simplicity, the nodes at the surface of the concrete, that are close to the impact point, are fixed in direction of impact. This is a reasonable assumption the enable to perform the computation.
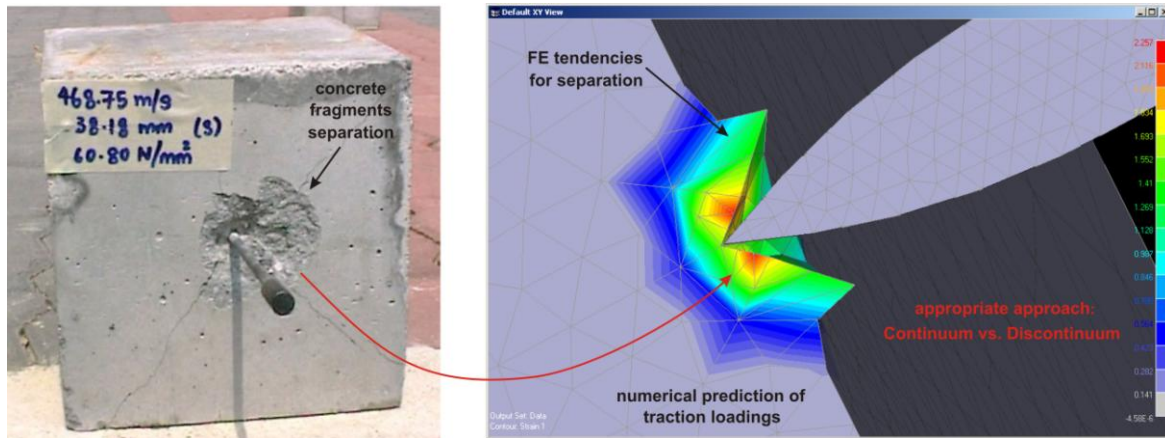
Figure 10.21 Experimental evidence and numerical prediction of damage zones around the zone of impact

10.4.2 Numerical simulation

It is very important to mention that in the present result, which is based on the numerical formulation under isothermal condition, the temperature over the contact surface is not accounted for. However, the experimental observations reveal that the presence of elevated temperature on the contact interface significantly influences the concrete mechanical behavior. Indeed, once the nail penetrates into the concrete block, the consequences of thermo-mechanical effects are responsible for its bearing capacity.

The dimensions of the concrete block are: length-height-width = $500 \times 500 \times 500$ mm. The mechanical properties of concrete are: Young's modulus $E_c = 30000$ N/mm^2, Poisson's ratio $\upsilon = 0.18$, uni-axial compressive strength $f_c = 45.0$ N/mm^2, tensile strength $f_t = 2.70$ N/mm^2, fracture energy $G_F = 0.10$ N/mm and concrete mass density $\rho_c = 2300$ kg/m^3. The mechanical behavior of the nail is assumed to be linear elastic with Young's modulus of 200000 N/mm^2 and mass density of 8000 kg/m^3. On the contact surface the frictional coefficient μ is assumed to be equal 0.5. The load is applied through the kinetic energy of nail. The numerical analysis is performed for nail impact velocity of 200 m/s. Unfortunately, since the analysis was performed on a single-processor laptop computer, the numerical simulations had to be stopped before the nail fully penetrated the concrete block due to the very high demand on CPU-time.

Fig. 10.22 shows the sequence of the nail penetration history, where, qualitative prediction is in accordance with the experimental observations. The mesh adaptation (remeshing) progressively increases the number of finite elements around the contact zone, enabling the continuous mesh adaptation of the contact surface. However, the mesh density out of the contact area remained unchanged.
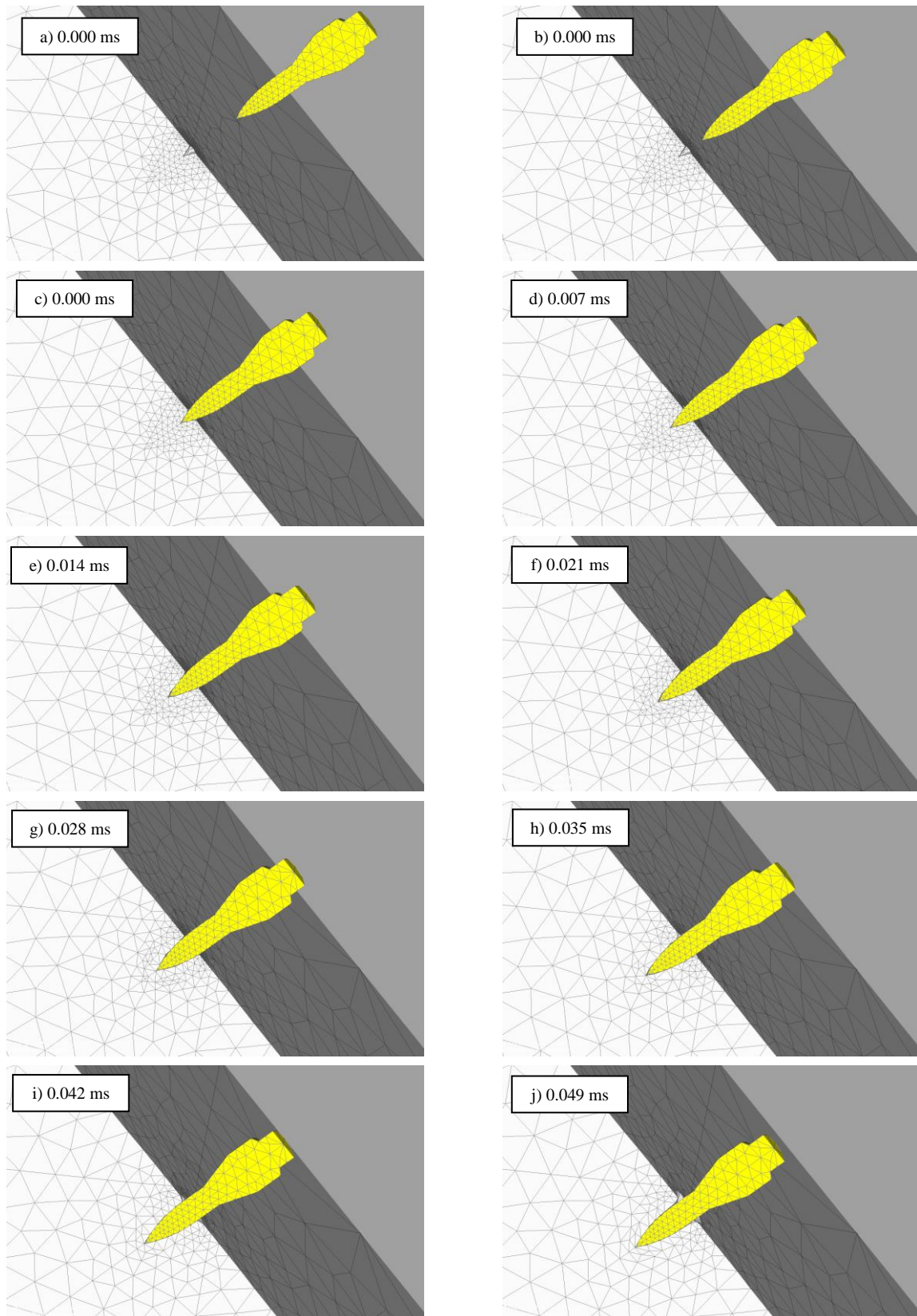
Figure 10.22 Sequences of nail penetration into a concrete block (progressive mesh adaptations)

10.4.2.1 Stress data transfer

The adequacy of the transfer operator T_2 and T_3 is proven by the asymmetric stress field σ_{13} illustrated in Fig. 10.23. Due to the frequent adaptations during the analysis, the mapping was performed 47 times. The consistency and the symmetry of the absolute stress value remained well preserved what confirms that the used mapping procedure is appropriated.
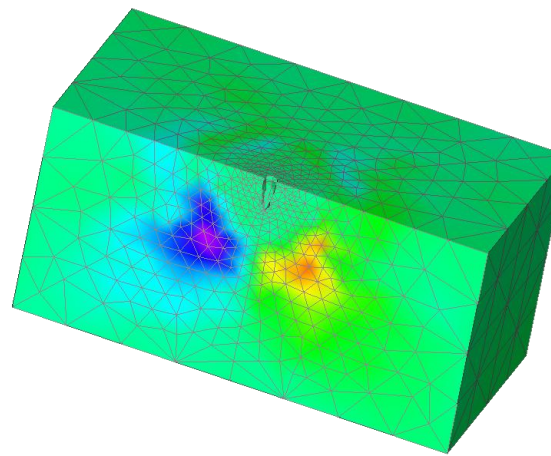

Figure 10.23 σ_{13} at the end of the numerical simulation

10.4.2.2 Stress oscillations

Apart from the remeshing and refinement procedures that showed to be suitable for the simulation of the penetration problem, the analysis of the outcome confirms that the transfer operators are adequate, as well. Indeed, the transfer operator T_2 used for the mapping of internal damage variables caused local stress oscillations. However, after the remeshing process, the induced oscillations disappear in the next few time steps (Fig. 10.24).

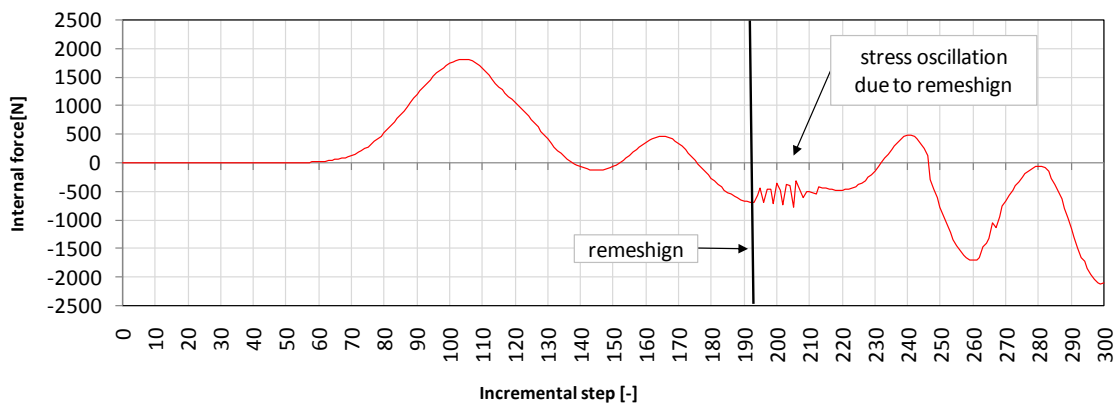**Figure 10.24** Oscillation of stresses after remeshing (after few time increments the oscillations disappear)

10.4.2.3 Velocity of penetration

As it was expected, the progressive degradation of the nail velocity has not been affected by the remeshing procedure performed on the concrete block (Fig. 10.25). Nevertheless, some minor oscillations of the nail velocity occurred after each remeshing procedure.
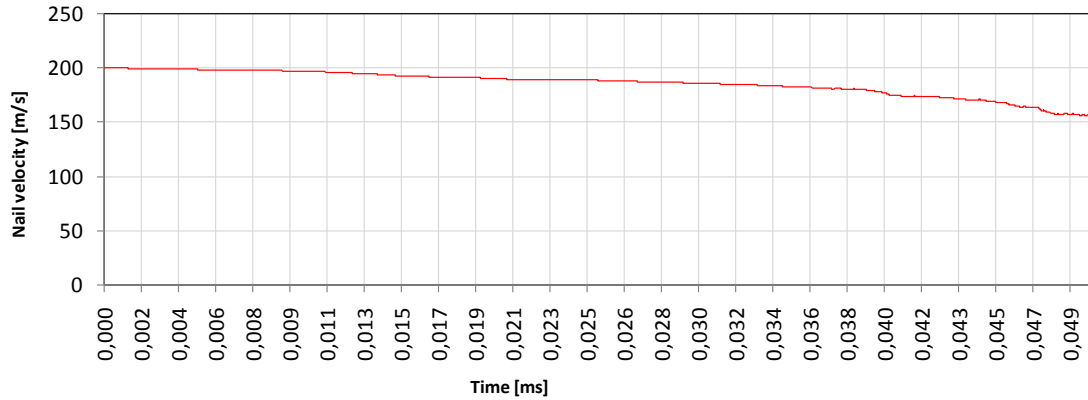
Figure 10.25 Nail velocity vs. time (computation stopped due to inappropriate CPU performance)

The abovementioned should be briefly discussed since in case of relatively larger contact surfaces Γ_c it may cause numerical instability. Namely, before each remeshing step, the internal forces on the contact interface Γ_c are in equilibrium. Since FE over Γ_c are the main reason for considering remeshing and refinement procedure (particularly the elements on the concrete block), it is clear that after such procedure the internal forces will not be exactly the same as before remeshing. Consequently, the next increment of the analysis must inevitably start from the non-equilibrated configurations. However, since the magnitude of residual forces is usually relatively small, the equilibrium state will be reached by iteration before the end of the current time increment.

10.4.2.4 Contact force

Since the contact forces are not history-dependent variable, their evolution is unaffected by remeshing procedure. As discussed earlier (*Chapter 6 – 6.4.1.4 Contact force interpolation*), the approximation of the contact force field is largely influenced by the spatial discretization over Γ_c (6.42). The contact force diagram related to the present numerical example, which was obtained according to the above introduced refinement procedure (8.5), is illustrated in Fig. 10.26.
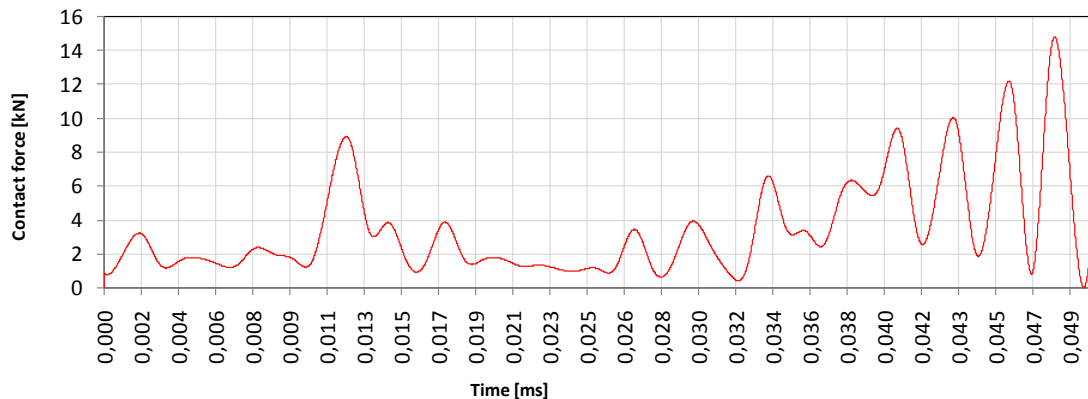
Figure 10.26 Predicted contact forces vs. time

10.4.3 Concluding remarks

The present numerical simulation demonstrated that the proposed finite element formulation is principally able to simulate complex problem of penetration of a nail into a concrete block. However, it should be mentioned that at the moment, only the first part of the author's intention has been solved (nail penetration). More difficult part, which is to numerically simulate the pull-out capacity after penetration, is not yet done.

According to the aforementioned remark, once the nail penetrates into the concrete body, the thermo-mechanical interaction on the contact surface has to be simulated in order to solve the nail pull-out problem. This is an especially intriguing and complex problem that should be dealt with in future. Furthermore, because of the complexity of the problem (material and geometrical nonlinearity, rate sensitivity, contact and remeshing), the program code has to be parallelized, and a more effective and a more robust mesh generator has to be used.

Chapter 11

Summary and conclusions

§ *Motivation*

In the present thesis, a three-dimensional finite element numerical formulation for concrete failure under high-energy impact loadings is proposed. Apart the evident importance of studying concrete response at impact load, the thesis arises from the motivation for simulating, and consequently studding concrete damage phenomena and non-elastic strain localization in impact analysis.

§ *Framework*

The numerical formulation lies in the framework of continuum mechanics and irreversible thermodynamics. In order to obtain an approximated solution of the displacement field, the finite element method is used to perform the discretization of governing differential equations in spatial regions occupied by bodies in collision. Particularly, the linear tetrahedral element is used for this purpose. According to the traditional practice, the temporal discretization is performed by finite difference method. Due to the non-linear nature of the event under

consideration, the solution process is based on the incremental–iterative solution strategy. For this purpose, the stresses and strains are calculated with respect to the system reference frame, which is successively updated according to the Update Lagrange formulation of finite strain.

§ *Rate sensitivity*

In order to numerically simulate the rate deepened response of concrete, which is widely evidenced in experimental tests, the model for strain rate dependency is based on the energy activation theory of bond ruptures. Accordingly, for static and quasi-static loading conditions, the proposed numerical formulation is sensitive to the rate dependency related to formation of microcracks and to creep of concrete between the microcracks. On the other hand, for elevated strain rates, the dominant influence of inertial forces is not included in the model. This is due to the fact that the inertial influence is not a part of the constitutive law. However, it emerges automatically from the dynamic equilibrium equation from the direct interaction between the constitutive law and inertial forces.

§ *Constitutive law*

The rate dependency model is implemented in the thermodynamically consistent M2-O microplane model for concrete. The macro-micro transition is performed by projecting the macroscopic Green-Lagrange strain tensor on microplanes with different orientations. Particularly, the microplane strains are calculated according to the relaxed kinematic constraint principle. Damage and cracking phenomena are modeled within the concept of smeared cracks. To assure objectivity of the analysis with respect to the size of the finite elements, the crack band method is used.

§ *Contact mechanics*

To perform a non-unilateral contact/impact analysis, the displacement solution space is restricted by the Lagrangian multipliers method. However, to preserve the benefits of the explicit time integration scheme, the contact description is formulated according to the forward incremental Lagrangian multipliers method. The energy dissipation related to friction is represented by the phenomenological Coulomb model. Its numerical implementation is conducted by performing a monitoring of contact reaction forces and relaxation of tangential displacements.

§ *Implementation*

To validate the proposed numerical formulation, the presented procedures are implemented into a program code named NACFAIL (**N**umerical **A**nalysis of **C**oncrete **Fa**ilure at **I**mpact **L**oading). For this purpose, the computer language FORTRAN95 has been used. All the subroutines are translated into a set of computational instructions by the Lahey/Fujitsu LF95 Compiler for 32-bit computational architecture.

§ *Verification*

The free fall drop weight experiment is numerically simulated in order to validate the proposed numerical formulation. In particular, the mass of the dropping hammer is assumed constant and the parametric study is obtained by varying the impact velocity i.e. the dropping altitudes. The dropping altitudes were prescribed to reproduce impact loadings of 2, 4, 6 and 8 m/s. All numerical simulations clearly predict the failure modes obtained by experiments. Namely, in case of relatively low impact loadings, i.e. quasi-static loading conditions, NACFAIL clearly predict the expected bending failure mode. However, by increasing the impact velocity up to 4 m/s, the failure mode is characterized by dominating bending crack enriched with two inclined lateral damage zones, which can be interpreted as incoming cracks at more elevated impact velocities. Furthermore, by increasing the impact velocity up to 6 m/s, a transition failure mode is obtained. The mode is characterized by a dominating bending crack and shaped shear fractures, not entirely articulated yet. In fact, for impact velocities of 6 m/s and 8 m/s, NACFAIL predicts the mixed mode of failure. From the perspective of beam failure modes, it is concluded that the numerical formulation is able to correctly predict failure mechanisms that dominate the beam rupture.

It is also demonstrated that the proposed finite element code is principally able to simulate complex problem of penetration of a steel anchor into a concrete block. However, due to the complexity of such events, the aim of the present numerical study is to establish numerical basis and directions for the development of numerical procedures that would deal with these problems in a more accurate manner. Indeed, mention that the final objective is to find the optimal shape of a nail (or anchor); such that the energy necessary for the pushing of the nail into a concrete is minimal but ensures maximal pull-out capacity. The solution lies in the simulation of the thermo-mechanical interaction on the contact interface. However, due to the complexity of the problem (material and geometric nonlinearity, rate sensitivity, contact and remeshing), it is clear that the program code had to be first parallelized.

§ *Conclusions*

Based on the experimental and numerical results obtained in the study of rate dependent failure of plain concrete beam under impact load, the following can be concluded. (i) Loading rate has significant influence on the resistance and failure mode of plain concrete beam. The comparison between numerical and experimental results shows that the used numerical model is able to correctly predict the rate dependent failure of plain concrete beam. (ii) For quasi-static load and relatively low impact load velocity, the beam fails in bending (mode- I fracture). With increase in impact velocity there is a transition of failure mode from dominant bending to dominant shear and the failure tends to be localized closer to impact zone. (iii) For relatively low strain rates (mode-I fracture) local inertia forces at the micro-crack tip control the beam response. The rate dependent constitutive law for concrete can account for the rate dependent response. For higher loading rates the influence

of loading rate on the beam response is mainly controlled by structural inertia forces. Consequently, for higher loading rates the geometry (size) of the beam should have significant influence on the failure. (iv) Because of the change of failure mode with increase in loading rate from bending to shear, in reinforced concrete beams loaded by higher loading rates, bending reinforcement would be ineffective. Instead, the shear reinforcement is required to prevent failure. (v) Velocity of the bending crack tip increases almost linearly up to the peak value of approximately 0.55 Rayleigh wave speed. The maximal velocity only slightly increases with the increase of impact velocity. The analysis indicates branching of bending crack. (vi) Further studies are needed to investigate dynamic crack propagation in more detail.

§ *Future work*

The future work will be primarily dedicated to parallelization of NACFAIL.

Bibliography

Ballew, D.W. (2004): ***Taylor Impact Test and Penetration of Reinforced Concrete Targets by Cylindrical Composite Rods***, thesis submitted to the Faculty of the Virginia Polytechnic Institute and State University in partial fulfillment of the requirements for the degree of Master of Science.

Başar, Y. & ***Weichert***, D. (2000): ***Nonlinear continuum mechanics of solids***, ***Fundamental mathematical and physical concepts***, Springer.

Batdorf, S.B. & ***Budianski***, B. (1949): ***A mathematical theory of plasticity on the concept of slip***, Technical Note No. 1871, National Advisory Committee for Aeronautics, Washington, DC.

Bathe, K.J. (1996): ***Finite element procedure***, 1996 by Prentice-Hall, Inc., Simon & Schuster / A Viacom Company, Upper Saddle River, New Jersey 07458, ISBN 0-13-301458-4.

Bažant, Z.P. & ***Caner***, F.C. (2005): ***Microplane model M5 with kinematic and static constraints for concrete fracture and anelasticity***. I: Theory, Journal of Engineering Mechanics-ASCE, 131 (1): 31-40. ISSN: 0733-9399.

Bažant, Z.P. & ***Gambarova***, P. (1984): ***Crack shear in concrete: Crack band microplane model***, Journal of Engineering Mechanics, ASCE 110, pp 2015-2035.

Bažant, Z.P. & ***Gettu***, R. (1992): ***Rate effect and load relaxation in static fracture of concrete***, ACI Material Journal, 89, pp 456–468.

Bažant, Z.P. & ***Oh***, B.H. (1983): ***Crack band theory for fracture of concrete***, Material and Structures, RILEM, 93 (16), pp 155-177.

Bažant, Z.P. & ***Oh***, B.H. (1986): ***Efficient numerical integration on the surface of a sphere***, Zeitschrift für angewandte Mathematik und Mechanik, ZAMM 66 (1), pp 37-49.

Bažant, Z.P. & ***Prat***, P.C. (1987): ***Creep of anisotropic clay: new microplane model***, Journal of Engineering Mechanics, ASCE 103 (7), pp 1050-1064.

Bažant, Z.P. & ***Prat***, P.C. (1988): ***Microplane model for brittle-plastic material - parts I and II***. Journal of Engineering Mechanics, ASCE, 114, pp 1672-1702.

Bažant, Z.P. (1997): ***Recent advances in Brittle-Plastic Compression Failure: Damage localization, Scaling and finite strain***, Computational plasticity: Fundamentals and Applications (Proc.,5th Int. Conf. On Comput. Plasticity, COMPLAS 5, held in Barcelona), D.R.J. Owen, W. Oñate and E. Hinton, Eds., publ. By Int. Center for Num. Meth. In Engrg., Barcelona, pp 3-19.

Bažant, Z.P., ***Adley***, M.D., ***Carol***, I., ***Jirásek***, M., ***Akers***, S.A., ***Rohani***, B., ***Cargile***, J.D. & ***Caner***, F. (2000a): ***Large strain generalization of microplane model for concrete and application***, Journal of Engineering Mechanics ASCE, 126, pp 971-980.

Bažant, Z.P., ***Caner***, F.C., ***Adley***, M.D., & ***Akers***, S.A. (2000b): ***Fracturing, rate effect and creep in microplane model for dynamics***, Journal of Engineering Mechanics, ASCE, 126(9), pp 962-970.

Belytschko, T., ***Liu***, W.K. & ***Moran***, M. (2001): ***Nonlinear Finite Elements for Continua and Structures***, John Wiley & Sons Ltd., Baffins Lane, Chichester, West Sussex PO19 1UD, England, ISBN 0-471-98773-5 (Cloth).

Bentur, A., ***Mindess***, S. & ***Banthia***, N. (1986): ***The behaviour of concrete under impact loading: Experimental procedures and method of analysis***, Materials and Structures / MatOriaux et Constructions, Vol. 19 - N ~ 113.

Bonet, J. & ***Wood***, R.D. (1997): ***Nonlinear continuum mechanics for finite element analysis***, published by the press syndicate of the University of Cambridge, The Pitt Building, Trumpington Street, Cambridge CB2 1RP, United Kingdom, ISBN 0-521-57272-X.

Bowen, R.M. (2007): ***Introduction to continuum mechanics for engineers*** (revised edition), First Edition Originally Published by Plenum Press 1989 as Volume 39 of Mathematical Concepts and Methods in Science and Engineering, ISBN 0-306-43050-9.

Brodersen, B. (2004): ***Ogden type materials in non-linear continuum mechanics***, Institut für Angewandte Mechanik, Spielmannstr, 11, 38106 Braunschweig, Germany.

Buchar, J., *Voldřich*, J., *Rolc*, S. & *Lazar*, M. (2002): ***Response of concrete to the impact of fragments simulating projectiles***, 20th International symposium on ballistics, Orlando, FL, pp 23–27.

Carol, I. & *Bažant*, Z.P. (1997): ***Damage and plasticity in microplane theory***, International Journal of Solids and Structures 34 (29), pp 3807-3835.

Carol, I., *Jirásek*, M. & *Bažant*, Z.P. (2001): ***A thermodynamically consistent approach to microplane theory: Part I, Free energy and consistent microplane stresses***, International Journal of Solids and Structures, 38, pp 2921-2931.

Carpenter, N.J., *Taylor*, J.R. & *Katona*, M.G. (1991): ***Lagrange constraints for transient finite element surface contact***, International Journal for numerical methods in engineering, Vol. 32, pp 103- 128.

Chaboche, J.L. (1988): ***Continuum damage mechanics - Part I***: General concepts and ***Part II***: Damage growth, crack initialization and crack growth, Journal of Applied Mechanics 55, pp 59-72.

Chawla, V. & *Laursen*, T.A. (1998): ***Energy Consistent Algorithms for Frictional Contact Problems***, International Journal for Numerical Methods in Engineering, 42, pp 799-827.

Cheng Zhu, M., *Quan Liu*, L. & *Sou-Yizheng* (1993): ***A mesh stability study of FEM explicit algorithms for structural large-scale deformation impact responses***, Acta Mechanica Solida Sinica (English Edition), Vol. 6, No. 3, Co-published by HUST and Pergamon Press.

Cirak, F. & *West*, M. (2005): ***Decomposition contact response (DCR) for explicit finite element dynamics***, International Journal for Numerical Methods in Engineering, 68 (8), pp 1078-1110, ISSN 0029-5981.

Comite Euro-International Du Beton - CEB (1988): ***Concrete Structures under Impact and Impulsive Loading***, Synthesis Report, Bulletin D'Information N0 187.

Crisfield, M.A. (1991): ***Non-linear finite element analysis of solids and structures***, Volume 1: Essentials, John Wiley & Sons, Bafins Lane, Chichester, West Sussex PO19IUD, England, ISBN 0471929565.

Crisfield, M.A. (2000): ***Non-linear finite element analysis of solids and structures***, Volume 2: Advanced topics, John Wiley & Sons, Bafins Lane, Chichester, West Sussex PO19IUD, England, ISBN 0 471 95649 X.

Dilger, W.H., *Koch*, R. & *Kowalczyk*, R. (1978): ***Ductility of plained and confined concrete under different strain rates***, American Concrete Institute, Special publication, Detroit, Michigen, USA.

Eligehausen, R., *Popov*, E.P. & *Bertero*, V.V. (1983): ***Local bond stress-slip relationship of deformed bars under generalized excitations***, Report No. UCB/EERC-83/23, Earthquake Engineering Research Center, College of Engineering, University of California, Berkeley, CA.

Freund, L. B. (1972a): ***Crack Propagation in an Elastic Solid Subjected to General Loading – PART I: Constant Rate of Extension***, Journal of the Mechanics and Physics of Solids, Vol. 20, pp 129-140.

Freund, L. B. (1972b): ***Crack Propagation in an Elastic Solid Subjected to General Loading – PART II: Non-uniform Rate of Extension***, Journal of the Mechanics and Physics of Solids, Vol. 20, pp 141- 152.

Gharehbaghi, S.A. & *Khoei*, A.R. (2008): ***Three-dimensional superconvergent path recovery method and its application to data transferring in small-strain plasticity***, International Journal of Computational Mechanics, 41, pp293-312.

Hirota, G. (2002): ***An Improved Finite Element Contact Model for Anatomical Simulations***, Dissertation, faculty of The University of North Carolina at Chapel Hill, Doctor of Philosophy in the Department of Computer Science.

Hutter, M., & *Fuhrmann*, A. (2007): *Optimized continuous collision detection for deformable triangle meshes*, research grant KF0157401SS5 in the PRO INNO II program, Germany.

Hutton, D.V. (2004): *Fundamentals of finite element analysis*, Published by McGraw-Hill, a business unit of The McGraw-Hill Companies, Inc., 1221 Avenue of Americans, New York, NY 10020, ISBN 0-07-239536-2.

Jirásek, M. (1993): *Modeling of Fracture and Damage in Quasibrittle Materials*, Dissertation, Northwestern University.

Kloosterman, G. (2002): *Contact Methods in Finite Element Simulations*, Printed by Ponsen & Looijen, Wageningen, Proefschrift Enschede. -Met lit. opg. –Met, samenvatting in het Nederlands, ISBN 90-77172-04-1.

Krausz, A.S. & *Krausz*, K. (1988): *Fracture kinetics of crack growth*, Kluwer, Dordrecht, The Netherlands.

Kuhl, E. & *Ramm*, E. (1998): *On the linearization of the microplane model*, Mechanics of Cohesive-Frictional Materials 3, pp 343-364.

Kuhl, E., *Ramm*, E. & *de Borst*, R. (2000): *An anisotropic gradient damage model for quasi-brittle materials*, Computer methods in applied mechanics and engineering, 183, pp 87-103.

Kuhl, E., *Steinman*n, P. & *Carol*, I. (2001): *A thermodynamically consistent approach to microplane theory: Part II, Dissipation and inelastic constitutive modeling*, International Journal of Solids and Structures, 38, pp 2933-2952.

Lai, W.M., *Rubin*, D. & *Krempl*, E. (1993): *Introduction to Continuum Mechanics* (Third edition), First published by Pergamon Press Ltd 1993, Reprinted in 1999 by Butterworth Heinemann is an imprint of Elsevier, 200 Wheeler Road, Burlington, MA 01803, ISBN 0 7506 2894 4.

Laursen, T.A., *Attaway*, S.W. & *Zadoks*, R.I. (1999): SEACAS Theory manual: Part III. *Finite element analysis in nonlinear solid mechanics*, Sandia report, Prepared by Sandia National Laboratories, Albuquerque, New Mexico 87185 and Livermore, California 94550, SAND98-1760/3.

Lehmann, L. (2008): *Lecture notes on solid mechanics*, Institut für Angewandte Mechanik, Technische Universität Braunschweig, Institute of Applied Mechanics, 38106 Braunschweig, www.infam.tu-braunschweig.de

Lemaitre, J. (1996): *A Course on Damage Mechanics*, Springer Verlag, ISBN 3540609806.

Liu, G.R. & *Quek*, S.S. (2003): *The finite element method – A practical course*, Butterworth-Heinemann, An imprint of Elsevier Science, Linacre House, Jordan Hill, Oxford OX2 8DP, 200 Wheeler Road, Burlington MA 01803.

Lubarda, V.A. (1999): *Deformation theory of plasticity revisited*, The Montenegrin Academy of Sciences and Arts, Messenger of the section of natural sciences, Vol. 13.

Malvern, L.E. (1969): *Introduction to the mechanics of a continuous medium*, Prentice Hall, Englewood Cliffs, New Jersey.

Marsden, J. & *Hughes*, T.J.R. (1983): *Mathematical foundations of elasticity*, Prentice Hall, Englewood Cliffs, New Jersey.

May, I.M., *Chen*, Yi, *Owen*, D.R.J., *Feng*, Y.T. & *Bere*, A.T. (2005): *Experimental testing and finite element simulation of the behaviour of reinforced concrete beams under impact loading*, VIII International Conference on Computational Plasticity, E. Oñate and D. R. J. Owen (Eds), CIMNE, Barcelona, 2005.

Nam, T.H. (2004): *Mechanical properties of the composite material with elastomeric matrix reinforced by textile cords*, Dissertation, Technical University of Liberec, Faculty of mechanical engineering.

Němeček, J., *Patzák*, B., *Rypl*, D. & *Bittnar*, Z. (2002): *Microplane models: computational aspects and proposed parallel algorithm*, Computers and structures, 80, pp 2099-2108.

Newmark, N.M. (1959): ***A method of computation for structural dynamics***, ASCE Journal of the Engineering Mechanics Division, Vol. 85n No. EM3.

Ngo, T. & *Mendis*, P. (2008): ***Computer simulation of concrete structures subjected to blast and impact***, Electronic Journal of Structural Engineering (8).

Nguyen, G.D. (2005): ***A Thermodynamic approach to constitutive modelling of concrete using damage mechanics and plasticity theory***, Dissertation, Trinity College at the University of Oxford.

Ožbolt, J. & *Bažant*, Z.P. (1992): ***Microplane model for cyclic triaxial behaviour of concrete***, Journal of Engineering Mechanics, ASCE 118 (7), pp 1395-1386.

Ožbolt, J. & *Bažant*, Z.P. (1996): ***Numerical smeared fracture analysis: Nonlocal microcrack interaction approach***, International Journal of Solids and Structures 39 (4), pp 635-661.

Ožbolt, J. & *Reinhardt*, H.W. (2001): ***Three-dimensional finite element model for creep-cracking interaction of concrete***, Proceedings of the sixth international conference CONCREEP-6, Ed. By Ulm, Bažant & Wittmann, pp 221-228.

Ožbolt, J. & *Reinhardt*, H.W. (2005): ***Rate dependent fracture of notched plain concrete beams***. Proceedings of the 7th international conference CONCREEP-7, Ed. By Pijaudier-Cabot, Gerard & Acker, pp 57-62.

Ožbolt, J., *Li*, Y. & *Kožar*, I. (2001): ***Microplane model for concrete with relaxed kinematic constraint***, International Journal of Solids and Structures, 38, pp 2683-2711.

Ožbolt, J., *Rah*, K.K. & *Meštrović*, D. (2006): ***Influence of loading rate on concrete cone failure***, International Journal of Fracture, DOI 10.1007/s10704-006-0041-3, 139: pp 239-252.

Pandolfi, A. & *Ortiz*, M. (2002): ***An efficient adaptive procedure for three-dimensional fragmentation simulations***, Engineering with Computers, 2002 Springer-Verlag London Limited, 18: pp 148–159.

Parisch, H. (1989): ***A consistent tangent stiffness matrix for three-dimensional non-linear contact analysis***, International Journal for Numerical Methods in Engineering, Vol. 28, pp 1803-1812.

Pivonka, P., *Ožbolt*. J., *Lackner*. R. & *Mang*, H.A. (2004): Comparative ***studies of 3D-constitutive models for concrete: application to mixed-mode fracture***, International Journal for Numerical Methods in Engineering, Volume 60 Issue 2, pp 549 – 570.

Prat, P.C. & *Gens*, A. (1994): ***Microplane formulation for Quasibrittle materials with anisotropy and damage***, In: Bažant, Z.P., Bittnar, Z., Jirásek, M., Mazars, J. (Eds.), Fracture and damage in Quasibrittle structures, E & Spon, pp 67-74.

Provot, X. (1997): ***Collision and self-collision handling in cloth model dedicated to design garments***, Canadian Information Processing Society, Canadian Human-Computer Communications Society In Graphics Interface, pp 177-189.

Ramm, E., *Erhard*, T. & *Wall*, W.A. (2005): ***Numerical modeling of transient impact processes with large deformations and nonlinear material behavior***, VIII International Conference on Computational Plasticity, E. Oñate and D. R. J. Owen (Eds), CIMNE, Barcelona, 2005.

Refaat, M.H. & *Meguid*, S.A. (1997): ***Updated Lagrangian formulation of contact problems using variational inequalities***, International Journal for Numerical Methods in Engineering, Vol. 40, pp 2975-2993.

Reinhardt, H.W. (1982): ***Concrete under impact loading - Tensile strength and bond***. Heron, Vol. 27, No.3.

Remennikov, A.M. & *Kaewunruen*, S. (2007): ***Resistance of railway concrete sleepers to impact loading***, Proceedings of the 7th International Conference on Shock and Impact Loads on Structures, Beijing, China, 17-19 October 2007, pp 489-496.

Ruigomez, J.M.G. (1985): ***Numerical modelling in large strain plasticity with application to tube collapse analysis***, Dissertation, A thesis submitted for the degree of Doctor of Philosophy in the Faculty of Engineering of the University of London.

Saatci, S. & **Vecchio**, J.V. (2009): ***Effect of Shear Mechanisms on Impact Behavior of Reinforced Concrete Beams***. ACI Structural Journal, Vol. 106, No. 1, pp 78-86.

Schlangen, E. (1993): ***Experimental and numerical analysis of fracture processes in concrete***, Proefschrift Technische Universiteit Delft. − Met lit., opg − Met samenvatting in het Nederlands, ISBN 90-9006167-3.

Shabana, A.A. (2008): ***Computational continuum mechanics***, Cambridge University Press, 32 Avenue of the Americas, New York, NY 10013-2473, USA, ISBN 978-0-521-88569-0.

Shen, J. (2000): ***Collision response analysis and fracture simulation of deformable objects for computer graphics***, Dissertation, A Thesis Submitted to the College of Graduate Studies and Research in Partial Fulfillment of the Requirements for the Degree of Doctor of Philosophy in the Department of Computer Science University of Saskatchewan.

Signorini, A. (1933): ***Sopra alcune questioni di elastostatica***, Atti della Societa Italiana per il Progresso delle Scienze.

Stoker, C. (1999): Developments ***of the arbitrary Lagrangian-Eulerian method in non-linear solid mechanics*** (applications to forming process), printed by FEBO druk, Enschede, ISBN 90-36512646.

Sukontasukkul, P. & **Mindess**, S. (2003): ***The shear fracture of concrete under impact loading using end confined beams***, Materials and Structures / Matdriaux et Constructions, Vol. 36, July 2003, pp 372-378.

Sukontasukkul, P., **Nimityongskul**, P. & **Mindess**, S. (2004): ***Measuring damage of concrete subjected to impact loading using the variations of elastic modulus***, Journal of Cement and Concrete Research (JCCR), Vol. 34, No. 11, Nov. 2004, pp 2127-2134.

Taylor, G.I. (1938): ***Plastic strain in metals***, Journal of the Institute of Metals 62, 307-324.

Taylor, R.L. (2002): ***A mixed-enhanced formulation for tetrahedral finite elements***, Internal report No. UCB / SEMM-99/02.

Truesdell, C. & **Noll**, W. (1992): ***The non-linear field theories of mechanics***, 2nd edition, Springer-Verlag (Berlin and New York), ISBN 3540550984.

Unosson, M. (2000): ***Numerical simulations of penetration and perforation of high performance concrete with 75mm steel projectile***, User report, Defence research establishment, FOA-R-00-01634-311-SE, ISSN 1104-9154.

Vossoughi, F., **Ostertag**, C.P., **Monteiro**, P.J.M. & **Albert**, R.D. (2006): ***Damage characterization of concrete panels due to impact loading by motionless X-ray laminography***, J Mater Sci, DOI 10.1007/s10853-006-0731-2, Springer Science + Business Media, LLC 2007.

Weerheijm, J. (1992): ***Concrete under impact tensile loading and lateral compression***, Dissertation, TU Delft, the Netherlands.

Weihe, S., **Kröplin**, B. & **de Borst**, R. (1998): ***Classification of smeared crack models based on material and structural properties***, International Journal of Solids Structures, Vol. 35, No.12, pp 1289-1308.

Willam, K.J., **Pramono**, E. & **Sture**, S. (1987): ***Fundamental issues of smeared crack models***, In: Shah, S., Swartz, S. (Eds.), SEM-RILEM Int. Conf. on Fracture of Concrete and Rock, pp 192-207.

Wilson, E.L. (1995): ***Static and dynamic analysis of structures***, Computers and Structures, Inc., 1995 University Avenue, Berkeley, California 94704 USA.

Wilson, E.L., **Taylor**, R.L., **Doherty**, W.P. & **Ghaboussi**, J. (1973): ***Incompatible displacement model***, In S.T. Fenves at al., Numerical and Computer Methods in Structural Mechanics, Academic Press, New York, pp 43-47.

Wriggers, P. (2002): ***Computational Contact Mechanics***, John Wiley & Sons Ltd, the Atrium, Southern Gate, Chichester, West Sussex PO19 8SQ, England.

Zienkiewicz, O.C. & ***Taylor***, R.L. (2002): ***Finite element method – For solid and structural mechanics***, Sixth edition, Elsevier Butterworth-Heinemann, Linacre House, Jordan Hill, Oxford OX2 8DP, 30 Corporate Drive, Burlington, MA 01803, ISBN 0 7506 6321 9.

Zienkiewicz, O.C. & ***Zhu***, J.Z. (1987): ***A simple error estimator and adaptive procedure for practical engineering purpose***, International Journal for Numerical Method in Engineering, 101, pp 207-224.

Zienkiewicz, O.C. & ***Zhu***, J.Z. (1992): ***The superconvergent path recovery (SPR) and a posteriori error estimates, Part I: the recovery technique***, International Journal for Numerical Method in Engineering, 33, pp 1331-1364.

Zienkiewicz, O.C., ***Taylor***, R.L. & ***Zhu***, J.Z. (2000): ***Finite element method – Its basis & fundamentals***, Sixth edition, Elsevier Butterworth-Heinemann, Linacre House, Jordan Hill, Oxford OX2 8DP, 30 Corporate Drive, Burlington, MA 01803, ISBN 0 7506 6320 0.

Zinn, R., ***Stangenberg***, F., ***Borgerhoff***, M., ***Chauvel***, D. & ***Touret***, J-P. (2007): ***Non-linear behaviour of concrete structures under severe impact***, Comportement non lineaire de structures en beton soumises a un choc severe, CONSEC'07 Tours, France.

Licensed programs

FEMAP – Finite Element Modeling and Post-processing, Version 7.0, Copyright © Structural Dynamics Research Corporation, SDRC – FEMAP, P.O. Box 1172, Exton, PA 19341, (610) 458-3660, fax: (610) 458-3665, e-mail: info@fmap.com, web: htpp://www.femap.com.

FORTRAN90 – ED – The Power Editor for Windows, Developed by: Neville Franks, Copyright © Soft As It Gets P/L 1991-1998, Ph. +61 3 9885 4445, fax: +61 3 9885 4444, e-mail: support@gestsoft.com, www: htpp://www.gestsorf.com, Version 3.80, Mar 16 1998.